Evaluatie en optimalisatie van verlijmde puntverbindingen
in toepassingen met constructief glas

Evaluation and Optimisation of Adhesive Point-Fixings in Structural Glass

Jonas Dispersyn

UNIVERSITEIT
GENT

For Lisa and Julia …

Acknowledgements

> I get by with a little help from my friends.
>
> *John Lennon*

Many people have contributed to this dissertation and I wish to thank all of them for their assistance and advice. Without them, this dissertation would not have been possible.

First of all, I would like to thank my supervisors Rudy Van Impe and Jan Belis. Thank you Rudy, for inspiring me through your courses to start research in structural engineering. Thank you Jan, for the vivid and passionate guidance and for the practical input. Your availability, helping hand, enthusiasm and interest during the past five years, were a big help and support. I could not have imagined having a better advisor and mentor for my PhD study. And last but not least thank you for the pleasant atmosphere you created at the Laboratory for Research on Structural Models (LMO).

Besides my advisors, I would like to thank the rest of my PhD jury: Luc Taerwe, Paul Ludwig Geiß, Stijn Hertelé, Christian Louter, Delphine Sonck and Dieter Callewaert. It was an honour to have insightful discussions with you during the thesis defence that undoubtedly improved the quality of my work.

During my PhD, I had the opportunity to join several international scientific teams. In particular, I would like to thank Christoph Odenbreit, Mike Tibolt and Vincent Dias for my stay at University of Luxembourg, Christiaan Louter and Manuel Santarsiero at École polytechnique fédérale de Lausanne and Paul Ludwig Geiß at Technische Universität Kaiserslautern. Thank you for the interesting and inspiring conversations we had and the nice and fun stay at your institutes. I would also like to express my gratitude to the colleagues that I encountered at training schools and international conferences. Vlad Silvestru, Jagoda Cupać, Joren Pelfrene, James Watson, Matthias Seel, Michal Netušiln, Klára Machalická, Dragos Stan and Fransesc Arbós Bellapart, thank you for the stimulating discussions and for all the fun we have had in the past five years.

Table of contents

Part II: Experimental and numerical work   29

Part IV: Appendices 231

Acronyms and symbols

Acronyms

3M	3M™ Scotch-Weld™ 9323 B/A
AISI	American Iron and Steel Institute
C	Compression
CBT	Corrected Beam Theory
CTOD	Crack Tip Opening Displacement
DAQ	Data Acquisition
DIC	Digital Image Correlation
DMA	Dynamic Mechanical Analysis
DMTA	Dynamic Mechanical Thermal Analysis
DSC	Differential Scanning Calorimetry
ECM	Experimental Compliance Method
EET	Enhanced Effective Thickness
EPDM	Ethylene Propylene Diene Monomer
EPFM	Elastic Plastic Fracture Mechanics
EVA	Ethylene Vinyl Acetate
FEA	Finite Element Analysis
GCC	Glass Consequence Class
GRP	Glass Reinforced Plastic
IGU	Insulating Glass Units
IP	Ionoplastic Polymers
ISE	Institution of Structural Engineers
LEFM	Linear Elastic Fracture Mechanics
LG	Laminated Glass
LVDT	Linear Variable Differential Transformer
MS	Modified Silane
NE	Nominal Strain
PEEK	Polyether Ether Ketone
POM	Polyoxymethylene
PTFE	Polytetrafluoroethylene
PVB	Polyvinylbutyral

RH	Relative Humidity
RHS	Rectangular Hollow Section
S	Shear
SBT	Simple Beam Theory
SG	SentryGlas®
SLG	Superposition of Local and Global component
SLJ	Single-Lap Joint
SLS	Service Limit State
SO	Soudaseal 270 HS
SSGS	Structural Sealant Glazing System
T	Tension
TAST	Thick Adherent Shear Test
TLC	Thin-Layer Cohesive failure
TR	Trace of a square matrix
TS	Technical Specification
ULS	Ultimate Limit State
UTM	Universal Testing Machine
UV	Ultraviolet

Symbols

A	Instantaneous cross sectional area
A	Corner distance
A_0	Initial cross-sectional area
B	left Gauchy-Green tensor
B	Corner distance
C	Edge distance
C_{ij}	Material constants
D	Corner distance
E	Young's modulus
E'	Storage (elastic) modulus
E''	Loss (viscous) modulus
$E_{adhesive}$	Adhesive Young's modulus
F	Applied force
G_0	Instantaneous shear modulus
G_i	Shear moduli associated with the i-th Maxwell element

G_{inter}	Shear modulus of the polymeric interlayer
K_m	Multiplication parameter
L	Final length of the specimen
L_0	Initial length of the specimen
ΔL	Deformation of the specimen
N, Q, M	Support reactions of the point-fixings
P_d	Resulting design force
R^2	Coefficient of determination
T_g	Glass transition temperature
U	Deflection of the glass
W	Strain energy function
b	Width of the specimen
b_m	Relevant pane width
$c_e(z)$	Exposure factor
c_0	Orography factor
c_{pe}	Pressure coefficient for external pressure
c_{pi}	Pressure coefficient for internal pressure
d_s	Shear displacement of the adhesive
e	Eccentricity
$f_{b,k}$	Characteristic value of the bending strength of prestressed glass
$f_{g,k}$	Characteristic value of the bending strength of glass
$\hat{h}_{eff,w}$	Deflection-effective thickness
h_i	Thickness of the i-th glass panel
$\hat{h}_{i,eff,\sigma}$	Stress-effective thickness
k	Stress concentration factor
k_0, k_1, k_2	Experimentally determined constants
k_i	Geometrical and material coefficients
k_l	Turbulence factor
k_{mod}	Factor for load duration
k_{sp}	Factor for glass surface profile
k_v	Factor for strengthening of prestressed glass
l	Overlap length of the adhesive layer
n_C	Number of test data for testing compression
n_S	Number of test data for testing shear
n_T	Number of test data for testing tension

q_b	Basic velocity pressure
$q_p(z_i)$	Peak velocity pressure
r_0	Initial radius of the specimen
$t_{adhesive}$	Adhesive thickness
t_{glass}	Glass thickness
v_b	Basic wind velocity
w_i	Wind pressure acting on internal surfaces of a structure
$\hat{y}_i$	Modelled data
$\bar{y}$	Average value
y_i	Test data
z_e	Reference height for external pressure
z_i	Reference height for internal pressure
γ	Shear strain
$\gamma_{M,a}$	Material partial factor for glass
$\gamma_{M,v}$	Material partial factor for prestressed glass
ε	Engineering or Cauchy strain
ε_T	True strain or Hencky strain
ε_x	Strain along the transversal axis
ε_y	Strain along the longitudinal axis
ε_z	Strain along the transversal axis
η	Non-dimensional shear parameter varying from zero (no shear transfer) to one (full shear transfer)
θ	Multi-axial angle
λ	Extension ratio
$\lambda_1, \lambda_2, \lambda_3$	Principal extension ratios
ν	Poisson's ratio
$\nu_{adhesive}$	Adhesive Poisson's ratio
ρ	Air density
$\sigma_1, \sigma_2, \sigma_3$	Principal stresses
σ_c	Principal compressive stress
σ_E	Engineering stress
σ_E	Experimental values for the stresses
$\sigma_{Fz}, \sigma_{Fxy}, \sigma_M$	Reaction stresses
σ_{global}	Global stress
σ_R	Design resistance of the glass element

σ_t	Principal tensile stress
σ_T	Theoretical values for the stresses
σ_T	True stress
σ_v	von Mises stress
σ_y	Yield strength
$\sigma_{\phi,max,d}$	Maximum tangential stress at the borehole
τ	Shear stress
τ_i	Relaxation times, associated with the i-th Maxwell element
ϕ	Connector diameter
ϕ_{hole}	Diameter of the borehole
ϕ_{loc}	Diameter of the local component

Material models

F	Deformation gradient tensor
G	Shear modulus
I_1, I_2, I_3	Invariants of the left Gauchy-Green deformation tensor
$\tilde{I}$	Generalized invariant
J_m	Value for the finite extension of the polymer chains in the Gent material model
N	Degree of the polynomial
T	Absolute temperature
a	Material parameter in the Van der Waals material model
k	Boltzmann constant
α_i	Material parameter in the Ogden material model
β	Material parameter in the Van der Waals material model
γ	Inverse of the Langevin function in the 8-Chain model
η	Material parameter in the Van der Waals material model
λ_m	locking stretch
λ_r	Relative elongation of the chain
μ	Shear modulus in the Gent material model
μ_i	Material parameter in the Ogden material model

Fracture Mechanics

A	Interfacial crack area
C	Compliance
G	Energy release factor
$G_{I,cr}$	Critical energy release factor for mode I
K_I	Stress intensity factor for mode I
$K_{I,cr}$	Critical stress intensity factor or fracture toughness
T	Tensile vector
Γ	Path which encloses the crack tip and with the start and end point on the two crack surfaces
U	Potential energy available for crack growth
V	Work associated with any external forces acting
W	Strain energy density

2a	Crack length
a_{ci}	Initial critical flaw depth
ds	infinitely small distance along path Γ
$f(\bar{a})$	Geometry factor
$f_{ct,inert}$	Inert strength corresponding to a constant loading
r_p	Magnitude of the plastic zone
r_y	Magnitude of the yielding zone
t	Glass thickness
u	Displacement vector
v	Crack propagation speed

σ	Normal stress
μ	Shear modulus

Samenvatting

De belangrijkste eigenschap van structureel glas, transparantie, heeft ervoor gezorgd dat het op grote schaal over de hele wereld wordt gebruikt en een integraal onderdeel is van de skyline van grote steden. Een traditioneel systeem om glas te verbinden met de onderliggende dragende constructie en om de globale transparantie te vergroten, zijn zogenaamde puntverbindingen. Met de huidige stand van techniek is het gebruikelijk om geboute puntverbindingen te gebruiken. Verlijmde puntverbindingen hebben echter verschillende voordelen ten opzichte van deze geboute puntverbindingen, zoals de mogelijkheid van spanningsherverdeling in het adhesief, geen verzwakking in het glas door de doorboring, het voorkomen van een koudebrug, etc. Deze voordelen, samen met de veelbelovende sterktewaarden, zijn belangrijke redenen waarom verlijmde puntverbindingen momenteel als een veelbelovend alternatief worden beschouwd.

In deze verhandeling is een ontwerpmethode voorgesteld voor glaspanelen ondersteund door verlijmde puntverbindingen middels een flowchart. De ontwerpmethode is gebaseerd op de tijd-efficiënte SLG-methode (Superpositie van Lokale en Globale componenten), ontwikkeld door Beyer voor het ontwerp van geboute puntverbindingen. Het ontwerp wordt verdeeld in twee onderdelen, namelijk het glasontwerp en het lijmontwerp. In het glasontwerp wordt de glasplaat gemodelleerd als de superpositie van een globale en een lokale component. Het numerieke globale model wordt opgebouwd met een minder dicht maaspatroon, terwijl het numerieke lokale model in detail wordt opgebouwd met een complexer en dichter maaspatroon. Door deze onderverdeling kan de spanningsverdeling op een zeer efficiënte en tijdbesparende wijze bekomen worden. De spanning in het glas en de vervorming van het glas centraal wordt onderzocht met het globale model. De spanning in de nabijheid van de connectie wordt onderzocht door de superpositie van de globale spanning en de maximale hoofdspanning in de lokale modellen. De lijmverbinding kan met behulp van één lokaal model onderzocht worden, namelijk het multi-axiale model.

De optredende spanningen in het glaspaneel en de lijmverbinding kunnen worden aangepast door verandering van geometrische parameters en materiaalparameters. Wanneer aan beide ontwerpen is voldaan, zal de beschouwde configuratie de optredende belastingen op kunnen nemen zonder falen.

De geschiktheid van de SLG-methode voor verlijmde puntverbindingen is onderzocht door een numerieke vergelijking tussen de spanningsverdelingen te bekomen enerzijds door de SLG-methode en anderzijds door een numeriek totaal model waarbij het totale glaspaneel met de verlijmde verbindingen in detail is gemodelleerd. Ondanks kleine afwijkingen, voorspelt de SLG-methode de optredende spanningen conservatief en nauwkeurig. De spanningsverdeling in de lijmlaag kan tevens ook worden bepaald middels de SLG-methode. Aangezien deze spanningsverdeling slechts bestaat uit de sommatie van de lokale spanningen, kan deze verdeling rechtstreeks bepaald worden door middel van het multi-axiale model.

De lokale modellen zijn numeriek gevalideerd voor verschillende geometrische eigenschappen (drie glasdiktes en drie connectordiameters), verschillende materiaaleigenschappen (twee lijmtypes) en drie verschillende belastingen (trek, afschuiving en multi-axiale belasting). Door de ondersteuning van het glaspaneel langsheen een omtrek met een diameter gelijk aan zes maal de connector diameter, wordt de vervorming van het glaspaneel ook in rekening gebracht. Deze vervorming brengt namelijk grote spanningsconcentraties aan in de lijmlaag. Het lokale multi-axiale model kan tevens worden gebruikt om de som van de lokale spanningen direct te bepalen.

De materiaalmodellen in de lokale modellen zijn bepaald voor een rubberachtig adhesief (MS-polymeer Soudaseal 270 HS) en een glasachtige adhesief (tweecomponenten epoxy 3M™ Scotch-Weld™ 9323 B/A). Tweecomponenten epoxy en acrylaten zijn thermohardende adhesieven. Het gedrag is meestal elastisch tot falen en het adhesief zal bezwijken bij relatief kleine rekken door voortplanting van een scheur. Veel lijmen zijn echter rubberachtig, zoals siliconen en MS-polymeren. Lokale vervormingen van kleinschalige proefstukken werden gemeten door middel van 3D-*Digital Image Correlation* (DIC). De vergelijking tussen de gegevens van de testmachine en de DIC toonde grote verschillen tussen de gemeten vervormingen. Dit bevestigt dat het gebruik van DIC nodig is om nauwkeurig de optredende spanningen op te meten in de proefstukken.

Het globale en totale model voor de verificatie van de SLG-methode zijn tevens experimenteel gevalideerd. De experimentele resultaten tonen aan dat de hoogste spanningen optreden voor de kleinste randafstanden. En zoals verwacht zijn de vervormingen aanzienlijk groter met kleine randafstanden. De numerieke analyses tonen spanningspieken die niet zichtbaar zijn in de experimenten. Dit benadrukt de voordelen en de noodzaak van numeriek onderzoek. Om de spanning in het glaspaneel of de lijmlaag te verminderen kunnen volgende handelingen ondernomen worden, in volgorde van afnemende invloed:

- Het aantal puntverbindingen verhogen;
- De afmetingen van het glaspanel verkleinen;
- De randafstand vergroten;
- De excentriciteit verkleinen;
- De connectordiameter vergroten;
- De glasdikte vergroten;
- De elasticiteitsmodulus van het adhesief verlagen;
- De randvoorwaarde veranderen naar scharnierend;
- De lijmdikte vergroten;
- De Poisson-factor van het adhesief verlagen.

Tevens zijn de faalcriteria voor de twee geselecteerde adhesieven door middel van experimenten bepaald. De faalbelasting verkregen met het faalcriterium *maximale glijding* voorspelt de experimentele faalbelasting zeer accuraat voor de MS-polymeer Soudaseal 270 HS. Door spanningssingulariteiten in de lijmlaag met de 2c-epoxy 3M™ Scotch-Weld™ 9323 B/A dient de "spanning op een afstand" methode toegepast te worden voor dit adhesief. Alleen het faalcriterium *maximale schuifspanning* met de schuifspanning bepaald op een afstand gelijk aan de totale lijmdikte van de spanningssingulariteit voorspelt de experimentele faalbelasting. Deze faalcriteria zijn ook toegepast op de lokale modellen en voorspellen de experimentele faalbelastingen conservatief en accuraat. Voor adhesieven tussen flexibele en stijf adhesieven, dienen beide faalcriteria te worden toegepast, de laagste faalbelasting zal de feitelijke faalbelasting zijn.

Summary

Its main property, i.e. transparency, has ensured that structural glass is used extensively throughout the world and has become an integral part of the skyline of major cities and constructions in general. Nonetheless, connections in structural glass members still represent a field of research of structural glass engineering which is developing and expanding rapidly. Traditional systems to connect glass to the supporting substructure and to improve the overall transparency, often consist of so-called point-fixings. With the current state of technology, it is common to use bolted solutions for point-fixings in glass. However, adhesive point-fixings have several advantages compared to bolted point-fixings, such as the stress redistributing ability of the adhesive, no weakening or residual stresses in the glass due to glass perforation, prevention of a thermal bridge, etc. These advantages, together with promising strength values are important reasons why adhesive bonding is currently considered a very promising alternative for structural glass point-connections.

In this work a design method for glass panels supported by adhesive point-fixings is proposed by means of a flowchart. The design is based on the time-efficient SLG-method (Superposition of Local and Global components), developed by Beyer for the design of bolted point-fixings. In the flowchart, the design is divided in two parts, i.e. the glass design and the adhesive design. In the former, the glass panel is separated in a global component and a local component. Due to the separation into one global component that can be built up with a less dense mesh pattern and one local component that is built up with a more complex and dense mesh pattern, the stress distribution can be determined in a very time-efficient manner. The stress and deformation in the field are examined by means of the global model. The stress in the vicinity of the connection is examined by the sum of the global stress and the maximum principal stress in the local models. For the adhesive design, only one local model can be considered, i.e. the multi-axial model.

By applying the obtained failure criteria the adhesive layer can be examined for the considered loads. The occurring stress in the glass panel and in the adhesive layer

can be altered by chancing geometrical parameters and material parameters. When both designs are satisfied, the design of glass panels supported by adhesive point-fixings for the considered configuration is completed.

The suitability of the SLG-method for adhesive point-fixings is examined by a FEA comparison between the stress distributions conducted on the one hand by the SLG-method and on the other hand by a FEA model in which the total glass plate with the adhesive connections is built up in detail with volumetric elements. Despite small deviations, the SLG-method predicts the occurring stresses in a glass panel supported by adhesive point-fixings conservatively and accurately. The stress distribution in the adhesive layer can also be determined by the SLG-method. As the stress distribution consists of only the sum of the local stresses in the SLG-method, these stresses are derived from the multi-axial model.

The local model is numerically validated for different geometrical properties (three glass thicknesses and three diameter connectors), different material properties (two adhesive types) and three different load conditions (tension, shear and multi-axial load). By supporting the glass panel along a circumference with a diameter equal to six times the connector diameter, the deformation of the glass panel is also taken into account. This deformation causes important stress concentrations in the adhesive layer. The multi-axial local model can be used to directly determine the sum of the local stresses.

The material models in the local model are obtained for a rubber-like adhesive (MS-polymer Soudaseal 270 HS) and a glassy adhesive (two-component epoxy 3M™ Scotch-Weld™ 9323). Two-component epoxies and acrylates are thermosetting adhesives. The behaviour of these materials is typically elastic until failure and will fail at relatively small strains by the initiation and propagation of a crack. However, many adhesives are rubber-like materials, such as silicones and MS-polymers. Local deformations of the small-scale test specimens were measured through 3D-DIC. The comparison between the data from the test machine and the DIC-output revealed major differences between the measured deformations. This confirms that the use of DIC is needed to accurately measure the occurring strains during the small-scale tests.

The total model for the validation of the SLG-method is experimentally validated. The experimental results demonstrate that the highest stresses are reached with

the smallest edge distances. As expected the deformations are significantly larger with small edge distances. The numerical analyses show stress peaks which are not visible in the experiments. This highlights the benefits and necessity of numerical investigation. To reduce the stress in the glass panel or adhesive layer following actions can be taken, in order of decreasing influence:

- Increase the number of connections;
- Decrease the panel size;
- Increase the edge distance;
- Decrease the eccentricity;
- Increase the connector diameter;
- Increase the glass thickness;
- Decrease the Young's modulus of the adhesive;
- Change the boundary condition to hinged;
- Increase the adhesive thickness;
- Decrease the Poisson ratio of the adhesive.

Furthermore, the failure criteria for the two selected adhesives were determined. The failure load obtained from the failure criterion *maximum shear strain* predicts the experimental failure load with a mere difference of 2% for the MS-polymer Soudaseal 270 HS. Due to the stress singularities in the adhesive layer with the 2c-epoxy 3M™ Scotch-Weld™ 9323 B/A the "stress at a distance" approach must be applied for this adhesive. Only the failure criterion *maximum shear stress* with the stress considered at a distance equal to the full adhesive thickness from the stress singularity predicts the experimental failure load. These failure criteria predict the experimental failure loads of the local models conservatively and accurately. For adhesives between flexible adhesives and stiff adhesives, both failure criteria must be applied, the lowest failure load will be the actual failure load.

Part I
Introduction
and state of the art

The Capitol Building of the United States of America,
seen from behind glass panels supported by bolted point-fixings.

Chapter 1: Introduction

> "Begin at the beginning," the King said, very gravely,
> "and go on till you come to the end: then stop."
> *Lewis Carroll, Alice in Wonderland*

1.1. Motivation and background

The main property of structural glass, i.e. transparency, has ensured that structural glass is used extensively throughout the world and has become an integral part of the skyline of major cities and constructions in general. Nonetheless, connections in structural glass members still represent a field of research of structural glass engineering, which is developing and expanding rapidly. Traditional systems to connect glass to the supporting substructure often consist of linear supports. By using such systems, the transparency of the facade is highly reduced. In contrast, the overall transparency improves significantly by using so-called point-fixings (Vyzantiadou & Avdelas 2004; Dodd 1997). Point-fixings are widely used in facades and canopies, as depicted in Figure 1.1.

With the current state of technology, it is common to use bolted solutions for point-fixings in glass. These fixings typically consist of locally installed metal pieces, of limited size, connecting the glass elements to the structure using bolts through the glass. Obviously, this requires the glass panel to be drilled in corner or edge zones, tempered and bolted (Siebert 2006). A relatively large amount of research has been performed on bolted point-fixings, most of which has focused on tensile and shear loads since point-fixings are mostly used as overhead glazing or in facades. The main conclusions drawn from these works are that the loadbearing capacity of glass with properly installed point-fixings depends mainly on the geometry of the point-fixing, the distance of the borehole to the edge, the used materials for the washer and the edge finishing of the borehole.
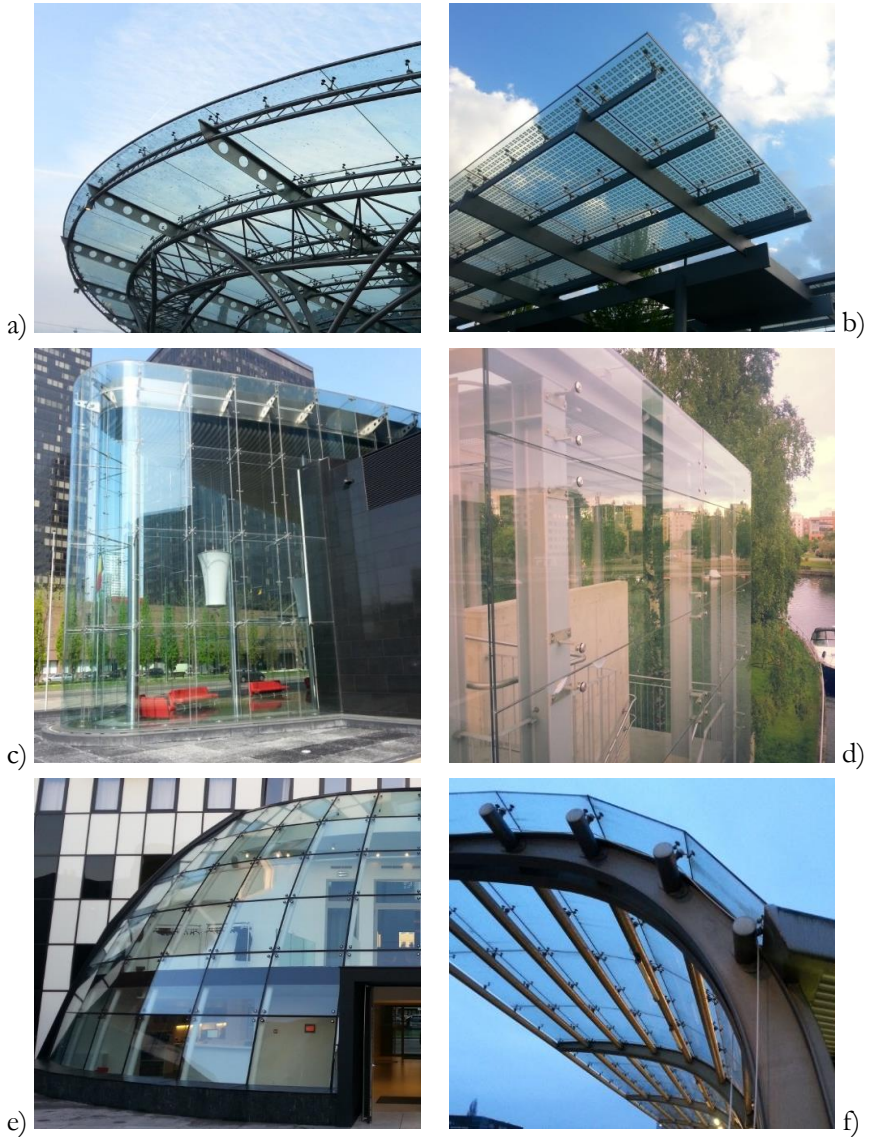
FIGURE 1.1: EXAMPLES OF BOLTED POINT-FIXINGS USED IN A **CANOPY** FOR (A) THE TRAIN STATION SINT-PIETERS IN GHENT, BELGIUM AND FOR (B) A BUS TERMINAL IN KAISERSLAUTERN, GERMANY, IN A **FACADE** FOR (C) THE FEDERAL PUBLIC SERVICE FINANCE BUILDING IN BRUSSELS, BELGIUM AND FOR (D) AN ELEVATOR IN TAMPERE, FINLAND AND IN A **COMBINATION** FOR (E) A RESTAURANT IN GHENT, BELGIUM AND FOR (F) A BUS TERMINAL IN GHENT, BELGIUM.

Although the use of bolted point-fixings is widespread, a major disadvantage of this type of connections is the significant weakening of the glass by the drilling process at the hole edges, which is where high stress peaks occur due to the transfer of forces by contact between metal and glass (Overend 2005; Maniatis 2006; Beyer 2007; Mocibob & Belis 2010).

The use of adhesive connections avoids this issue because the glass is directly bonded to the metal connector. Indeed, adhesive bonds can be very suitable to avoid high stress concentrations in the glass by redistributing local stresses, although this is obviously influenced by the stiffness of the specific adhesive product considered (Goss 2002; Blandini 2007; Overend et al. 2011; Blyberg et al. 2012; Santarsiero 2015). This stress-redistributing ability, together with promising strength values and the absence of boreholes are important reasons why adhesive bonding is currently considered a very promising alternative for structural glass point-connections.

1.2.   Thesis objectives

Despite these advantages, relatively little research has been performed on this type of connections. This is partially because of the enormous bandwidth of physical properties of adhesives together with their nonlinear properties and unknown lifetime behaviour (Yu et al. 2001; Feng et al. 2005; Khalili et al. 2009). This makes it challenging to model them correctly in a e.g. finite element program. Furthermore the enormous amount of adhesive products, each with specific properties and application ranges, is one of the reasons why designers are doubtful about adhesive point-fixings.

Although the knowledge about adhesive point-fixings is growing, many shortcomings still exist (Sitte et al. 2011; Overend et al. 2013; Dispersyn et al. 2014; Santarsiero 2015). A first step in the process to improve this situation is the determination of a proper design method for adhesive point-fixings. In the following, a proposal for a design method is therefore made for adhesive point-fixings based on the existing design methods for bolted point-fixings.

1.3. Structure of the thesis

This work is divided in three parts, as shown in Figure 1.2. In the first part an overview is given of the existing research about bolted and adhesive point-fixings. The second part contains all experimental and numerical work. Based on this work, a proposal for a design method for adhesive point-fixings is made in the third part together with the conclusions and further research.
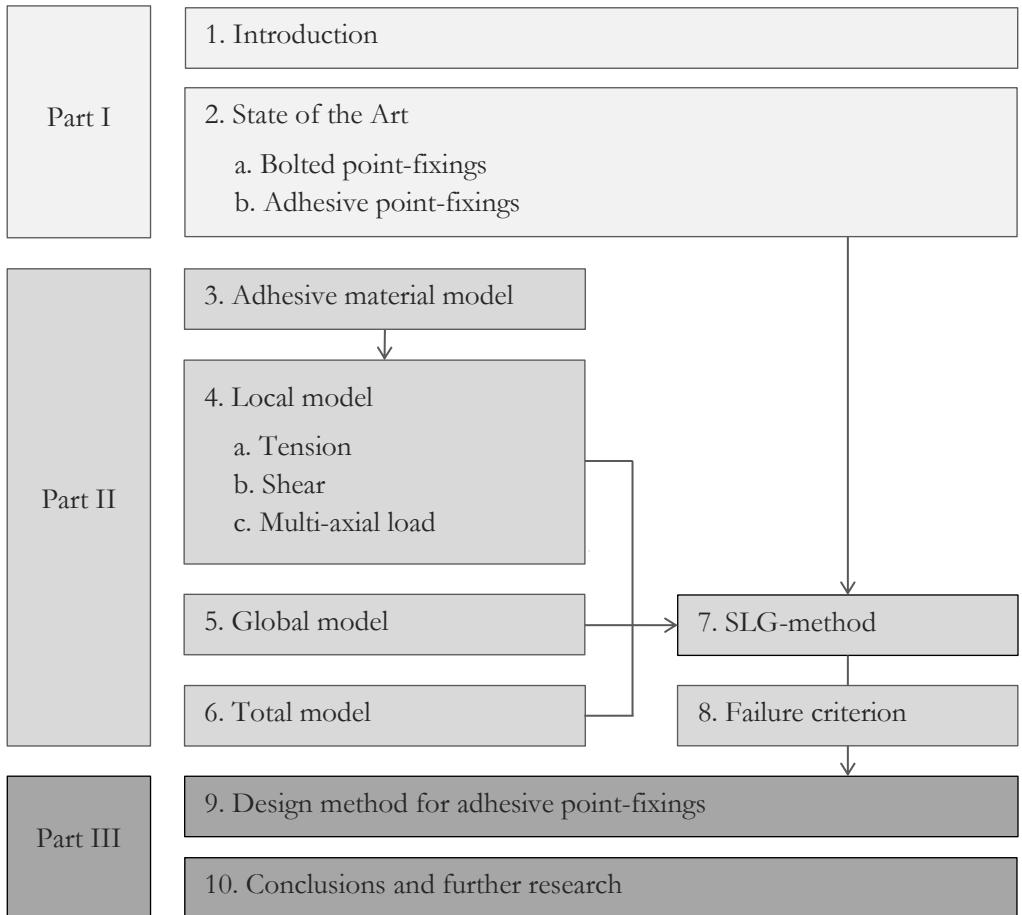
FIGURE 1.2: OUTLINE DIAGRAM OF THE THESIS

Part 1   In **Chapter 2**, an overview is given of the current design methods for bolted point-fixings in glass structures. These design methods will constitute the basis for a design method for adhesive point-fixings. Furthermore, an overview of existing research on adhesive point-fixings is given.

Part 2   The determination of the material model for two selected adhesive is given in **Chapter 3**. These material models are used in **Chapter 4**, for the validation of the local numerical model. This validation is performed for three load configurations, i.e. tension, shear and multi-axial load. The development and validation of a global numerical model of a full-scale glass panel supported by discrete point-fixings is performed in **Chapter 5**. The conducted experiments and numerical models for the total model are described in **Chapter 6.** The validation of the SLG-principle for adhesive point-fixings is conducted in **Chapter 7**. A failure criterion for adhesive point-fixings is selected in **Chapter 8**.

Part 3   A design method for adhesive point-fixings is proposed in **Chapter 9**. This method is developed from the SLG-method together with the selected failure criterion. Finally, conclusions for this thesis and recommendations for further research are given in **Chapter 10**.

Chapter 2: State of the art

> We can know only that we know nothing.
> And that is the highest degree of human wisdom.
> *Leo Tolstoy, War and Peace*

2.1. General

As mentioned in Chapter 1, the overall transparency of glass structures can be improved by using so-called **bolted point-fixings** (Vyzantiadou & Avdelas 2004; Siebert & Herrmann 2010). This type of connection requires the glass panel to be drilled near the corners or edges, and subsequently to be tempered and bolted (Siebert 2006), as depicted in Figure 2.1b, c and d. A recent technology prevents drilling through the glass by using so-called undercut point-fixings, as illustrated in Figure 2.1d. These connections do not penetrate the insulation cavity in insulating glass units (IGU).

The drilling will significantly weaken the glass at the holes, which is exactly the position where relatively high peak stresses occur when forces are transferred. This disadvantage could be avoided efficiently with adhesive bonding technologies, as depicted in Figure 2.1a. Indeed, adhesive bonds can be very suitable to avoid high stress concentrations in the glass by redistributing local stresses (Blandini 2007; Blyberg et al. 2012; Goss 2002).

The combination of bolted point-fixings and adhesive bonding gives **adhesive point-fixings**, as depicted in Figure 2.1e. This type of connection combines the advantage of increased transparency of bolted point-fixings and the advantage of stress redistributing ability of adhesive glass-steel connections (Blandini 2007; Overend et al. 2011; Blyberg et al. 2012; Nhamoinesu & Overend 2012). In this work, the determination of a proper design method for adhesive point-fixings is made based on the existing design methods for bolted point-fixings. In the next paragraphs, these existing design methods and several influencing parameters will be discussed.
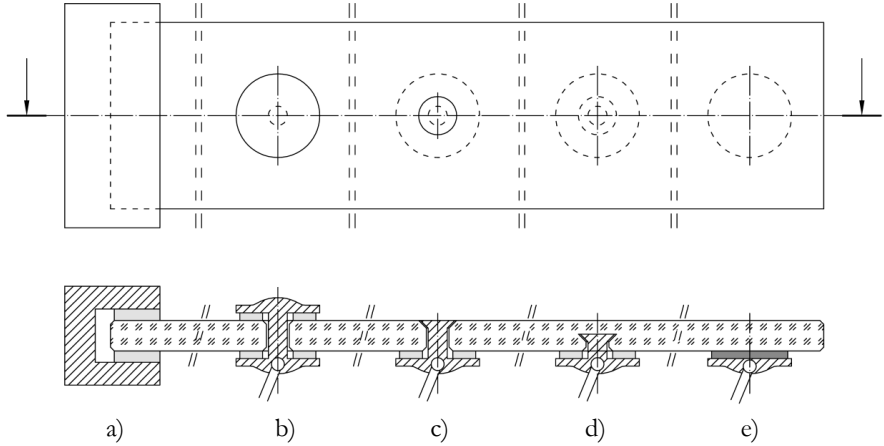
FIGURE 2.1: SCHEMATIC REPRESENTATION (CROSS-SECTION) OF THREE DIFFERENT WAYS TO CONNECT GLASS PANELS TO THE UNDERLYING STRUCTURE WITH (A) LINEAR ADHESIVE SUPPORT, (B), RAISED HEAD BOLTED POINT-FIXING, (C) COUNTERSINK BOLTED POPINT-FIXING, (D) UNDERCUT BOLTED POINT-FIXINGS AND (E) ADHESIVE POINT-FIXING.

2.2. Bolted point-fixings

Point-fixings in glass structures are usually bolted point-fixings and are produced in several different geometries. The different components of a general bolted point-fixing, i.e. a V2003 fixed bolt type with cylindrical head of Sadev (2015), is depicted in Figure 2.2. The different components are given in Table 2.1. The bushing in this configuration is fabricated in POM, but can also fabricated in aluminium, PEEK, nylon, etc.
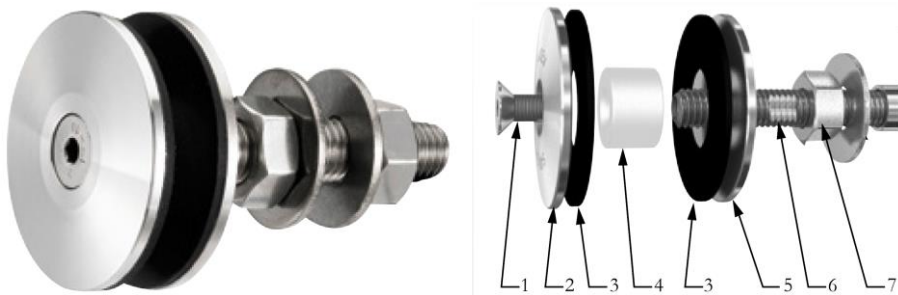
FIGURE 2.2: COMPONENTS OF A FIXED CYLINDRICAL HEAD BOLTED POINT FIXING (SADEV 2015).

No.	Name	Material
1, 7	Bolt	Stainless steel (AISI 316L)
2	External plate	Stainless steel (AISI 316L)
3	Contact washer	EPDM rubber
4	Bushing	Polyoxymethylene (POM)
5	Glass nut	Steel (X2 Cr Ni Mo)
6	Threaded axle	Stainless steel (AISI 316L)

Extensive experimental research has been carried out on this type of connections. Most of the current research focusses on tensile and shear loads (Siebert 2005; Haese 2007; Siebert 2007). The conclusion can be drawn that the loadbearing capacity of glass with properly installed point-fixings depends mainly on the edge distance and the geometry of the point-fixing, i.e. the diameter, raised head fixture (Figure 2.1b) or countersink fixture (Figure 2.1c), hinged or clamped systems, etc.

Mocibob and Crisinel (2007) performed in-plane (shear and compression) loading tests on bolted point-fixings in glass panels. As in fully-transparent pavilions, the glass panels can be used as wind bracing elements to stabilize and strengthen the pavilion. High compressive and shear loads are introduced in the glass panels and are transferred through the bolted point-fixings to the underlying structure. The most important conclusion was that the load should be adequately introduced into the glass panels. This depends strongly on the material of the bushing between the bolt and the glass panel. Heat strengthened glass specimens of different thicknesses (6 mm of monolithic glass, 6/1.52/6 and 8/1.52/8 of laminated glass) were tested. The research showed that an injected mortar is an adequate solution for uniform load introduction. Depending on the bolt diameter and support conditions, failure loads from 10 kN (eccentric shear test with an M16 bolt) to 48 kN (axial compressive test with an M20 bolt) were reached.

A glass panel in a facade under a wind load is loaded with a combination of shear and tensile forces (Wellershoff et al. 2004; Tibolt et al. 2013). Both investigations validated a numerical model with experimental data. The different load angles that Tibolt et al. investigated are shown in Figure 2.3. The failure load of the glass panels increased with increasing loading directions, i.e. glass panels supported by bolted point-fixings better withstand shear forces.
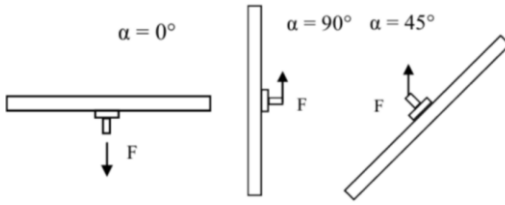
Bolted point-fixings normally require fully tempered glass, due to the high stress concentration at the borehole. However, research conducted at Ghent University proves that annealed float glass can be used to transfer considerable loads, reaching more than 12 kN for the configuration of 8 mm + 8 mm glass with a bolt of 10 mm in a hole of 16 mm and a preloading moment of 20 Nm (Callewaert et al. 2007). This research concluded that the maximum shear load of bolted point-fixings depends on the glass thickness, the edge distance, the diameter of the bolt and the material of the interlayer.

Typically, experiments on bolted point-fixings are used to validate a numerical model in a Finite Element Analysis (FEA). With this numerical model, the occurring stresses and strains can be investigated more thoroughly (Panait et al. 2005). The validation is usually obtained by measuring the strains on the glass surface with strain gauges (Siebert 2003; Tibolt et al. 2013). However, the occurring stresses can also be measured using the photo-elastic method as described in the work of Radim et al. (2008), or estimated with an analytical method (Maniatis 2006b; Maniatis 2006a; Baitinger & Feldmann 2010b). With the latter, the stress distributions around the borehole can be analytically determined. Another analytical method was developed by Seel and Siebert (2012), based on the classic plate theory of Kirchhoff. The analytical method of Seel and Siebert gives the stress for circular and ring-shaped plates under rotationally symmetrical and rotationally anti-symmetrical loading as shown in Figure 2.4. This method is also applicable for adhesive point-fixings.
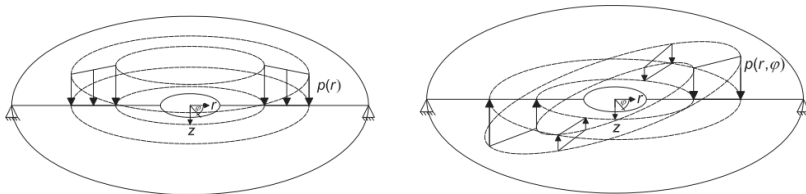
FIGURE 2.4: PLATES UNDER ROTATIONALLY SYMMETRICAL AND ROTATIONALLY ANTI-SYMMETRICAL LOAD (SEEL & SIEBERT 2012).

A difficulty with FEA models is the validation of the contact washer material and the bushing material. These components prevent direct contact between the bolt and the glass panel. The group of plastics is the most uncertain factor in the investigation of point-fixings in structural glass. The enormous bandwidth of physical properties of the thermoplastic and thermosetting materials together with nonlinearity effects make it difficult to model them correctly in the finite element analysis (Herrmann 2005).

The main purpose of numerical models is to study the stress and strain distributions in the glass in function of several parameters, for example the diameter of the hole, the diameter of the bolt, the thickness of the glass panel, etc. In the research of Mocibob and Belis (2010), experimental and numerical analyses have been performed on axially compressively loaded glass panels. The numerical model gives relatively high stress concentrations in the borehole at the contact point, as depicted in Figure 2.5. This is also visible in the experiments since the initial fractures typically start at this point. These stress concentrations consist of maximal principal compressive and tensile stresses, leading to the conclusion that the compressed samples failed due to a complex, two-dimensional stress state. A smaller diameter will lead to a higher stress concentration at the borehole.

The prestressing of prestressed bolts has a positive impact on the stress state in the glass panel (Bernard & Daudeville 2009; Bernard 2008). Furthermore, decreasing the friction coefficient between the glass and the bushing also has a positive impact.
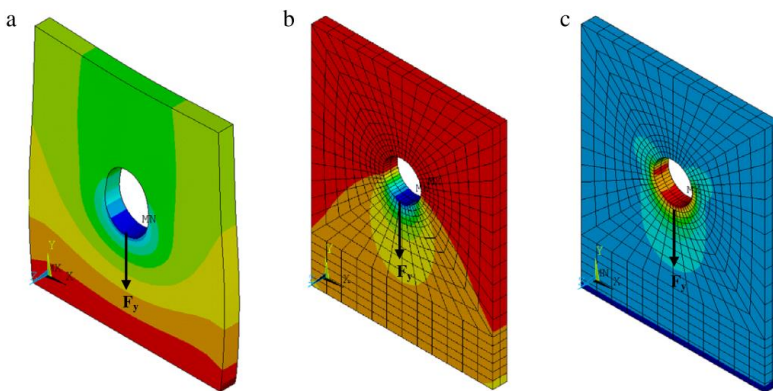
FIGURE 2.5: NUMERICAL RESULTS FOR A GLASS PANEL SUBJECTED TO A COMPRESSIVE LOAD OF 20 KN: (A) BOREHOLE DEFORMATION, (B) PRINCIPAL COMPRESSIVE STRESS σ_c DISTRIBUTION AND (C) PRINCIPAL TENSILE STRESS σ_t (MOCIBOB & BELIS 2010)

To investigate the tempering process on the stress state, Bernard modelled the thermal tempering process and came to the conclusion that not only the strength increased but also that the tempering process implied a certain amount of crack healing. The modelling of the tempering process is also used by Nielsen et al. (2009), where the residual stresses at the boreholes were investigated.

2.2.1. Influence of the corner and edge distance

The distance between the centre of the borehole and the corner, i.e. the corner distance, and the distance between the centre of the borehole and the edge, i.e. the edge distance, also have a great influence on the mechanical behaviour of glass panels connected with bolted point-fixings. The experimental and numerical research of Rex et al. (2003) shows that the initial stiffness of a bolt bearing on a single steel plate increases with increasing distance. Theoretical and experimental studies of pinned connections in steel plates that have been published over the past 65 years are discussed by Duerr and Asce (2006). With increasing distance the limit state load will increase proportionately.

The research of Klinkenberg et al. (1998) was one of the first research projects on the influence of the corner and edge distance for glass panels supported by bolted point-fixings. The optimal position of the connection was determined from FEA. The stresses decrease with increasing corner and edge distances. The analytical results and initial experimental investigations by Overend (2005) of the conventional point-fixings demonstrate that an optimum hole diameter exists for a given corner and edge distance. The largest stress peaks can be found for the smallest edge distance with the largest glass panel width. In her doctoral dissertation, Maniatis also investigated the influence of the edge distance of bolted point-fixings (Maniatis 2006b; Maniatis 2006a). The principal tensile stresses increase with the reduction of the edge distance. In the numerical investigation of Nielsen et al. (2009) the influence of the edge distance is investigated on the minimal value of the residual compressive in-plane stress at the surface of the hole resulting from the tempering process. This stress will decrease when decreasing the edge distance. Hence, the strength of the panel will reduce when reducing the edge distance. Interpolation curves have been proposed to predict the average failure load based on the distance between the hole and the panel edge by Amadio et al. (2008). It can be observed that the specimen strength rises as the edge distance increases. Furthermore, the influence of the edge distance is investigated

by FEA and validated by empirical methods by Overend et al. (2013). The maximal peak principal stress occurs with the smallest edge distance. The principal stress will decrease with an increase of edge distance.

A general conclusion from literature is that the maximal occurring stresses will reduce with increasing the corner and edge distance, which results in a higher strength of the glass panel. Due to its significant influence, the corner and edge distance for bolted point-fixings are described in several guidelines and standards (CSTB 3574-V2 2012; DIN 18008 2010; EN 12150-1 2015). In these guidelines and standards the influence is not described, only the minimal or maximal edge distance is specified depending on the diameter of the borehole ϕ_{hole} and the glass thickness t_{glass}. Table 2.2 gives a summary of standards according to Figure 2.6 for minimal values of the corner distances A, B and D, and of the edge distance C.
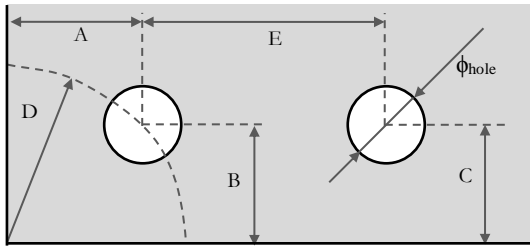
FIGURE 2.6: DEFINITIONS OF THE SYMBOLS.

TABLE 2.2. SUMMARY OF THE MINIMUM AND MAXIMUM CORNER AND EDGE DISTANCE ACCORDING TO GUIDELINES AND STANDARDS.

	CSTB 3574-V2, 2012	EN 12150-1, 2015	DIN 18008, 2010
A [mm]	$> 2 \cdot t_{glass} + 0.5 \cdot \phi_{hole}$	$\geq 2 \cdot t_{glass} + 0.5 \cdot \phi_{hole}$	$\geq 80 \text{ mm} + 0.5 \cdot \phi_{hole}$ $\leq 300 \text{ mm} + 0.5 \cdot \phi_{hole}$
B [mm]	$> 2 \cdot t_{glass} + 0.5 \cdot \phi_{hole}$	$\geq 2 \cdot t_{glass} + 0.5 \cdot \phi_{hole}$	$\geq 80 \text{ mm} + 0.5 \cdot \phi_{hole}$ $\leq 300 \text{ mm} + 0.5 \cdot \phi_{hole}$
C [mm]	$> 2 \cdot t_{glass} + 0.5 \cdot \phi_{hole}$	$\geq 2 \cdot t_{glass} + 0.5 \cdot \phi_{hole}$	$\geq 80 \text{ mm} + 0.5 \cdot \phi_{hole}$ $\leq 300 \text{ mm} + 0.5 \cdot \phi_{hole}$
D [mm]	$\geq 6 \cdot t_{glass} + 0.5 \cdot \phi_{hole}$ for $t_{glass} \leq 12$ mm $\geq 4 \cdot t_{glass} + 0.5 \cdot \phi_{hole}$ for $t_{glass} \geq 15$ mm	$\geq 6 \cdot t_{glass} + 0.5 \cdot \phi_{hole}$	
E [mm]		$\geq 2 \cdot t_{glass} + d$	$\geq 80 \text{ mm} + \phi_{hole}$

2.2.2. Design methods for bolted point-fixings

Over the years several design methods have been developed for bolted point-fixings in structural glass. Almost all developed design methods make use of FEA. In the next paragraph several existing design methods are explained.

Kasper (2006) developed a design methodology based on tests and numerical analysis. In the research the first step consisted of small scale tests on glass plates with a centric point-fixing where the load was introduced at variable angles (0°, 22.5°, 45°, 90°). Using strain gauges the glass strain was measured along predefined paths. With these strains an FEA-model was validated. Finally, the value and position of the maximal tensile stresses, the strains and tensile stresses along the paths were determined with the FEA-model. These stresses can be used as numerical benchmarking data. For the design of a connection, the designer has to model his own FEA-model of the point-fixing and validate it with the numerical benchmarking data. Subsequently, the designer can use design codes to see whether the occurring stresses will not exceed the maximum glass stresses (Overend 2005).

The design method developed by B. Siebert (2006) is also based on tests and numerical analysis, similar to the approach by Kasper. However, in addition to the approach by Kasper, the meshing of the finite element model was also verified. First of all, a simple plate was modelled and the resulting stresses were compared to analytical results of the research of Young and Budynas (2002) to check the suitability of the element type. Small scale bolted point-fixing tests were conducted first with an aluminium interlayer, since the clearly defined properties of aluminium make it easier to validate the FEA-model. With this validation the elements and contact elements derived earlier were validated. Afterwards, the same tests were conducted with a more elastic interlayer. The strain values served as numerical benchmarking data. The design method consisted of modelling the small scale test and comparing the generated results for strain and stress to the values of the numerical benchmarking data. The achieved validated model was subsequently extended to the geometry of the plane to be designed and the results for stresses and deformation were verified against the resistance and design limits.

In analogy with Kasper and Siebert, Brendler used tests and numerical analysis to develop his design method (Brendler & Schneider 2004). However, instead of comparing the strains, Brendler used the load-deformation behaviour of the point-fixing as the validation parameter. Small scale tests were conducted to investigate the stiffness of the point-fixings and to determine the load-deformation curves. The point-fixings were mounted into steel plates and loaded into different directions to determine the longitudinal and transversal stiffness. These stiffness values were used as numerical benchmarking data. In this design method, a designer first has to model the point-fixing in a rigid plate subjected to tension and compression, so the head stiffness of the point-fixing can be validated. Secondly the stiffness in longitudinal direction has to be checked. Hereby the joint is modelled as a spring. In a third step the transverse stiffness is verified in the same way. These three steps are illustrated in Figure 2.7. Finally the glass plane is modelled with the obtained point-fixing model.
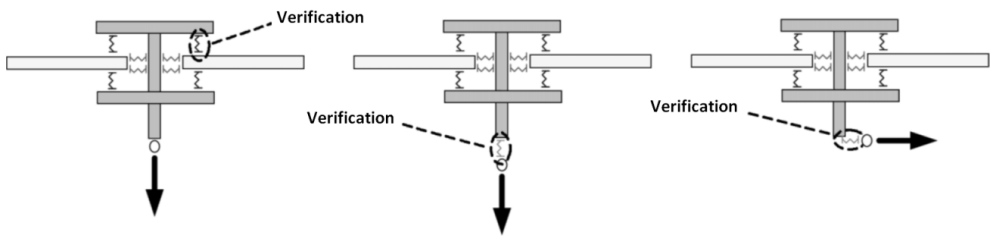
FIGURE 2.7: THE VERIFICATION OF THE HEAD STIFFNESS, THE STIFFNESS IN LONGITUDINAL DIRECTION AND THE TRANSVERSE STIFFNESS (BRENDLER & SCHNEIDER 2004).

Aluminium or polymer prefabricated bushings are placed between the glass and the bolt or a resin mortar is injected to avoid contact between the steel and the glass to prevent high stress concentrations. As mortar is often used to solve alignment problems caused by the lamination of drilled glass panels, Baitinger transformed her analytical method into a simplified formula especially for the use of Hilti HIT-HY 270, a two component hybrid system composed of an organic and an inorganic curing mechanism (Baitinger & Feldmann 2010a; Baitinger & Feldmann 2010b). The simplified formula is given in Eq. (2.1), with $\sigma_{\emptyset,max,d}$ the maximum tangential stress at the borehole, P_d the resulting design force, k_i coefficients to consider the design of the joint as well as production and erection tolerances, b_m the relevant pane width, K_m the multiplication parameter and σ_R the design resistance of the glass element.

$$\sigma_{\emptyset,max,d} = \prod_{i=1}^{5} k_i \cdot \left(1.2 + 2.2\frac{K_m}{b_m}\right) \cdot \frac{P_d}{d_0 \cdot t} \leq \sigma_R \qquad (2.1)$$

It is obvious that most of the methods described above require a lot of computation time and consequently have a great cost, especially for complex geometries. Therefore Beyer developed a time-efficient design method for the design of bolted point-fixings (Beyer 2007; Beyer 2008; Beyer & Unterweger 2007). This method appears to offer a very appealing basis for the design of glass plates supported with adhesive point-fixings, in particular because of its time-efficiency.

The solution that Beyer proposes, is based on the principle of superposition. This approach is already known from beam theory, in which complex structures are divided into global and local components. Based on the principle of Saint-Venant, Beyer assumes that changing geometrical characteristics of the point-fixing only have an influence on the stress distribution in a local region around the joints, while the influences decrease further away from the connection. This principle allows to separate the entirety from the connections (the global component), and the connections from the entirety (the local component). This concept of superposition of a local and global component is called the SLG-method. The principle of the SLG-method for bolted point-fixings is depicted in Figure 2.8.

The entire glass plate is modelled as the global component in which the point-fixings are represented by springs with a certain stiffness given in datasheets. A certain zone surrounding the joints (the local component) is not taken into account. From this global model, deflections and stresses in the field are determined and checked with design values. Using this model the stresses at the boundary between the global and local component can also be determined, which will further onwards be referred to as the global stress σ_{global}. Furthermore the support reactions of the point fittings (N, Q, M) are determined.
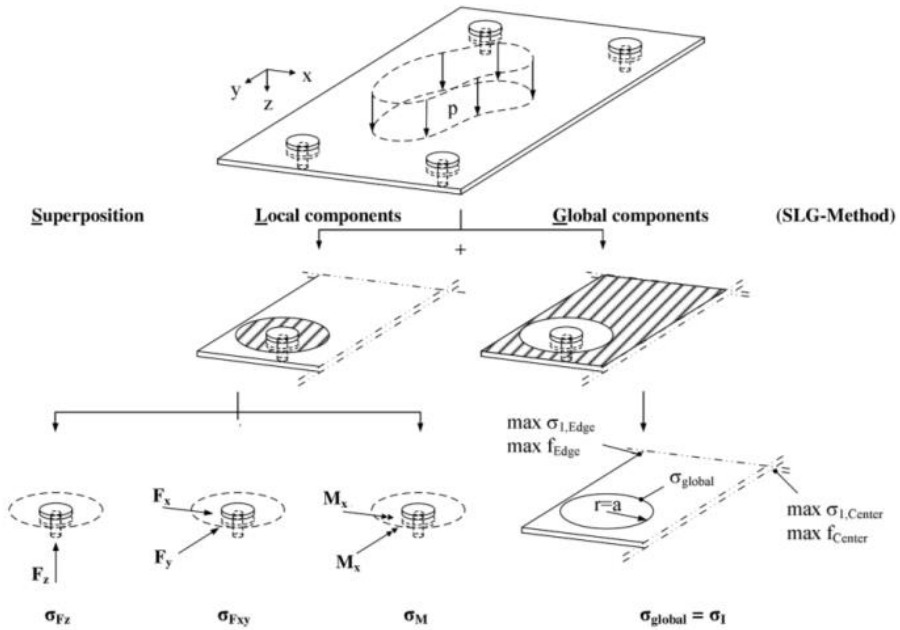
FIGURE 2.8: PRINCIPLE OF THE SLG-METHOD (BEYER 2007).

Larger stresses will be present around the borehole compared to the stresses in the field due to the Saint-Venant's principle. This is taken into account by multiplying the global stresses by a stress concentration factor k, as depicted in Figure 2.9. This stress concentration factor is derived from FEA, in which a plate with the exact borehole geometry is modelled and subjected to bending.
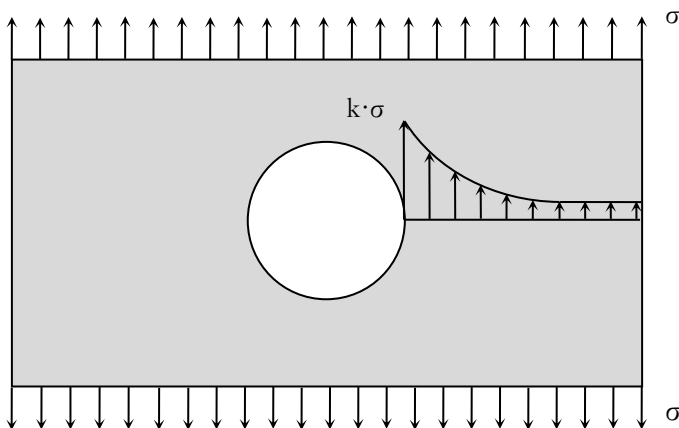
FIGURE 2.9: STRESS CONCENTRATION DUE TO THE SAINT-VENANT'S PRINCIPLE.

For the local design, the glass plate around the borehole and the connection are modelled in detail representing the local component. The diameter of the local component ϕ_{loc} for bolted point-fixings is determined to be at least six times the diameter of the borehole ϕ_{hole}, as is expressed in Eq. (2.2). By applying the reaction forces and moments on the connection derived from the global component, the reaction stresses σ_{F_z}, $\sigma_{F_{xy}}$ and σ_M are determined. The sum of these stresses and the global stresses must be less than the critical stress σ_R for the glass plate according to Eq. (2.3). Beyer validated the SLG-method by comparing stress distributions in glass plates in experiments with the distributions derived with the SLG-method. The proposed solution turned out to be a good method to approximate the stress distribution in a glass plate connected with bolted point-fixings. Due to the separation into one global component that can be built up with less complex elements and one local component that can be built up with more complex volumetric elements, the stress distribution can be determined in a very time-efficient manner.

$$\phi_{loc} \geq 6 \cdot \phi_{hole} \tag{2.2}$$

$$\sigma_{F_z} + \sigma_{F_{xy}} + \sigma_M + k \cdot \sigma_{global} \leq \sigma_R \tag{2.3}$$

2.3.   Adhesive point-fixings

As mentioned above, the main disadvantage of bolted point-fixings is the drilling of the glass. Furthermore, the bolt will act as thermal bridge and can cause leakages in an IGU. These disadvantages could be avoided efficiently with adhesive bonding technologies. The stress redistributing ability of adhesives, together with promising strength values are important reasons why adhesive glass-steel connections are currently frequently used for structural glass connections (Pye & Ledbetter 1998; Overend et al. 2011; Belis et al. 2011; Zangenberg et al. 2012; Santarsiero 2015). Beyond the stress redistributing ability, adhesive point-fixings have even more advantages compared with bolted point-fixings:

- No weakening or residual stresses in the glass due to glass perforation;
- Use of regular annealed glass possible;
- Less problems with moisture and dirt accumulation at the point fixing;
- Prevention of a thermal bridge.

Adhesive point-fixings have also disadvantages compared to bolted point-fixings:

- No proper quality control;
- Influenced by temperature, moisture, UV-radiation and time;
- Complex material behaviour of the adhesives.

The ideal adhesive for adhesive point-fixings should be flexible enough to deal with differential thermal expansions and strong enough to withstand the loads applied on the point-fixing. The most commercial adhesive types and their properties are summarized in Table 2.3 and depicted in Figure 2.10.

TABLE 2.3: DIFFERENT ADHESIVE TYPES AND THEIR GENERAL PROPERTIES (SILVESTRU & ENGLHARDT 2014)

Adhesive type	General properties
Silicones	- Low strength and stiffness; - High durability and resistance against moisture and UV-radiation; - Hyper-elastic material behaviour.
MS-polymers	- Medium strength and stiffness; - Medium resistance against moisture and UV-radiation; - Hyper-elastic material behaviour.
Polyurethanes	- Medium strength and stiffness; - Low resistance against UV-radiation; - Hyper-elastic material behaviour.
Acrylates	- Generally high shear strength and small optimal thickness; - Generally low resistance against moisture; - Visco-elastic material behaviour.
Epoxies	- High strength and stiffness, brittle - Small optimal thickness; - Linear-elastic material behaviour.
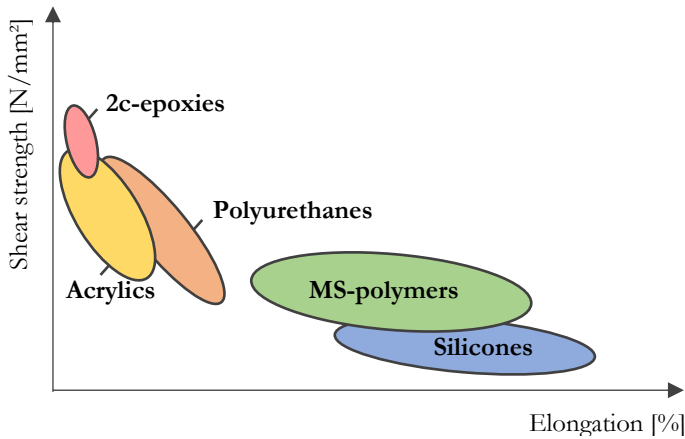
FIGURE 2.10: CLASSIFICATION OF THE DIFFERENT ADHESIVE TYPES

Despite the advantages of adhesive point-fixings, there has been limited research performed on adhesive point-fixings. This is partially because of the enormous bandwidth of physical properties of adhesives together with their nonlinear properties. This makes it challenging to model them correctly in a finite element program. The characterisation of the material behaviour has been mostly done by obtaining stress-strain curves from tensile tests on bulk material (Weller et al. 2009; Bos & Veer 2007; Dias et al. 2012; Santarsiero et al. 2014). However, the adhesive can react mechanical differently in an adhesive connection than in bulk material (Dean et al. 1996). This has been confirmed by the research of Hagl (2010), where the comparison between uniaxial material tests and circular point-fixings showed different working principles of the adhesive material. Therefore, Weller and Vogt (2008) obtained the material properties of the adhesive from butt-bonded hollow cylinders for the numerical investigation of adhesive point-fixings. According to Weller and Vogt, the closed ring-shaped geometry produces a homogenous state of stress along the circumference. The stress distributions in the adhesive with the butt-bonded hollow test are illustrated in Figure 2.11. However since the same load is transferred in both the substrates and the adhesive, and the substrates are mostly much stiffer than the adhesive, the axial strains in the adhesive will be much higher than those in the adherent. This will also cause much larger lateral (Poisson's) strains in the adhesive. Where the two materials join, the lateral strains are limited by the stiffer adherent. This restriction will cause large radial shear stresses in the adhesive at the interface. Since the adhesive is applied in a thin film form, these radial shear stresses together with the tension will introduce complex stresses in the adhesive (Adams et al. 1997).

$$\sigma_x = \frac{F_x}{A} = \frac{4 \cdot F_x}{\pi \cdot (d_a^2 - d_i^2)} \qquad \tau_{xy} = \frac{M_t}{W_p} = \frac{16 \cdot M_t \cdot d_a}{\pi \cdot (d_a^2 - d_i^2)}$$
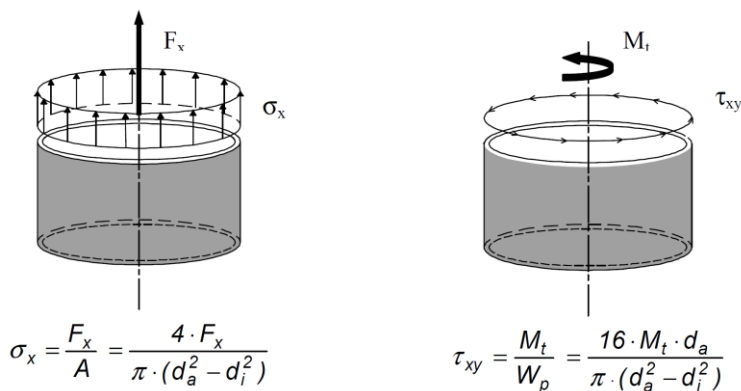
FIGURE 2.11: STRESS DISTRIBUTION FOR TENSION (LEFT) AND TORSION (RIGHT) (WELLER & VOGT 2008)

When the adhesive is assumed to be linear elastic, simple calculations can be done to obtain a first insight into the behaviour of the adhesive point-fixing under varying parameters. Santarsiero et al. (2013) and Santarsiero & Louter (2013) investigated the influence of the Young's modulus of the adhesive, the Poisson's ratio of the adhesive, the diameter and the thickness, modelling the adhesive behaviour as linear elastic. The general conclusion was that adhesive connections exhibit a relatively complex behaviour due to large nonlinearities that cannot be neglected.

Bues et al. (2009) did research on the influence of the shape of the point-fixing with silicone, i.e. convex, concave or standard fitting depicted in Figure 2.12. The concave point-fixing were accompanied by the largest failure loads, followed by the standard and the convex fixing. Mostly silicones are used for glass-steel connections; however in the work of Puller & Sobek (2008) three different acrylate adhesives were tested for adhesive point-fixings with a diameter of 50 mm in tension and shear. Depending on the adhesive type, tensile strengths of 20 kN and shear strengths of 40 kN were reached. The results of the tensile and shear tests are depicted in Figure 2.13.
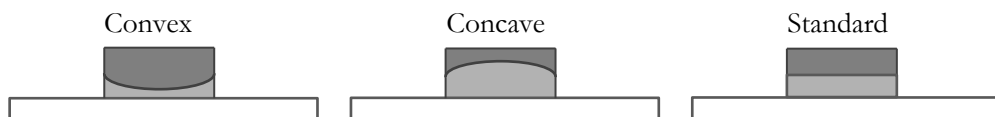
FIGURE 2.12: DIFFERENT SHAPES OF A POINT-FIXING (BUES ET AL. 2009)
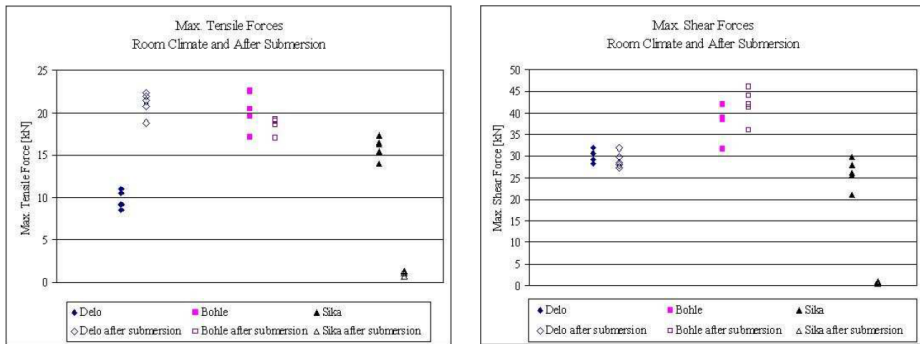
FIGURE 2.13: MAXIMUM TENSILE FORCES (LEFT) AND MAXIMUM SHEAR FORCES (RIGHT) (PULLER & SOBEK 2008).

The influence of the thickness of the adhesive layer is investigated in the work of Weller and Schadow (2007). Point-fixings with a diameter of 60 mm and different adhesive thicknesses were loaded in tension and shear. The main conclusion that could be drawn from the results was that the thinner the adhesive layer, the higher the strength of the adhesively bonded joint is. Furthermore, an important factor for the strength of the adhesive connection is the surface condition of the adherents. This can be improved by a mechanical treatment or a chemical treatment. Both methods show a high improvement of the adhesive strength (Weller & Tasche 2005; Weller & Kothe 2011).

Tests on large specimens with adhesive point-fixing are uncommon. At Ghent University, canopies with adhesive point fixings were experimentally tested (Belis et al. 2012). The tests followed a fixed schedule consisting of different steps, based on testing for normal, non-accessible overhead glazing (Siebert 2007; Haldimann et al. 2008). The canopies consisted of a glass panel of 1 m x 1 m supported by four adhesive point-fixings and was initially loaded with a load of 1.5 kN/m² for 24 hours. Secondly, all the glass panels were broken by a ball drop or a hammer-driven centre punch. Finally, the broken glass plates were loaded with a static load of 0.5 kN/m². The configuration with the heat-strengthened glass panels did not fail. The tempered glass panels only resisted the final load for 12 hours. The failure was due to thin layer failure of the glass, and not to failure of the adhesive bond. This is illustrated in Figure 2.14.

In the doctoral research of Santarsiero (2015), two transparent adhesives for adhesive point-fixings were used: the ionomer SentryGlas® (SG) from Kuraray and the Transparent Structural Silicon Adhesive (TSSA) from Dow Corning. The latter has been recently commercialized for adhesive point-fixings in structural glass applications. Compared to standard silicone adhesives used in glass applications, TSSA exhibits higher stiffness and strength. It should be noticed that, conversely to SG, TSSA is exclusively intended to realize adhesive point-fixings. TSSA is a one-component addition-cured silicon with no by-products, characterized by nanosilica and cross-linked polymers (Santarsiero 2015). In the work, the mechanical behaviour of laminated connections at varying temperature, strain rate and loading condition was studied by experimental, analytical and numerical investigations. The outcome was a failure criterion in function of the equivalent stress, the hydrostatic stress, the temperature and the strain rate.

2.4.   Adhesive point-fixings applications

The use of adhesive point-fixings in practical construction compared to bolted point-fixings is rather limited up till today. A project in which these point-fixings were constructed with TSSA is the Euridice building in Feluy (Belgium) of Dow Corning, as depicted in Figure 2.15 (Sitte & Wolf 2012). The large insulating glass panels have a length of 3200 mm and a width of 1877 mm and the edge distance ranges from 70 to 110 mm. Other smaller projects with TSSA as an adhesive point-fixings have been realized in Germany, Poland, Switzerland, Japan, Italy and the United States of America (Santarsiero 2015).

FIGURE 2.15: DOW CORNING EUROPEAN DISTRIBUTION CENTER, EURIDICE WAREHOUSE, FELUY, BELGIUM, ADHESIVE PRODUCER: DOW CORNING (PHOTOS COURTESY OF DOW CORNING).

In the work of Van Hulle et al. (2011) adhesive point-fixings with TSSA were tested in shear for several durability tests (4 and 12 weeks exposition to 90% R.H. and 50°C). The reduction of the strength was about 10% compared to the non-aged specimens. Depending on the fabrication process the strength could increase about 20%.

The energetic benefit of using adhesive point-fixings with TSSA compared to bolted point-fixings was investigated on a IGU 6-12-6 by Appelfeld et al. (2015) and is illustrated in Figure 2.16. The boundary conditions for the thermal models were +20°C interior, -10°C exterior and the relative humidity was 40%. The heat flow through this specific detail was reduced from 62.0 W/m for bolted point-fixings to 25.3 W/m for adhesive point-fixings. The condensation on the glass and the fixings bolds with bolted point-fixings, indicated by the thick red line, was not present with adhesive point-fixings.
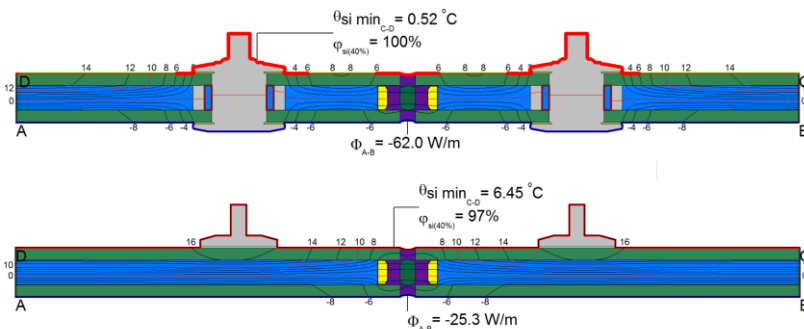
FIGURE 2.16: THERMAL MODEL FOR BOLTED AND ADHESIVE POINT-FIXINGS WITH TSSA (APPELFELD ET AL. 2015).

Another example of an adhesive point-fixing in structural glass is the Floreasca City Center in Bucharest constructed by Al Promt (Figure 2.17). Due to the curvature of the glass panels in the corner of the building, traditional bolted point-fixings could not be used. The adhesive point-fixings with a large diameter were fabricated with the silicone Sikasil® SG500, and for this adhesive, a minimal diameter of 144 mm was needed to bond the glass unit to the point-fittings.

FIGURE 2.17: FLOREASCA CITY CENTER, BUCHAREST, ADHESIVE PRODUCER: SIKA NV (PHOTOS COURTESY OF AL PROMT).

Adhesive point-fixings constructed with an epoxy adhesive are used by Bellapart in the roof of the Würth La Rioja Museum in Agoncillo, La Rioja (Spain), illustrated in Figure 2.18. The diameter of the connectors are 60 mm and are produced out of stainless steel grade AISI 316 with a specific surface roughness to increase adhesion. All connectors are bonded through a 0.8 mm thick layer of 3M™ DP-490 epoxy adhesive.

FIGURE 2.18: ROOF OF THE WÜRTH LA RIOJA MUSEUM IN AGONCILLO, LA RIOJA (SPAIN), EACH GLASS PANEL IS SUPPORTED BY FOUR ADHESIVE POINT-FIXINGS (PHOTOS COURTESY OF BELLAPART)

It is clear that despite the knowledge about adhesive point-fixings is still growing, a lot of shortcomings still exist in the research. For instance, there is more systematic investigation needed on the influence of several parameters, such as the diameter of the point-fixing, glass thickness, load directions, type of adhesive and more specifically the stiffness of the adhesive. Furthermore research on environmental parameters, such as humidity, UV-radiation and temperature, is needed to develop a proper design method for adhesive point-fixings between metal and constructive glass.
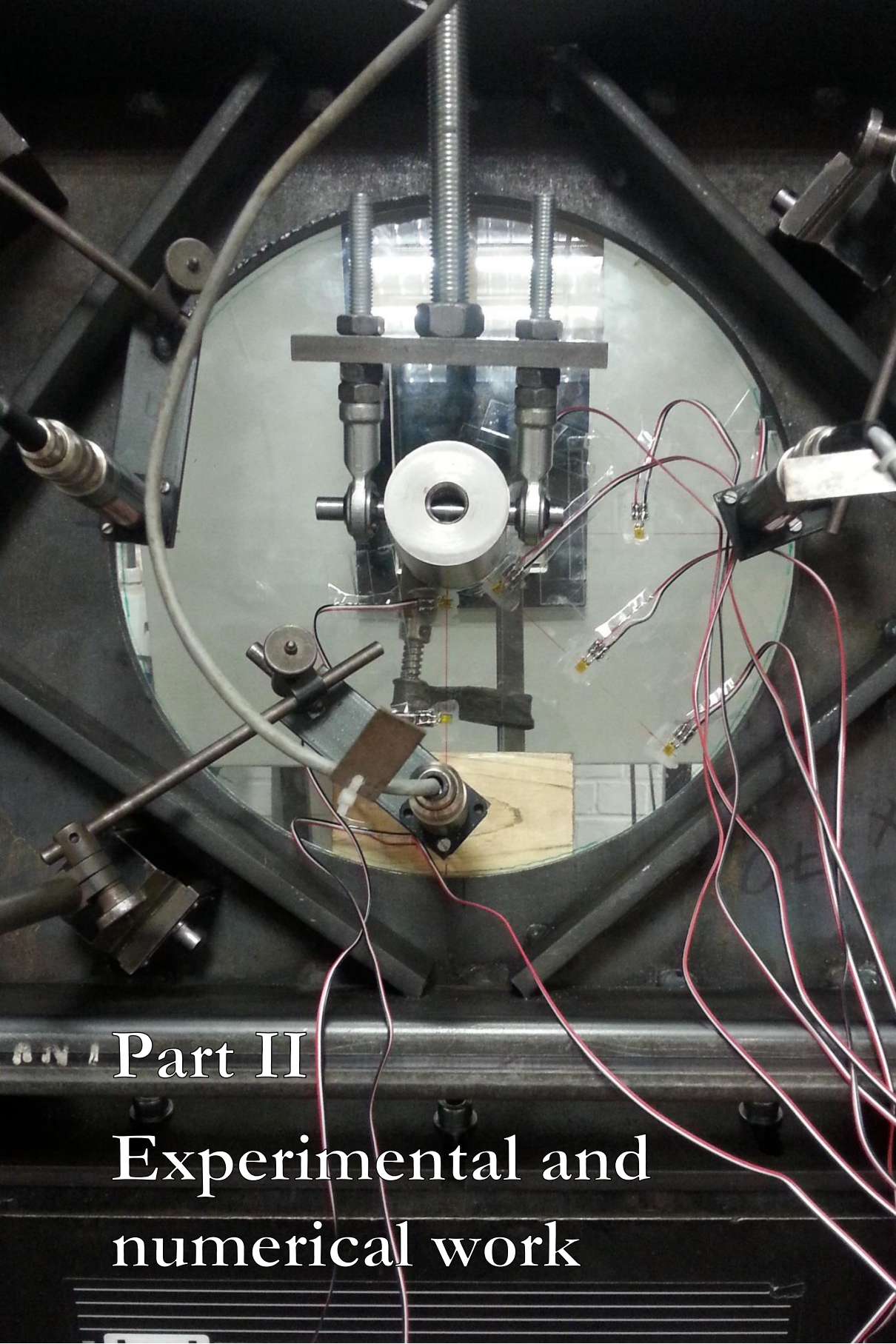
Part II

Experimental and
numerical work

Multi-axial test with an eccentricity of 45 mm
and a multi-axial angle of 67.5°.

Chapter 3: Adhesive material model

> I have not failed. I've just found 10 000 ways that won't work
>
> *Nikola Tesla*

3.1. Introduction

In following chapters of this dissertation, numerical analyses will be performed. Numerical analyses provide a fast and cost-effective way to analyse and optimise the mechanical performance of adhesive connections. Nowadays a lot of finite element programs are available on the market, most of them are suitable to model adhesive connections. With these FEA, the stress distributions and deformations can be determined in a bonded structure. However the accuracy of the numerical results depends on the validity of the used material models which describe the deformation behaviour of the adhesive and on the availability of suitable material property data for these models. The aim of this chapter is to determine the material models for two selected adhesives.

The choice of material model depends on the adopted adhesive material. Two-component epoxies and acrylates are thermosetting adhesives. These kinds of adhesives are usually brittle materials that will fail at relatively small strains by the initiation and propagation of a crack. The behaviour of these materials is typically elastic until failure. However, many other adhesives are rubber-like materials, such as silicones and Modified Silane (MS) polymers. With these adhesives, due to the rubber phase that occurs, relatively large strains (>5%) can appear prior to failure. This requires the use of material models that describe the non-linear mechanical behaviour to obtain a good calculation under high deformations, i.e. hyperelastic material models. These material models are presented as mathematical expressions, which can be implemented in the used finite element software. The determination of the material constants in the mathematical expressions, the so-called calibration of the material models, is done by fitting the mathematical functions to experimental curves using a least squares method.

The suitability of the used material model is often examined by modelling the experiments that are used for the calibration, e.g. an uniaxial tensile test on bulk material, in the finite element software. The numerical results from this finite element model are then compared to the experimental results (Arruda & Boyce 1993; Meunier et al. 2008; Hoss & Marczak 2009). This comparison is called the validation of the material model. Indeed, with this kind of validation, it is very likely that the validation will give good results, considering that the numerical results are compared to the same experimental results that are used as input-data. This kind of validation will only give information about the suitability of the used material constants. Also, the adhesive can react differently in an adhesive connection than in bulk material (Weller & Vogt 2009; Dean et al. 1996).

Therefore, it is recommended to implement the selected and calibrated material model in the numerical model for an adhesive connection for a good validation. The validation consists of comparing the numerical results to the experimental results of the same adhesive connection. This process will be iterative since it is not known in advance which of the several possible models will correspond best. Those additional validation experiments are best derived from the final geometrical configuration of the adhesive joint. In this chapter these validation experiments consist of adhesively bonded steel point-fixings loaded in tension and in a combination of tension and shear, which is in line with the main load conditions expected for adhesive point-fixings.

3.2. Theoretical background

Adhesives usually consists of long chain molecules, so-called polymers. The term elastomer is the combination of elastic and polymer and is often used interchangeably for rubber-like materials. Elastomers present a very complicated mechanical behaviour that mostly exceeds the linear elastic theory and usually contains large deformations and plastic and viscoelastic properties (Chagnon et al. 2004). Elastomers are basically super-condensed gases, because most primary monomers are gases, and after polymerization have long chain molecules which will be in an amorphous (rubber), glassy or crystalline phase. During crosslinking, the molecules are chemically fastened together at various points to form a network. They make stationary positions to prevent slippage of chains.

When subjected to an applied stress, polymers may deform by either or both of two fundamentally different atomistic mechanisms. The lengths and angles of the chemical bonds connecting the polymer chains may distort, moving the polymer chains to new positions of greater internal energy. This is a small motion and occurs very quickly, requiring only $\approx 10^{-12}$ seconds. If the polymer has sufficient molecular rotation, larger-scale rearrangements of the polymer chains may also be possible. Depending on the rotation, a polymer molecule can extend itself in the direction of the applied stress, which decreases its conformational entropy (the molecule is less "disordered"). Elastomers respond almost entirely by this entropic mechanism, with little distortion of their covalent bonds or change in their internal energy. The rate at which the polymer's chains can change direction quantifies the amount of mobility of the polymer molecules. This rate depends mostly on the glass transition temperature T_g. The value of T_g is so an important descriptor of polymer thermomechanical response.

At temperatures much above T_g the deformation rate of the polymer molecules is so high as to be essentially instantaneous, and the polymer acts in a rubber-like manner in which it exhibits large, instantaneous, and fully reversible strains in response to an applied stress (Roylance 2001). Rubber-like materials have a typical 'S' shaped stress-strain diagram and are unique in being soft, very extensible and very elastic, which describes hyperelastic behaviour. Conversely, at temperatures much lower than T_g, the deform rate is so low as to be negligible. Here the chain uncoiling process is essentially "frozen out" so the polymer is able to respond only by bond stretching. It now responds instantaneously and reversibly but being incapable of being strained beyond a few percent before fracturing in a brittle manner. In the range near T_g, the material is midway between the glassy and rubbery regimes. Its response is a combination of viscous fluidity and elastic solidity, and this region is termed visco-elastic behaviour. Factors that enhance mobility, such as absorbed diluents, expansive stress states and lack of bulky molecular groups, all tend to produce lower values of T_g (Roylance 2001).

Hyperelastic behaviour   In general, more flexible adhesives present a very complicated mechanical behaviour that often exceeds linear elastic theory. Very large reversible strains can occur at rubber-like polymers in a certain state. The stresses are no longer linearly proportional to the strains at large deformations; the

material's behaviour is hyperelastic. An appropriate way to describe the behaviour of hyperelastic materials is the use of the strain energy function W (Dias et al. 2014). This function relates the strain energy density of a material to the deformation gradient according to Eq. (3.1).

$$W = f(I_1, I_2, I_3) \tag{3.1}$$

With:

W = strain energy function

I_1, I_2 and I_3 = the three invariants of the left Gauchy-Green deformation tensor given in terms of the principal extension ratios λ_1, λ_2 and λ_3 defined as the ratio between the final length to the initial length, by:

$$I_1 = \lambda_1^2 + \lambda_2^2 + \lambda_3^2$$
$$I_2 = \lambda_1^2\lambda_2^2 + \lambda_2^2\lambda_3^2 + \lambda_1^2\lambda_3^2$$
$$I_3 = \lambda_1^2\lambda_2^2\lambda_3^2$$

These expressions for the three invariants are derived from Eq. (3.2), (3.3) and (3.4).

$$I_1(B) = TR(B) \tag{3.2}$$

$$I_2(B) = \frac{1}{2}[tr(B)^2 - tr(B^2)] \tag{3.3}$$

$$I_3(B) = det(B) \tag{3.4}$$

With TR the trace of a square matrix, representing the sum of its diagonal entries. The expression of the left Gauchy-Green tensor B is given in Eq. (3.5), with F the deformation gradient tensor.

$$B = F.F^T \tag{3.5}$$

According to Chagnon et al. (2004) an efficient hyperelastic model must conform to four main qualities:

- It should have the ability to exactly reproduce the whole 'S' shaped response of rubbers;

- The change of deformation modes should not be problematic, i.e. if the model behaves satisfactorily in tension, it should also be quite accurate in simple shear or in a equibiaxial extension;
- The number of relevant material parameters should be small;
- The mathematical formulation should be as simple as possible for the numerical performance of the model.

The material models are generally distinguished in two main groups: purely micromechanical-based network models and phenomenological models.

The **micromechanical-based network models** are based on statistical mechanics of idealized networks of cross-linked long-chain molecules (Boyce & Arruda 2000). The governing parameters in micromechanical models relate macroscopic mechanical behaviour to the causative physical/chemical structure. Prominent examples for micromechanical models are the 3-chain and 8-chain models which have been proven to be appropriate for moderate to large elastic deformations of rubber-like materials (Boyce & Arruda 2000; Miehe 2004). The second group of material models, the **phenomenological models**, rely on continuum mechanics, often using polynomial formulations in terms of strain invariants or principal extension ratios derived from the fitting of experimental results. Such empirical functions generally lack a connection to the molecular structure of the material which results in a less direct physical interpretation of the governing parameters (Miehe 2004). Owing to their polynomial form, these models may result in unrealistic results beyond the deformation range within which their material parameters are determined. The polynomial model based on the first and second invariant is given in Eq. (3.6) where C_{ij} are material constants. When only the first invariant is taken into account (j=0), the reduced polynomial model is obtained (Rivlin & Saunders 1997; Dias et al. 2014).

$$W = \sum_{i+j=1}^{N} C_{ij} \, (I_1 - 3)^i \cdot (I_2 - 3)^j \qquad (3.6)$$

The Mooney-Rivlin model, which was originally proposed by Mooney (Mooney 1940), can be considered as one of the simplest forms of the invariant-based models. The formulation of the Mooney-Rivlin model is given by the first order (N=1) of the polynomial model. The Neo-Hooke model constitutes the simplest

specification of the Mooney–Rivlin model series (Treloar 1943). It only considers the first order (N=1) of the reduced polynomial model (j=0). Another well-known phenomenological model has been suggested by Yeoh in the form of the third-order (N=3) polynomial of only the first invariant I_1 (j=0) (Yeoh 1990). Finally, the model proposed by Ogden (Ogden 1972) is probably the best known example of the principal extension ratio-based material models.

An overview of the above-mentioned material models for both micromechanical and phenomenological material models for incompressible materials is given in Figure 3.1. The material parameters in the strain energy potential are determined by fitting the strain energy function to stress-strain data based on a non-linear least square optimization method, the so-called calibration of the material parameters. It should be noted that fitting results should always be checked with the recommended strategies such as using a different model and providing more data points. However, models with few material parameters are preferred for the purpose of computational efficiency (Ali et al. 2010; Steinmann et al. 2012). In this work, 14 material models were calibrated and validated. A summary of these 14 material models is given in Appendix A.
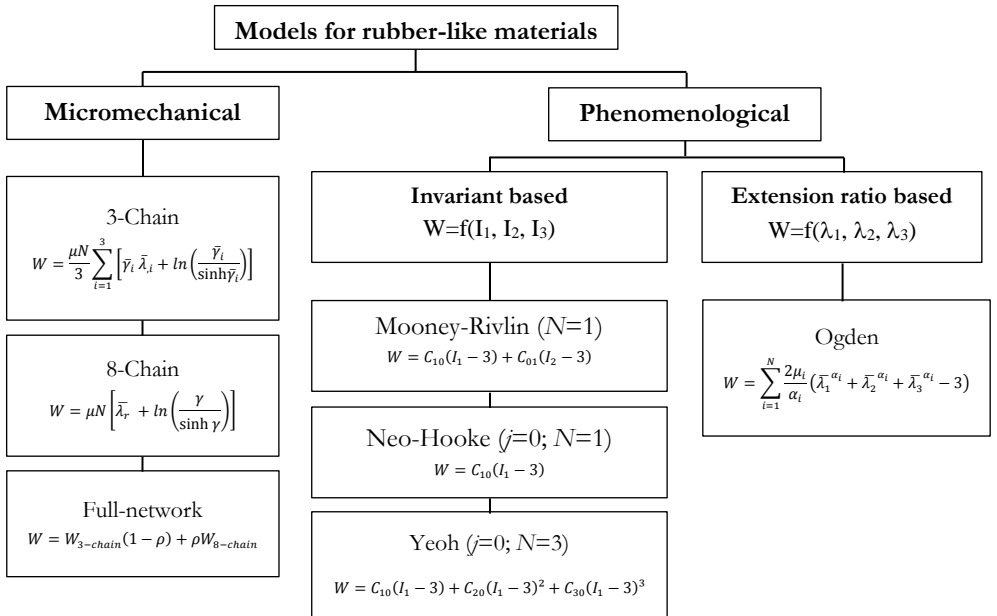

FIGURE 3.1: OVERVIEW OF MICROMECHANICAL AND PHENOMENOLOGICAL MATERIAL MODELS FOR INCOMPRESSIBLE MATERIALS.

3.3.   Materials and methods

3.3.1. Adhesives

The ideal adhesive for adhesive point-fixings should be flexible enough to deal with differential thermal expansions and strong enough to withstand the loads applied on the point-fixing. The selection of two adhesives is made based on earlier research. An extensive experimental programme on adhesives for structural applications with glass has been performed by researchers of Ghent University and Delft University of Technology to help designers to select potential adhesives based on specific environmental exposures and loading conditions (Belis et al. 2011). As a more flexible adhesive, the one-component MS-polymer **Soudaseal 270 HS** (SO) adhesive was selected, a hybrid polymer adhesive with a base of polyurethane and silicone. This adhesive combines the advantages of a polyurethane adhesive and a silicone, which gives a strong and flexible bond. The colour of the adhesive is white. Typical applications are elastic structural bonding in car-, train- and aerospace industries. As a more stiff adhesive, the structural two-component epoxy **3M™ Scotch-Weld™ 9323 B/A** (3M) was selected. This adhesive cures in 14 days at room temperature or with mild heat to form a tough, impact resistant structural polymer material. A chemical reaction is initiated by mixing a modified epoxy with a modified amine. It has an excellent adhesion to a wide variety of substrates such as metals, glass, ceramics and plastics. Once cured it provides high shear and peel strength over a wide temperature range.

3.3.2. Glass transition temperature

The determination of the glass transition temperature T_g for the two selected adhesives is done by Dynamic Mechanical Thermal Analysis (DMTA). In DMTA a specimen (e.g. a cured adhesive) is subjected to a Dynamic Mechanical Analysis (DMA) for different temperatures. In DMA the specimen is subjected to a mechanical oscillation at fixed resonant frequencies. From DMTA, the storage (elastic) modulus E' and the loss (viscous) modulus E'' are determined in function of the temperature. From these moduli the glass transition temperature is determined. T_g is the temperature of the point of inflection of the decrease in the storage modulus curve. This point corresponds often with the peak of the loss modulus data (ISO 6721-11 2012).

The bulk samples of the two adhesives were fabricated with a mould of polytetrafluoroethylene (PTFE). After curing, the samples were stored for a time period of 4 weeks at a constant temperature of 21° C and a relative humidity of 45% without any UV-radiation in a climatic chamber. The curing process of SO is moisture curing. Since the chosen fabrication method implied sealing off the sample from air, extra water was mixed with the adhesive before injecting it into the mould to increase its moisture content. After contacting the manufacturer of SO, this extra amount of humidity was set to 5%. The mixing ratios by weight of the two components of the epoxy 3M are 27 to 100, respectively. The weighing of each component was done with a balance ($\pm$ 0.1 gram). The components were mixed manually in a specific PTFE cartridge, which was then installed on the mould. The curing of the adhesive took place inside the mould at 20°C. After two hours the adhesive was sufficiently cured to be removed from the mould.

A sample of 40 x 10 x 4 mm was loaded in oscillating tension in the DMTA machine. First a static load was applied on the specimen with a value set by the maximum of either 100 N or the force needed for a strain of 1%. Afterwards additional 10 loading cycles were applied for each temperature step with a magnitude set by the maximum of either 40 N or the force needed for a strain of 0.2%. The used DMTA-machine of the University of Kaiserslautern is depicted in Figure 3.2 together with a tensile sample.

a)
b)
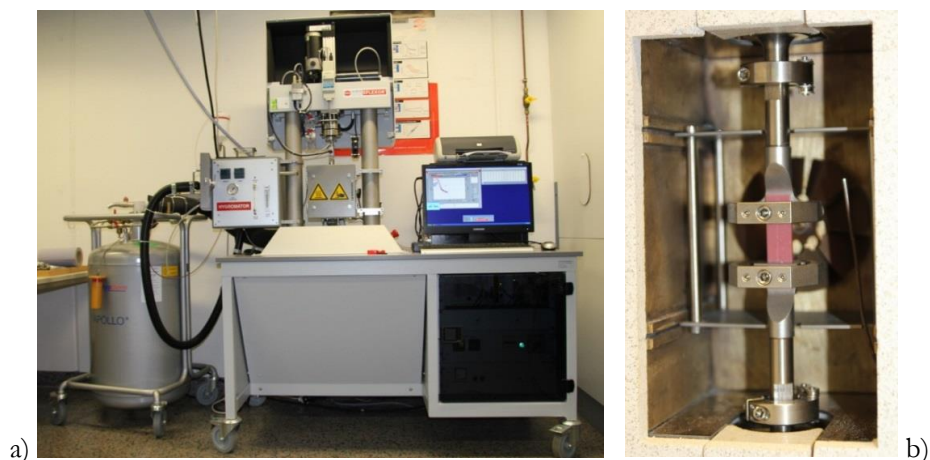
FIGURE 3.2: A) DMTA TESTING MACHINE OF THE UNIVERSITY OF AND B) THE TENSILE CONFIGURATION.

The temperature range was set from -100°C to 20°C in steps of 5°C for the MS-polymer samples and from -20°C to 120°C with a step of 2°C for the epoxy samples. High frequencies may cause resonance in the samples while low frequencies take a very long time. As a result, the samples were subjected to frequencies of 1 Hz, 3.162 Hz and 10 H. The results are shown in Figure 3.3a for the MS-polymer and in Figure 3.3b for the epoxy. The glass transition temperature has a value of **-64.3°C** for the MS-polymer SO and **83.1°C** for the 2c-epoxy 3M.

a)   b)
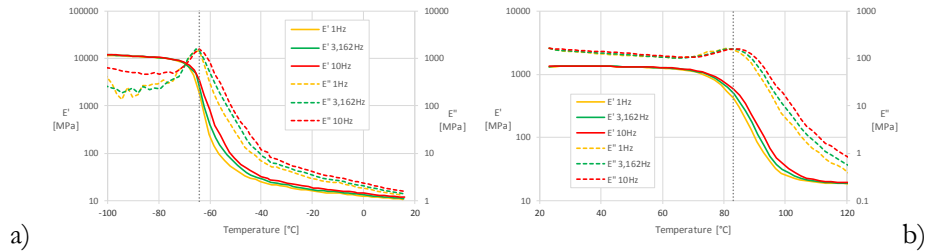
FIGURE 3.3: TENSILE DMTA OF A) THE MS-POLYMER SAMPLES AND B) THE EPOXY SAMPLES.

With the DMTA machine it was also possible to perform compression tests on bulk material. A square sample of 10 mm length and thickness 4 mm was fabricated. Samples mounted between the compression clamps of the MS-polymer and the epoxy are depicted in Figure 3.4. The sample of the MS-polymer SO was placed horizontally to prevent buckling of the sample.

a)   b)
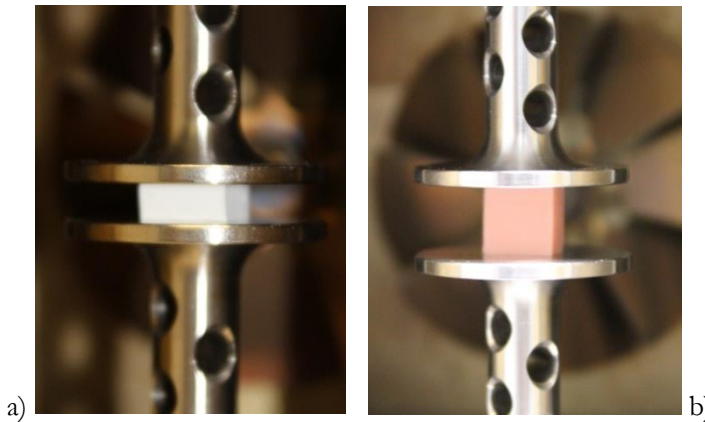
FIGURE 3.4: THE COMPRESSION TEST CONFIGURATION FOR A) THE MS-POLYMER SO AND B) THE 2C-EPOXY 3M.

To obtain a constant pressure during the test a contact force of 2,0 N was set. The temperature range was set from -100°C to 20°C for the MS-polymer samples and from 20°C to 120°C for the epoxy samples with a step of 2°C and the same three frequencies as in the previous test were set. The results of the compression DMTA for the MS-polymer SO are presented in Figure 3.5a and in Figure 3.5b for the 2c-epoxy 3M. The glass transition temperature is equal to **-63.4°C** for the MS-polymer SO and **72.1°C** for the 2c-epoxy 3M.
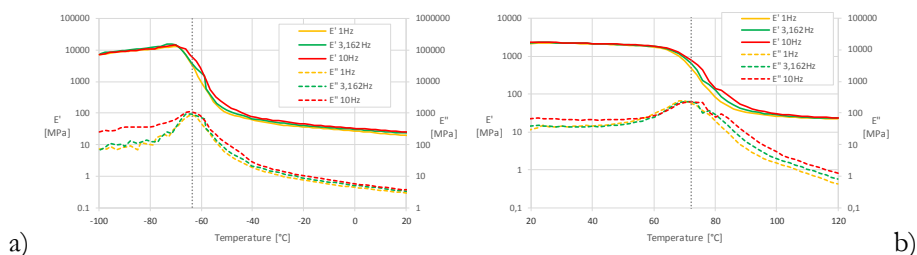

FIGURE 3.5:COMPRESSIVE DMTA OF A) THE MS-POLYMER SAMPLES AND B) THE EPOXY SAMPLES.

Since there is a relatively large difference between the values of the glass transition temperature for the epoxy samples, T_g was also measured with another method, i.e. Differential Scanning Calorimetry (DSC) for the 2c-epoxy 3M. DSC is a thermo-analytical technique in which the difference in the amount of heat required to increase the temperature of a sample and reference is measured as a function of temperature. The underlying basic principle is that when the sample undergoes a physical transformation such as a phase transition, more or less heat will need to flow to it than the reference to maintain the same temperature. Whether less or more heat must flow to the sample depends on whether the process is exothermic or endothermic. For example, as a solid sample melts to a liquid it will require more heat flowing to the sample to increase its temperature at the same rate as the reference. This is due to the absorption of heat by the sample as it undergoes the endothermic phase transition from solid to liquid. Likewise, as the sample undergoes exothermic processes (such as crystallization) less heat is required to raise the sample temperature. By observing the difference in heat flow between the sample and reference, DSC is able to measure the amount of heat absorbed or released during such transitions. DSC may also be used to observe more subtle physical changes, such as glass transitions. Glass transitions occur as the temperature of an amorphous solid is increased. These transitions appear as a step in the baseline of the recorded DSC signal. This is due to the sample

undergoing a change in heat capacity. An epoxy sample was subjected to an increasing temperature rate of 20°C/min. The outcome of this temperature cycle is depicted in Figure 3.6 and the glass transition temperature is determined at a value of **74.6°C**.
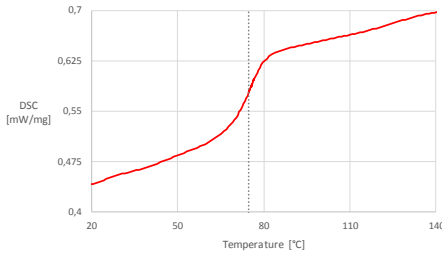
FIGURE 3.6: DSC RESULTS FOR THE EPOXY 3M.

The glass transition temperature of SO can be set to around **-64°C** and to **75°C** for 3M. Since the working temperature is higher than the glass transition temperature for SO, the adhesive is assumed to be a rubber-like adhesive and will behave hyperelastically. This type of behaviour can be modelled by means of phenomenological and micromechanical material models, as mentioned above. The accuracy of these material models is accomplished by additional validation experiments. Since the working temperature is lower than the glass transition temperature for 3M, the adhesive is assumed to behave linear elastically. This behaviour can be characterised by the Young's modulus and the Poisson's ratio.

3.3.3. Tensile tests

Since the material models will be more accurate if experimental data is obtained for different load directions (Sasso et al. 2008; Stumpf & Marczak 2010), the calibration of the material models was performed with the experimental data obtained from uniaxial tensile, compressive and shear experiments. All these experiments were performed on a Zwick/Roell 10kN ProLine testing machine with a load cell of 0.5 kN or 10 kN.

The tensile experiments were performed by subjecting the tensile test samples to a tensile load. Five tensile test samples for each adhesive were produced according to the European standard EN ISO 527 (1996), a commonly used standard to make dumbbell samples. The shape and dimensions of the used dumbbell specimen type 1A according to ISO 527 are illustrated in Figure 3.7.
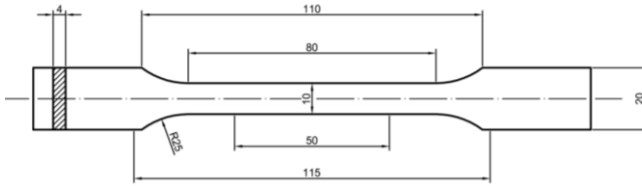
The mould that was used consists of an intermediate layer and a body of PTFE, a stiff material with a low solid surface free energy. The total configuration of the mould is depicted in Figure 3.8. According to standard ISO 527 a displacement rate between 1 mm/min and 500 mm/min must be applied on the dumbbell specimens. Exploratory tests were performed to determine the applied displacement rate. To obtain the best measurements, low displacement rates were preferred. Due to the long elongation at failure of the MS-polymer and time constraints, a 5 mm/min displacement rate was applied for SO and 1 mm/min for 3M.

Cover layer – PMMA (10 mm)

Intermediate layer – PTFE (1 mm)

Body layer – PTFE (4 mm)

Intermediate layer – PTFE (1 mm)

Rigid layer – Trespa® (10 mm)
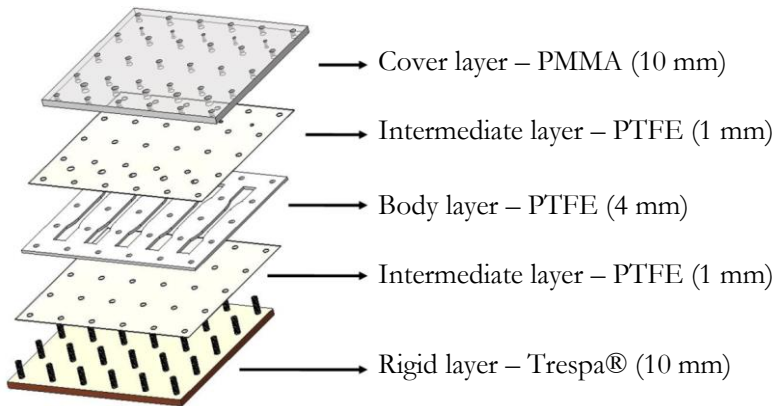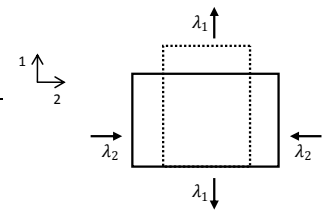
For uniaxial tension, the specimen will be elongated in only one direction. With the elongation according to $\lambda_1 = \lambda$, the assumption of isotropy gives the two others principal extension ratios $\lambda_2 = \lambda_3 = \lambda^{-1/2}$. Due to the assumption of (near) incompressibility, the third invariant of the deformation tensor will be: $I_3 = \lambda_1^2 \lambda_2^2 \lambda_3^2 = 1$. From the occurring elongations consecutively the deformation gradient tensor F, the left Gauchy-Green tensor B, the three strain invariants can be determined and finally the principal Cauchy stresses σ_i, $i \in \{1,2,3\}$ can be defined according to Eq. (3.7) with p a Lagrange multiplier (Ogden et al. 2004). This derivation for the situation of uniaxial tensile is summarised in Table 3.1.

$$\sigma_i = \lambda_i \frac{\vartheta W}{\vartheta \lambda_i} - p \tag{3.7}$$

TABLE 3.1: DETERMINATION OF THE PRINCIPAL CAUCHY STRESSES FOR UNIAXIAL TENSION.

$$F = \begin{bmatrix} \lambda_1 & 0 & 0 \\ 0 & \lambda_2 & 0 \\ 0 & 0 & \lambda_3 \end{bmatrix} = \begin{bmatrix} \lambda_1 & 0 & 0 \\ 0 & \lambda_1^{-1/2} & 0 \\ 0 & 0 & \lambda_1^{-1/2} \end{bmatrix} \qquad B = \begin{bmatrix} \lambda_1^{\,2} & 0 & 0 \\ 0 & \lambda_1^{-1} & 0 \\ 0 & 0 & \lambda_1^{-1} \end{bmatrix}$$

$$I_1 = 2\lambda_1^{-1} + \lambda_1^{\,2}$$

$$I_2 = \lambda_1^{-2} + 2\lambda_1$$

$$I_3 = 1$$

$$\sigma_{11} = 2\left[\frac{\partial W}{\partial I_1} + \frac{1}{\lambda_1}\frac{\partial W}{\partial I_2}\right]\left[\lambda_1 - \frac{1}{\lambda_1^{\,2}}\right]$$

$$\sigma_{22} = 0$$

$$\sigma_{33} = 0$$

For the hyperelastic material models, with the expression of the principal stresses and uniaxial tensile data, the material coefficient can be determined of the used material model. For example, in Figure 3.1 the strain energy function W is depicted for the material model of Neo-Hooke, i.e. $W = C_{10}(I_1 - 3)$. The relationship between the principal stress σ_{11} and the elongation λ_1 can now be expressed in function of the unknown material coefficient C_{10}, given by Eq. (3.8). This equation is then fitted to the test data for uniaxial tension, from which the material parameter C_{10} is ultimately determined. This procedure is implemented to determine all the material coefficients of all the selected material models.

$$\sigma_{11} = 2C_{10}\left[\lambda_1 - \frac{1}{\lambda_1^{\,2}}\right] \tag{3.8}$$

3.3.4. Compressive tests

In realistic situations the adhesive in an adhesive joint is usually not only loaded in tension. Complex stress distributions occur when the adhesive is loaded in several types of loading. Hyperelastic material models derived from solely uniaxial tensile tests are insufficient in that case. Hence, to take the compressive mode into account, compressive tests are indispensable. With compressive tests, the test samples can be typical blocks or cylinders (ISO 604 2002; ASTM D695 2010). In this research five cylindrical compression specimens were produced in a PTFE-mould with a diameter of 30 mm and a height of 15 mm for each adhesive (ISO 604 2002). The applied displacement rate was 1 mm/min. The principal Cauchy stresses for uniaxial compression are derived in the same way as for uniaxial tension displaced in Table 3.1.

3.3.5. Shear tests

A very frequently used test to determine the material properties of adhesives under shear is the single-lap joint (SLJ) (ASTM D1002; ASTM D3163; DIN 54451; ISO 4587). As shown in Figure 3.9, the applied forces are not co-linear and will therefore introduce a bending moment in the joint. The adherents will bend due to eccentricity and the adhesive layer will not only be loaded in shear but will also have tearing stresses at the ends of the joint. This introduces stress concentrations at the ends of the joints which can cause plastic regions in the adherents and/or adhesives and early failure.
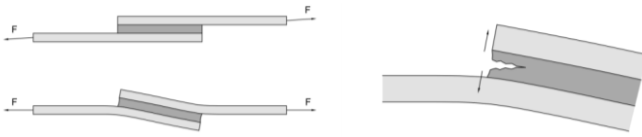
FIGURE 3.9: BENDING MOMENT DUE TO THE ECCENTRICITY IN A SLJ.

This problem can be partially improved by using the thick adherent shear test (TAST) (ASTM D3983; ASTM D5656; DIN 14869-2; ISO 11003-2). The adhesive overlap is created by removing half of the thickness of each thick adherent. Together with the increased stiffness of the connection due to the thicker adherents, this led to the believe that there are no significant transverse peeling loads. The simplest analysis assumes that the adherents are rigid and the adhesive will only deform in shear. The shear stress will be evenly distributed along the adhesive layer (see Figure 3.10a) and can easily be determined by dividing the applied force by the glued surface. This is shown in Eq. (3.9), where τ is the shear stress, F the applied force, b the width of the adhesive layer and l the overlap length of the adhesive layer. Although this equation is used in several standards, the assumptions that the adherents are rigid and that the adhesive will only deform in shear, are not entirely correct. In fact, with very stiff adhesives, e.g. epoxies and acrylates, the adherents will also deform under the tensile force. This will cause non-uniform shear stresses in the adhesives, so-called differential shear. Due to the differential shear, shear stress concentration will occur at the ends of the joint. This was first brought into account by Volkersen (1938) in his analytic method to describe the shear stress distribution in single lap joints. The effect of differential shear is shown in Figure 3.10b.

$$\tau = \frac{F}{b \cdot l} \qquad\qquad (3.9)$$
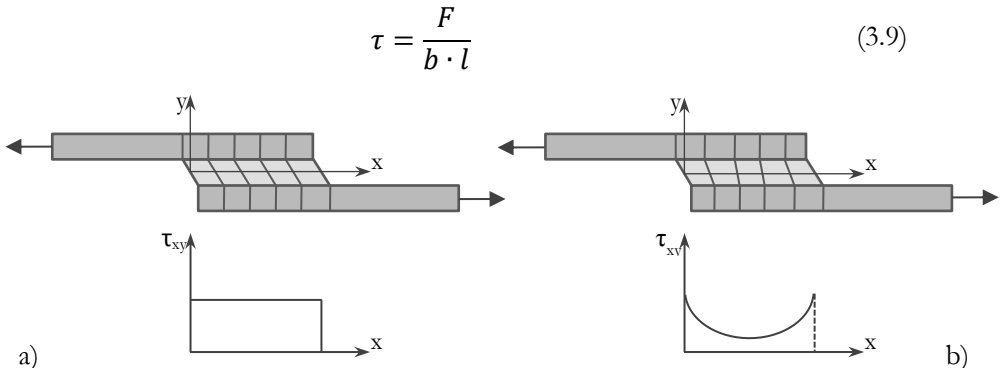
FIGURE 3.10: SHEAR STRESS DISTRIBUTING WITH A) A RELATIVE FLEXIBLE ADHESIVE AND B) A RELATIVE STIFF ADHESIVE.

The technical datasheet of the MS-polymer SO gives a Young's modulus around 2 MPa (Soudal 2003). For this adhesive the TAST can be used since the aluminium adherents with an elasticity modulus of 70000 MPa are significantly stiffer than the adhesive. The dimensions of the used TAST configuration according to DIN 14869-2 are depicted in Figure 3.11. Five TAST were performed.
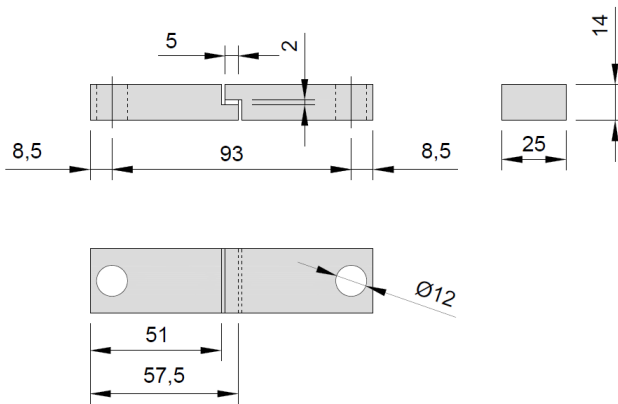
FIGURE 3.11: DIMENSIONS OF THE THICK ADHERENT TEST IN MM.

The Young's modulus of the epoxy 3M is much higher. Since the ratio between the adhesive stiffness and the adherents stiffness for this adhesive will be too high, stress concentration will occur at the edges. So the TAST is not suitable to determine the shear characteristics for the epoxy 3M. The Iosipescu (notched beam) shear test is a shear test on bulk material and is described in the American standard ASTM D5379 (see Figure 3.12). This test is originally designed to

determine the shear properties of composite materials. Recent research has shown that the Iosipescu test can also be used for adhesives (Almeida & Monteiro 2000; Xu et al. 2004; da Silva et al. 2011; Daiyan et al. 2012). With this test a straight beam with two 90° V-notches or U-notches is clamped between two pairs of loading rails. A pure and uniform shear stress distribution is obtained between the notches when two forces couples are applied so that two counter acting moments are generated, as depicted in Figure 3.13. The shear stress can easily be calculated by Eq. (3.10) with F the applied load, b the width between the notches and t the thickness of the specimen.

$$\tau = \frac{F}{b \cdot t} \tag{3.10}$$

The stress distribution and strains between the notches are quite uniform at low forces. However at higher forces stress concentration occurs at the notch tips and causes failure of the specimens prior to the maximal shear stress of the stress-strain curve being reached (Seneviratne et al. 2010).
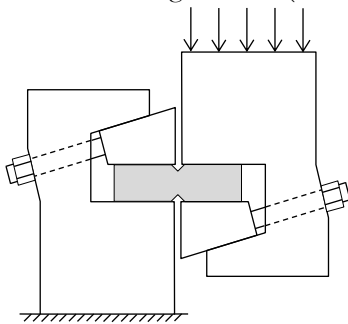
FIGURE 3.12: V-NOTCHED BEAM SHEAR TEST (ASTM D5379).
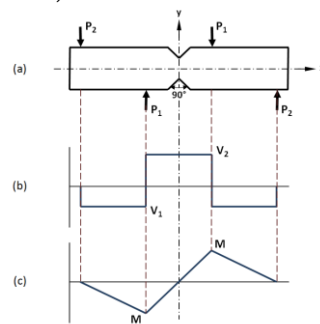
FIGURE 3.13: A) GEOMETRY OF THE TEST SPECIMEN AND LOADING CONFIGURATION FOR THE IOSIPESCU TEST WITH B) THE SHEAR DIAGRAM AND C) THE MOMENT DIAGRAM (BASED ON ALMEIDA & MONTEIRO, 2000).

In the research of Seneviratne et al. (2010) several specimen geometries were tested and the U-notched specimens showed the preferred results. These types of notched samples are already used in other researches (Harman et al. 2008). In the presented research five V-notched specimens as well as five U-notched specimens were used to obtain the complete stress-strain curve of the adhesive. The dimensions of the specimens are depicted in Figure 3.14. A thickness of 4 mm was selected to prevent in-plane bending of the specimens which can occur with thinner specimens (Daiyan et al. 2012).
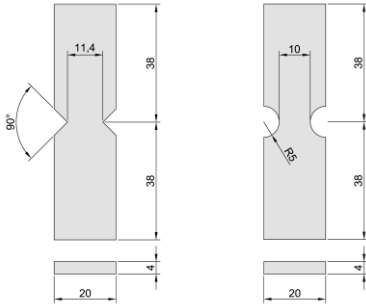
FIGURE 3.14: DIMENSIONS OF THE V-NOTCHED AND U-NOTCHED SPECIMENS IN MM.

The fabrication of the specimens was done in the same way as the dumbbell and compression specimens, i.e. the adhesive is poured and cured in a PTFE-mould. The applied displacement rate was 1 mm/min for the TAST and the Iosipescu shear test. The determination of the principal Cauchy stresses for pure shear is given in Table 3.2.

TABLE 3.2: DETERMINATION OF THE PRINCIPAL CAUCHY STRESSES FOR PURE SHEAR.

$$F = \begin{bmatrix} \lambda_1 & 0 & 0 \\ 0 & 1 & 0 \\ 0 & 0 & \lambda_1^{-1} \end{bmatrix}$$

$$I_1 = I_2 = \lambda_1^2 + \lambda_1^{-2} + 1$$

$$I_3 = 1$$

$$B = \begin{bmatrix} \lambda_1^2 & 0 & 0 \\ 0 & 1 & 0 \\ 0 & 0 & \lambda_1^{-2} \end{bmatrix}$$

$$\sigma_{11} = 2 \left[\frac{\partial W}{\partial I_1} + \frac{\partial W}{\partial I_2} \right] \left[\lambda_1 - \frac{1}{\lambda_1^3} \right]$$

$$\sigma_{22} = 2 \left[\frac{1}{\lambda_1^2} \frac{\partial W}{\partial I_1} + \frac{\partial W}{\partial I_2} \right] \left[\lambda_1^2 - 1 \right]$$

$$\sigma_{33} = 0$$

3.3.6. Additional validation experiments

With the above described tests the material characteristics of the two adhesives were determined. For the MS-polymer, the material constants of the material models for hyperelastic behaviour were determined by curve-fitting the mathematical functions to the experimental curves using a least squares method and for the 2c-epoxy the Young's modulus and Poisson's ratio were determined. To determine to suitability of the calibrated material model for the MS-polymer, additional validation experiments were conducted. These experiments consisted of two adhesively bonded point-fixings of stainless steel AISI 316L with a diameter of 50 mm (see Figure 3.15). The adhesive thickness of the MS-polymer SO was equal to 2 mm according to the technical data sheets of the producer.

This validation of the material model was conducted for two load configurations, i.e. one in uniaxial tension and one in a combination of tension and shear. The load condition where the adhesive was only loaded in tension was obtained by loading perpendicular to the adhesive layer. The combination of tension and shear was obtained by loading under an angle of 45° to the adhesive layer. The configuration of the tensile and tensile/shear additional validation experiment is illustrated in Figure 3.15. The displacement rate for the two load configurations was equal to 1 mm/min. All tests were performed at ambient temperature and humidity, i.e. 23.5°C and 40% RH.
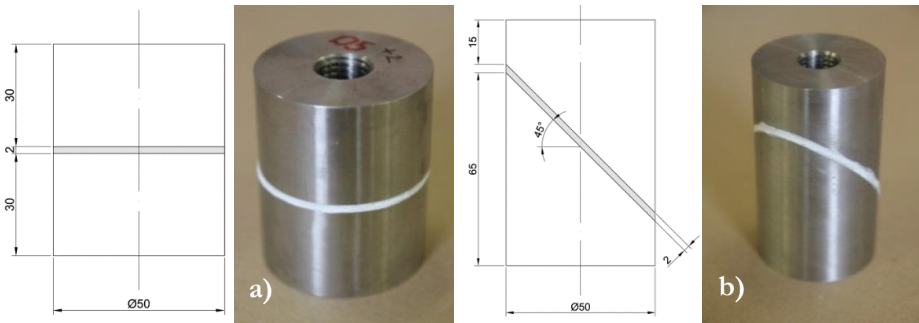
FIGURE 3.15: TEST CONFIGURATIONS IN MM. OF THE ADDITIONAL VALIDATION EXPERIMENTS FOR A. UNIAXIAL TENSION AND B. COMBINATION OF TENSION AND SHEAR FOR THE MS-POLYMER SO.

3.3.7. Digital image correlation

It is important to measure the complete deformation of the bulk material and adhesive layer to obtain valuable measurements. As the dumbbell specimens deformed over their entire length instead of deforming only at the narrow section, recording the displacements of the clamps was not sufficient. For this reason, digital image correlation (DIC) was chosen to measure the full-field surface deformation of all test specimens. DIC is a measurement method where occurring deformations of test specimens are calculated after the application of a random speckle pattern. It is a full field measurement method which implies that, unlike a traditional extensometer (considering the relative displacement of only two points), the deformations of an entire surface area of interest can be investigated. The measurement consists of taking photos of the specimen at regular, discrete moments during the test. Afterwards, the photos are correlated by adequate software, the occurring deformations being calculated from the relative speckle

movement. As such, relative or absolute displacements, in-plane strains in different directions, virtual strain gauges and virtual extensometers can be read out of the correlation software. In this research, the DIC software was also used to calculate the occurring lateral contraction to determine the real specimen section and thus the true stress instead of the commonly used engineering stress. Recent research demonstrated that DIC is highly complementary to conventional strain measurements techniques as strain gauges or LVDTs in structural adhesive testing (Van Lancker et al. 2016a). For an in-depth mathematical background and more details, the reader is referred to literature (Sutton et al. 2009; Hertelé et al. 2013).

The images were collected by a stand-alone system of *Limess Messtechnik GmbH & Software*, consisting of two synchronized monochromatic 14 bit cameras having a resolution of 2452 x 2054 pixels (5 megapixels). The DIC measurements were performed using hardware and a software license of Soete Laboratory, Ghent University. The dull black paint speckles were sprayed on the white bulk material. The paint was sufficiently flexible and ductile to withstand the occurring strains, so that no slip could occur between the pattern and the specimens. Of course, the pattern itself may not reinforce the specimen. A sufficient number of speckles, i.e. ±50% coverage of the specimen surface, was applied. The size of the random speckles was chosen with the aim of obtaining an optimal accuracy, roughly 3x3 pixels per speckle, (Sutton et al. 2009). The use of two cameras rather than one allows to include the third dimension into the analysis of displacements, the stereo-vision system 3D DIC. The displacements and strains were analysed using the VIC-3D software from *Correlated Solutions Inc.*

The test specimen itself was illuminated by two cold light sources, over which a cloth was stretched to promote a diffuse light intensity. The cameras could be positioned horizontally or vertically, as depicted in Figure 3.16a for a horizontal setup and in Figure 3.16b for a vertical setup for a tensile test. The vertical positioning was maintained for all tests, except for the compressive tests where the cameras were positioned horizontally. To construct stress-strain diagrams, strain values were determined by means of DIC and the force was measured by the tensile machine. A data acquisition (DAQ) connection between the analogous machine output and the DIC software coupled the captured images (i.e., strain information) with their corresponding forces (i.e., stress information), from which the stress-strain diagrams were derived.
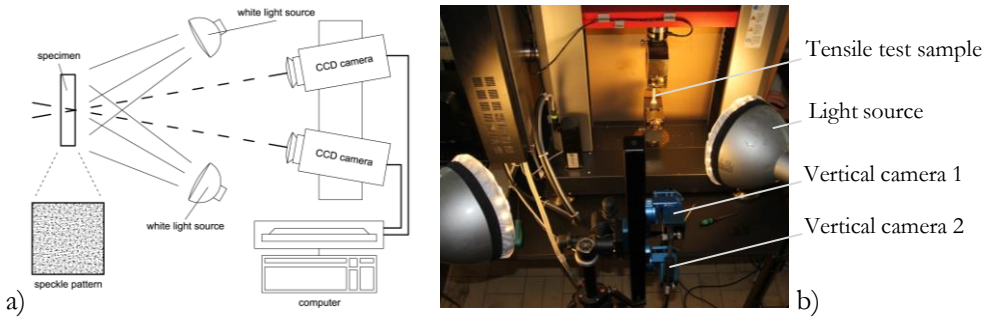
FIGURE 3.16: A) VISUALISATION OF THE SETUP FOR HORIZONTAL 3D-DIC (VAN LANCKER ET AL. 2016A) AND B) VERTICAL POSITIONING OF THE CAMERAS AND LIGHTS FOR A TENSILE TEST.

3.4.   Small-scale test results

The determination of the material coefficient for the hyperelastic material models, the so-called calibration of the material models, is based on a non-linear least squares method between a theoretical stress-strain diagram and an experimental stress-strain diagram. The theoretical relationship between the principal stresses and the strains was determined by the procedure explained by Eq. (3.8). The experimental relationship was determined by uniaxial small-scale tests, i.e. tensile, compression and pure shear tests. For the linear elastic material model, the material properties were gained from tensile and pure shear small scale tests.

3.4.1. Tensile tests

As mentioned before, the tensile properties were determined by uniaxial tensile tests on the bulk material in the shape of dumbbells. For this test method, the standard ISO 527 was followed. The test specimen was loaded under a constant speed according to its longitudinal axis until fracture occurred. From the recorded load and strains, the corresponding stress-extension ratio diagrams were determined. Often the engineering strain and stress are used for the diagram, however with DIC it is possible to determine the true strain and stress.

Engineering strain and stress

The engineering strain or Cauchy strain ε_E is the ratio between the deformation $\varDelta L$ to the initial length L_0 of the test specimen and is expressed by Eq. (3.11) with

L the final length of the specimen. For elongation the engineering strain will be positive and for compression negative. The extension ratio λ is defined as the ratio between the final length of the specimen L to the initial length L_0 and is expressed by Eq. (3.12). The engineering stress σ_E is calculated as the ratio between the applied load F and the initial cross-sectional area A_0 and is given by Eq. (3.13).

$$\varepsilon_E = \frac{L - L_0}{L_0} = \frac{\Delta L}{L_0} \tag{3.11}$$

$$\lambda = \frac{L}{L_0} = \varepsilon_E + 1 \tag{3.12}$$

$$\sigma_E = \frac{F}{A_0} \tag{3.13}$$

True strain and stress

However, the engineering strain is a small strain measure which is invalid once the strain is no longer 'small' ($\approx 5\%$). True strain or Hencky strain ε_T is a non-linear strain measure that is dependent upon the final length of the model and is given by Eq. (3.14). The cross sectional area will also deform by the applied load due to the Poisson effect, for tensile tests the cross sectional area will decrease as depicted in Figure 3.17. This means that the occurring stress will increase. The true stress σ_T is determined by the instantaneous load F acting on the instantaneous cross sectional area A, as given in Eq. (3.15).

$$\varepsilon_T = ln(1 + \varepsilon_E) = ln(\lambda) \tag{3.14}$$

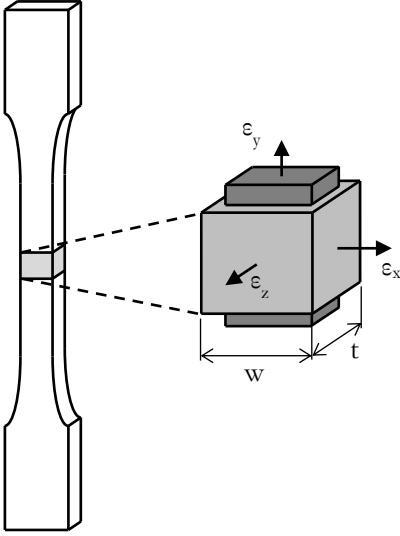$$\sigma_T = \frac{F}{A} \tag{3.15}$$

FIGURE 3.17: OCCURRING DEFORMATION FOR A DUMBBELL SPECIMEN LOADED UNDER TENSION.

The instantaneous cross sectional area A in Eq. (3.15) could be derived from the measured strains. As depicted in Figure 3.17, the width w and thickness t of the specimen will decrease by the transversal strains ε_x and ε_z respectively. As the bulk material is isotropic, the transversal strains will be equal. The instantaneous cross sectional area A was then derived as in Eq. (3.16).

$$A = w \cdot (1 + \varepsilon_x) \cdot t \cdot (1 + \varepsilon_z)$$

$$= w \cdot \exp(\varepsilon_{Tx}) \cdot t \cdot \exp(\varepsilon_{Tz})$$

$$= A_0 \cdot \exp(2 \cdot \varepsilon_{Tx}) \tag{3.16}$$

The stress-extension ratio diagram for the five tested tensile specimen was calculated from the measured load and strains with Eq. (3.14) and (3.15). From these five stress-extension ratio diagrams, an average stress-extension ratio diagram was calculated by means of an interpolation of the abscissa values for each dataset using Matlab®. The corresponding ordinate values were calculated by interpolation between the original ordinate values. With this approach, the interpolation must always be smaller than the measurement frequency. The abscissa values were interpolated every 0.001. After the interpolation, the average value of the ordinate value was calculated per abscissa value. The local true strain on the surface of the sample was determined by DIC. This allowed a stress-strain

analysis in which deformation occurs uniformly. Figure 3.18 and Figure 3.19 show a picture sequence of the test for tensile tests on the MS-polymer SO and the epoxy 3M, respectively. Furthermore, the strain along the longitudinal axis ε_y is depicted on the figures. From Figure 3.18 it is clear that the occurring strains are almost uniformly distributed along the longitudinal axis for SO. Strains also occurred at the wide section of the dumbbell specimen. For the epoxy sample in Figure 3.19 the strain is uniformly distributed at small elongations. However, at large elongations strain concentration occurred at the place where failure would initiate, resulting in a non-uniformly distributed strain. These observations substantiates the use of DIC to measure the strains.
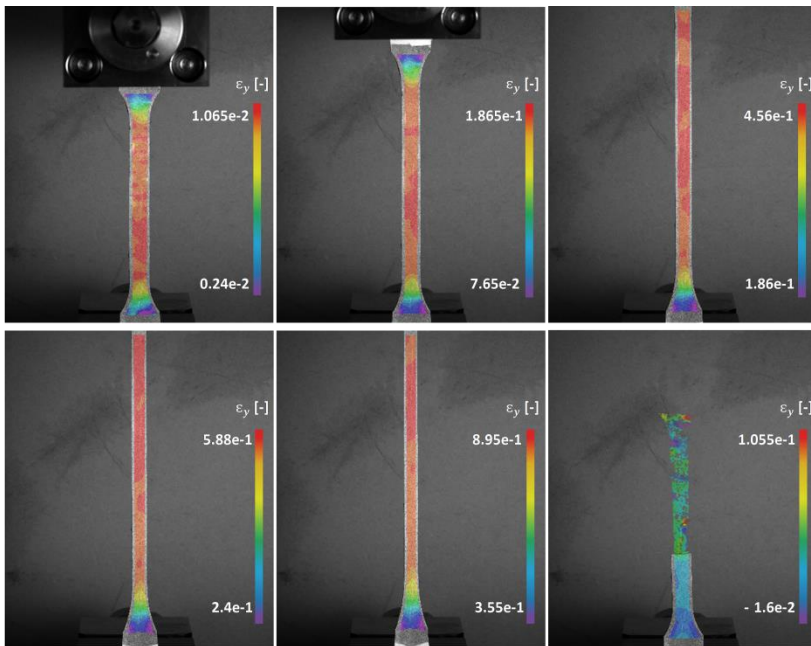
FIGURE 3.18: PHOTO SEQUENCE OF THE UNIAXIAL TENSILE TEST FOR SO.
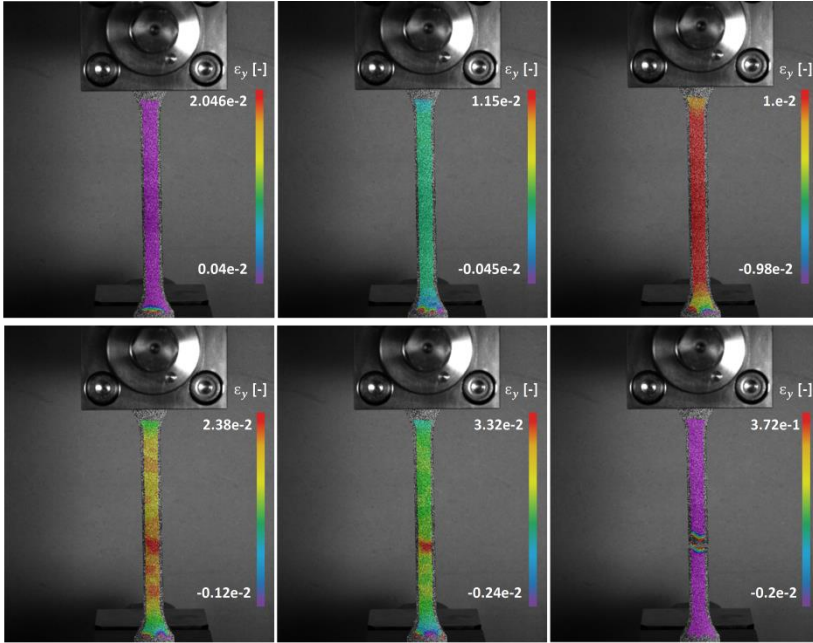
FIGURE 3.19: PHOTO SEQUENCE OF THE UNIAXIAL TENSILE TEST FOR 3M.

The individual curves together with their average diagram are plotted in Figure 3.20. The curves are all reasonably close to each other. The tensile curve for SO does not follow the expected S-curve for hyper-elastic materials. To exclude elastic-plastic behaviour, tensile tests were performed till an extension rate of 1.3 and unloaded. This cycle was five times performed and the maximal residual extension rate was smaller than 1.0005. The latter demonstrates that no yielding occured and that the assumption of hyper-elastic behaviour for SO is valid. The almost linear curve for 3M and the brittle failure due to the initiation and propagation of a crack, demonstrates the linear elastic behaviour.
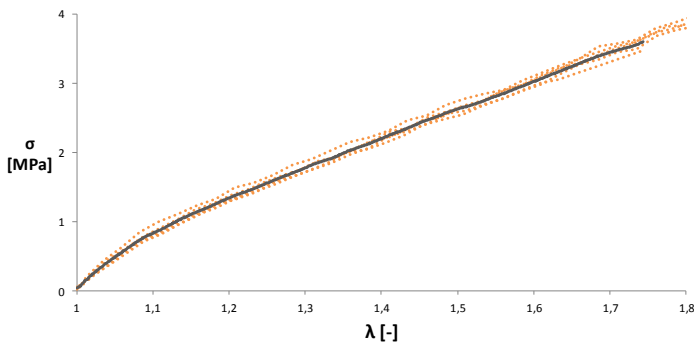
a)
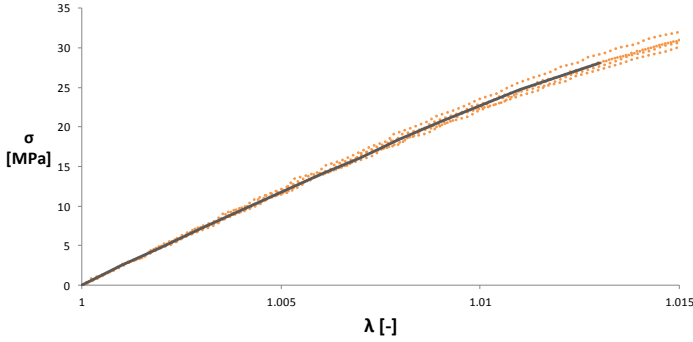
b)

FIGURE 3.20: AVERAGE STRESS-EXTENSION RATIO DIAGRAM FOR THE TENSILE TEST FOR A) SO AND B) 3M.

From the tensile test data the Young's modulus E was also derived. Since SSO is considered non-linear, the Young's modulus will only give an indication of the adhesive stiffness for this adhesive. The modulus of elasticity E was determined with Eq. (3.17) according to the standard ISO 527 (1996), with $\Delta\varepsilon$ equal to 0.2. As mentioned above transversal contraction will occur due to Poisson's effect. The Poisson ratio ν was determined by Eq. (3.18) with ε_x and ε_z the strains along the transversal axes and ε_y the strain along the longitudinal axis (see Figure 3.17). These values were measured by DIC.

$$E = \frac{\Delta\sigma}{\Delta\varepsilon} \tag{3.17}$$

$$\nu = -\frac{\varepsilon_x}{\varepsilon_y} \ or \ -\frac{\varepsilon_z}{\varepsilon_y} \tag{3.18}$$

The values for these material properties are summarized in Table 3.3. There was no difference in Poisson ratio measured with the strain along the width of the specimen or measured along the thickness, which proves the isotropic behaviour of the adhesives. The Poisson ratio of 0.494 for SO implies that the MS-polymer is almost a perfectly incompressible material and that the assumption of hyperelastic material for the MS-polymer was correct.

TABLE 3.3: MATERIAL PROPERTIES

Adhesive	Young's modulus [MPa]	Poisson ratio [-]
SO	9.019 ($\pm$921E-03)	0.494 ($\pm$1.917E-03)
3M	2267.37 ($\pm$57.56)	0.392 ($\pm$4.340E-03)

3.4.2. Compression tests

As mentioned above, the compression properties were determined by five uniaxial compression tests on the bulk material in the shape of cylinders with a diameter of 30 mm and a height of 15 mm. The test specimens were loaded under a constant speed according to its longitudinal axis to 10 kN, the maximal load of the test machine. To minimize friction between the compression plates and the specimens, the compression plates were covered with a PTFE-spray. From the recorded load and deformation, the corresponding stress-strain diagram could be determined.

As for the tensile properties, the true strain and stress were derived by means of DIC. As the bulk material is isotropic, the transversal strains are equal. The instantaneous cross sectional area A could be derived as in Eq. (3.19) with r_0 and A_0 the initial radius and initial surface of the specimen, respectively. The local true strain on the surface of the sample is determined by DIC.

$$
\begin{aligned}
A &= \frac{[r_0 \cdot (1 + \varepsilon_x)]^2 \cdot \pi}{4} \\
&= \frac{[r_0 \cdot \exp(\varepsilon_{Tx})]^2 \cdot \pi}{4} \\
&= \frac{r_0{}^2 \cdot \exp^2(\varepsilon_{Tx}) \cdot \pi}{4} \\
&= A_0 \cdot \exp(2 \cdot \varepsilon_{Tx})
\end{aligned}
\tag{3.19}
$$

Figure 3.21 shows a picture sequence of the test for compression tests on the MS-polymer SO. For the determination of the instantaneous cross sectional area A, the strain along the transversal axis ε_{Tx} is needed, this strain is also depicted on the figures. Also here, the stress-extension ratio diagram for the five tested specimen are calculated with Eq. (3.14) and (3.15). From these diagrams an average stress-extension ratio diagram was calculated by means of an interpolation of the abscissa values using Matlab®. The individual curves together with their average diagram are plotted in Figure 3.22.
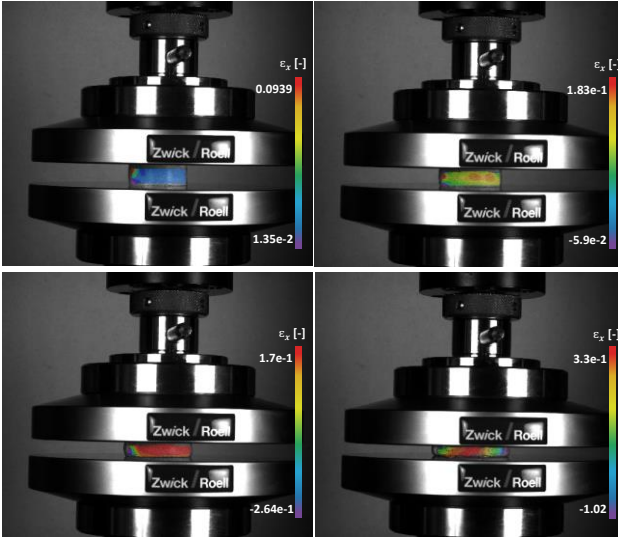
FIGURE 3.21: PHOTO SEQUENCE OF THE UNIAXIAL COMPRESSIVE TEST FOR SO.
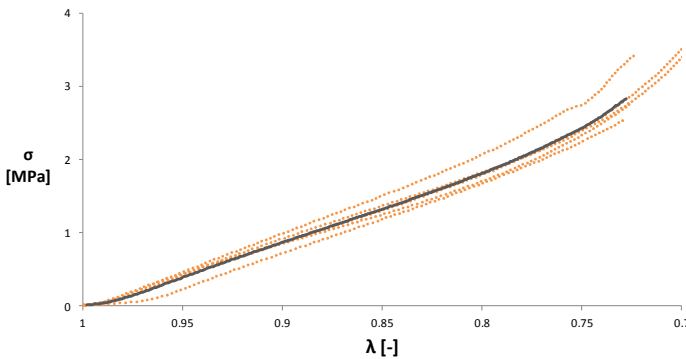
FIGURE 3.22: AVERAGE STRESS-EXTENSION RATIO DIAGRAM FOR THE COMPRESSION TEST FOR SO.

3.4.3. Shear tests

Thick Adherent Shear Test

In contrast to the tests on pure bulk material, such as the tensile and compression tests, it was not possible to directly measure the strains on the adhesive with TAST. This was due to the very small area of interest, as well as due to the rough surface of the adhesive layer. Therefore, instead of measuring the deformation of the adhesive, the displacements of the two adherents were measured. This method is also described in the corresponding standard DIN 14869-2 (2004). Due to the

large difference in stiffness between the adhesive SO and the aluminium adherents, the adherents did not deform, as depicted in Figure 3.23. This indicates that by measuring the relative displacement of the substrates, the shear properties could be properly calculated. The shear stress was evenly distributed along the adhesive layer and could be determined by Eq. (3.9). As mentioned before, this argument does not apply in the case of more stiff adhesives.
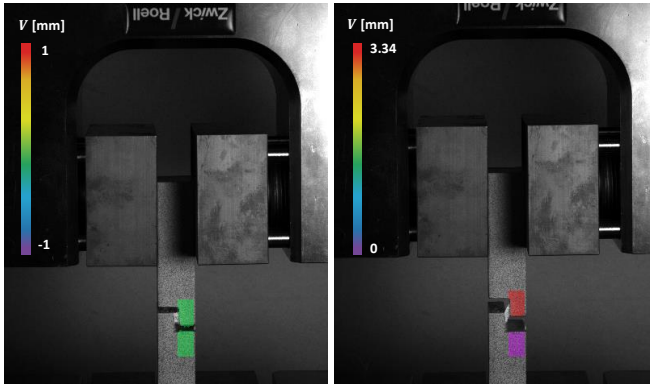
FIGURE 3.23: PHOTO SEQUENCE OF THE THICK ADHERENT SHEAR TEST FOR SO.

The occurring shear strain γ was determined by Eq. (3.20) with t the average value of the thickness and d_s the shear displacement of the adhesive. The obtained stress-extension ratio diagrams are depicted in Figure 3.24 together with the average diagram.

$$tan\ \gamma = \frac{d_s}{t} \cong \gamma \tag{3.20}$$
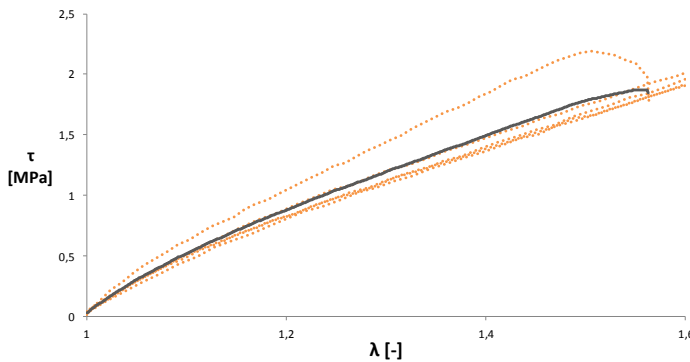
FIGURE 3.24: AVERAGE STRESS-EXTENSION RATIO DIAGRAM FOR TAST FOR SO.

Iosipescu Shear Test

As mentioned above, TAST will not give proper shear properties for stiff adhesives. For the determination of the shear characteristics of the stiff epoxy, the Iosipescu Shear Test, (V-Notched Beam Test) was used (ASTM D5379 2012). The test specimens were placed in a specially designed clamp mechanism. The mechanism consisted of two parts that were connected to each other by a ball bearing system. The bearing system ensured that no bending moments were generated and that pure shear was introduced in the specimen. The lower part of the mechanism was placed on a pressure plate, while the upper part was connected to the load cell, as depicted in Figure 3.25.

FIGURE 3.25: TEST SETUP OF THE IOSIPESCU SHEAR TEST

The test setup was designed so that the centre of the specimen was placed on the axis of the occurring deformation. The standard required the strains to be measured at the centre by means of two strain gauges at an angle of 45° to obtain the occurring shear strain in the specimen. These strains could be easily obtained through DIC. DIC also offers the possibility to give the deformation of the entire specimen, whereas strain gauges will only give the local deformations. With V-notched specimens, the stress distribution and strains between the notches were uniform at low forces, however at higher forces stress concentration occurred at the notch tips, causing failure of the specimens prior to the maximal shear stress of the stress-strain curve being reached. To solve this, U-notched specimens were also tested according to literature (Seneviratne et al. 2010; Harman et al. 2008). In Figure 3.26 a picture sequence of DIC on the tested specimen is depicted for V-notched specimens and U-notched specimens, respectively. As one can see, the stress concentrations at the notches are concentrated more at the V-notch.
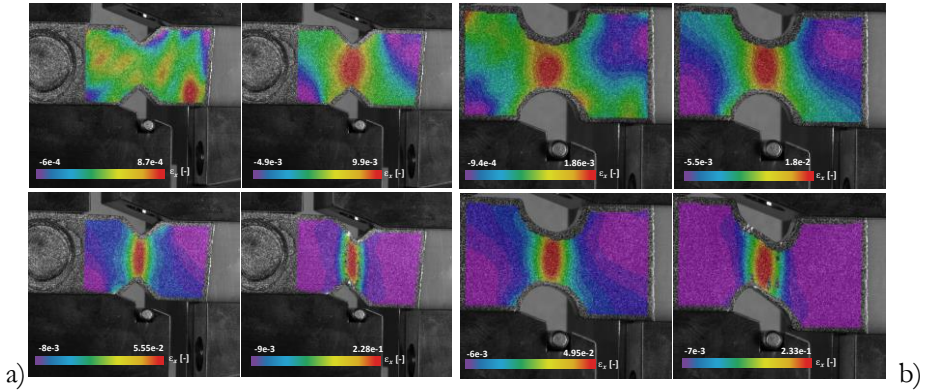
FIGURE 3.26: PHOTO SEQUENCE OF THE IOSIPESCU SHEAR TEST FOR 3M WITH A) V-NOTCHED AND B) U-NOTCHED SPECIMEN.

The shear strain was determined by taking the sum of the strain under two angles (+45° and -45°) between the two notches, as given in Eq. (3.21). These strains were determined by DIC.

$$\gamma = |\varepsilon_{+45}| + |\varepsilon_{-45}| \tag{3.21}$$

The obtained stress-strain curves of the V-notch and U-notch specimens are depicted in Figure 3.27. The toughness of the adhesive is very clear with yielding at a shear stress of 23.02 MPa and 22.24 MPa for the V- and U-notch specimens, respectively. After the yielding, strain softening and strain hardening occurs. Furthermore, the diagrams below show that the stress-strain behaviour is very similar for both types of specimens. The focus in this dissertation is on the linear elastic behaviour of the adhesive. The linear part before the yielding, confirms the assumption that the epoxy 3M will behave as a linear elastic material till an shear extension ratio of around 1.055.

a)

b)
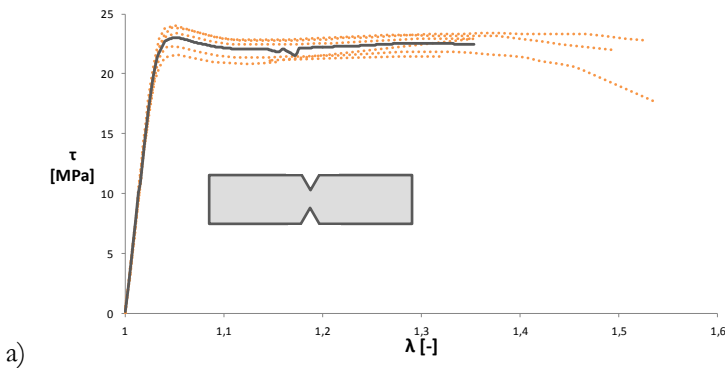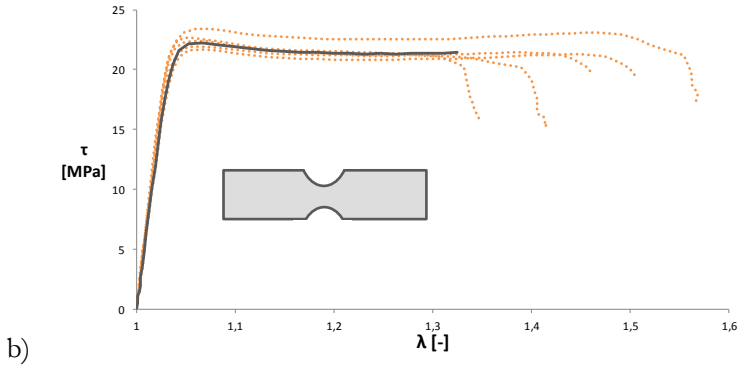
FIGURE 3.27: STRESS-STRAIN DIAGRAMS OF IOSIPESCU SHEAR TEST FOR 3M WITH A)V-NOTCHED AND B) U-NOTCHED SPECIMEN.

The determination of the shear modulus is calculated by considering only a small amount of the linear stress-strain curve with Eq. (3.22), where $\Delta\tau$ is the difference in shear stress over a $\Delta\gamma$ zone with a length of $(4000 \pm 200)\cdot10^{-6}$. This $\Delta\gamma$ zone starts with a value for γ between $1.5\cdot10^{-3}$ and $2.5\cdot10^{-3}$ (ASTM D5379 2012).

$$G = \frac{\Delta\tau}{\Delta\gamma} \tag{3.22}$$

For the Iosipescu shear tests on 3M the difference in geometry will only have a small influence on the result. The shear modulus is equal to 767 MPa and 724 MPa for the V-notched specimens and U-notched specimens, respectively. The difference is due to the lower stress concentrations in the U-notched specimens, resulting in a less inclined curve. Homogeneous isotropic elastic materials have their elastic properties uniquely determined by any two moduli. Consequently, the shear modulus can also be derived from the Young's modulus and Poisson's ratio, according to Eq. (3.23). With a Young's modulus of 2267.4 MPa and a Poisson's ratio of 0.39, derived from the tensile small-scale tests, the shear modulus is equal to 815.6 MPa. This is a difference of 6% and 11% with the shear modulus for the V-notched specimens and U-notched specimens, respectively. These values imply that 3M behaves almost linear and that the assumption of a linear elastic material model till a shear strain of around 5.5% is correct.

$$G = \frac{E}{2(1 + \nu)} \tag{3.23}$$

3.4.4. Additional validation experiments

As with TAST, it was not possible to directly analyse the strains on the adhesive for the additional validation experiments. Again this was due to the narrow area of interest and the rough surface of the adhesive layer. Therefore, instead of measuring the deformation of the adhesive, the relative displacement of the two connectors of the additional validation experiments was measured. As can be seen in Figure 3.28, due to the large difference in stiffness between the connectors and the adhesive, the connectors did not deform. This methodology was used for both the tensile and tensile/shear additional validation experiment.
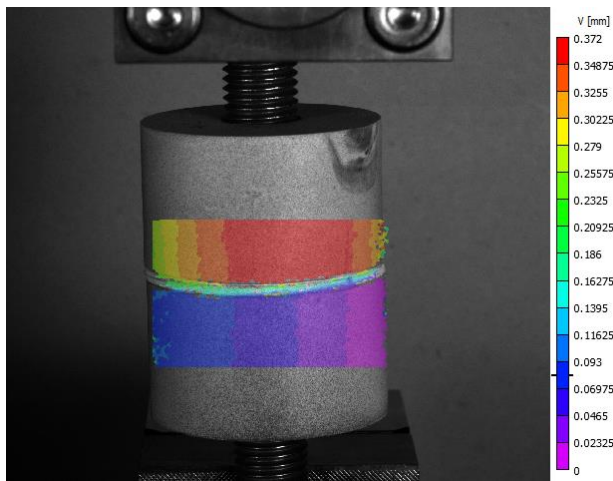
FIGURE 3.28: DISPLACEMENT OF THE CONNECTORS FOR THE TENSILE ADDITIONAL VALIDATION EXPERIMENT FOR SO.

With these tests for SO, cohesive failure occurred in the adhesive. This is visible in the force-deformation diagram in Figure 3.29. Three different zones can be distinguished, i.e. (a) no cohesive failure, (b) start of cohesive failure and (c) complete cohesive failure. In Figure 3.30, the three occurring deformations for these zones are depicted. For the validation of the material model, only zone (a) was taken into account.
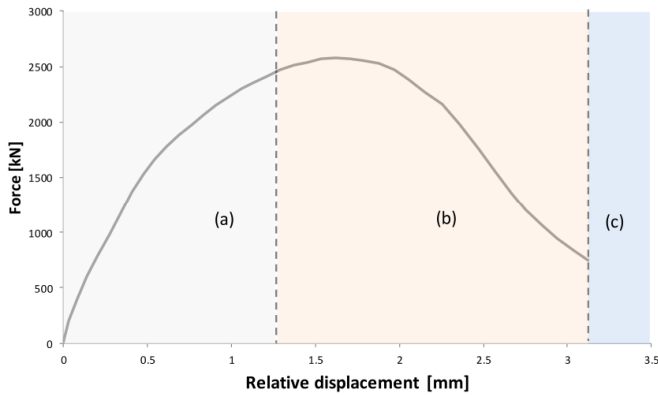
FIGURE 3.29: FORCE-DEFORMATION DIAGRAM FOR THE TENSILE/SHEAR ADDITIONAL VALIDATION EXPERIMENT FOR SO.
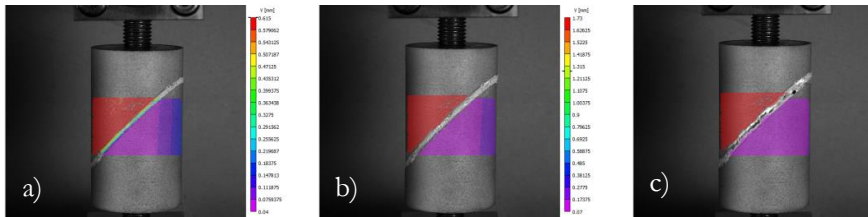
FIGURE 3.30: THE THREE OCCURRING ZONES WITH THE TENSILE/SHEAR ADDITIONAL VALIDATION EXPERIMENT FOR SO.

3.5.   Identification of the material model for SO

3.5.1. Determination of the material model coefficients

The obtained tensile, compressive and shear properties could now be used to determine the material model coefficients, i.e. the calibration, of the different hyperelastic material models for SO. 14 material models were calibrated and finally validated by the finite element model. In this way the material model with the best prediction was determined.

The calibration of the material model is the fitting of a predetermined equation (the material model) with the average experimental stress-strain curve. This fitting is done by optimizing the coefficients (material constants) in the equations. The equations were established by following the calculation procedure as for Eq. (3.8).

The optimizing of the coefficient was done by means of a non-linear least squares analysis (Ogden et al. 2004; Sasso et al. 2008; Dias et al. 2014). Steinmann, Hossain, and Possart (2012) used the Curve Fitting Toolbox of Matlab®, a graphical interface. The latter was also used here for the curve fitting with the Baker-Ericksen inequalities taken into account. The Baker-Ericksen (1954) inequalities impose conditions on the material, namely that for a compressible isotropic elastic material under deformation the largest stress must correspond with the largest occurring strain. Truesdell, Noll, and Pipkin (2004) stated that there is compliance with this condition, if the derivative of the strain energy function to the first strain invariant is greater than zero, and the derivative to the second strain invariant is not negative, as given in Eq. (3.24) and (3.25).

$$\frac{\partial W}{\partial I_1} > 0 \tag{3.24}$$

$$\frac{\partial W}{\partial I_2} \geq 0 \tag{3.25}$$

Figure 3.31 depicts the curve fitting of the 14 selected material models on the uniaxial tensile test curve. All 14 material models give accurate curve fittings. The curve fitting as in Figure 3.31 was also performed for uniaxial compression and shear. As mentioned above, the accuracy of the material model is increased by fitting it with more load conditions. So a fitting of the three load conditions was performed with their respective data sets. This fitting is based on the least squares analysis proposed by Stumpf and Marczak (2010). They used the following method, where the error function E should be kept as small as possible:

$$E = \sum_{i=1}^{n_T} \left(\sigma_{T_i} - \sigma_{E_i} \right)^2 + \sum_{j=1}^{n_S} \left(\sigma_{T_j} - \sigma_{E_j} \right)^2 + \sum_{k=1}^{n_C} \left(\sigma_{T_k} - \sigma_{E_k} \right)^2 \tag{3.26}$$

whereby n_T, n_S and n_C are the number of test data for testing tension, shear and compression respectively, and σ_T and σ_E are the theoretical and experimental values for the stresses. This method gives the advantage to model multiple deformation states with a single set of material parameters. Although theoretically the most optimal material model is reached by calibrating for all three load conditions, calibrations for only two load conditions were also investigated, yielding in 98 different material models.
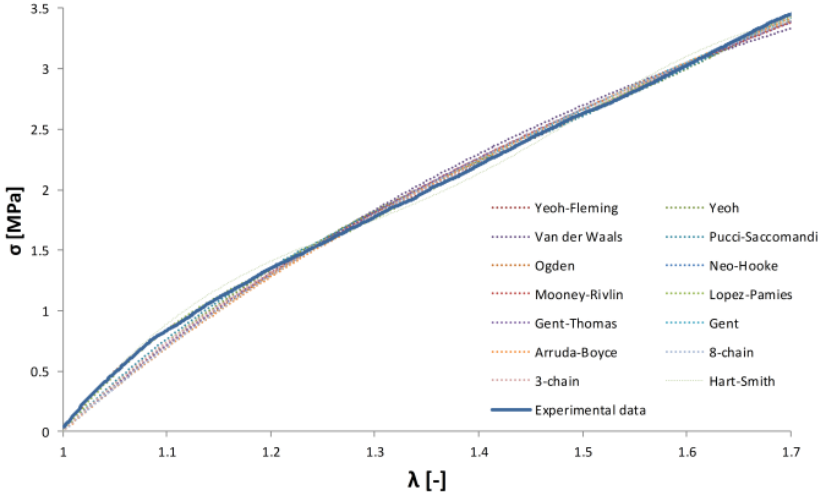
FIGURE 3.31: CURVE FITTING OF THE MATERIAL MODELS FOR THE TENSILE TEST

The fitting was also assessed by the value of a fit parameter, i.e. the coefficient of determination R^2, given by Eq. (3.27). The model provides a perfect fitting with a R^2 value equal to 1.

$$R^2 = 1 - \frac{\sum_i (y_i - \hat{y}_i)^2}{\sum_i (y_i - \bar{y})^2} \qquad (3.27)$$

In the above equation y_i, $\hat{y}_i$ and $\bar{y}$ are equal to the test data, the modelled data and the average value, respectively. In Table 3.4 the material constants of the 14 calibrated material models are summarized together with their coefficient of determination for each of the considered load conditions separately and their combinations.

TABLE 3.4: MATERIAL CONSTANTS AND COEFFICIENT OF DETERMINATION OF THE MATERIAL MODELS FOR TENSION (T), COMPRESSION (C) AND SHEAR (S) SEPARATELY AND THEIR COMBINATIONS.

		Tension (T)	Compression (C)	Shear (S)	T-C	T-S	C-S	T-C-S
Mooney-Rivlin	C10	0.144	-6.431	0.362	0.855	2.156	2.000	2.207
	C01	0.178	7.487	0.362	0.658	-1.395	-1.184	-1.404
	R²	0.995	0.974	0.997	0.977	0.955	0.983	0.889
Neo-Hooke	μ	2.524	2.111	1.448	2.601	2.092	1.773	2.180
	R²	0.995	0.973	0.997	0.967	0.671	0.455	0.660
Gent-Thomas	C1	1.192	25.35	0.837	1.015	1.960	1.724	1.932
	C2	0.370	-73.41	-0.396	1.435	-3.996	-3.000	-3.650
	R²	0.995	0.9923	0.998	0.977	0.903	0.692	0.817

		Tension (T)	Compression (C)	Shear (S)	T-C	T-S	C-S	T-C-S
Hart-Smith	C10	-0.871	11.410	0.719	1.016	2.656	4.432	2.929
	C1	-2.564	-43.83	0.000	0.000	-0.175	-0.265	-0.235
	C01	8.300	-32	0.579	1.436	-6.141	-11.7	-6.792
	R²	0.996	0.999	0.998	0.977	0.952	0.950	0.909
Ogden (N=1)	μ_1	2.755	0.253	1.228	4.595	0.781	1.481	1.083
	α_1	1.873	14.04	2.301	1.263	3.889	2.329	3.301
	R²	0.995	0.991	0.998	0.976	0.795	0.457	0.718
Yeoh	C1	1.355	0.727	0.715	1.488	1.077	1.239	1.3073
	C2	-0.173	13.76	-0.007	-0.301	-0.298	-0.555	-0.560
	C3	0.084	-159.	0.017	0.123	0.238	0.180	0.333
	R²	0.997	0.998	0.998	0.979	0.727	0.574	0.700
Gent	μ	2.524	2.111	1.414	2.601	1.742	1.773	2.080
	J_m	99640	-6100	21.43	34389	3.883	404510	12.749
	R²	0.995	0.974	0.998	0.965	0.710	0.455	0.663
Yeoh-Fleming	A	1.156	0.545	0.687	0.884	0.435	0.958	0.788
	B	-0.074	140	-0.084	0.938	3.024	1.014	1.868
	C	0.718	1.118	0.349	0.605	0.680	0.255	0.517
	I_m	2.970	-866.6	2.994	5.983	5.382	-91.89	4.963
	R²	0.999	0.992	0.999	0.979	0.7271	0.576	0.699
Pucci-Saccomandi	μ	7.558	8.085	1.375	1.109	1.9	1.897	6.7
	J_m	-2.435	-10	10	3.886	3.719	4.000	-2.601
	C2	-9	-9	0	3.185	-0.569	-0.712	-7.265
	R²	0.9985	0.992	0.999	0.978	0.902	0.692	0.959
Lopez-Pamies	μ_1	2.431	-1.403	-3.157	2.814	1.564	17.721	2.593
	μ_2	0.962	2.763	5.034	0.166	1.060	-15.22	0.226
	α_1	1.141	-621.1	0.142	-0.631	2.500	3.729	-1.589
	α_2	-42.46	7.791	0.459	6.263	-8.723	4.162	6.843
	R²	0.999	2.763	0.998	0.979	0.9227	0.803	0.897
Van der Waals	μ	2.504	1.462	1.495	2.995	2.548	2.036	2.857
	α	7.858	-4.342	0.7075	0.878	2.363	1.836	2.586
	β	1.159	3.021	5.77	-0.091	-0.019	1.815	-0.192
	λ	17.52	31.97	3.415	2.895	-2.430	-2.558	2.39
	R²	0.992	0.995	0.998	0.979	0.985	0.986	0.965
Arruda-Boyce	μ	2.524	1.502	1.222	2.601	1.893	1.503	1.987
	N	19090	-98970	19970	409950	19970	20030	19970
	R²	0.995	0.970	0.998	0.967	0.4213	0.243	0.449
3-chain	μ	4.603	0.543	1.303	5.768	6.277	5.320	1.473
	N	0.396	0.68	17.050	0.332	-0.002	0.001	6.242
	R²	0.998	0.991	0.998	0.974	0.671	0.455	0.701
8-chain	μ	7.107	-3.671	4.982	4.607	1.088	3.082	1.699
	N	-0.041	0.580	0.069	-0.638	2.098	-0.657	4.016
	R²	0.995	0.967	0.998	0.974	0.711	0.479	0.664

3.5.2. Validation of the material models

For the validation of SO, the 98 calibrated material models above were implemented in two numerical models, i.e. the numerical tensile and tensile/shear additional validation experiment resulting in 196 numerical models. The final mesh distribution of the two models for SO are depicted in Figure 3.32. A convergence study demonstrated that the best results were obtained with the element type C3D8H and with five elements along the thickness of the adhesive layer. To avoid mesh singularities in the centre of the circular connector a square mesh pattern was inserted inside the circular pattern. The tie-constraint between the metal point-fixings and the adhesive was modelled as a master-slave surface, with the adhesive each time as the slave surface. The material models were implemented as subroutines with dependent state variables in Abaqus®. The stainless point-fixings were modelled as linear elastic material with a young's modulus of 195000 MPa and a Poisson's ratio of 0.3 (Outeiro et al. 2006). The load-displacement output of the numerical models was then compared to the experimental load-displacement curves.
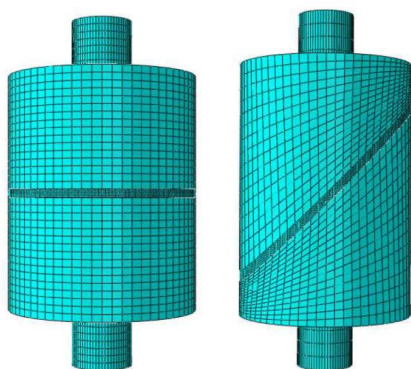

FIGURE 3.32: MESH CONFIGURATION OF THE NUMERICAL TENSILE AND TENSILE/SHEAR ADDITIONAL VALIDATION EXPERIMENT FOR SO.

Figure 3.33 shows the most optimal material models for the additional tensile validation experiment for SO. Two models provided a good prediction for both the initial stiffness and the occurring deformations, i.e. Ogden and Pucci-Saccomandi. The model of Gent-Thomas gave an even better approach to the initial stiffness but failed in the prediction of the deformations. The same comparison of the optimal material models for the tensile/shear additional validation experiment was performed in Figure 3.34
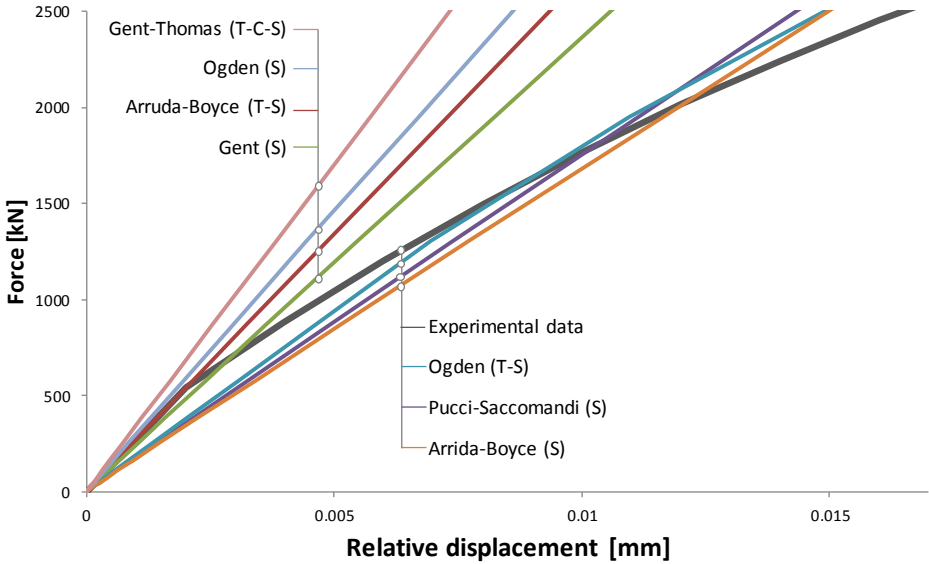
FIGURE 3.33: COMPARISON OF THE OPTIMAL MATERIAL MODELS FOR THE TENSILE ADDITIONAL VALIDATION EXPERIMENT, CALIBRATED WITH TENSILE (T), COMPRESSIVE (C) AND/OR SHEAR (S) EXPERIMENTAL DATA.
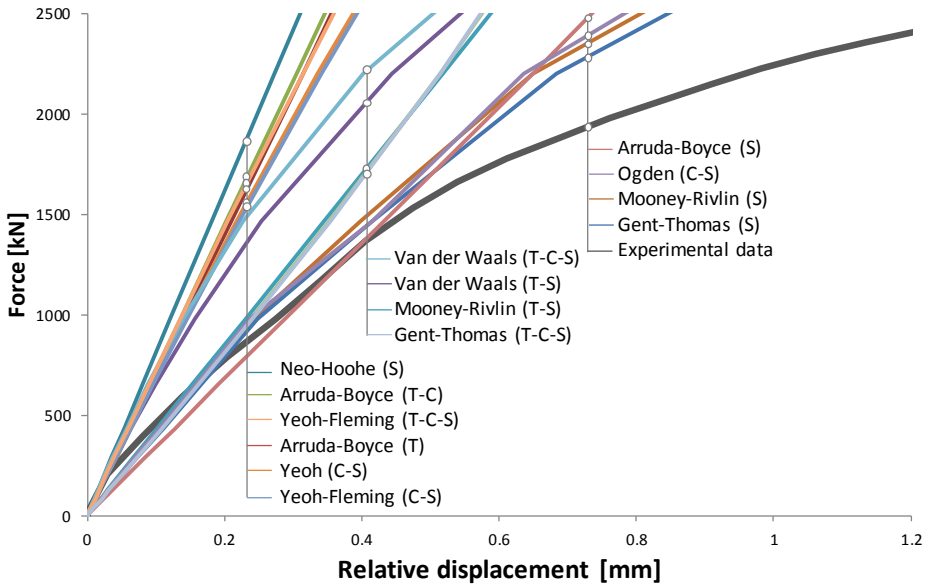

FIGURE 3.34: COMPARISON OF THE OPTIMAL MATERIAL MODELS FOR THE TENSILE/SHEAR ADDITIONAL VALIDATION EXPERIMENT, CALIBRATED WITH TENSILE (T), COMPRESSIVE (C) AND/OR SHEAR (S) EXPERIMENTAL DATA.

The proposed material models for the two load configurations are summarized in Table 3.5, based on how well the material model predicts on the one hand the initial stiffness of the connection and on the other hand the deformation of the connection. This comparison of the optimal material models shows that calibration with test data from shear provides the best results. In contrast to what is argued in literature, it is not always advantageous to use and combine test data from as many experimental set-ups as possible.

TABLE 3.5: PROPOSED OPTIMAL MATERIAL MODELS FOR THE TWO LOAD CONFIGURATIONS FOR SO.

Connection	Criteria	Optimal material models	
Tensile point-fixing	Initial stiffness	Arruda-Boyce:	Tension-Shear
		Ogden:	Shear
		Gent-Thomas:	Tension-Compression-Shear
	Deformation	Pucci-Saccomandi:	Shear
		Ogden:	Tension-Shear
		Arruda-Boyce:	Shear
Tensile/shear point-fixing	Initial Stiffness	Arruda-Boyce:	Tension-Compression
		Yeoh-Fleming:	Tension-Compression-Shear
		Van der Waals:	Tension-Shear
	Deformation	Ogden:	Compression-Shear
		Mooney-Rivlin:	Shear
		Gent-Thomas:	Shear

3.6.   Summary and conclusions

In this chapter different material laws were compared for a rubber-like adhesive, the MS-polymer Soudaseal 270 HS (SO), and a tough adhesive, the two-component epoxy 3M™ Scotch-Weld™ 9323 (3M). The flexible adhesive SO is modelled as a hyper-elastic material. This is done by means of phenomenological and micromechanical material models, of which the calibration is carried out by means of test data from tensile, compressive and shear tests on the adhesive as a bulk material. These test data were used to calibrate the models, using a non-linear least squares method.

The epoxy 3M can be modelled with linear elastic behaviour till an shear extension ratio of around 1.055. Linear elastic behaviour is characterized by the Young's modulus and the Poisson's ratio.

Dumbbells, solid cylinders and thick adherend shear test specimens were made. Local deformations of the test specimens have been measured through three-dimensional digital image correlation (DIC). The comparison between the data from the test machine and the DIC-output revealed major differences between the measured deformations. This confirms that the use of DIC is needed to accurately measure the occurring strains during the small-scale tests.

For SO, the Poisson's ratio was determined to be 0.49. Consequently, the material is near to incompressible. Fourteen material models for the MS-polymer SO as a hyper-elastic material were calibrated by means of the acquired test data. The calibration is accomplished for seven combinations of the test data, i.e. tension, compression, shear, tension-compression, tension-shear, compression-shear and tension-compression-shear, resulting in 98 calibrated material models. To validate these material models, an additional validation test was performed consisting of two adhesively connected steel point-fixings. This additional validation experiment was performed with a horizontal contact surface and with an angled contact surface of 45°. The same configurations were implemented in the finite element software Abaqus®, where the adhesive material was modelled with the 98 calibrated material models. For the validation, the load-displacement output of the numerical models were compared to the experimental load-displacement.

For 3M, the Young's modulus is equal to 2267.4 MPa, the Poisson's ratio to 0.39 and the shear modulus to 767.0 MPa and 723.9 MPa for the V-notched specimens and U-notched specimens, respectively.

After comparison of the numerical displacements with the experimental, it appeared that the material models, calibrated by shear tests or by a combination of shear tests yielded the best results for SO. In contrast to what is argued in literature, it is not always advantageous to use and combine test data from as many experimental set-ups as possible. No optimal model was achieved, however the material model developed by Ogden (1973) calibrated by results from only shear tests or in a combination with tension or compression predicted the experimental results the best based on the initial stiffness and deformation.

Chapter 4: Local model

> It's a magical world, Hobbes, Ol' buddy …
> … let's go exploring!
> *Bill Watterson – The complete Calvin and Hobbes*

4.1.   Introduction

Almost all developed design methods for bolted point-fixings make use of FEA. It is obvious that most of these methods described require significant computation time and consequently have a great cost, especially for complex geometries. Therefore Beyer developed the time-efficient SLG-method for the design of bolted point-fixings (Beyer 2007; Beyer 2008). Due to the separation into one global component that can be built up with a less dense mesh pattern and one local component that is built up with a more complex and dense mesh pattern, the stress distribution can be determined in a very time-efficient manner.

This method appears to offer a very appealing basis for the design of glass plates with adhesive point-fixings. The validation of the SLG-method will consist of a FEA comparison between the stress distribution obtained from the superposition of local models and global model and the stress distribution in a total model, as depicted in Figure 4.1. In this chapter, the aim is to develop the validated numerical local models, indicated with in Figure 4.1. The local component is validated for different geometrical properties, such as the glass thickness and diameter connector, different material properties, such as the adhesive type, and three different load conditions, such as tension, shear and multi-axial load. The diameter of the local component ϕ_{loc} for bolted point-fixings is determined to be at least six times the diameter of the borehole ϕ_{hole}, as expressed in Eq. (2.2). This distance was also verified and used for the study of adhesive point-fixings.
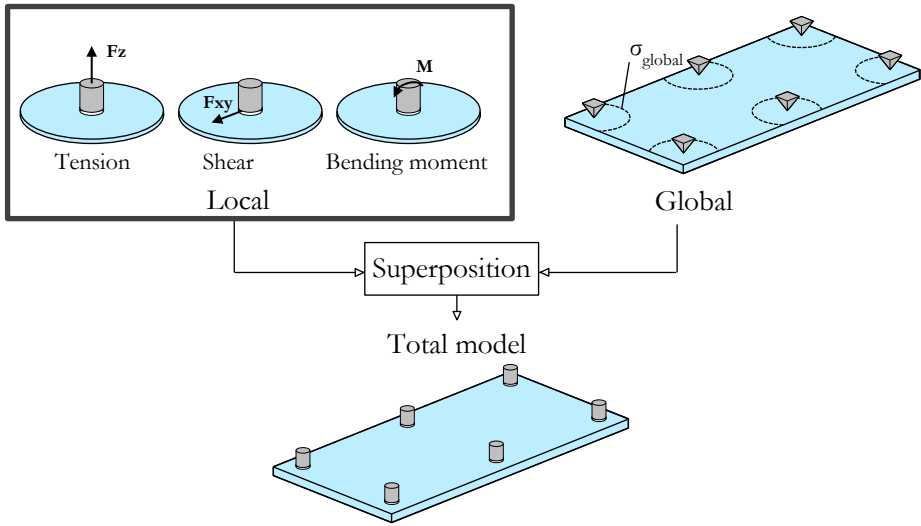
FIGURE 4.1: SLG-METHOD FOR ADHESIVE POINT-FIXINGS.

By supporting the glass panel along a circumference with a diameter equal to six times the connector diameter, the deformation of the glass panel was also taken into account. The investigation of the entire connection is innovative considering that previous studies that have been performed on adhesive point-fixings focus mainly on the adhesive bond between the glass and metal connector by supporting the glass panel right next to the connector (§Chapter 2). The experiments in these previous works neglect the deformation of the glass panel, which does not correspond to reality. Indeed, the deformation of the glass can cause stress concentrations in the adhesive layer. The chapter is subdivided according to the three load conditions, starting with the tensile load condition.

4.2.   Tension

As depicted in Figure 1.1, point-fixings can be used for supporting glass facades or glass canopies. In the case of glass canopies, the supports will mostly be placed underneath the glass panel so the connection is generally loaded under pressure by the dead load of the glass panel and possibly under tension by wind suction. However, when the support is placed on top of the glass panel, the connection will almost continuously be loaded in tension by the dead load of the glass panel. Mechanical self-weight supports are mostly described for structural sealant glazing

systems (SSGS) according to the ETAG 002 (2002) as depicted in Type I, II and III in Figure 4.2. Hence, additional mechanical self-weight supports will be used for adhesive point-fixings loaded in constant shear. With these mechanical self-weight supports the adhesive connection will only be loaded by horizontal actions, with tensile forces the determining factor for the design. The tensile experiments will be used to validate the tensile factor σ_{Fz} in Eq. (2.3).
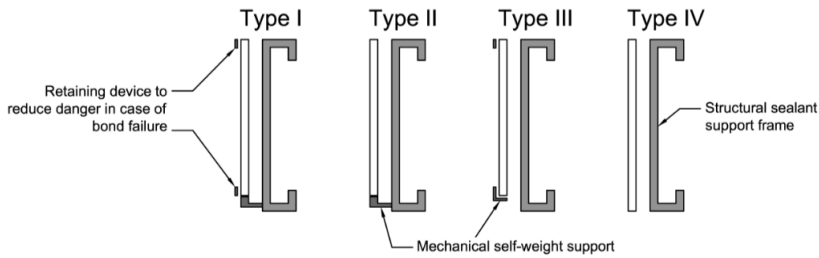

FIGURE 4.2: SCHEMATIC EXAMPLES OF THE DIFFERENT TYPES OF SSGS, BASED ON ETAG 002 (2002).

4.2.1. Test specimens and materials

Chapter 2 demonstrated that many parameters have an influence on the stress distributions and strength of adhesive point-fixings, such as the diameter of the connection, the thickness of the glass, the tempering process, the shape of the connector, the type of adhesive, environmental parameters, etc. To obtain a complete validated numerical model, experiments were conducted with different geometrical parameters and material characterisations. Three different diameters were combined with three different glass thicknesses according to Table 4.1, for the two selected adhesives, i.e. the MS-polymer Soudaseal 270 HS (SO) and the 2c-epoxy 3M™ Scotch-Weld™ 9323 B/A (3M). The combination of 10 mm glass thickness and 50 mm connector diameter was taken as the reference case.

TABLE 4.1: TEST COMBINATIONS.

Glass thickness [mm]

4	**10**	19		
X		X	30	
	X		**50**	Connector diameter [mm]
X		X	70	

In the experiments, simple supports were used, consisting of a steel plate with a circular opening that had a diameter equal to six times the diameter of the fitting. The width and length of the glass plate were seven times the fitting diameter. For the validation, the strain on top of the glass panel at three different distances from the centre on the glass plate were measured using strain gauges. The positions of the strain gauges were determined by means of a preliminary FEA model. The dimensions of the glass plate, the circumference of the support and the positions and directions of the strain gauges are illustrated in Figure 4.3. The strain gauges of type FAE-12S-35-S6E-J with an accuracy of 1% were used for all the strain measurements in this dissertation. Due to economic reasons, the strains of only four out of ten test specimens for each configuration were completely determined, where the six remaining specimens were used to measure the variation between the specimens and measured only the strain ε_2. At the same three distances from the centre, denoted as U_1, U_2 and U_3, the deflection of the glass was measured by using three linear variable differential transformers (LVDT). The used LVDTs in this dissertation have an stroke range of 20 mm and an accuracy of 0.1% of the stroke range. However, due to practical constraints, for the configuration with a connector diameter of 30 mm U_1 is measured at a distance of 30 mm from the centre and for the configuration with a connector diameter of 70 mm U_3 at a distance of 172.5 mm. A certain scatter of the experimental results is expected due to small imperfections that could have occurred during the production process of the connector and the glass and also during the fabrication process of the connection.
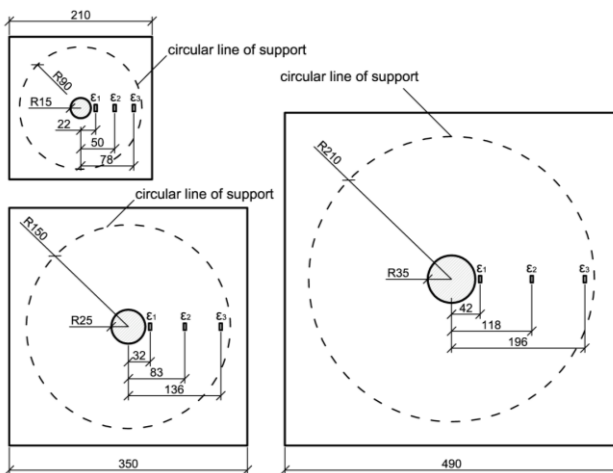

FIGURE 4.3: DIMENSIONS IN MM. OF THE GLASS PLATES WITH POSITION OF THE STRAIN GAUGES FOR A CONNECTOR DIAMETER OF 30 MM, 50 MM AND 70 MM.

The optimum adhesive thickness of the MS-polymer SO is 2 mm and for the 2c-epoxy 3M 0.2 mm according to the technical data sheets of the producers. The thicknesses were carefully ensured by the use of high precision milled steel brackets. These brackets ensured that the connector was always 2 mm or 0.2 mm above the glass panel. They are illustrated in Figure 4.4 with a connector diameter of 50 mm. After applying the adhesive on the connector, the connector and the bracket were placed on the air side of the glass panel and excess adhesive material was removed. Of every configuration, ten specimens were fabricated and tested; with 10 configurations this resulted in a total of 100 experimental specimens. Before testing, the specimens were stored for four weeks in a climatic chamber at a constant temperature of 21°C and a relative humidity (RH) of 45% without any UV-radiation to ensure the full curing of the adhesives.

FIGURE 4.4: EXAMPLE OF THE BRACKET WITH A CONNECTOR OF Ø 50 MM FOR THE MS-POLYMER SO (LEFT) AND THE 2C-EPOXY 3M (RIGHT).

The material properties of the two selected adhesives were determined in Chapter 3. For SO, the stretch based phenomenological material model developed by Ogden (1973) gave the best results. The mathematical expression of the Ogden material model is given by Eq. (4.1). The obtained material constants μ_1 and α_1 were equal to 0.781 and 3.889, respectively. For 3M, the linear elastic material characteristics were determined and were equal to 2267 MPa and 0.39 for the Young's modulus and the Poisson's ratio, respectively.

$$W = \sum_{i=1}^{N} \frac{2\mu_i}{\alpha_i} \left(\lambda_1^{\alpha_i} + \lambda_2^{\alpha_i} + \lambda_3^{\alpha_i} - 3 \right) \qquad (4.1)$$

The metal cylinder was made of stainless steel EN 10088-1 1.4404 (AISI 316L), a commonly used type of stainless steel, and the glass was annealed soda-lime float glass. In the numerical research, the adherents were modelled using linear elastic behaviour, using the material properties given in Table 4.2. The material properties of glass and stainless steel were derived from literature (Outeiro et al. 2006; Haldimann et al. 2008)

TABLE 4.2: MATERIAL PROPERTIES OF THE ADHERENTS.

	Young's modulus E [MPa]	Poisson's ratio v [-]
Stainless steel EN10088-1 1.4404	195000	0.30
Annealed float glass	70000	0.23

4.2.2. Test method

As stated above, the local component is defined as the glass plate with a diameter six times the diameter of the connector. In the experiments, the circumference was simply supported and the fitting was loaded with a tensile force until failure. To test the specimens under uniaxial tension, a special test frame was fabricated. A visualization of the test frame for the reference configuration is depicted in Figure 4.5. An aluminium plate between the glass panel and the steel test frame protected the glass panel. The tensile tests were performed on a universal electro-mechanic test machine Instron 5800R (frame 4505 retrofitted with a digital controller 8800). A load cell of 10 kN or 100 kN was used and the value of the load was measured.

4.2.3. Numerical model

The finite element software Abaqus® was used to build a three-dimensional finite element model to numerically analyse the connection. Due to symmetry only a quarter of the glass plate was modelled. Since stress concentrations were expected around the connector, local refinement of the mesh pattern was introduced. To avoid mesh singularities in the centre of the circular connector, a square mesh pattern was applied inside the circular pattern. The mesh refinement around the connector and the square pattern are illustrated in Figure 4.6. In this figure the path along the x-axis is also depicted where the nominal strains perpendicular to this path were determined.
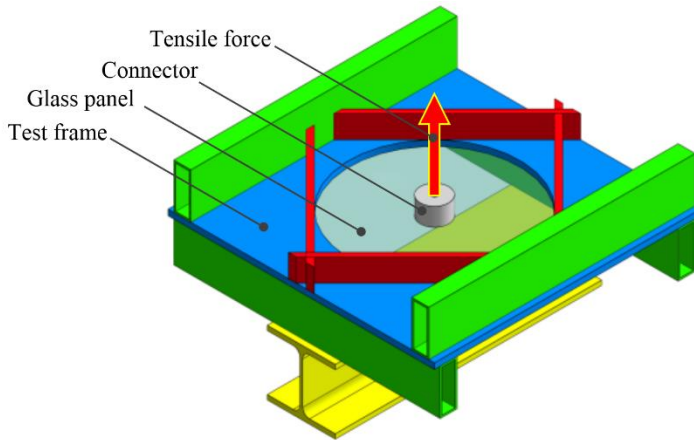
FIGURE 4.5: TEST FRAME FOR UNIAXIAL TENSILE TESTS FOR THE REFERENCE CONFIGURATION, I.E. CONNECTOR DIAMETER OF 50 MM AND A GLASS THICKNESS OF 10 MM.
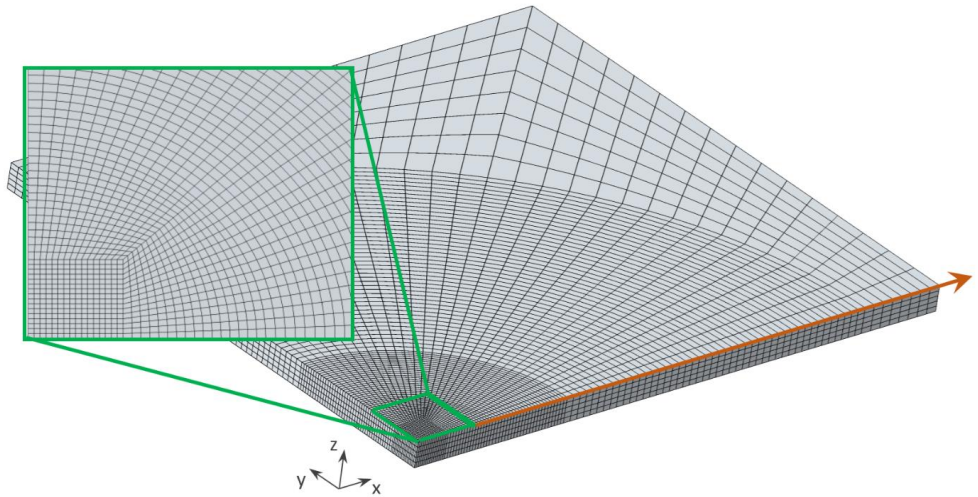

FIGURE 4.6: DETAIL OF THE REFINED MESH PATTERN AT THE CENTRE FOR THE REFERENCE CONFIGURATION.

As strain gauges measure the deformation as the ratio of change in length-to-length, nominal strain in Abaqus® was used for the validation. The nominal strain in Abaqus® is defined as the ratio of change in length to length in the reference configuration, which is the same as the measured strain. Along the circular line of support, the upward displacement is prevented as the boundary condition for U_z is set to zero.

The adhesive layer was connected to the glass and the metal connector by means of a tie-constraint. The tie-constraint between glass-adhesive and metal-adhesive was modelled as a master-slave surface, with the adhesive layer each time as the slave surface. Surface-to-surface was selected as discretization method and for the position tolerance method Abaqus® determined the nodes to be tied using the default position tolerance. This kind of constraint specifies that the mesh size of the slave surface has to be smaller than the mesh size of the master surface. A convergence study demonstrated that when the mesh of the adhesive layer was four times finer than the glass and steel mesh the best results were obtained. This refinement also allowed to investigate thoroughly the stresses that occurred in the adhesive layer.

For the continuum element types, a distinction can be made between linear and quadratic interpolation, with either full or reduced integration. Different element geometries are available: tetrahedral, wedge and hexahedral. As the parts used in the model have regular shapes (cylinder, prism), the best volume element which can be used is a hexahedron (hex) element. These have a better convergence speed than the other volume elements available in Abaqus®. Some specific problems which are inherent to the chosen element type can be present.

A first problem is **shear-locking**. This problem only affects the performance of fully integrated, linear (C3D8) elements subjected to bending loads. These elements function well under direct or shear loads. However, when bending is present, the nodes and accompanying interpolation functions are unable to approximate the deformations. The behaviour of a linear element subjected to a bending moment is illustrated in Figure 4.7. In reality, the top and bottom side are curved while the vertical edges are subjected to a rotation. This allows to maintain the orthogonality between horizontal and vertical edges and no shear stresses are introduced. However, when using a linear element, the vertical and horizontal edges are not perpendicular after deformation which means that spurious shear stresses are introduced at the integration points. This results in smaller deformations which implies a stiffer behaviour of the material. The quadratic elements are not subjected to this problem since the edges are able to adjust to a certain curvature.
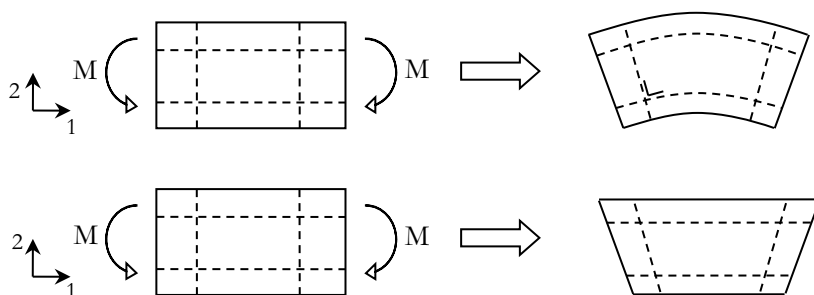
Another solution to solve shear-locking is the use of linear elements with reduced integration (C3D8R). When using elements of a reduced type, the stiffness matrix is not calculated exactly and completely (since terms of higher order are omitted). However, these elements tend to be too flexible because they experience their own numerical problem called **hourglassing**. Since the only integration point of an element is located in its centre, no deformations will be registered at the position of the integration point when subjected to a bending moment. The problem can affect the entire model which leads to incorrect results. Especially in coarse meshes, this zero-energy mode can propagate through the mesh, producing incorrect results. The hourglassing effect is illustrated in Figure 4.8 for a C3D8R element subjected to bending. The length of and the angle between the dotted visualisation lines in Figure 4.8 remains unchanged, which means that all components of stress at the element's single integration point are zero. This bending mode of deformation is thus a zero-energy mode because no strain energy is generated by this element distortion. The element is unable to resist this type of deformation since it has no stiffness in this mode.
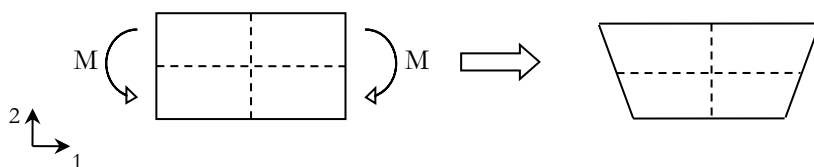
A third possible problem is **volumetric locking**. This occurs in fully integrated elements when the material behaviour is (almost) incompressible ($\nu > 0.475$). It

results in overly stiff behaviour of the material for deformations that should not experience any volume changes. The kinematic constraints inherent to an incompressible material behaviour constrain the volume of the element's integration points to be constant. This can make the element over-constrained which induces the overly stiff behaviour. Consider an element under hydrostatic pressure (Figure 4.9), the element's volume cannot change under this load when the material is incompressible. Hence, it is impossible to compute the pressure stress based on the displacements of the nodes which means that a pure displacement formulation is inadequate. This problem can be solved by using hybrid elements. Hybrid elements (H) are equipped with an extra degree of freedom which calculates the stresses in the element directly. The nodal elements are then only used to calculate shear strains and shear stresses. A summary of characteristic behaviour of hexagonal elements is given in Table 4.3.
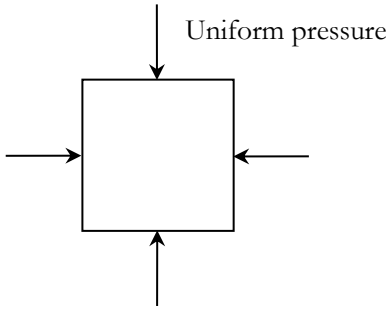

Uniform pressure

FIGURE 4.9: ELEMENT UNDER HYDROSTATIC PRESSURE (ABAQUS 2014).

TABLE 4.3: BEHAVIOUR OF THE AVAILABLE HEXAGONAL ELEMENTS WITH RESPECT TO SPECIFIC PROBLEMS (++ = EXCELLENT, - - = POOR).

Element	Type	Shear Locking	Hourglassing	Volumetric Locking	CPU computation time
C3D8	Linear	- -	++	- -	+
C3D8H	Linear, hybrid	- -	++	++	+
C3D8R	linear, reduced	++	- -	++	++
C3D20	Quadratic	-	++	-	- -
C3D20R	quadratic, reduced	++	++	++	-

The used element types and sizes are summarized in Table 4.4 for the two selected adhesives. The element size is the size of one element in the centre of the

connection. Here, 20-nodes quadratic brick elements were used. The number of elements along the adhesive thickness is set on ten for the FEA model with SO and four with 3M. This causes small elements in the adhesive layer and hence in the other components. The ratio of the height to the width of an element in the centre of the adhesive layer for SO and 3M is 0.98 and 1.28, respectively. The ratio for an element at the edge of the connection is 0.5 and 0.65, respectively. A maximum of 2 and a minimum of 0.5 is advised for the ratio (ABAQUS 2014). By using reduced integration for the glass and the steel connector, the calculation time is reduced. Due to the near incompressibility of the MS-polymer, a hybrid formulation is used for the adhesive elements of the MS-polymer. General, static step-by-step numerical analyses are performed by means of the implicit Abaqus® solver.

TABLE 4.4: ELEMENT SIZE AND TYPE FOR THE THREE MATERIALS.

Material	Element type	Element size [mm]	
		SO	3M
Glass	C3D20R	0.818	0.156
Steel	C3D20R	0.818	0.156
MS-polymer	C3D20H	0.205	/
2c-epoxy	C3D20	/	0.039

4.2.4. Results and discussion

Experimental results

The failure mechanisms of the samples can be divided into three categories: glass failure, adhesive failure and cohesive failure. Adhesive failure occurred only with SO and always in combination with cohesive failure. An example of this is depicted Figure 4.10c together with an example of glass failure (Figure 4.10a) and cohesive failure (Figure 4.10b & d). A thin film of epoxy remained when cohesive failure occurred with 3M; this phenomenon is also known as the thin-layer cohesive (TLC) failure pattern (Lee et al. 2009). This thin film is visible in Figure 4.10d on the glass panel.
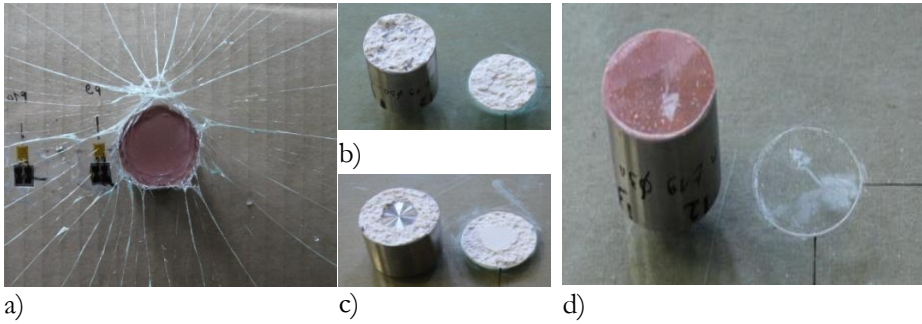
FIGURE 4.10: EXAMPLE OF A) GLASS FAILURE, B) COHESIVE FAILURE, C) COMBINATION OF ADHESIVE AND COHESIVE FAILURE AND D) THIN LAYER COHESIVE FAILURE.

The maximum tensile forces corresponding to glass failure and failure in the adhesive layer for all configurations are depicted in Figure 4.11, where the letter t is used to indicate the glass thickness and the letter D for the connector diameter. For example, t19D30 refers to a specimen with a glass thickness of 19 mm and a connector diameter of 30 mm. Tensile forces up to 8 kN were obtained with SO and up to 15 kN with 3M. The high failure tensile forces prove that adhesive point-fixings are indeed a good alternative for the connection of glass panels to the underlying structure. The adhesive ensures that no boreholes are needed, which gives stronger and visually more appealing glass panels. Furthermore, a larger fitting diameter increased the adhesive strength of the MS-polymer SO. This was not noticeable when using the epoxy 3M. Using 3M the thickness of the glass had a bigger influence on the strength than the diameter. Indeed, the thin glass plates deformed much more than the thicker glass plates, and the corresponding curvature under the connector introduced stress concentrations at the edge of the connector. These stress concentrations caused the connection to fail faster compared to thicker plates. Thicker glass plates were so stiff that the glass plate stayed relatively straight during the test, causing almost only uniaxial tensile stresses in the adhesive layer. This phenomenon was not affected by the diameter. From this it can be concluded that the diameter is more determinative for more flexible adhesives and the glass thickness for rather stiff adhesives. The scatter of the experimental results for failure in the adhesive layer for a glass thickness of 19 mm for 3M is most likely due to small imperfections that occurred during the fabrication process of the connection. Despite that the thickness of the adhesive has been ensured carefully and with high precision, very small differences in thickness will always occur. These differences have a major influence on the strength of the connection, especially when the stress concentrations are small.
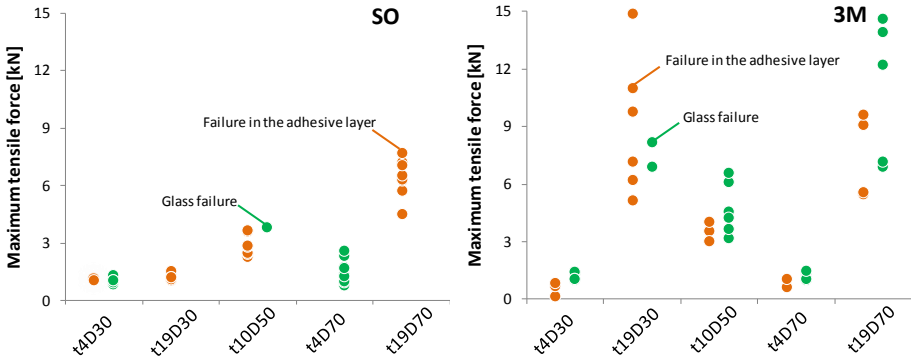
FIGURE 4.11: MAXIMUM TENSILE FORCES CORRESPONDING TO GLASS FAILURE AND FAILURE IN THE ADHESIVE LAYER FOR SO AND 3M.

Validation of numerical results

As mentioned above, three strain gauges were used to measure the occurring strains in the glass panel together with the displacement of the glass panel at three locations. These strain gauges and deformations formed one path. The obtained experimental results were used to validate the developed numerical model. The comparison between the experimental and numerical values was performed for the five geometrical configurations and for the two selected adhesives. The numerical nominal strains NE22 and vertical displacements U33 were obtained for the predefined path (Figure 4.6). In Abaqus® 11, 22 and 33 are the components in the x-, y- and z-direction, e.g. NE22 is the nominal strain in y-direction. The applied tensile force was the minimal force that was obtained for each configuration regardless of the failure mode. The applied tensile forces are summarized in Table 4.5 for each configuration. The comparison for the numerical strains and the strains measured during the experiments are illustrated in Figure 4.12 for the specimens with the relatively flexible adhesive SO and in Figure 4.13 for the specimens with the relatively stiff adhesive 3M. The dots represent the experimentally measured strains and the full line is the strain from the finite element model. Any outliers have been omitted. The dotted lines represent the edge of the connection and the support, respectively. Despite of a certain scatter of the experimental result, a good agreement between the numerical and experimental results is achieved.

From these graphs, the influence of the stiffness of the adhesive is very distinguishable. Bonded by a relatively flexible adhesive, the glass can deform unimpededly, in contrast to a relatively stiff adhesive bond, where the glass deformations under the connection are hindered by the adhesive. The strains even become zero or smaller for most configurations with the stiff adhesive; only with a glass thickness of 19 mm and a connector diameter of 30 mm larger strains were obtained in the centre of the glass panel. This phenomenon influences the position of the maximal strain and, consequently, the position of the maximal stresses. However, for specimens with flexible adhesives, the glass panel will also be locally prevented to bend for a small connector diameter and a small glass thickness, the glass will behave similar to the specimens with the stiff adhesive.
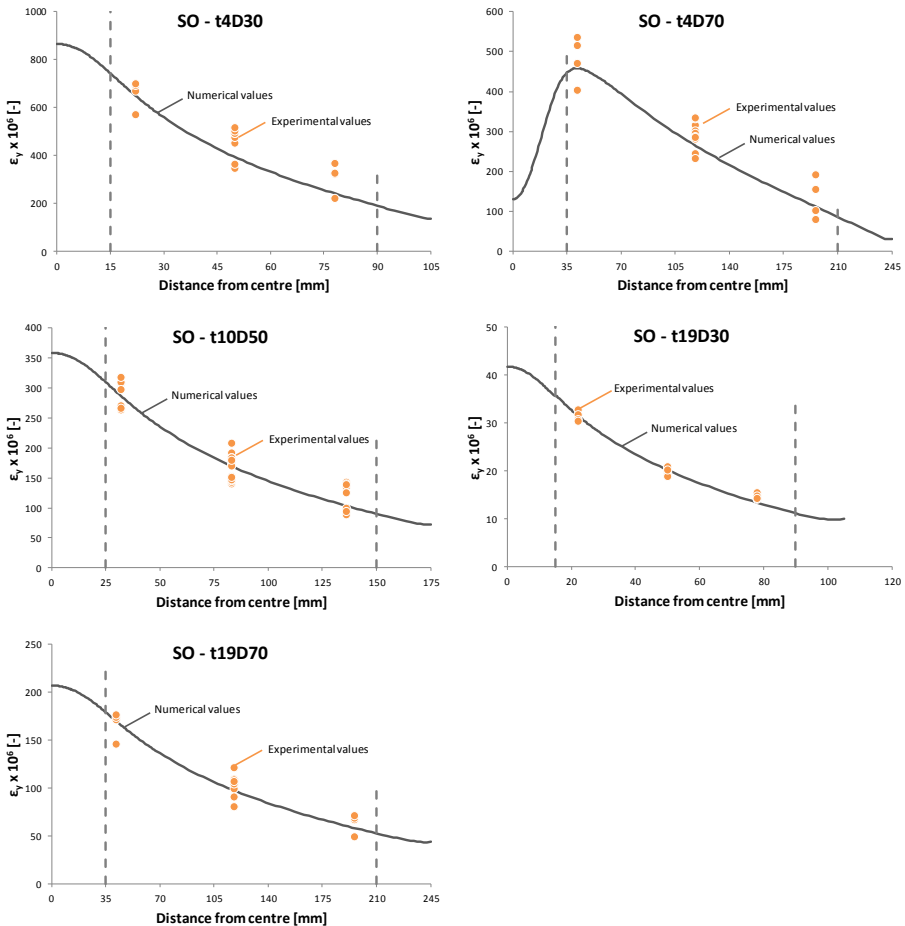
FIGURE 4.12: VALIDATION OF THE NUMERICAL STRAIN ε_Y OF THE LOCAL MODEL FOR SO.

TABLE 4.5: MINIMAL TENSILE FORCE FOR EACH CONFIGURATION

	SO	3M
t4 D30	0.8 kN	0.6 kN
t4 D70	0.7 kN	0.5 kN
t10 D50	2.1 kN	2.9 kN
t19 D30	0.9 kN	4.9 kN
t19 D70	4.4 kN	4.7 kN
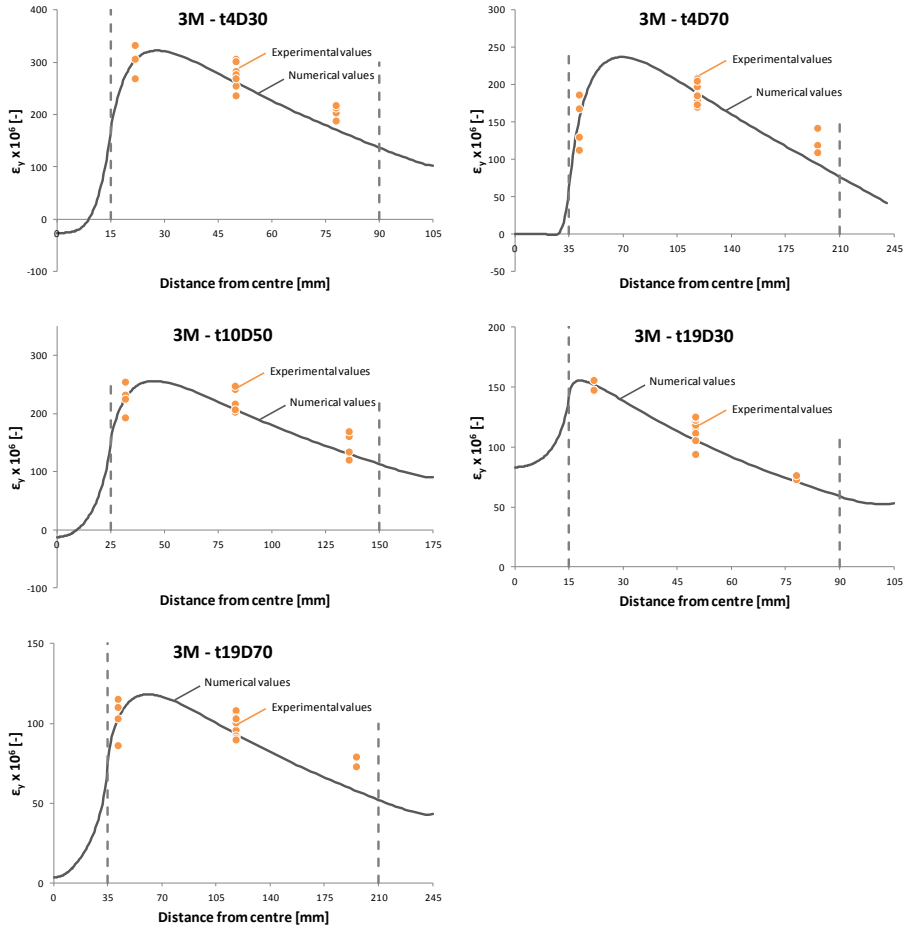
FIGURE 4.13: VALIDATION OF THE NUMERICAL STRAIN ε_Y OF THE LOCAL MODEL FOR 3M.

As can be seen in Figure 4.12 and Figure 4.13, the location of maximal strain for the specimen is at the centre of the glass panel for the flexible adhesive and outside the connection for the stiff adhesive. This difference was also observed in the experiments by the location of the crack initiation when the specimens fail due to glass failure. The crack initiation for the specimens with SO was mostly situated under the connection as depicted in Figure 4.14a and was situated close to the connection for the specimens with 3M as depicted in Figure 4.14b, corresponding with the location of maximal strain.

a)   b)
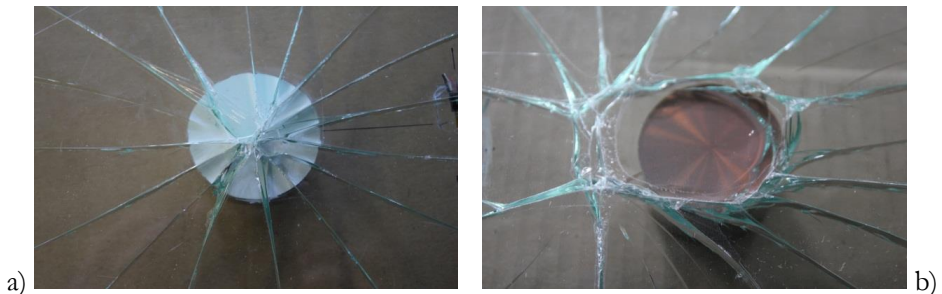
FIGURE 4.14: THE LOCATION OF THE CRACK INITIATION FOR A) SO HS AND B) 3M.

Since the relatively flexible adhesives do not significantly impede the deformations of the glass plate, it is also possible to calibrate these adhesives with the analytical method developed by Seel and Siebert (2012). This analytical method gives the maximal principal stresses on the top and bottom side of a circular glass plate loaded with a rotationally symmetric load. The relatively flexible adhesive will introduce an almost rotationally symmetric load on the glass plate, in contrast to the relatively stiff adhesive 3M. As the glass panel can almost freely deform under the connection with SO, this is not the case with 3M where the glass panel is locally strengthen due to the stiff and thin adhesive layer and the stiff connector. The glass panel will remain almost plane under the connector with 3M. However, as mentioned above this assumption is only true when the diameter of the connection is small enough and the glass thickness is thick enough. The comparison was made for the reference configuration SO-t10D50 with a load of 2 kN and is illustrated in Figure 4.15. The stress distributions derived from both methods correspond well in general. In detail, the curves correspond better at the centre of the glass panel and less at the support. This is probably due to the different geometry in the analytical method, i.e. the glass plate is circular in the analytical method and in the FEA the glass panel is a square plate that is circularly supported.
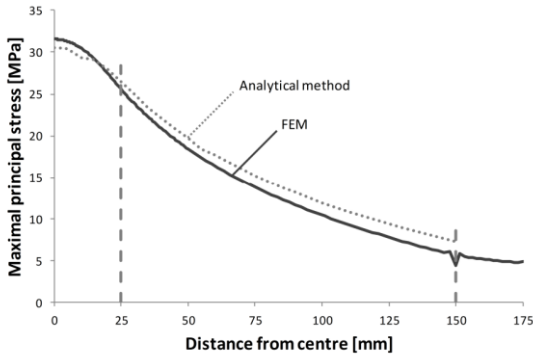
FIGURE 4.15: COMPARISON OF THE MAXIMAL PRINCIPAL STRESSES IN THE GLASS PLATE OBTAINED WITH AN ANALYTICAL METHOD AND THE FEA.

As mentioned above, the displacements were also measured and compared with the numerical deformation of the glass panel. The applied tensile forces were the same as for the validation of the strains (Table 4.5). The comparison for the numerical deformation U3 and the displacements measured during the experiments are illustrated in Figure 4.16 for the specimens with the relatively flexible adhesive SO and in Figure 4.17 for the specimens with the relatively stiff adhesive 3M. The dots again represent the experimentally measured deformations and the full line is the deformation U3 from the finite element model. The scatter of the experimental values is larger compared to the experimental values of the strains. The maximal deformations of the specimens with a glass thickness of 19 mm were too small to measure properly with LVDTs and are therefore not depicted. Furthermore, the deformation with a diameter of 30 mm with SO was also too small. A good comparison between the experimental and numerical values can be obtained. The difference in adhesive type is also clear here; the glass panel will remain straight under the connection for the 3M-specimens and will deform under the connection for the SO-specimens. Furthermore, as expected, the thinner the glass panel, the larger the deformation.
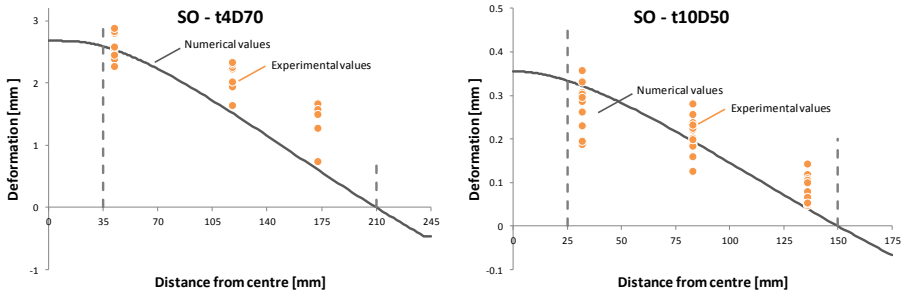
FIGURE 4.16: COMPARISON OF THE NUMERICAL AND EXPERIMENTAL DEFORMATION U3 OF THE LOCAL MODEL FOR SO.
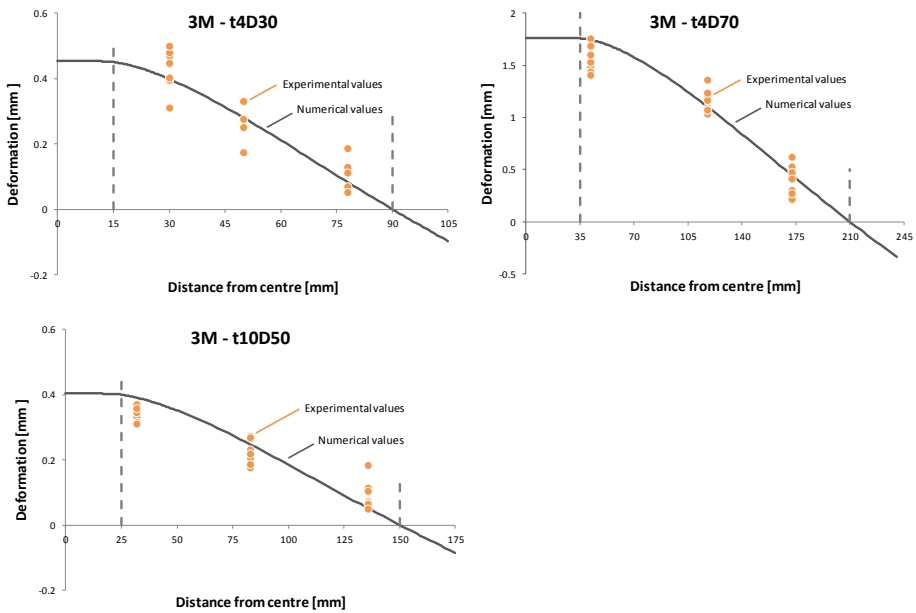

FIGURE 4.17: COMPARISON OF THE NUMERICAL AND EXPERIMENTAL DEFORMATION U3 OF THE LOCAL MODEL FOR 3M.

4.2.5. Parametric study

The validated numerical model now enables a more thorough investigation of the geometrical and material aspects of an adhesive point-fixing loaded in tension. In this paragraph, firstly the diameter of the connector (ϕ) is described together with the thickness of the glass (t_{glass}). Next, the study of the adhesive thickness ($t_{adhesive}$) together with the Young's modulus of the adhesive ($E_{adhesive}$) and finally the influence of the Poisson ratio ($\nu_{adhesive}$) is described. The values for each parameter

are summarized in Table 4.6 for a flexible adhesive and in Table 4.7 for a stiff adhesive. The maximum value of the maximal principal stress was obtained for the glass panel and the adhesive layer. With these values the influence of each parameter was investigated. Indeed, the maximal principal stress is often used as a failure criterion for structural glass and adhesives (Crocombe et al. 1990; Clark & McGregor 1993; Dean et al. 2004; Haldimann et al. 2008; Christensen 2013). Also the maximal deflection of the glass panel was obtained. The hyperelastic material model of the MS-polymer corresponds for small deformations to an linear-elastic material model with a Young's modulus of 9.02 MPa and a Poisson's ratio of 0.49. For the convenience in the parametrical study a Young's modulus of 10 MPa and a Poisson's ratio of 0.49 was used to simulate a flexible adhesive. For the simulation of a stiff adhesive a Young's modulus of 2000 MPa and a Poisson's ratio of 0.39 was used. The applied force on the numerical model was always equal to 1 kN.

TABLE 4.6: THE INVESTIGATED PARAMETERS AND THEIR VALUES FOR THE FLEXIBLE ADHESIVE.

Parameter	Symbol and unit		Values
Connector diameter	ϕ	[mm]	30, 50, 70, 100
Glass thickness	t_{glass}	[mm]	2, 4, 9 ,12 15, 19
Adhesive thickness	$t_{adhesive}$	[mm]	0.5, 1, 2, 5, 10
Adhesive Young's modulus	$E_{adhesive}$	[MPa]	0.5, 1, 5, 10, 20, 50
Adhesive Poisson's ratio	$\nu_{adhesive}$	[-]	0.47, 0.48, 0.49, 0.495, 0.499

TABLE 4.7: THE INVESTIGATED PARAMETERS AND THEIR VALUES FOR THE STIFF ADHESIVE.

Parameter	Symbol and unit		Values
Connector diameter	ϕ	[mm]	15, 30, 50, 70, 100
Glass thickness	t_{glass}	[mm]	2, 4, 9 ,12 15, 19
Adhesive thickness	$t_{adhesive}$	[mm]	0.05, 0.1, 0.2, 0.5, 1
Adhesive Young's modulus	$E_{adhesive}$	[MPa]	50, 200, 1000, 2500, 5000, 10000
Adhesive Poisson's ratio	$\nu_{adhesive}$	[-]	0.35, 0.37, 0.39, 0.41, 0.43

Connector diameter and glass thickness

The influence of the diameter of the connection was studied for values between 15 and 100 mm, and the glass thickness varied between 2 and 19 mm. These values were studied for two types adhesive layers, i.e. a flexible and a stiff adhesive. As mentioned before, the flexible adhesive was modelled with a thickness of 2 mm, a Young's modulus of 10 MPa and a Poisson's ratio of 0.49 and the stiff adhesive with a thickness of 0.2 mm, a Young's modulus of 2000 MPa and a Poisson's ratio of 0.39. The maximum value for the maximal principal stress in the glass panel for each studied connector and glass thickness is depicted in Figure 4.18a. An increasing diameter had a positive effect on the stresses, i.e. decreasing the occurring stresses. A larger diameter will support the glass panel over a larger surface, resulting in lower stresses. The maximal principal stresses in the adhesive layers are given in Figure 4.18b. Also the maximum value for the maximal principal stress decreases with an increase of the connector diameter and glass thickness. However, the effect of the connector diameter is more pronounced with the flexible adhesive and the effect of the glass thickness is more pronounced with the stiff adhesive. This confirms the assumptions from the experiments that thin glass panels will yield larger stress concentrations for stiffer adhesives and that the diameter is more determinative for more flexible adhesives.

Specimens with a larger diameter will have a larger deflection, as is visualised in Figure 4.18c. The decrease of stiffness of the glass panel is due to the increase of the size of the glass panel. Indeed, with the SLG-method the size of the glass panel depends on the diameter, i.e. the width and length of the glass panel is equal to seven times the connector diameter and the support diameter is equal to six times the connector diameter. When the glass panel has a fixed geometry and support diameter, one would expect that the glass deformation would decrease with increasing connector diameter. The increase in thickness of the glass will increase the moment of inertia of the glass panel. This increase of the rigidity of the panel will result in lower stresses and deformations. The reduction in stress between 9 mm and 19 mm thick glass is an average factor of 3.5, while the used volume will only rise with a factor of 2.1, so there is an economical benefit as well.
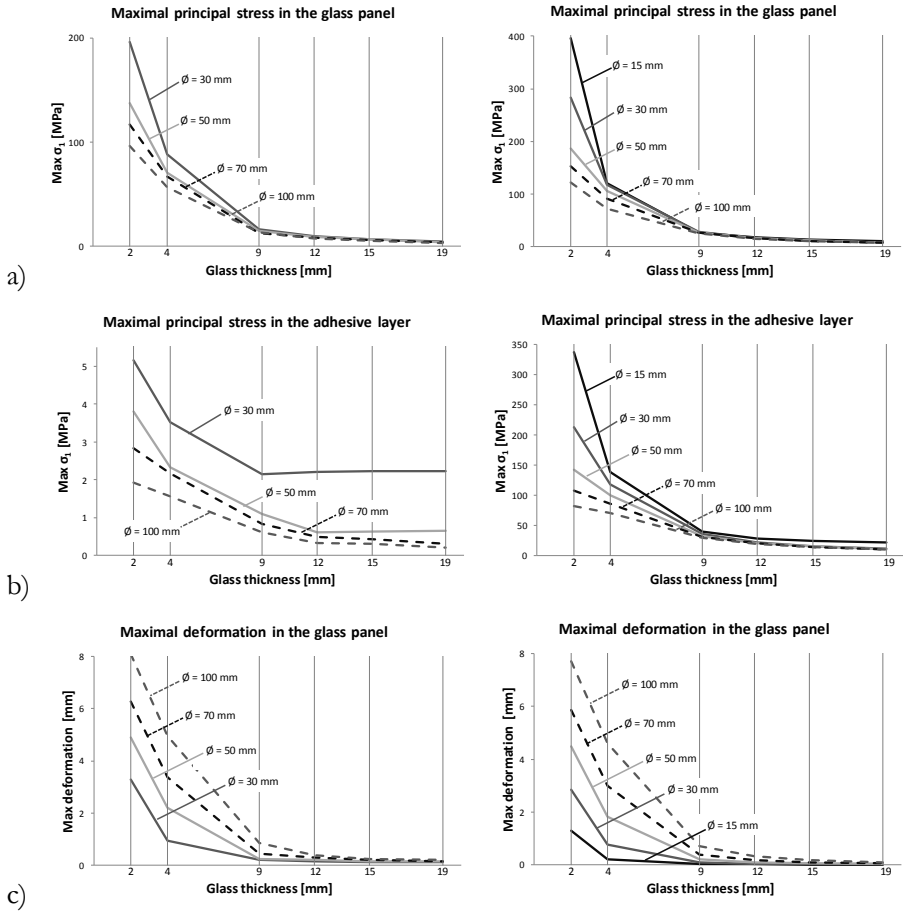
FIGURE 4.18: MAXIMUM VALUE OF THE MAXIMAL PRINCIPAL STRESS IN A) THE GLASS PANEL, B) THE ADHESIVE LAYER AND C) THE MAXIMAL DEFORMATION OF THE GLASS PANEL IN FUNCTION OF THE GLASS THICKNESS AND CONNECTOR DIAMETER WITH (LEFT) A FLEXIBLE ADHESIVE AND (RIGHT) A STIFF ADHESIVE FOR A LOAD OF 1 KN.

Adhesive thickness and Young's modulus

The values of the Young's modulus of the adhesive from Table 4.7 were applied on the reference configuration, i.e. a glass thickness of 10 mm and a connector diameter of 50 mm. The Poisson's ratio was kept constant on a value of 0.49 for a flexible configuration and 0.39 for a stiff configuration. The influence of the adhesive thickness and Young's modulus on the stress in the glass is illustrated in Figure 4.19a. With increasing Young's modulus of the adhesive, the maximum principal stress in the glass panel raised. This effect was less pronounced for lower Young's moduli. Also by reducing the adhesive thickness, the adhesive behaved more stiff and larger stress concentration aroused.

However, the maximal deformation of the glass panel increased with increasing the adhesive stiffness for small Young's moduli, as is depicted in Figure 4.19c, and decreased with increasing adhesive stiffness for larger Young's moduli. This phenomenon is also visible with decreasing the adhesive thickness. With thick and flexible adhesives, the adhesive layer will be the part that deforms the most and so reducing the deformation of the glass panel. However, this effect has a threshold; from a certain stiffness the adhesive layer will locally strengthen the connection and thus restricting the movement of the connection and decrease the deformation again. This effect is also visible in the adhesive layer, depicted in Figure 4.19b; from the threshold value the stress in the adhesive layer will increase more pronounced. For this configuration, for a Young's modulus of 5 MPa, the deformation was independent of adhesive thickness.

This effect is not visible with the stiffer configuration. Thick and flexible adhesive layers will increase the deformation capacity of the glass panel but the stresses in the glass panel will reduce due to the higher mobility of the connection. From Figure 4.19b, the adhesive Young's modulus has a larger influence on the maximum value of the principal stress in the adhesive layer than in the glass panel. The stress concentrations in the adhesive layer will increase more rapidly with increasing adhesive stiffness.
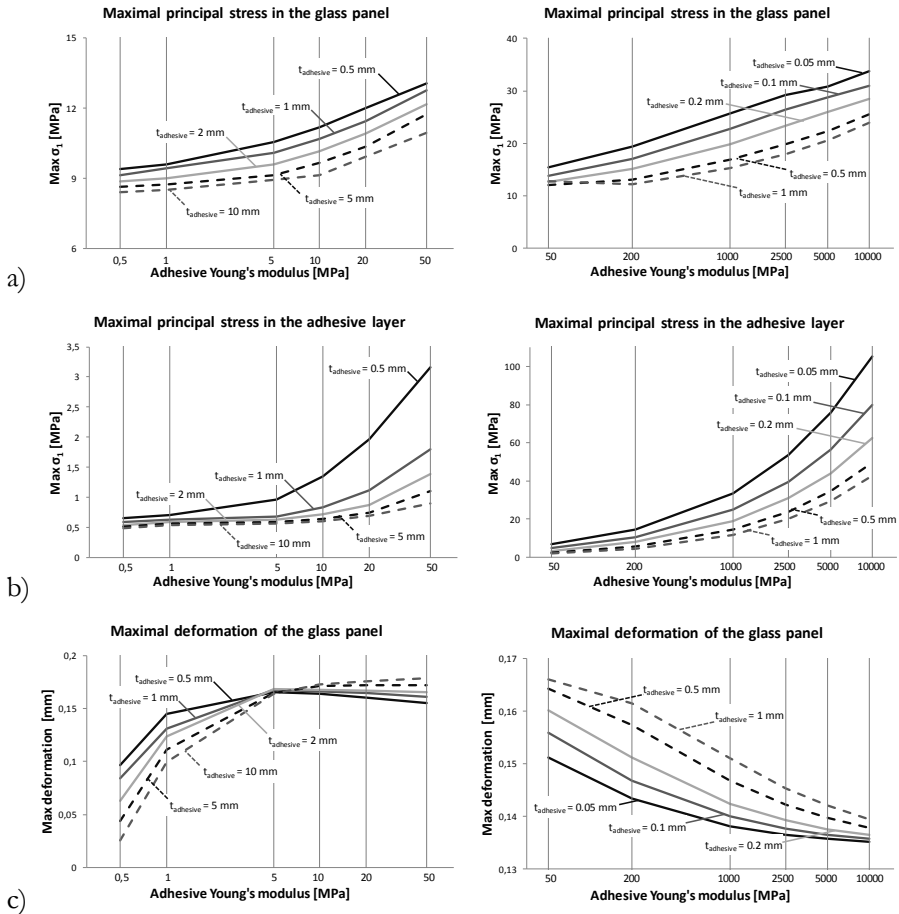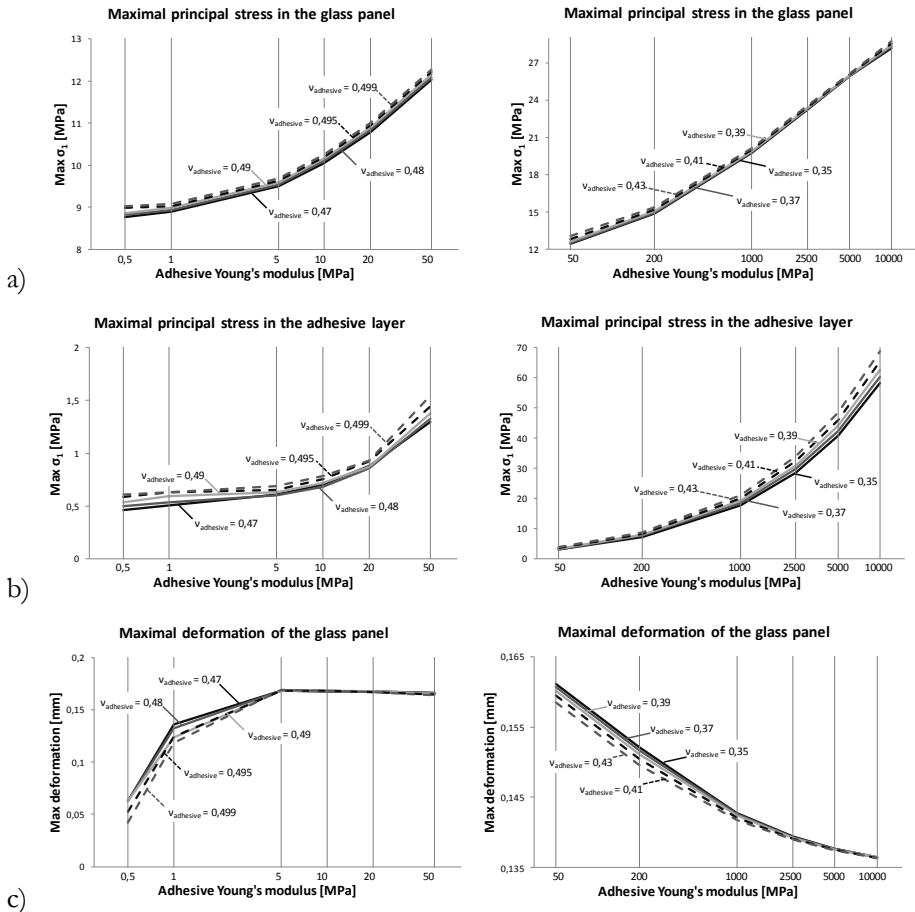
FIGURE 4.19: MAXIMUM VALUE OF THE MAXIMAL PRINCIPAL STRESS IN A) THE GLASS PANEL, B) THE ADHESIVE LAYER AND C) THE MAXIMAL DEFORMATION OF THE GLASS PANEL IN FUNCTION OF THE ADHESIVE THICKNESS AND ADHESIVE YOUNG'S MODULUS FOR (LEFT) A FLEXIBLE CONFIGURATION AND (RIGHT) A STIFF CONFIGURATION WITH A LOAD OF 1 KN.

Adhesive Poisson's ratio

To investigate the influence of the Poisson's ratio, the adhesive layer is modelled with five values of the Poisson's ratio for each Young's modulus as summarised in Table 4.6 and Table 4.7. The reference configuration, i.e. a glass thickness of 10 mm and a connector diameter of 50 mm, is used once more for the geometrical parameters. The adhesive thickness is kept constant on a value of 2 mm and 0.2 mm for the flexible and stiff configuration, respectively. The influence of the adhesive Poisson's ratio in function of the Young's modulus is illustrated in Figure 4.20a for the maximum value of the maximal principal stress in the glass panel. The influence of the Poisson's ratio is rather small compared to the influence of the adhesive Young's modulus. A decrease in the adhesive Poisson's ratio will reduce the maximal occurring stresses in the glass panel slightly. The maximum values for the maximal principal stress in the adhesive layer are depicted in Figure 4.20b. Again the influence is small and the stress depends proportionally on the Poisson's ratio. This effect is practically only observable for larger values for the adhesive Young's modulus. The increase in stress with increasing adhesive Poisson's ratio can be attributed to the increase of the transversal deformation of the adhesive layer. However, this transversal deformation is constrained by the boundary conditions, i.e. the steel connector and the glass panel, resulting in an increase of the maximal principal stresses in the adhesive layer and glass panel. This observation was also noticeable in previous research (Dispersyn et al. 2014; Santarsiero 2015).

FIGURE 4.20: MAXIMUM VALUE OF THE MAXIMAL PRINCIPAL STRESS IN A) THE GLASS PANEL, B) THE ADHESIVE LAYER AND C) THE MAXIMAL DEFORMATION OF THE GLASS PANEL TIN FUNCTION OF THE ADHESIVE POISSON'S RATIO AND ADHESIVE YOUNG'S MODULUS FOR (LEFT) A FLEXIBLE CONFIGURATION AND (RIGHT) A STIFF CONFIGURATION FOR A LOAD OF 1KN.

4.3.   Shear

In the previous paragraph, adhesive point-fixings under uniaxial tension were studied. In this paragraph, the focus is on adhesive point-fixings under shear. As depicted in Figure 1.1 adhesive point-fixings can also be used to support glass facades. In this configuration without mechanical self-weight supports, the connection will predominantly be loaded by vertical actions, i.e. the dead load of the glass panel. The aim of this paragraph is to validate and investigate the shear component of the numerical local component, i.e. σ_{Fxy} of Eq. (2.3). Metal connectors used for the connection between glass panels and their surroundings exist in a lot of shapes. Therefore, the load on the glass panel will have a certain eccentricity that varies with the shape of the connector. With a parametric study, the obtained FEA-model was then used to study the mechanical effect of geometrical and material parameters, such as the connection's diameter, load eccentricity, adhesive thickness and the adhesive modulus of elasticity.

4.3.1. Test specimens and materials

The experiments were conducted with three different eccentricities and two adhesive types. Since the diameter of the local component must be at least six times the diameter of the connector diameter, the width and length of the glass plate was set at seven times the connector diameter. With a 50 mm connector diameter, this resulted in a glass panel of 350 mm by 350 mm which was supported along the vertical edges over an area with a width of 20 mm. The thickness of the glass panel was equal to 10 mm, i.e. the reference configuration of the tensile experiments. For the validation, the strain at three different distances from the centre on the glass plate were measured using strain gauges. The positions of the strain gauges were determined by means of a preliminary FEA model and are depicted in Figure 4.21a. The tests were interrupted before failure to preserve the panels for reuse. After each test, the panel was rotated about the z-axis by 90° and tested again. This process was repeated four times, resulting in gaining a complete strain distribution in the glass panel. The fourth turn was to compare the measured strains with strains in the first position to detect possible effects of e.g. fatigue of the adhesive. The strain distribution can be presented by four strain paths which include all strain gauges, as depicted in Figure 4.21b. As a result of symmetry, strain paths 45° and 135° yielded the same outcome. Due to economic reasons the

strains of two out of five test specimens were completely determined, i.e. ε_1 till ε_6. The three remaining specimens were used to measure the variation between the specimens and only ε_1 and ε_4 was measured.

The selection of the adhesives was made in Chapter 3 and was the same as for the tensile experiments, i.e. the MS-polymer Soudaseal 270 HS (SO) and the 2c-epoxy 3M™ Scotch-Weld™ 9323 B/A (3M). The shear specimens were produced in the same way as the tensile specimens. For each adhesive type, five specimens were fabricated and tested; for three load eccentricities this gave a total of 150 experiments. Before testing, the specimens were stored for four weeks in a climatic chamber at a constant temperature of 21°C and a relative humidity of 45% without any UV-radiation. The material properties of the two selected adhesives were determined in Chapter 4 and were described in previous paragraphs.
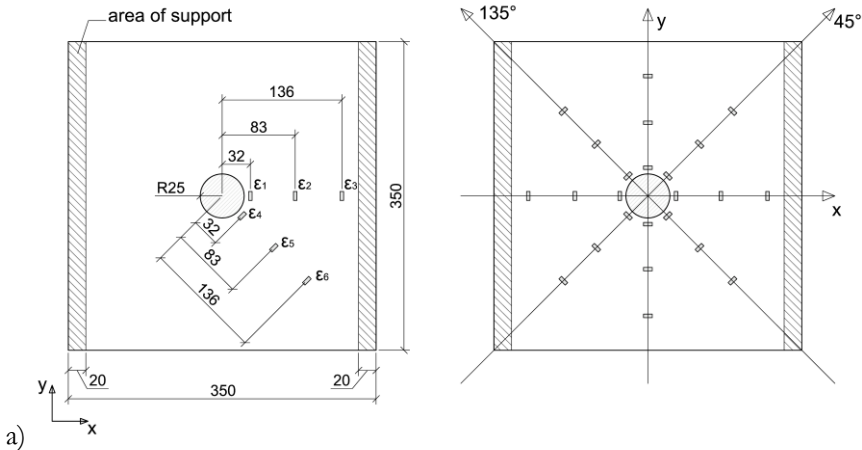
FIGURE 4.21: A) DIMENSIONS IN MM. OF THE GLASS PLATE WITH POSITION OF STRAIN GAUGES. B) THE FOUR STRAIN PATHS INCLUDING ALL STRAIN GAUGES.

4.3.2. Test method

As stated above, the local component is the glass plate with a diameter at least six times the diameter of the connector. In the experiments, the glass plate was supported along the vertical edges over an area with a width of 20 mm, as depicted in Figure 4.21, and the connector was loaded with a shear force until a certain threshold value. The back side of the glass panel was supported over the entire surface by a steel plate covered with a PTFE-film to minimize friction. The front side was supported over a width of 20 mm by two steel bars, which were also

coated with a PTFE-film. The shear force was applied by a push bar on the connector at a distance of 0 mm, 15 mm and 25 mm from the outer edge of the adhesive layer. The test configuration is depicted in Figure 4.22 and a visualisation of the test setup for the three eccentricities in Figure 4.23 for SO. The tests were performed on a universal electro-mechanic Zwick/Roell 10kN ProLine testing machine with a load cell of 10 kN using a displacement rate of 1 mm/min. A threshold load of 0.4 kN was chosen for the soft MS-polymer SO and 1,5 kN for the stiff 2c-epoxy 3M.
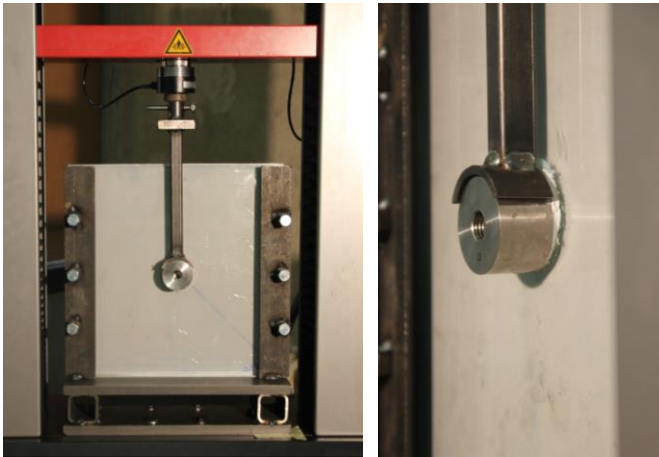
FIGURE 4.22: TEST SETUP FOR SHEAR
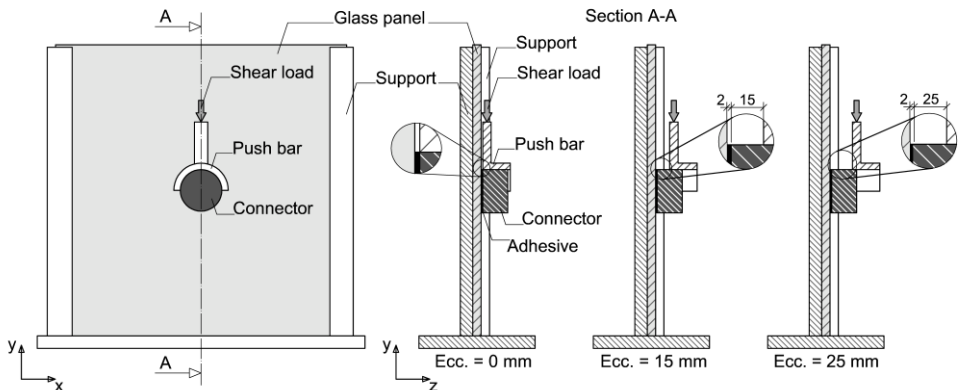
FIGURE 4.23: SETUP FOR SHEAR TESTS ON ADHESIVE POINT-FIXINGS FOR THE THREE ECCENTRICTIES WITH SO. (DIMENSIONS IN MM).

4.3.3. Numerical model

The finite element software Abaqus® was used to build a three-dimensional finite element model and to numerically analyse the connection. Due to symmetry only half of the glass plate was numerically modelled. Since stress concentrations were again expected around the connector, local refinement of the mesh pattern was introduced. The same square mesh pattern as in the numerical tensile model was applied inside the circular pattern to avoid mesh singularities in the centre of the connector. At the back side of the glass panel a rigid body was modelled to simulate the test frame, this rigid body prevents only backward movements. The front side of the glass panel was completely constrained along the support area with a width of 20 mm. The applied force was equal to 350 N for the MS-polymer and 1000 N for the 2c-epoxy. Again the adhesive layer was connected to the glass and the metal connector by means of a tie-constraint with the same properties as in the numerical tensile model. The contact between the connector and the push bar was modelled as a surface-to-surface contact with a hard contact pressure-overclosure relationship. The latter minimizes the penetration of the slave surface into the master surface at the constraint location and does not allow the transfer of tensile stress across the interface. Also separation after contact was enabled. Between the rigid body and the glass panel frictionless behaviour was applied. An exploded view of the separate parts and their contact properties in the numerical shear model is depicted in Figure 4.24. The element sizes and types for the different components in the numerical shear model were the same as for the numerical tensile model and are summarized in Table 4.4.

4.3.4. Validation of numerical results

As mentioned before, six strain gauges were used during each test to measure the occurring strains in the glass panel. By rotating the panel 90° about the z-axis after each test, the strains at 24 locations were gained. The obtained experimental results were used to validate the developed numerical model. The comparison between the experimental and numerical values is performed for the three eccentricities and two selected adhesives. This comparison is illustrated in Figure 4.25 for an eccentricity of 0 mm, in Figure 4.26 for an eccentricity of 15 mm and in Figure 4.27 for an eccentricity of 25 mm. In these graphs the dots represents the experimentally measured strains, the full line is the numerical strain. Due to symmetry, the results for strain paths 45° and 135° are the same and are put together. Despite a certain scatter in the experimental results, a good agreement between the numerical and experimental results is achieved. Moreover, for the stiff adhesive, glass deformations under the connection are impeded by the adhesive. The strains even become zero or smaller in the centre of the glass panel. As expected, the strains increase with increasing eccentricity, due to the increase of the bending moment. Based on the comparison between the numerical and experimental values for the strains, it can be concluded that the FEA model for shear is hereby validated. As expected, the highest strains occur along path y. The used test method did not give measurable fatigue in the adhesive layer.
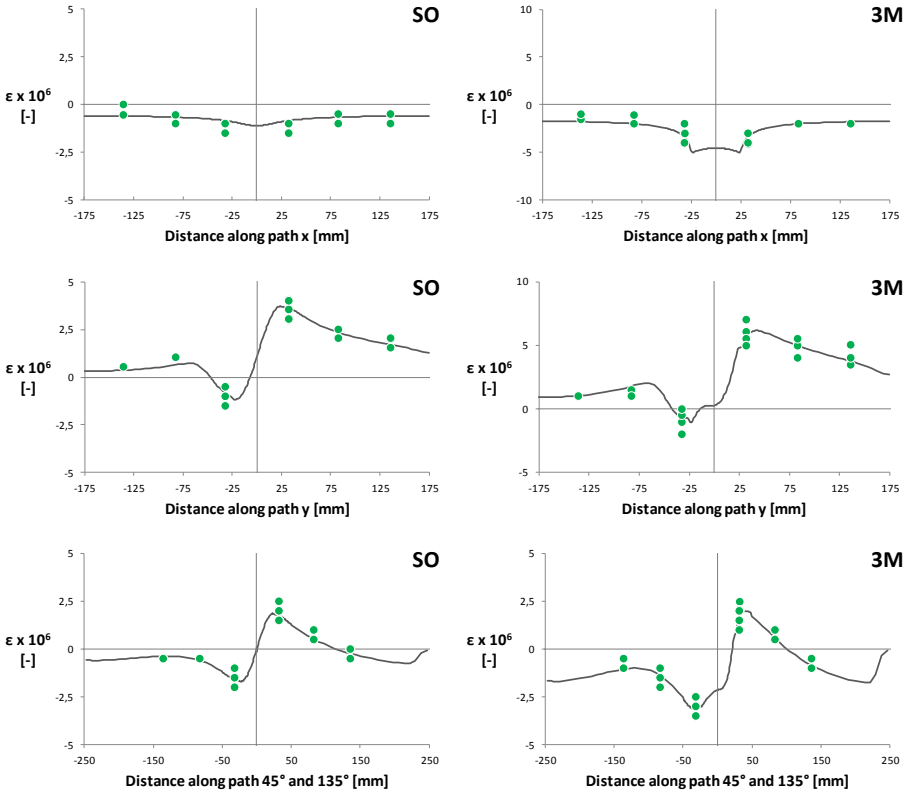
FIGURE 4.25: COMPARISON BETWEEN THE NUMERICAL AND EXPERIMENTAL VALUES ALONG THE FOUR STRAIN PATHS FOR THE MS-POLYMER SO AND THE 2C-EPOXY 3M FOR AN ECCENTRICITY OF 0 MM.
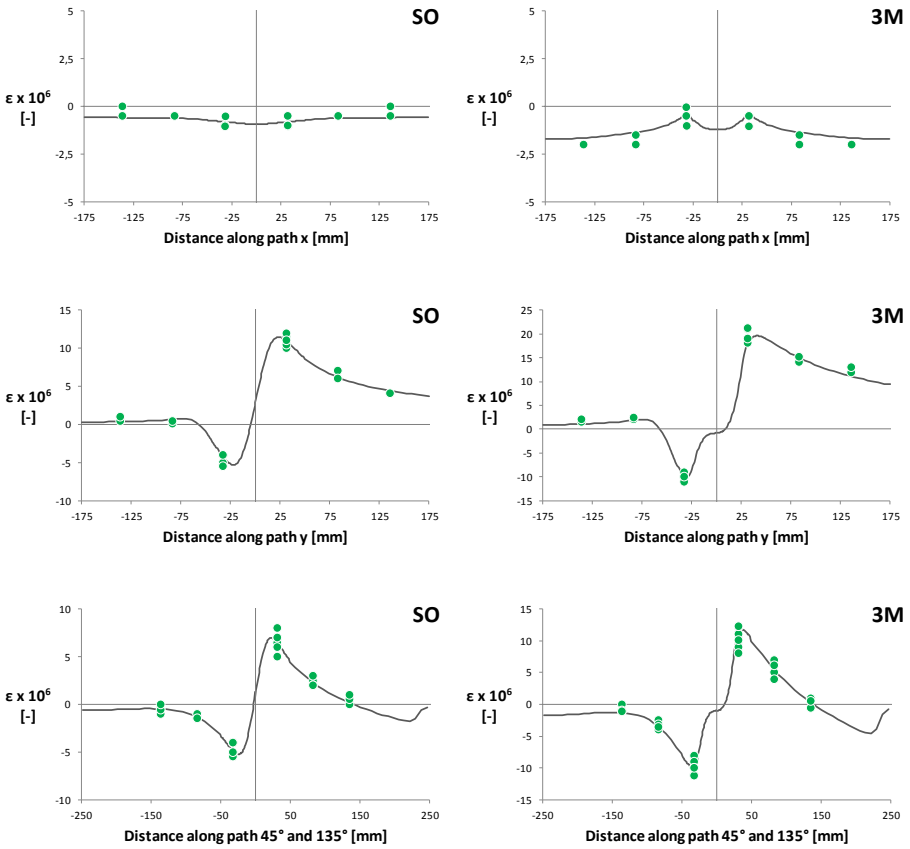
FIGURE 4.26: COMPARISON BETWEEN THE NUMERICAL AND EXPERIMENTAL VALUES ALONG THE FOUR STRAIN PATHS FOR THE MS-POLYMER SO AND THE 2C-EPOXY 3M FOR AN ECCENTRICITY OF 15 MM.
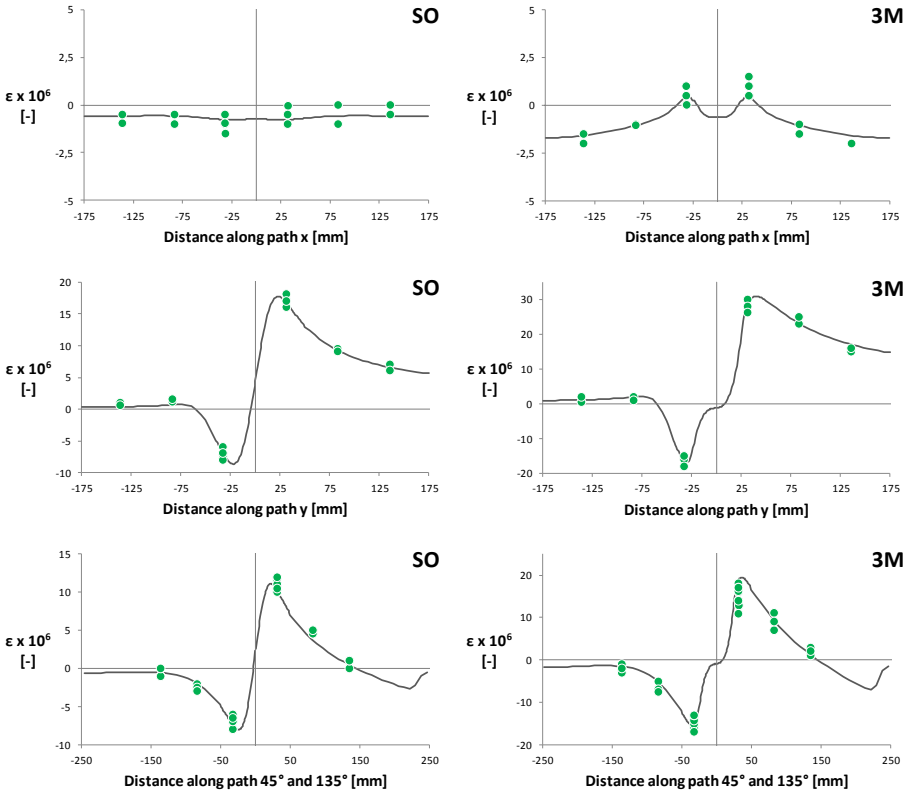
FIGURE 4.27: COMPARISON BETWEEN THE NUMERICAL AND EXPERIMENTAL VALUES ALONG THE FOUR STRAIN PATHS FOR THE MS-POLYMER SO AND THE 2C-EPOXY 3M FOR AN ECCENTRICITY OF 25 MM.

4.3.5. Parametric study

The validated numerical shear model enables a thorough investigation of geometrical and material parameters of a point-fixing loaded in shear. Firstly the diameter of the connector (ϕ) was investigated together with the eccentricity (e). Next, the adhesive thickness ($t_{adhesive}$) together with the Young's modulus of the adhesive ($E_{adhesive}$) was studied. The values for each parameter are summarized in Table 4.8. The maximum value of the maximal principal stress is obtained for the glass panel and the adhesive layer separately, together with the maximum value of the shear stress in the adhesive layer. The applied force for every configuration in this parameter study equals 1 kN.

TABLE 4.8: INVESTIGATED PARAMETERS AND CORRESPONDING VALUES.

Parameter	Symbol and unit	Values
Connector diameter	ϕ [mm]	15, 30, 50, 70
Eccentricity	e [mm]	0, 15, 30, 45, 60
Adhesive thickness	$t_{adhesive}$ [mm]	0.05, 0.1, 0.2, 0.5, 1
Adhesive Young's modulus	$E_{adhesive}$ [MPa]	50, 200, 1000, 2500, 5000, 10000

Connector diameter and load eccentricity

This parametric study was only performed on the stiff adhesive, which was modelled with a thickness of 0.2 mm, a Young's modulus of 2000 MPa and a Poisson's ratio of 0.39. The maximal principal stress in the glass panel for each studied connector diameter is depicted in Figure 4.28a in function of the load eccentricity. An increasing diameter has a positive effect on the stresses. A larger diameter will support the glass panel over a larger surface, resulting in lower stresses. The maximal principal stress in the adhesive layer is given in Figure 4.28b and the maximum value for the shear stress in the adhesive layer in Figure 4.28c. Further, the maximum value for the maximal principal stress decreases with an increase of the connector diameter. As expected, with increasing eccentricity the stresses in the glass panel and adhesive layer will increase due to the increasing bending moment. The influence of the eccentricity is more pronounced for smaller diameters. Moreover, the influence of the eccentricity is almost linear, i.e. doubling the load eccentricity will result in almost a doubling of the stress
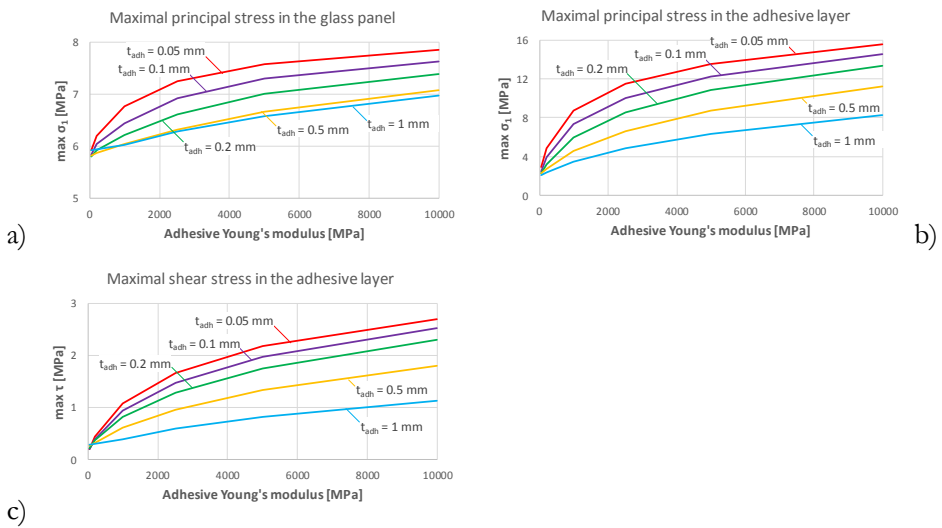

a)

b)

c)
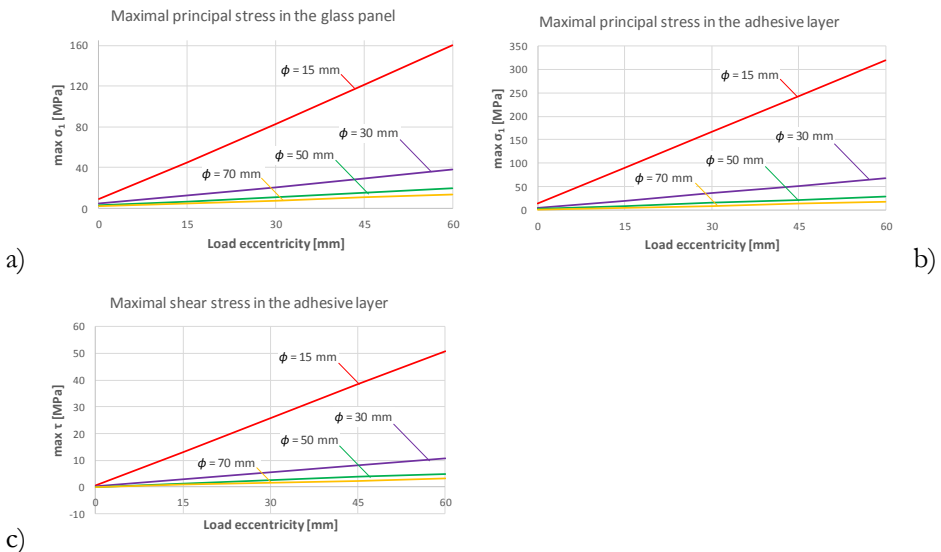
FIGURE 4.28: MAX. VALUE OF THE MAXIMAL PRINCIPAL STRESS IN A) THE GLASS PANEL, B) THE ADHESIVE LAYER AND C) THE MAXIMUM VALUE OF THE SHEAR STRESS IN THE ADHESIVE LAYER IN FUNCTION OF THE CONNECTOR DIAMETER AND ECCENTRICITY.

Adhesive thickness and Young's modulus

The experiments showed that the Young's modulus of the adhesive has a significant influence on the occurring strains in the glass panel. The values from Table 4.8 are applied on the reference configuration, i.e. a connector diameter of 50 mm and a load eccentricity of 15 mm. The Poisson's ratio was kept constant on a value of 0.39. The influence of the adhesive thickness and Young's modulus is illustrated in Figure 4.29. The maximum principal stress in the glass panel will rise with an increase of the Young's modulus of the adhesive. Also, by reducing the adhesive thickness, the adhesive will behave stiffer and larger stress concentrations in the glass panel will arise. The latter is also visible in the adhesive layer; thick and flexible adhesive layers will decrease the stresses in the glass panel due to the higher mobility of the connection. In contrast to thinner and stiffer adhesive layers which locally strengthen the connection and thus restrict the movement of the connection and introduce higher stresses.

FIGURE 4.29: MAX. VALUE OF THE MAXIMAL PRINCIPAL STRESS IN A) THE GLASS PANEL, B) THE ADHESIVE LAYER AND C) THE MAXIMUM VALUE OF THE SHEAR STRESS IN THE ADHESIVE LAYER IN FUNCTION OF THE ADHESIVE THICKNESS AND YOUNG'S MODULUS.

4.4. Multi-axial loading

In the previous paragraphs, adhesive point-fixings under uniaxial tension and shear were studied. In this paragraph, adhesive point-fixings loaded with a combination of tension and shear will be studied. Adhesive point-fixings can be used to support glass facades, as depicted in Figure 1.1c and d. In this configuration, the connection will predominantly be loaded by vertical actions, i.e. the dead load of the glass panel, but horizontal actions will also occur, i.e. wind loads. Moreover, point-fixings can also be used for supporting glass panels under an angle as depicted in Figure 1.1e and f. In these situations, the connections will also be multi-axially loaded, i.e. a combination of tension and shear. The angle between the resultant force and the tensile force can vary, as it depends on the magnitude of the wind load or the angle of the glass panel. To gain a validated model, experiments were performed with three load eccentricities (15 mm, 30 mm and 45 mm), three multi-axial angles (22.5°, 45° and 67.5°) and the two selected types of adhesives.

4.4.1. Test specimens and materials

As for the tensile and shear experiments, the SLG-method was also used to set the dimensions of the test specimens. The diameter of the local component ϕ_{loc} was determined to be at least six times the diameter of the borehole ϕ_{hole}, as expressed in Eq. (2.2). The width and length of the glass plate were seven times the connector diameter. The connector diameter was set on 50 mm, resulting in a glass panel of 350 mm by 350 mm which was supported along a circumference with a diameter of 300 mm. The thickness of the glass panel was equal to 10 mm, as depicted in Figure 4.30.
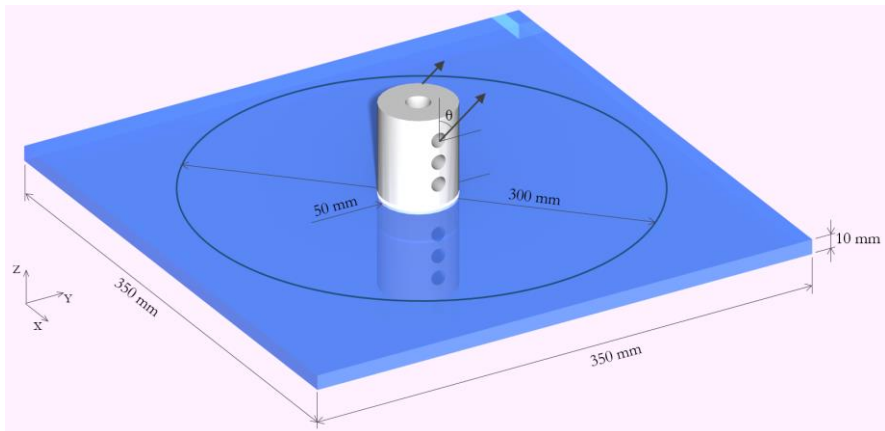
FIGURE 4.30: DIMENSIONS OF THE GLASS PLATE FOR THE MULTI-AXIAL LOCAL COMPONENT.

The tests were performed using a universal electro-mechanical test machine Instron 5800R (frame 4505 retrofitted with a digital controller 8800). A load cell of 10 kN was used to obtain the test results presented here. The load of the connector was measured by the test machine. Furthermore, to validate the multi-axial local component, the strains at the surface of the glass panel were measured by means of strain gauges. The strain at three different distances from the centre on the glass plate was measured. The positions of the strain gauges were also here determined by means of a preliminary FEA model. Due to economic reasons the stresses of only two out of five test specimens were completely determined, where the three remaining specimens were used to measure the variation between the specimens. The dimensions of the glass plate, the circumference of the support and the positions of the strain gauges for these two types are illustrated in Figure 4.31a and b. The tests were interrupted before failure to preserve the panels for reuse. Since the specimens were symmetrical, the number of needed strain gauges could be reduced. After measuring the strains at the upper side of the panel, the panel was rotated about the z-axis by 180° to measure the strains at the lower side of the panel. As a result of symmetry, three strain paths were set, as depicted in Figure 4.31c. As previously described, an adhesive point-fixing can be subjected to wind loads and gravity resulting in a tensile force and a shear force respectively. Combining both forces results in a load which acts on the connection under a certain angle. The angle between the resultant force and the tensile force (wind load) is defined as the multi-axial angle. This angle is illustrated as θ in Figure 4.32.
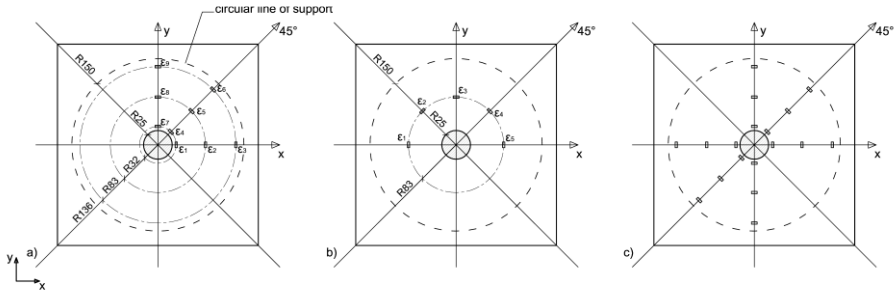
FIGURE 4.31: POSITIONING OF THE STRAIN GAUGES FOR THE TWO TYPES A) AND B), AND C) THE THREE RESULTING STRAIN PATHS.
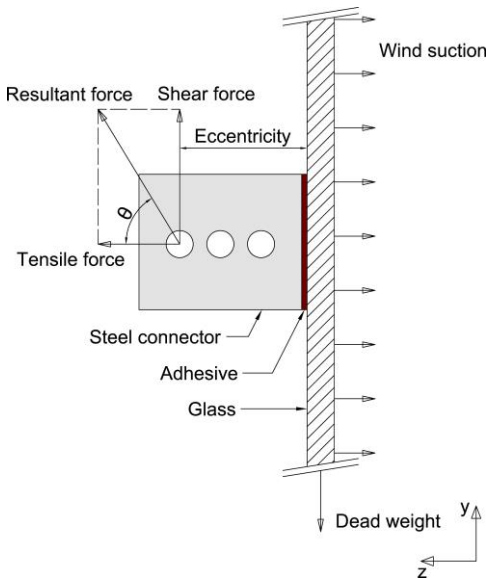
FIGURE 4.32: DEFINITION OF THE MULTI-AXIAL ANGLE θ.

Chapter 2 and the previous paragraphs demonstrated that many parameters have an influence on the stress distributions and strength of adhesive point-fixings. As in the previous paragraphs, experiments were conducted with different geometrical and material parameters to obtain a complete validated numerical model. As mentioned above, tree different multi-axial angles and three different eccentricities were used for the two adhesives. To obtain sufficient understanding of the reciprocal effect of the parameters, a full factorial design was preferred. Table 4.9 summarises the values of the varying parameters. Each combination consisted of five test specimens to deal with variations between the specimens, hence a total of 180 tests were performed.

Multi-axial angle [°]

22.5	45.0	67.5		
X	X	X	15	
X	X	X	30	Eccentricity [mm]
X	X	X	45	

4.4.2. Test method

The three tested eccentricities are also visible in Figure 4.32. As described earlier, the MS-polymer Soudaseal 270 HS (SO) and the epoxy 3M™ Scotch Weld™ 9323 B/A (3M) were used to determine the influence of the stiffness of the adhesive on the behaviour of the adhesive point-fixing. To ensure that the adhesive thicknesses were maintained, custom-made brackets were used during the curing of the adhesives, as depicted in Figure 4.33 for the MS-polymer. The adhesive thickness of SO was equal to 2 mm according to the technical data sheet of the producer and equal to 0.2 mm for the epoxy 3M. To avoid climatic influences during the curing process the specimens were stored for four weeks in a climatic chamber at a constant temperature of 21°C and a relative humidity of 45% without any UV-radiation.

FIGURE 4.33: EXAMPLE OF THE BRACKET FOR THE MS-POLYMER SO WITHOUT ADHESIVE (LEFT) AND WITH ADHESIVE (RIGHT).

To test the specimens under a multi-axial angle, a special test frame was fabricated. A visualization of the test frame is depicted in Figure 4.34. By supporting the glass panel under a well-defined angle and by loading the connector with a vertical force, a multi-axial load condition was obtained. Since the test frame was modular, the frame could be used for the three selected angles and eccentricities. The test frame

consisted of three main parts: (i) an underlying structure which was connected with the test machine, (ii) a movable structure which consisted of a steel plate with an opening which supported the glass panel, and (iii) two leverages that connected the movable structure to the underlying structure. These leverages could be attached at different locations to realize the three selected angles between the movable and underlying structure, as illustrated in Figure 4.35. From preliminary experiments the failure load of 0.58 kN for SO and 8.10 kN for 3M was determined. For the soft MS-polymer a load of 0.35 kN was chosen as the threshold value and 1.5 kN for the stiff 2c-epoxy.
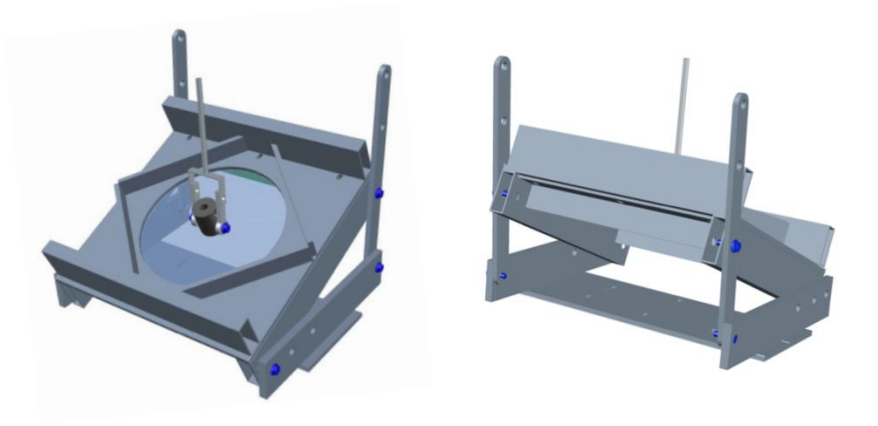
FIGURE 4.34: 3D VISUALIZATION OF THE TEST FRAME FOR THE MULTI-AXIAL EXPERIMENTS.
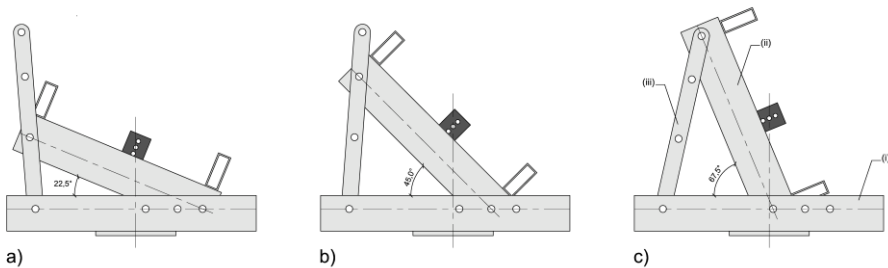
FIGURE 4.35: THE THREE LOAD CONFIGURATIONS UNDER AN ANGLE OF A) 22.5°, B) 45.0° AND C) 67.5°.

4.4.3. Numerical model

Once again, the finite element software Abaqus® was used to build a three-dimensional finite element model to numerically analyse the connection. Due to symmetry only half of the glass plate was numerically modelled and local

refinement of the mesh pattern was introduced. The same square mesh pattern as in the numerical tensile and shear model was applied inside the circular pattern to avoid mesh singularities. The boundary conditions during the experiments are illustrated in Figure 4.36. These were taken into account in the numerical model. Along the circular line of support, the upward displacement was prevented as the boundary condition for U_z was set to zero and at the edge as $U_y = 0$. The load was introduced as a y- and z-component, representing the shear and tensile force, respectively. The amplitude of each component depended on the multi-axial angle. The two boundary conditions and the components of the applied load are depicted in Figure 4.37.
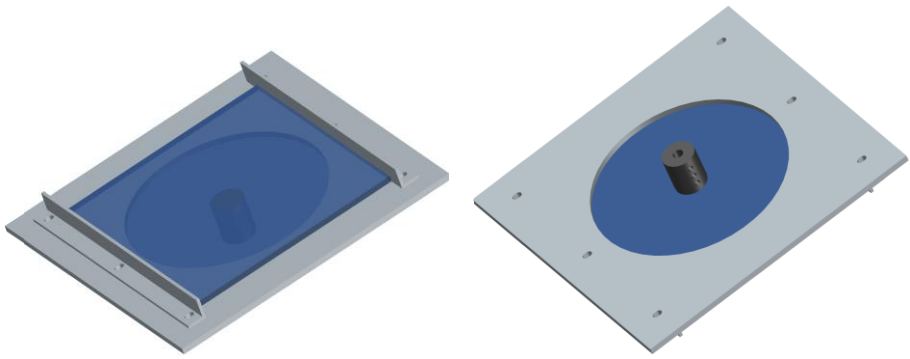
FIGURE 4.36: BOUNDARY CONDITIONS DURING THE EXPERIMENTS.
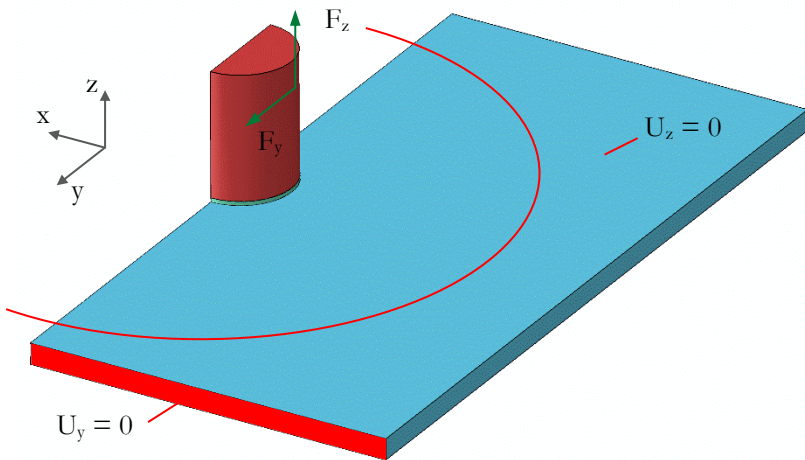
FIGURE 4.37: BOUNDARY CONDITIONS IN THE NUMERICAL MODEL.

Again, the adhesive layer is connected to the glass and the metal connector by means of a tie-constraint with the same properties as in the numerical tensile and shear model. The element sizes and types for the different components in the numerical multi-axial model were the same as for the numerical tensile and shear model and are summarized in Table 4.4.

4.4.4. Validation of numerical results

As mentioned before, six strain gauges were used during each test to measure the occurring strains in the glass panel. By rotating the panel 180° after each test, the strains were obtained at 18 locations. The obtained experimental results were used to validate the developed numerical model. The comparison between the experimental and numerical values is performed for the three eccentricities, the three multi-axial angles and the two selected adhesives. The applied load was equal to 0.3 kN for SO and 1.45 kN for 3M. The results are presented along the three strain paths which include all strain gauges. The strain gauges measured the strains perpendicular to these paths, as depicted in Figure 4.31c. The graphs are always constructed in the same way, with the dots representing the experimentally measured strains and the full line the numerical strain. Four configurations are depicted in Figure 4.38 and Figure 4.39, the other 14 configuration are given in Appendix B. Also here, as expected, a certain scatter in the experimental results occurred. Nevertheless, a good agreement between the numerical and experimental results is achieved. As with the tensile and shear tests, for the stiff adhesive, glass deformations under the connection are impeded by the adhesive. The strains even become zero or smaller in the centre of the glass panel. Moreover, the strains along the paths 45° and y increase with increasing eccentricity, due to the increase of the bending moment. This influence is more prominent with larger multi-axial angles. With larger multi-axial angles, the shear component will increase, increasing the bending moment acting on the glass panel. However, with increasing multi-axial angle the strains decrease as the connection is loaded in shear more than in tension. Shear forces will introduce lower strains in the glass panel than tensile forces. The strains along path x are not influenced by the eccentricity, as the tensile component depends on the multi-axial angle and not the eccentricity. The strains will decrease with an increase of the multi-axial angle. Based on the comparison between the numerical and experimental values for the strains, it can be concluded that the multi-axial FEA model is hereby validated.
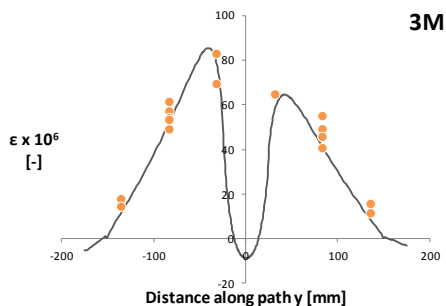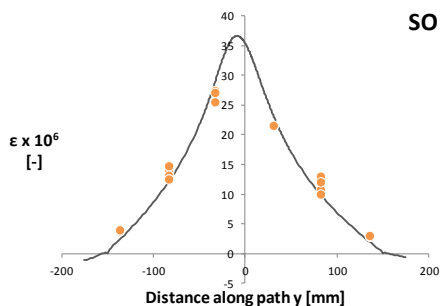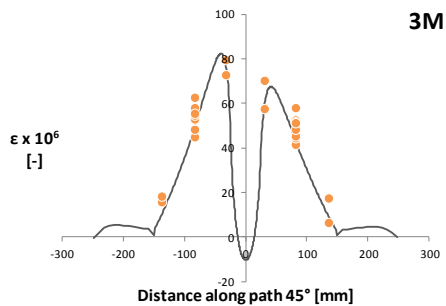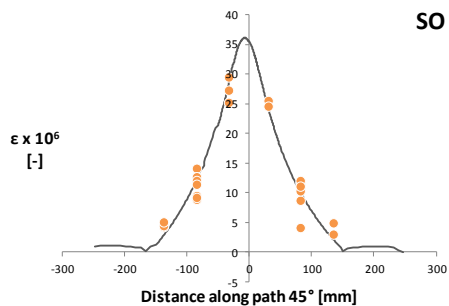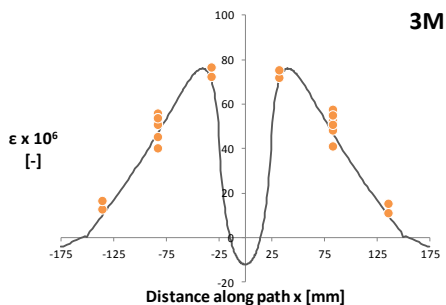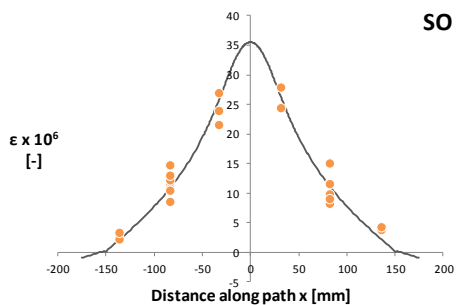
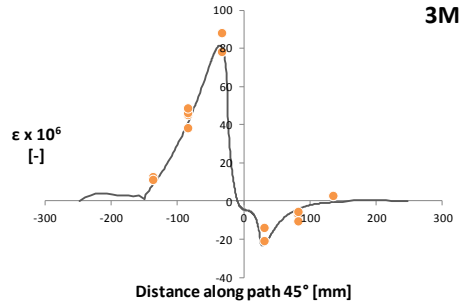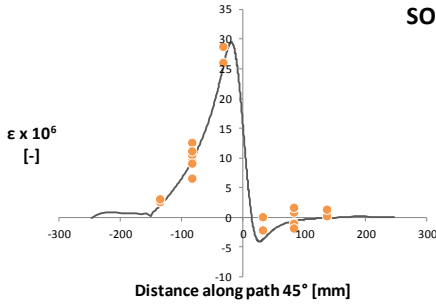**FIGURE 4.38**: CONFIGURATION WITH ECCENTRICITY OF 15 MM AND A MULTI-AXIAL ANGLE OF 22.5°.
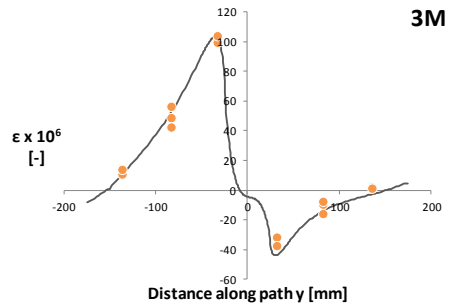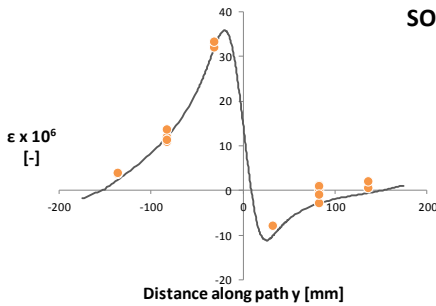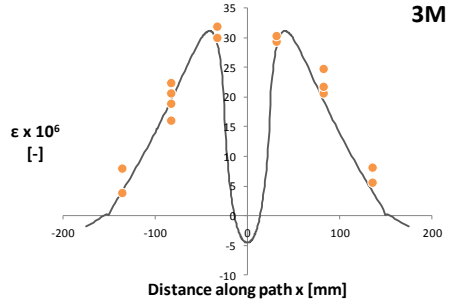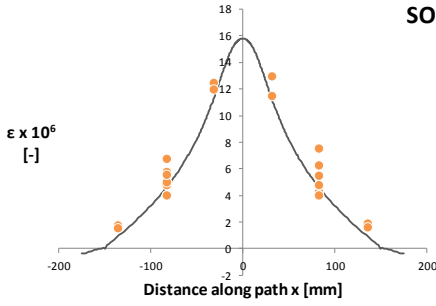
FIGURE 4.39: CONFIGURATION WITH ECCENTRICITY OF 45 MM AND A MULTI-AXIAL ANGLE OF 67.5°.

4.4.5. Superposition of the local stresses

As mentioned before, the SLG-method consists of the superposition of a global and local component. The sum of the stresses σ_{Fz}, σ_{Fxy} and σ_M from the local component and the global stress σ_{global} multiplied with a stress concentration factor k must be less than the critical stress σ_R according to Eq. (2.3). The local stresses σ_{Fz}, σ_{Fxy} and σ_M are derived by applying each support reaction (F_z, F_{xy}, M) on the local model with F_{xy} determined by Eq. (4.2). These support reactions are derived from the global model. The forces applied on the multiaxial model from previous paragraph contain all these three support reactions. So instead of using a local numerical model for each support reaction, the multi-axial model can be used to determine directly the sum of the local stresses. This superposition is shown in Figure 4.40. The applied force F, multiaxial angle θ and eccentricity e can be easily determined with Eq. (4.3), (4.4) and (4.5), respectively.

$$F_{xy} = \sqrt{F_x^2 + F_y^2} \tag{4.2}$$

$$F = \sqrt{F_z^2 + F_{xy}^2} \tag{4.3}$$

$$\theta = cos^{-1}\left(\frac{F_z}{F}\right) \tag{4.4}$$

$$e = \frac{M}{F_{xy}} \tag{4.5}$$

The validation of this principle of superposition can be performed with the developed local numerical models from the previous paragraphs. Only a numerical model for the moment is developed additionally. The validation consist of a comparison between the sum of the local stresses and the stresses obtain from the multi-axial model, as given in Eq. (4.6).

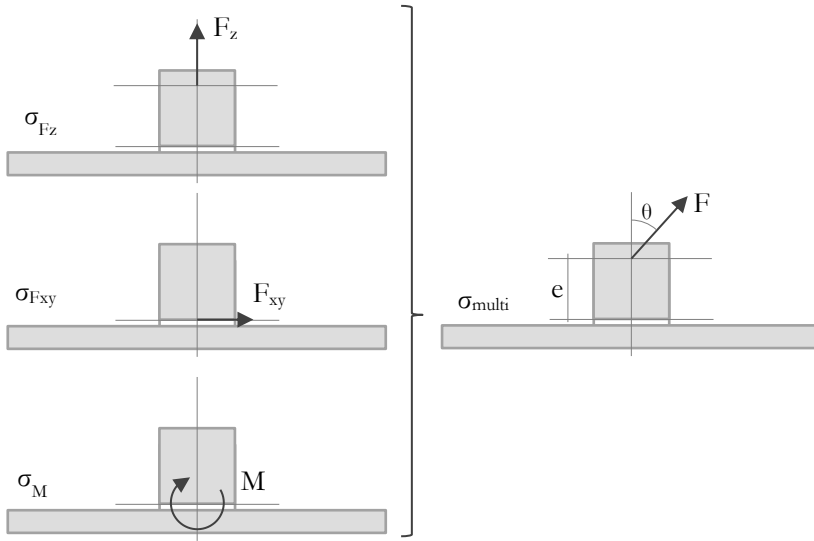$$\sigma_{F_z} + \sigma_{F_{xy}} + \sigma_M = \sigma_{multi} \tag{4.6}$$

The stress S22 is compared along the path y according to Figure 4.21 and Figure 4.31, as along this path the highest stresses occur. This comparison is performed for four configurations of the eccentricity and the multi-axil angle, i.e. E0-A0 (an eccentricity of 0 mm and an angle of 0°), E15-A22.5, E30-A45 and E45-A67.5 for the 2c-epoxy, as the epoxy gave the most complex stress distributions. These four comparisons are given in Figure 4.41. As expected, the stress from the multi-axial model corresponds very well with the superposition of the local stresses. This enables a thorough study of the stress components of the multi-axial model. In Figure 4.42 the different local components (tension, shear and moment) are given with the superposition of these components. As the superposition for E0-A0 only consists of the tensile component, this graph is not depicted. This superposition shows that the tensile force and bending moment induce the highest stresses in the glass panel. The magnitude of the latter will increase with an increase of the eccentricity and multi-axial angle, while the former decreases with an increase of the multi-axial angle. The shear component has a smaller influence on the stresses on the glass panel.
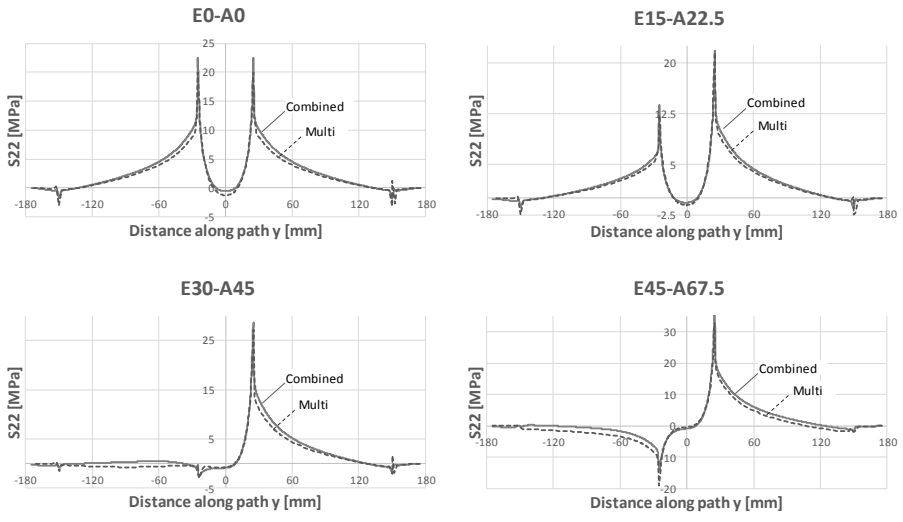
E0-A0

E15-A22.5

E30-A45

E45-A67.5

FIGURE 4.41: COMPARISON BETWEEN THE SUPERPOSITION OF THE LOCAL STRESSES (COMBINED) WITH THE STRESS FROM THE MULTI-AXIAL MODEL (MULTI).

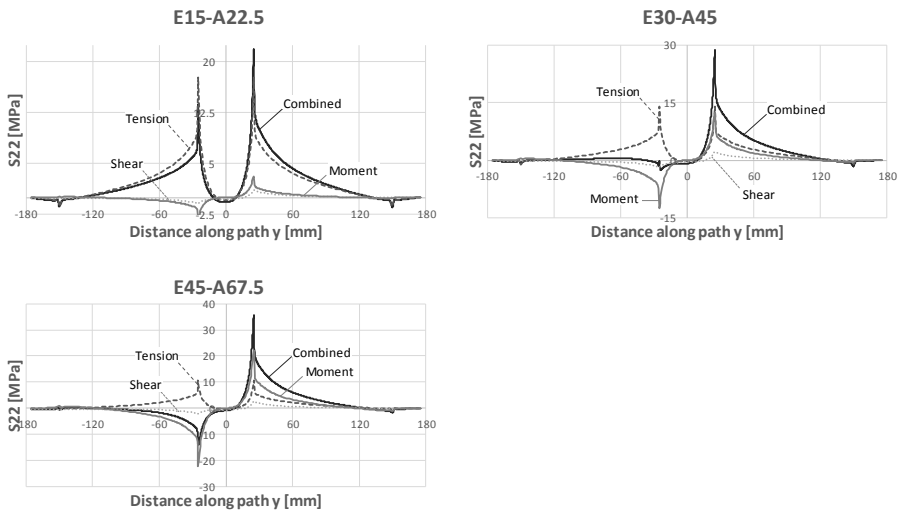## E15-A22.5

E30-A45

E45-A67.5

FIGURE 4.42: THE DIFFERENT LOCAL COMPONENTS OF THE SUPERPOSITION.

4.5.   Summary and conclusions

In this chapter, the mechanical behaviour of adhesive point-fixings under three different load configurations (uniaxial tension, uniaxial shear and multi-axial load) was investigated. The entire connection was studied by supporting the glass panel at a circumference equal to 6 times the diameter of the connection. To gain a total validated local model, the experiments were performed with three different diameters (30 mm, 50 mm and 70 mm), three different glass thicknesses (4 mm, 10 mm and 19 mm), three load eccentricities (0 mm, 15 mm and 25 mm), three multi-axial angles (22.5°, 45.0° and 67.5°) and two adhesive types (SO – 3M).

The experimental results were used to validate the numerical local models for the three load configurations. For the validation, the strains in the glass panel at three different distances from the centre were measured using strain gauges. The numerical results corresponded well with the experimental values. Based on the comparison between the numerical and experimental values for the strains and deformations, it can be concluded that the local FEA models are hereby validated.

For tension, it can be concluded from the experiments that the connector diameter is more determinative for more flexible adhesives and the glass thickness for rather stiff adhesives. The location of maximal strain was at the centre of glass panel for the configuration with the flexible adhesive and at the outside of the connector with the stiff adhesive. This was also observed by the location of the crack initiation when the specimens fail due to glass failure. For shear, the experiments demonstrated that the occurring strains are higher in case of a stiff adhesive and for a larger eccentricity. In the three load configurations, glass deformation under the connection was impeded by the adhesive connection for the stiff adhesive. The strains even become zero or smaller in the centre of the glass panel. With larger multi-axial angles, the shear component increase, increasing the bending moment acting on the glass panel. However, with increasing multi-axial angle the strains decrease as the connection is loaded in shear more than in tension. Shear forces will introduce lower strains in the glass panel than tensile forces.

The obtained FEA models were then used to study the influence of geometrical and material parameters more thoroughly, such as the connection's diameter, the glass thickness, the adhesive modulus of elasticity, etc. Furthermore, the multi-axial local model can be used to directly determine the sum of the local stresses.

Chapter 5: Global model

A little nonsense now and then,

is cherished by the wisest men.

Roald Dahl, Charlie and the Great Glass Elevator

5.1.   Introduction

The validation of the SLG-method will consists of a FEA comparison between the stress distributions obtained by on one hand by the SLG-method and on the other hand by a FEA model in which the total glass plate with the adhesive connections is built up in detail with volumetric elements. The stress distribution in the total model will be compared to the distribution obtained from the superposition of the local and global model. The local models were validated in previous chapter. The aim of this chapter is to validate the global model, indicated in Figure 5.1. As mentioned in Chapter 2, the distance of the connection to the edge or corner of the glass panel has a great influence on the mechanical behaviour of glass panels supported by bolted point-fixings.
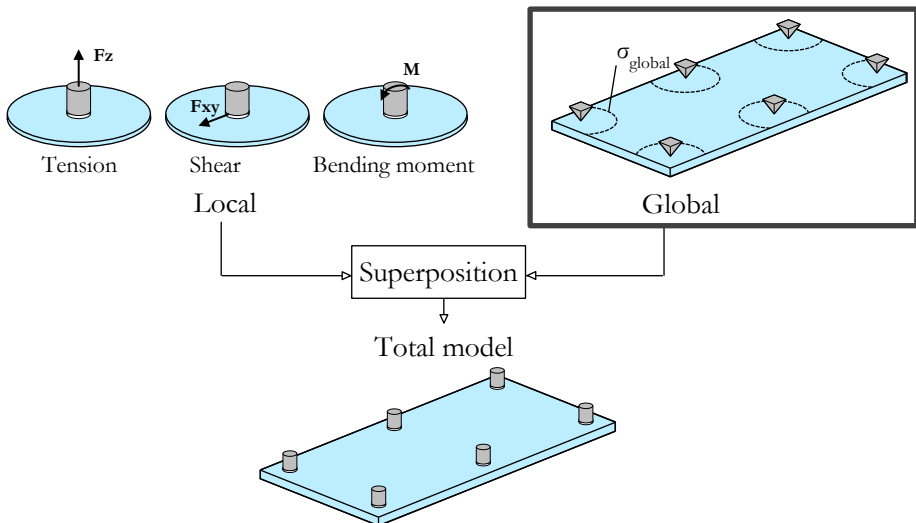

FIGURE 5.1: SLG-METHOD FOR ADHESIVE POINT-FIXINGS.

5.2.   Materials and methods

5.2.1. Test specimens and experimental setup

As described in Chapter 2, the global component is very generally modelled, implying that the connections are modelled as discrete pinned joints. From this FEA model the global stress is obtained at a distance from the point-fixings equal to three times the connection diameter. To validate the numerical global component, experiments were conducted. As depicted in Figure 1.1, point-fixings can be used for supporting glass facades or glass canopies. In the case of glass canopies, the supports will mostly be placed underneath the glass panel so the connection is generally loaded under pressure by the dead load of the glass panel. Mechanical self-weight supports are mostly described for structural sealant glazing systems (SSGS) according to the ETAG 002 (2002) as depicted in Type I, II and III in Figure 4.2. Hence, additional mechanical self-weight supports will be used for adhesive point-fixings loaded in constant shear, as e.g. is the case in vertical facades with SSGS. With these mechanical self-weight supports the adhesive connection will only be loaded by horizontal actions. These remarks considered, only compressive forces for the validation of the global model were considered.

The test specimen consisted of a full-scale glass panel of 1 m by 2 m with a nominal glass thickness of 10 mm supported by four discrete point-fixings. Point-fixings of only 10 mm diameter were made to resemble the discrete supports, as depicted in Figure 5.2. Since only compressive load is considered, a rubber (shore 70A hardness) was used between the steel connector and the glass panel, which highly improved the efficiency of the experiments. The use of a rubber results in an economic benefit because one full-scale panel could be used for different edge distances. The glass was annealed soda-lime silicate (float) glass with a Young's modulus of 70000 MPa and a Poisson's ratio of 0.23 (Outeiro et al. 2006; Haldimann et al. 2008).

FIGURE 5.2: DISCRETE POINT-FIXINGS WITH A DIAMETER OF 10 MM.

To obtain a complete validated numerical model, the experiments were conducted with five different edge distances, i.e. 35 mm, 105 mm, 175 mm and 245 mm. In literature and in real in-service bolted point-fixings, the edge distance is general between 60 mm and 150 mm (De Jaegher 2014). By also considering values smaller and larger, a larger range is obtained to investigate the influence of the edge distance. A modular test frame was produced. The applied uniform load was a uniform out-of-plane pressure, applied by 60 sand bags with a mass of 1.35 kg each, resulting in a total uniform load of 395 N/m². The loaded glass panel is depicted in Figure 5.3. The applied load is lower than the wind load that generally acts on glass panels, however, the load is still high enough for a validation. Using a numbered grid on the glass plate, the sand bags were always applied in the same sequence and positioning pattern.

FIGURE 5.3: LOADED TEST SETUP.

The setup enabled two different supporting conditions, i.e. a hinged and a fixed supporting condition. In detail, the hinged supporting condition was obtained by using a ball bearing between the support and the underlying frame as depicted in Figure 5.4a. For the fixed supporting system a bolt was used, as depicted in Figure 5.4b. As depicted in Figure 5.2, only the hinged connection was used in the experiments. Also visible in Figure 5.4 is the groove that made it possible to vary the edge distance between 0 and 250 mm. Since this groove is fabricated in a RHS profile, an extra reinforcement was applied by a block of steel which transferred the pressure load to the underlying foundation. The steel block also served as an anchor for the connection.
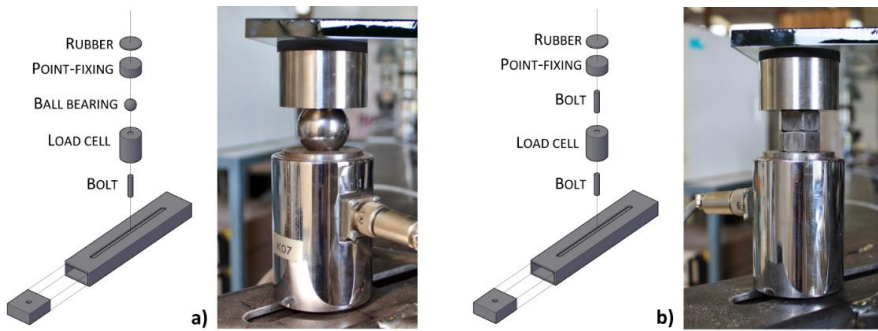

FIGURE 5.4: GRAPHICAL REPRESENTATION (LEFT) AND ACTUAL CONFIGURATION (RIGHT) OF A) THE HINGED CONNECTION BY MEANS OF A BALL BEARING AND B) THE FIXED CONNECTION BY MEANS OF A BOLT.

5.2.2. Test method

The numerical global model was validated by means of the occurring deflections and stresses in the glass panel. The deflection of the glass panel under the considered load was measured with five LVDTs. The deflection under de dead load of the glass panel was not measured. The stresses at the top surface of the glass panel were measured using 25 strain gauges forming four stress paths. The positions of the LVDTs and the four stress paths were determined with a preliminary FEA. The LVDTs are represented by small crossed circles in Figure 5.5 and the strain gauges by full grey rectangles.
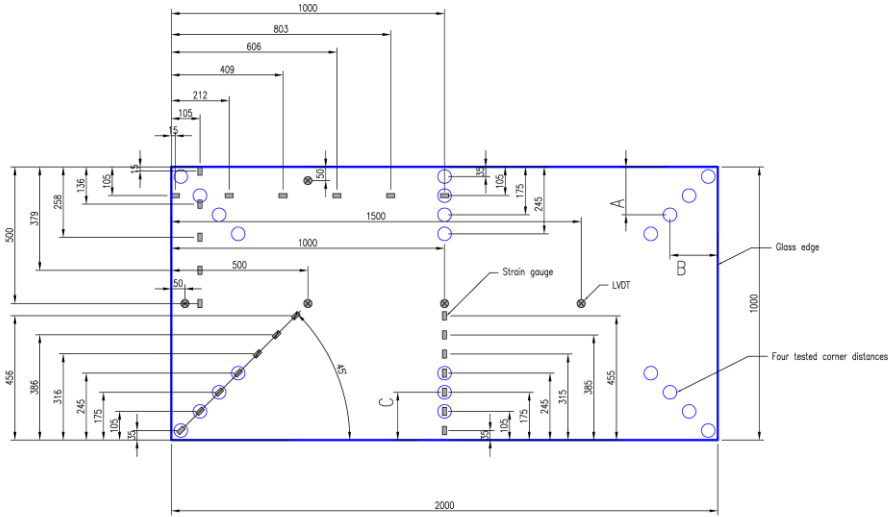
FIGURE 5.5: POSITIONS OF THE FIVE LVDT'S AND THE 25 STRAIN GAUGES (IN MM).

5.3.   Numerical model

The finite element software Abaqus® version 6.14 was used to build a finite element model. The geometry consists of a rectangular glass panel of 1 m by 2 m and a glass thickness of 10 mm. The load is applied for the uniform load configuration as a pressure load of 0.395 kN/m² acting on the glass surface.

As the connection can be pinned or clamped to the underlying structure, the point-fixing can be modelled in several ways, depending on the specific degrees of freedom, i.e. pinned or clamped. Both boundary conditions are depicted in Figure 5.6.
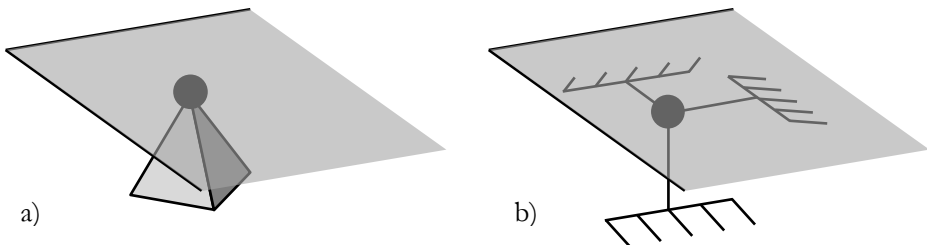

FIGURE 5.6: TWO BOUNDARY CONDITIONS TO MODEL THE POINT-FIXING IN THE GLOBAL COMPONENT: A) PINNED AND B) CLAMPED.

For the validation, a hinged discrete point was modelled. For this type of model, shell elements are an obvious option. Nevertheless, previous research has shown that shell elements in comparison with volumetric elements do not reduce the calculation time significantly and in some cases even increase the calculation time (De Jaegher 2014; Devos 2014; Tournoy 2014). Also shell elements did not give a good correspondence with the experimental values. Consequently, the element type C3D20R, a 20-nodes quadratic brick element with reduced integration, was used with three elements over the glass thickness. A mesh refinement was applied around the point-fixing, as depicted in Figure 5.7. After a convergence study it became clear that three elements are sufficient between the panel edge and the point-fixing. This is equal to the number of elements that also Beyer (2007) proposed in his design-method.
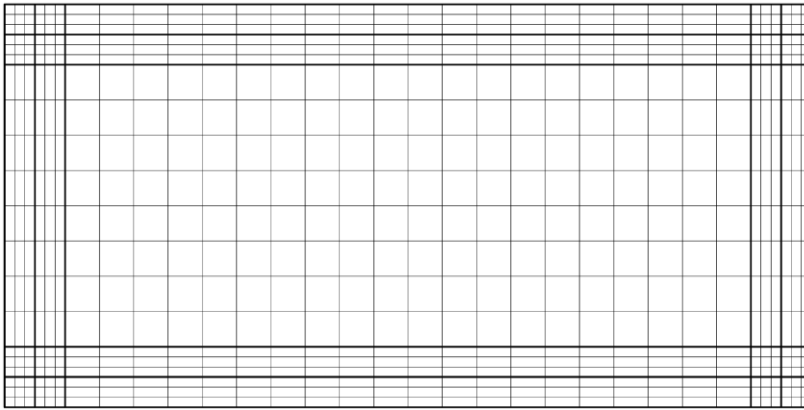
FIGURE 5.7: GRAPHICAL REPRESENTATION OF THE MESH REFINEMENT AROUND SUPPORTS.

5.4. Validation of the global model

As mentioned above, 25 strain gauges were used to measure the occurring strains on the top surface of the glass panel. From these measured strains the stresses can be calculated with Hooke's law. These calculated stresses form four stress paths, i.e. one along the long axis of the glass plate, two along the short axis and one at an angle of 45°. The positions of these stress paths with their names are depicted in Figure 5.8, the rectangles represent the strain gauges. Four displacement transducers also form one path along the long axis. This path and the remaining measuring point are also depicted in Figure 5.8, where the LVDTs are represented by crossed circles.
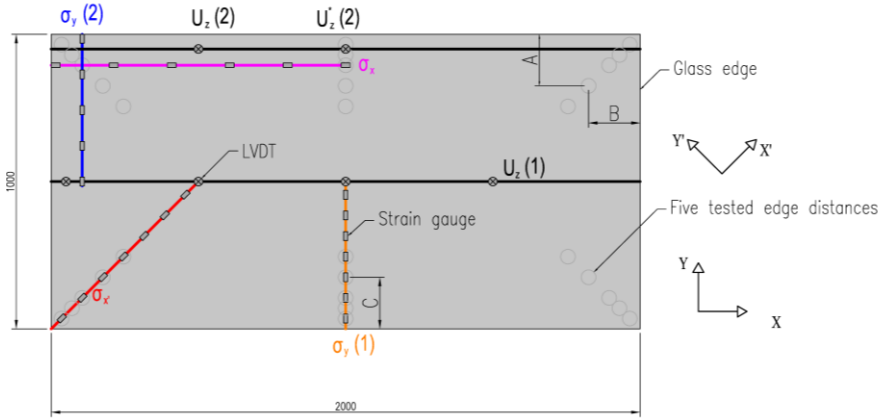
FIGURE 5.8: LOCATION OF THE FOUR STRESS PATHS OF THE STRAIN GAUGES (σ_x, $\sigma_{x'}$, σ_y (1) AND σ_y (2)) AND THE LVDTS (ALL DISTANCES ARE IN MM).

The obtained experimental results were used to validate the developed numerical model. The numerical stresses were obtained for the predefined four stress paths (Figure 5.8). All configurations that were tested were compared with the numerical model. In Figure 5.9 the comparison is made between the numerical and experimental results, with the four representing the stress paths and the lower two the deformation paths. The dots represent the experimentally measured stresses and deformations and the full line are the stresses and deformations from the finite element model. Furthermore, on the graphs the considered path is depicted in each graph. The legend for all graphs is given in Table 5.1.

Besides the high stress concentrations at the discrete points, the numerical stress values give a good correspondence with the experimental stress values. The values for the deformation from FEA are reasonably close to the experimental values. This demonstrates that the numerical global model is reliable and, hence, could be used as global model.

TABLE 5.1: LEGEND FOR THE COMPARISON GRAPHS FOR THE FULL SCALE NUMERICAL MODEL.

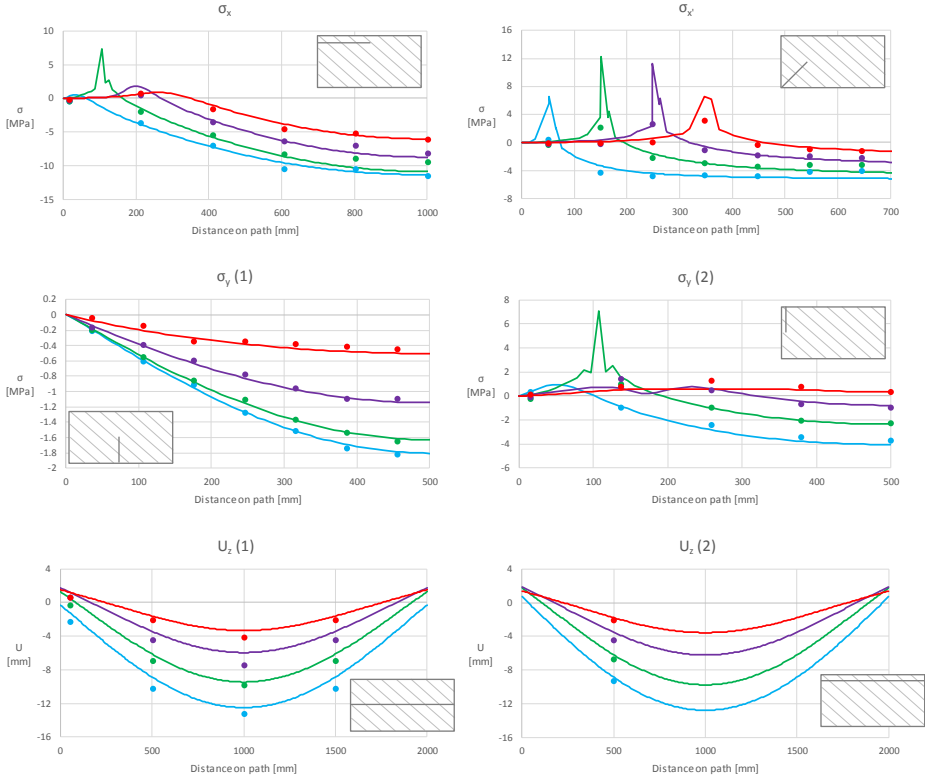| Edge distance [mm]	Numerical values	Experimental values
35	⎯⎯⎯⎯	●
105	⎯⎯⎯⎯	●
175	⎯⎯⎯⎯	●
245	⎯⎯⎯⎯	●

FIGURE 5.9: COMPARISON BETWEEN THE NUMERICAL AND EXPERIMENTAL VALUES ALONG THE FOUR STRESS PATHS AND TWO DISPLACEMENT PATHS FOR THE GLOBAL MODEL FOR FOUR EDGE DISTANCES.

5.5.   Summary and conclusions

In this chapter, the global model for the SLG-method was experimentally validated. A transversally loaded glass panel was experimentally investigated by means of a modular test frame for a glass panel of 1 m by 2 m supported by discrete point-fixings. The experimental results of four different edge distances were used to validate the numerical model. The numerical results corresponded very well with the experimental values. With a smaller corner and edge distance the field stress was more prominent. In contrast, the stresses were more uniform with larger distances.

Chapter 6: Total model

> If a cluttered desk is a sign of a cluttered mind,
> of what, then, is an empty desk a sign?
> *Albert Einstein*

6.1. Introduction

In this chapter, the aim is to develop a validated total numerical model of a full scale glass panel supported by adhesive point-fixings, i.e. the total model, as indicated in Figure 6.1. As mentioned in Chapter 2, together with the diameter of the connection, the distance of the connection to the edge or corner of the glass panel has a great influence on the mechanical behaviour of glass panels supported by bolted point-fixings. These parameters are expected to play a crucial role for adhesive point-fixings. However, for adhesive point-fixings the influence of the edge and corner distance and the connection diameter has not yet been extensively investigated. This chapter presents the results of an experimental study of the influence of these parameters on adhesive point-fixings together with a parametric study.
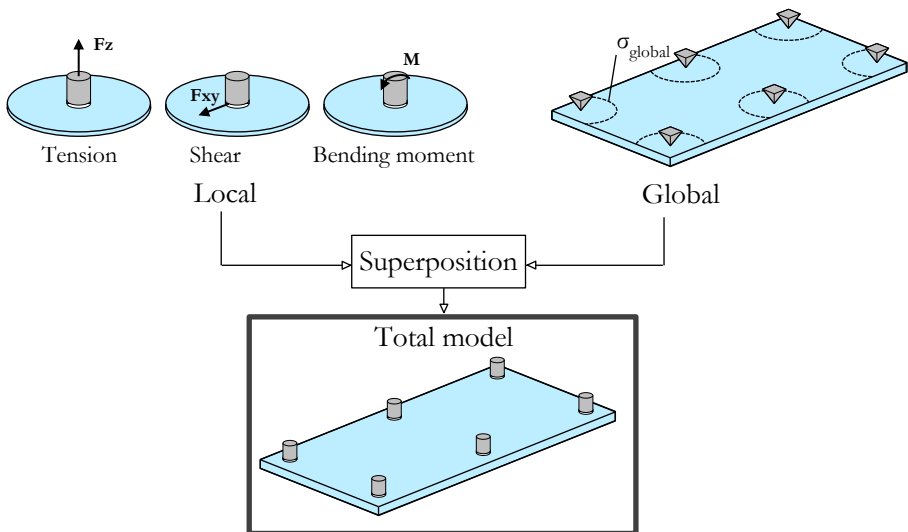

FIGURE 6.1: SLG-METHOD FOR ADHESIVE POINT-FIXINGS.

6.2. Materials and methods

6.2.1. Test specimens and experimental setup

Considering the remarks mentioned in previous chapter, only compressive forces for the validation of the total model were considered. Due to membrane forces, the adhesive connections were not only loaded in compression but also in shear, given a complex state of forces acting on the connections. Since only compressive load is considered, a rubber (shore 70A hardness) was used as a replacement of the adhesive, which highly improved the efficiency of the experiments. The use of a rubber results in an economic benefit because one full-scale panel could be used for different edge distances. The rubber acts the same as more flexible adhesives under pressure such as silicones and MS-polymers. The rubber was connected by a double-sided tape to the connector and the glass panel. The double-sided tape by Tesa® could be removed from the glass using an appropriate amount of peeling force. The double-sided tape has a thickness of 0.24 mm compared to a thickness of 5.64 mm for the rubber, this will ensure that the double-sided tape has a negligible influence on the mechanical behaviour of the glass panel and the connections. Furthermore, the short-term tests were performed at room temperature, hence no creep occurred due to its visco-elastic behaviour. For safety reasons, it is very likely that laminated glass (LG) will be used in real-world applications. However, a single float glass panel was used in the experiments, as it led to an easier and more economical test setup and reduced the variables. The interpretation of the results was also more straightforward because time and temperature would otherwise have an influence on the mechanical behaviour of the glass panel.

The same test specimen of Chapter 5 was used, i.e. a full-scale glass panel of 1 m by 2 m with a nominal glass thickness of 10 mm supported by adhesively connected point-fixings, by means of a rubber to a metal connector. For the metal connector a cylinder was made of stainless steel EN 10088-1 1.4404 (AISI 316L) and the glass was annealed soda-lime silicate (float) glass. The used material properties are listed in Table 6.1. The material properties of glass and stainless steel were derived from literature (Outeiro et al. 2006; Haldimann et al. 2008). Whereas the material properties of the rubber were obtained from small-scale compressive tests on the rubber discs used for the experiments.

Material	Young's modulus [MPa]	Poisson's ratio [-]
Glass	70 000	0.23
Stainless steel	195 000	0.30
Rubber	0.65	0.49

To obtain a complete validated total numerical model, the experiments were conducted with different geometrical parameters and load configurations, i.e. five edge distances, two load configurations, two load locations, two boundary conditions, three different diameters and two support configurations. From the 240 possible combinations, 68 combinations were experimentally performed for the validation. The values/configurations for the investigated parameters are listed in Table 6.2. In literature and in real in-service bolted point-fixings, the edge distance is general between 60 mm and 150 mm (De Jaegher 2014). By also considering values smaller and larger, a larger range is obtained to investigate the influence of the edge distance. The diameter of bolted point-fixings in literature and in real in-service facades is general between 45 and 65 mm (De Jaegher 2014). Also here, values are considered smaller and larger than 50 mm to obtain a larger range of the diameter.

TABLE 6.2: INVESTIGATED PARAMETERS WITH THEIR VALUES/CONFIGURATIONS

Edge distance	[mm]	35 – 70 – 105 – 175 – 245
Load type	[-]	Uniform – concentrated
Load location	[-]	Symmetrical – asymmetrical
Boundary conditions	[-]	Hinged – fixed
Diameter	[mm]	30 – 50 – 70
Support configuration	[-]	4 point-fixings – 6 point-fixings

The same modular test frame of Chapter 5 was used to examine the influence of the edge distance, i.e. a distance of 35 mm, 70 mm, 105 mm, 175 mm and 245 mm were tested. In Figure 6.2 a schematic overview and photograph of the test setup are depicted. In this figure three positioning plates are also visible; these were used to ensure that the glass panel was placed at the same position each time. The uniform load configuration for the symmetrical load location was the same as in Chapter 5, i.e. a total uniform load of 395 N/m². For the concentrated load configuration, a steel weight of 7.011 kg (68.78 N) was placed in the centre of the

glass plate. This weight was placed on a rubber with a measured thickness of 5.64 mm thickness and 70 mm diameter to avoid direct contact between the steel and the glass. For the two load types, two load positions were considered, i.e. symmetric and asymmetric load location. The symmetric load was achieved by placing the sand bags on the entire surface or the concentrated load in the centre of the glass panel. The asymmetric load was achieved by placing the sand bags on only one half of the glass surface or the concentrated load in the centre of the half of the glass panel. The four possible load types and load locations are depicted in Figure 6.3. As depicted in Figure 5.4, the setup enabled two different supporting conditions, i.e. a hinged and a fixed supporting condition. The depicted connector has a diameter of 50 mm and a height of 30 mm, the connector diameter was easily altered, i.e. 30 mm or 70 mm. As depicted in Figure 6.2, the modular frame was constructed for a maximum of six point-fixings. By removing the two inner supports a support configuration of four point-fixings was achieved. As in Chapter 5, the numerical total model was also validated by means of the occurring deflections and stresses in the glass panel, measured with five LVDTs and 25 strain gauges, respectively, as depicted in Figure 5.5.

FIGURE 6.2: GRAPHIC REPRESENTATION OF THE EXPERIMENTAL CONFIGURATION AND THE ACTUAL EXPERIMENTAL CONFIGURATION FOR SIX POINT-FIXINGS WITH A DIAMETER OF 50 MM.

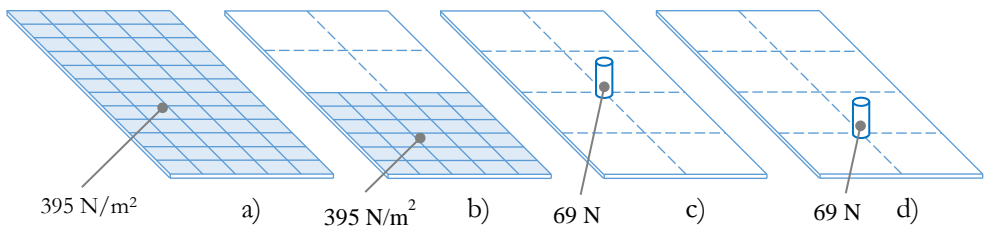395 N/m² a)   395 N/m² b)   69 N c)   69 N d)

FIGURE 6.3: THE FOUR POSSIBLE COMBINATIONS OF THE LOAD TYPE AND LOAD LOCATION; A) SYMMETRIC UNIFORM, B) ASYMMETRIC UNIFORM, C) SYMMETRIC CONCENTRATED LOAD AND D) ASYMMETRIC CONCENTRATED LOAD.

6.3.   Numerical model

The finite element software Abaqus® version 6.14 was used to build a three-dimensional finite element model and to numerically analyse the glass panel supported by point-fixings. The geometry consists of a rectangular glass panel of 1 m by 2 m and a thickness of 10 mm, adhesively connected by means of a rubber to a metal connector with a height of 30 mm. Due to double symmetry for the symmetrical load location only a quarter of the glass panel was modelled. For the asymmetrical load location only half of the plate was modelled. The displacement's constraints were modelled as close as possible to the real test conditions and the test setup geometry. In the numerical model, the rubber is connected by means of a tie-constraint to the glass and metal connector to simulate an adhesive connection. The load is applied for the uniform load configuration as a pressure load of 0.395 kN/m² and for the concentrated configuration as a pressure load of 17.872 kPa acting on a circular surface with a diameter of 70 mm.

Extra attention was paid to the location around the connector where refinement of the mesh pattern was introduced since stress concentrations were expected to occur here. To avoid mesh singularities in the centre of the circular connector a square mesh pattern was inserted inside the circular pattern. The mesh refinement around the connector and the square pattern are illustrated in Figure 6.4. The tie-constraint between glass-rubber and metal-rubber was modelled as a master-slave surface, with the rubber each time as the slave surface. A convergence study demonstrated that the best results are obtained when the mesh of the rubber is three times finer than the glass and steel mesh. This refinement also allowed to investigate the stresses that occur in the adhesive layer.
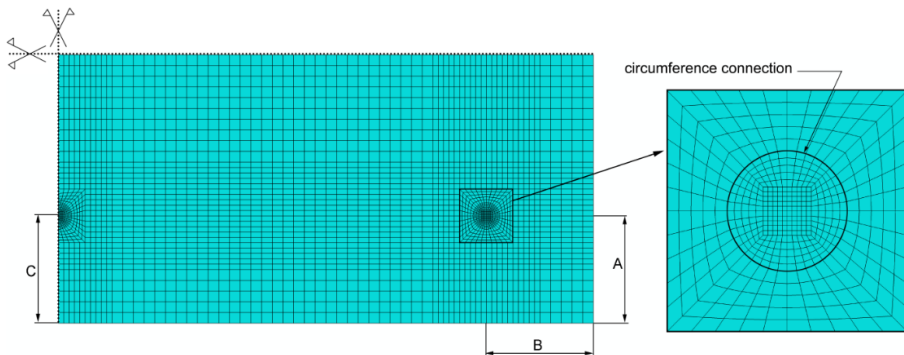

FIGURE 6.4: MESH PATTERN OF THE NUMERICAL MODEL WITH MESH REFINEMENT AROUND THE CONNECTORS FOR THE CONFIGURATION WITH SIX 50 MM. POINT-FIXINGS.

A convergence study was performed to determine which element type and element size gives the most accurate results with the lowest CPU-time. The convergence study yielded C3D20 elements for the glass panel and the connectors, and C3D8H for the rubber, which are depicted in Figure 6.5. C3D20 elements have the property of quadratic interpolation, which means there are 27 integration points. C3D8H elements have the property of linear interpolation, which means only 8 integration points are available. The more integration points, the more accurate, but the longer the calculation time for a same mesh patron. Due to the nearly incompressibility of the rubber, hybrid (H) formulation is used for the adhesive layer.
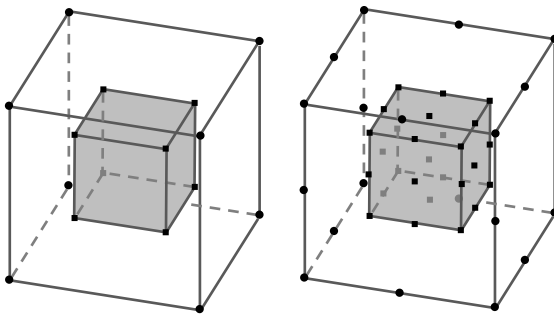
The element types and sizes are summarized in Table 6.3. The number of elements is the number of elements along the circumference of the connection. For a connector diameter of 50 mm, the element size in the centre of the connection is 5 mm for the glass and the steel and 1.67 mm for the rubber. This ensures that at least 3 elements are in the thickness of the rubber. The dimensions of an element along the edge and of an element in the centre of the adhesive layer is depicted in Figure 6.6. The maximum advised ratio of 1/2 has not been exceeded (ABAQUS 2014). General, static step-by-step numerical analyses are performed by means of the implicit Abaqus solver.

TABLE 6.3: ELEMENT SIZE AND TYPE FOR THE THREE MATERIALS.

Material	Element type	Number of elements
Glass	C3D20	16
Steel	C3D20	16
Rubber	C3D8H	48
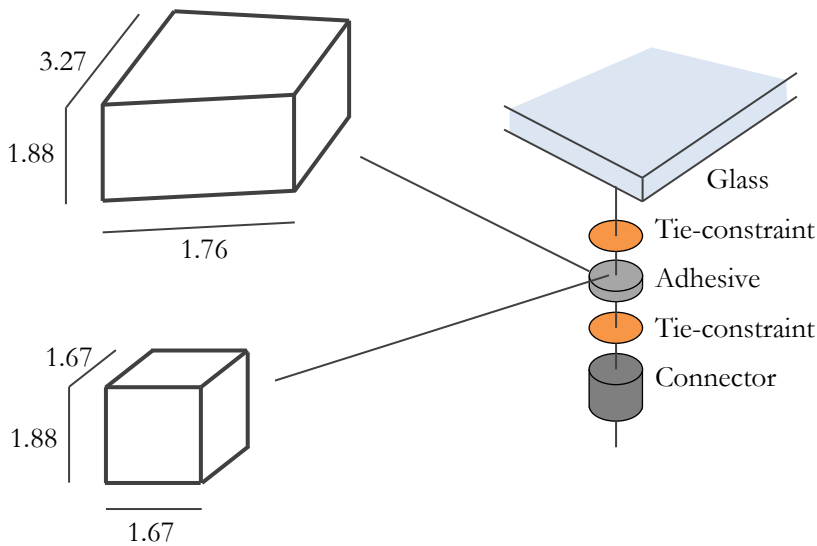
FIGURE 6.6: DIMENSIONS OF AN ELEMENT ALONG THE EDGE AND OF AN ELEMENT IN THE CENTRE OF THE ADHESIVE LAYER (ALL DIMENSIONS ARE IN MM.)

6.4.　　Validation of the total model

As mentioned above, 25 strain gauges were used to calculate the occurring stresses on the top surface of the glass panel. These calculated stresses form four stress paths and four LVDTs also form one path along the long axis. These paths are depicted in Figure 5.8 in Chapter 5, with the rectangles representing the strain gauges and the crossed circles the LVDTs. For certain configurations the displacement U_z (2) is measured on an alternative position instead, denoted as U_z* (2).

The numerical stresses were obtained for the predefined four stress paths. All 68 configurations that were tested were compared with the numerical model. A few selected comparisons are given in Figure 6.7 to Figure 6.9, with the four representing the stress paths and the lower two the deformation paths. The dots represent the experimentally measured stresses and deformations and the full line are the stresses and deformations from the finite element model. Furthermore, on the graphs the considered path is depicted in the upper right corner of each graph. The legend for all comparison graphs is clarified in Table 6.4. Other configurations are given in Appendix C.

TABLE 6.4: LEGEND FOR THE COMPARISON GRAPHS FOR THE FULL SCALE NUMERICAL MODEL

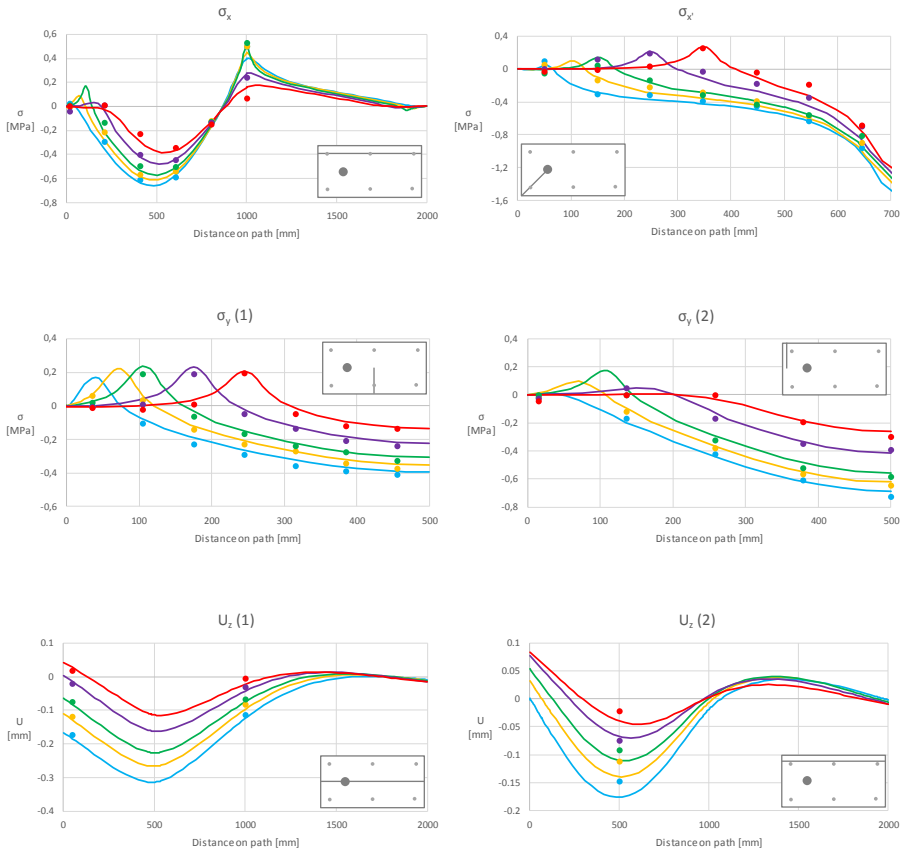| Edge distance [mm]	Numerical values	Experimental values
35		●
70		●
105		●
175		●
245		●

FIGURE 6.7: CONFIGURATION WITH ASYMMETRICAL CONCENTRATED LOAD AND SIX 50 MM FIXED POINT-FIXINGS.
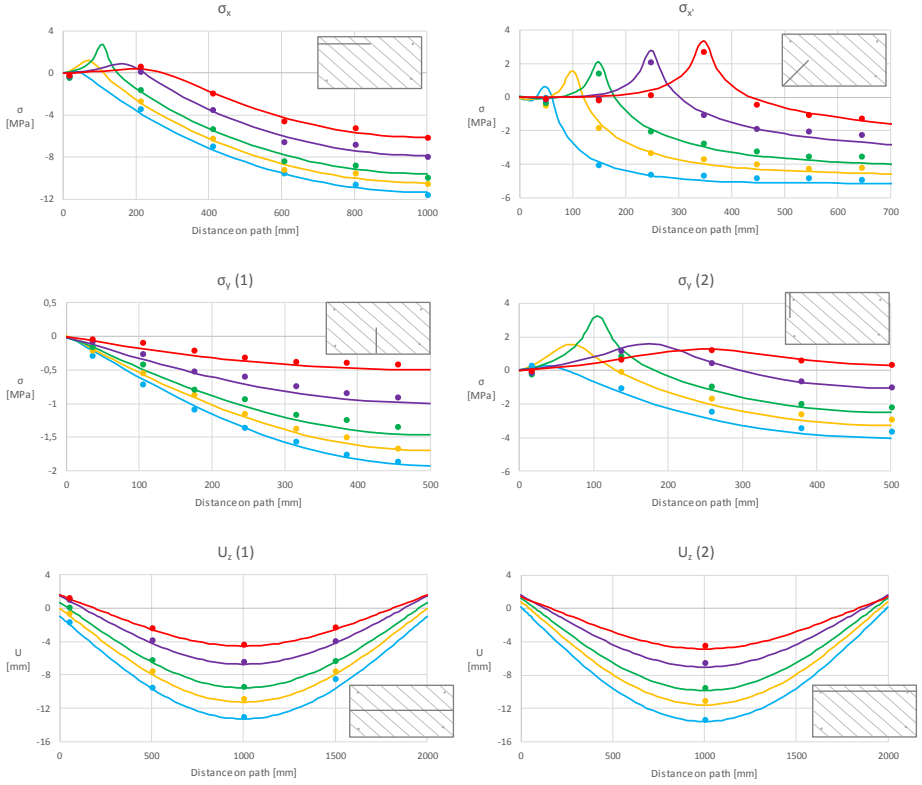
FIGURE 6.8: CONFIGURATION WITH SYMMETRICAL UNIFORM LOAD AND FOUR 30 MM FIXED POINT-FIXINGS.
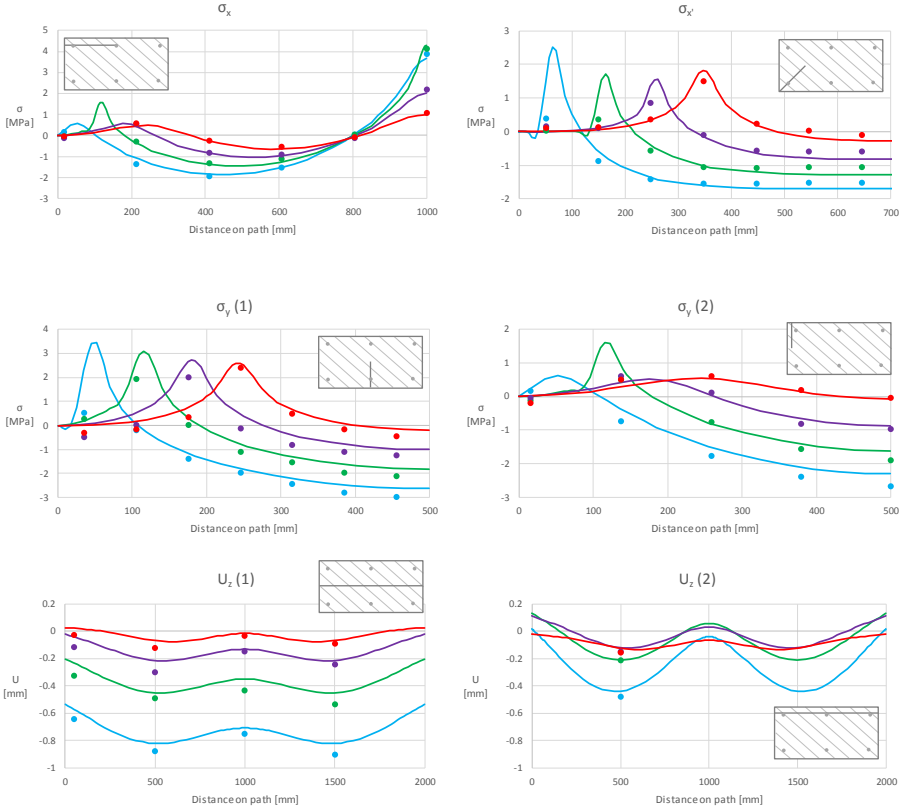
FIGURE 6.9: CONFIGURATION WITH SYMMETRICAL UNIFORM LOAD AND SIX 50 MM HINGED POINT-FIXINGS.

Despite a certain small difference between the experimental and numerical results, a good agreement between the numerical and experimental results is achieved. A potential cause for the small differences can be the limited number of strain gauges along a stress path. This is also visible in the graphs, where the numerical results demonstrate stress peaks which were not measured in the experimental values. However, due to the high number of measured values, i.e. 25 strain gauges and five LVDTs, no more DAQ channels were available and consequently measuring more points was not possible. The values for the deformation from FEA are reasonably close to the experimental values.

The good correspondence between the numerical and experimental values demonstrates that the numerical model is reliable and, hence, could be used to model glass panels supported by adhesive point-fixings with other geometric and material characteristics than used in the experiments. It also substantiates the assumption that a flexible adhesive under compression could be replaced by a rubber.

The highest stresses are obtained with a support configuration of four point-fixings, a symmetrical uniform load with a fixed boundary condition and a small edge distance and connector diameter, i.e. 35 mm and 30 mm, respectively. Logically, four point-fixings will introduce higher stresses than six point-fixings since each connection will receive higher loads with the former configuration. The symmetrical uniform load configuration is the configuration with the highest total load on the glass panel and hence will introduce the highest stresses. Higher stresses are reached with the fixed connection due to the more restricted boundary condition. Due to the fixed rotation of the fixed connection system, lower displacements are also observed with the fixed connection system than with the hinged connection system. The numerical results demonstrate stress peaks which were not visible in the experimental values, illustrating the benefit of FEA. With a smaller corner distance stress peaks will be more prominent. In contrast, the stresses will be more uniform with larger distances. A smaller diameter will support the glass panel over a smaller surface, resulting in higher stresses and deformations.

6.5.   Parametric study

The validated numerical model now enables to investigate more thoroughly the geometrical and material aspects of a glass panel supported by adhesive point-fixings. This paragraph describes the parametric study that was performed. Firstly the influence of the corner and edge distance was studied, defined as *A* and *B* for the corner distance and *C* for the edge distance as in Figure 6.4. Next, the diameter of the connection with the thickness of the glass, adhesive thickness together with the young's modulus of the adhesive and the width of the panel was investigated. Then the influence of the viscoelastic material parameters of laminated glass panels was investigated and finally a comparison between adhesive and bolted point-fixings is made. The investigated parameters and their values are summarized in Table 3.5.

TABLE 3.5: THE INVESTIGATED PARAMETERS AND THEIR VALUES.

Parameter	Symbol and unit		Values
Edge distance A	A	[mm]	35, 70, 105, 140, 175, 210, 245, 280, 315
Edge distance B	B	[mm]	35, 70, 105, 140, 175, 210, 245, 280, 315
Edge distance C	C	[mm]	35, 70, 105, 140, 175, 210, 245, 280, 315
Connector diameter	ϕ	[mm]	30, 50, 70
Glass thickness	t_{glass}	[mm]	4, 8, 10, 14, 19
Adhesive thickness	$t_{adhesive}$	[mm]	1, 2, 5
Adhesive Young's modulus	$E_{adhesive}$	[MPa]	10, 100, 1000, 10 000, 100 000
Adhesive Poisson's ratio	$\nu_{adhesive}$	[-]	0.47, 0.48, 0.49, 0.495, 0.499
Interlayer		[-]	SG – PVB
Load duration		[s]	1h – 1d

Corner and edge distance The maximal value for the maximal principal stress σ_1 on the glass panel was determined to investigate the influence of each parameter. Indeed, the maximal principal stress is typically used as a failure criterion for structural glass (Haldimann et al. 2008). Figure 6.10 illustrates the combinations that were studied with a glass panel of 2 m x 1 m x 10 mm, a connector diameter of 50 mm and a symmetrical uniform load of 397.3 Pa. In Figure 6.11 the maximum value of the maximal principal stress for every combination is illustrated. Each distance was first separately studied while the other distances were kept at 105 mm (Figure 6.11a). Secondly, the influence on each other was studied by keeping one distance constant at 105 mm (Figure 6.11b, c and d). The corner distance *B* had the largest influence on the maximal principal stress. In contrast, the corner distance *A* had the lowest influence. This is in good agreement with the findings of previous research (Klinkenberg et al. 1998). An optimal edge distance could be found between 175 mm and 245 mm while the other distance were kept constant at a distance of 105 mm. The maximal value of the maximal principal stress was located at the middle connections. However, the location changed to the corner connections when the corner or edge distance was larger than 280 mm.
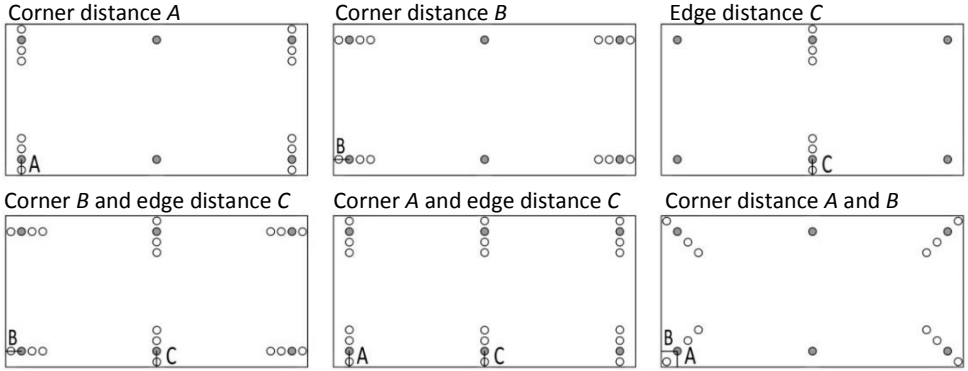
FIGURE 6.10: INDICATION OF THE INFLUENCE OF EACH INDIVIDUAL EDGE DISTANCE (TOP) AND TWO VARYING DISTANCES (BELOW).
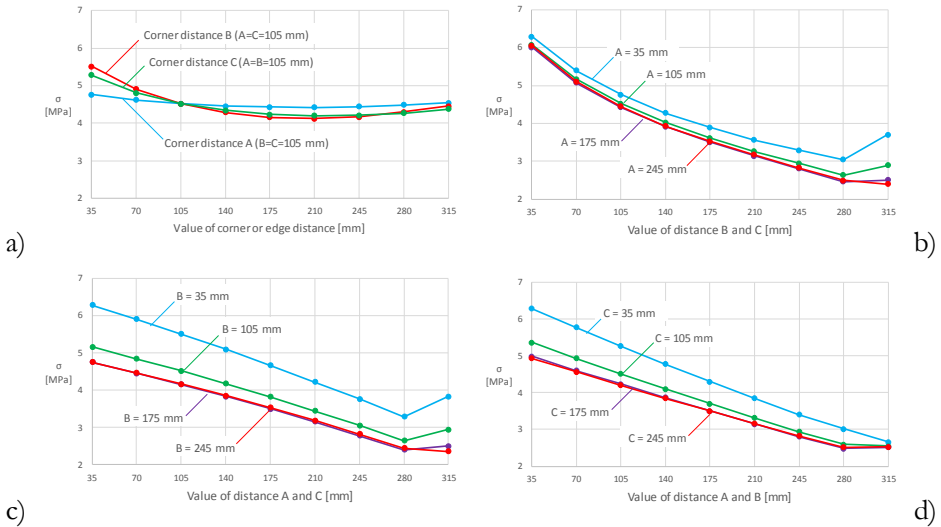

FIGURE 6.11: INFLUENCE OF THE EDGE AND CORNER DISTANCE ON THE MAXIMAL PRINCIPAL STRESS σ_1 FOR A) EACH DISTANCE, B) EQUAL DISTANCES FOR *B* AND *C*, C) EQUAL DISTANCES FOR *A* AND *C* AND D) EQUAL DISTANCES FOR *A* AND *B*.

The maximal deflection of the glass panel was also determined for the same combination as described above. The results for the maximal deflections are depicted in Figure 6.12. In Figure 6.12a, an increase of deflection occurred when the corner distance *B* was equal to 245 mm (*A* = *C* = 105 mm). The position of maximal deflection then changed from the centre of a half panel to the edge of the panel, as depicted in Figure 6.13. This is also visible in the other figures. Based on the maximal deformation, an optimal combination of two distances could be found when the third distance was fixed.
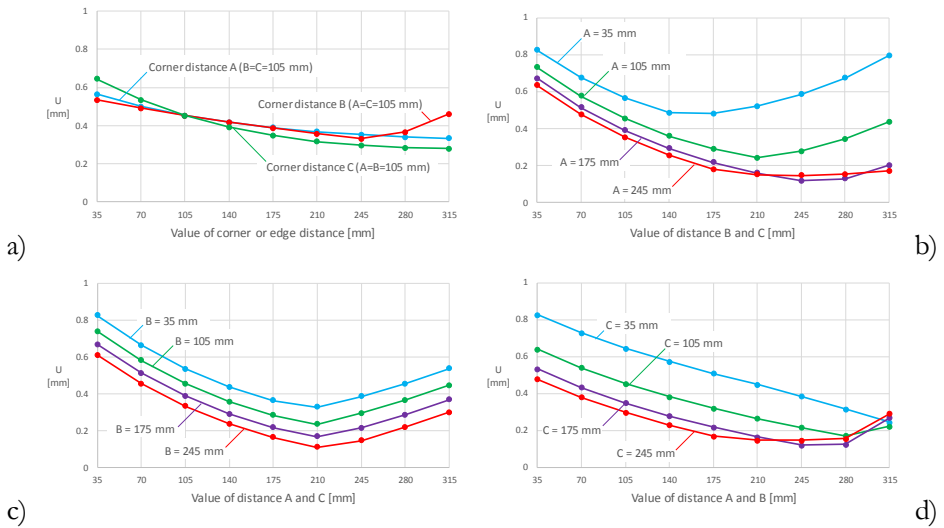
FIGURE 6.12: INFLUENCE OF THE EDGE AND CORNER DISTANCE ON THE MAXIMAL DEFORMATION FOR A) EACH DISTANCE, B) EQUAL DISTANCES FOR *B* AND *C*, C) EQUAL DISTANCES FOR *A* AND *C* AND D) EQUAL DISTANCES FOR *A* AND *B*.

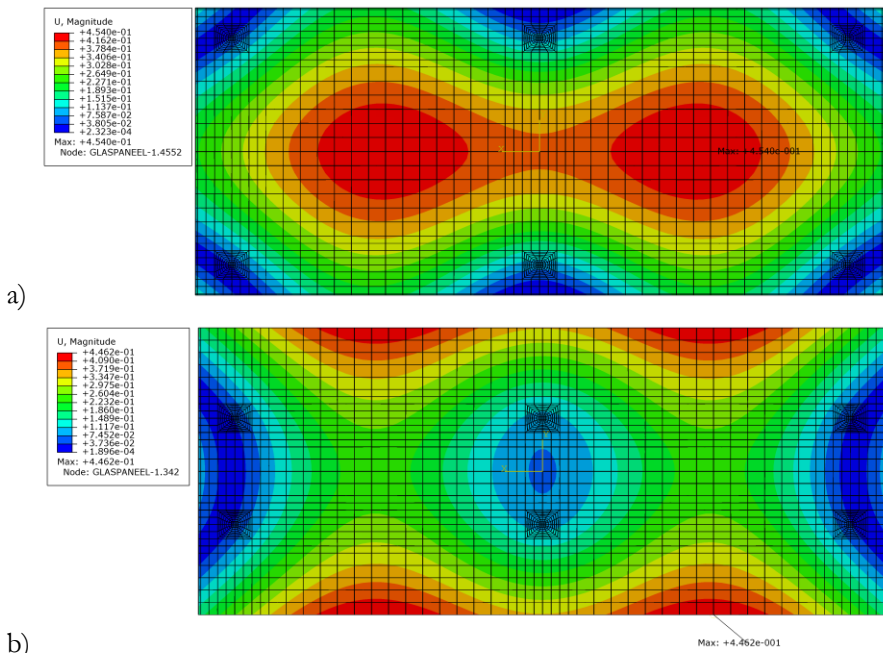**FIGURE 6.13**: CONTOUR PLOT OF THE DEFORMATION FOR CONFIGURATION WITH A) A = B = C = 105 MM AND B) A = C = 315 MM AND B = 105 MM.

Connection diameter and glass thickness The influence of the glass thickness of the connection was studied for values between 4 and 19 mm, the minimal and maximal thickness of structural glass used in buildings. The diameter varied between 30 and 70 mm. The corner and edge distances were fixed at a value of 105 mm. The maximal value of the maximal principal stress and deflection is depicted in Figure 6.14a and b. An increasing diameter had a positive effect on the stresses and the deflections. A larger diameter will support the glass panel over a larger surface, resulting in lower stresses and deformations. However, a larger diameter will have a less visual appearance. The increase in thickness of the glass will increase the moment of inertia of the glass panel. As expected, the increase of the rigidity of the panel will result in lower stresses and deformations.
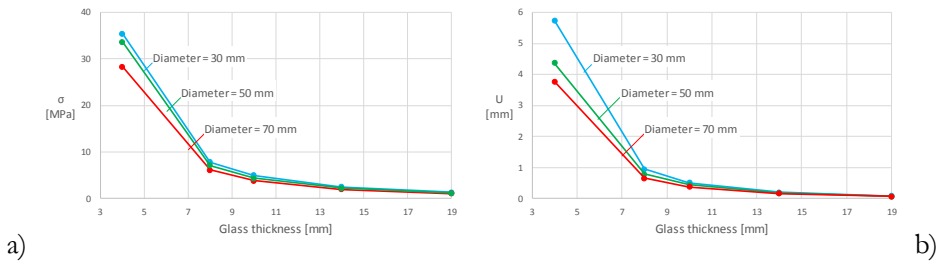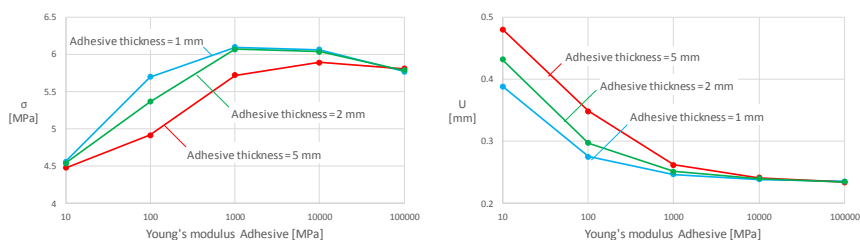

a)   b)

FIGURE 6.14: INFLUENCE OF THE GLASS THICKNESS AND THE CONNECTION DIAMETER FOR A) MAXIMAL OCCURRING MAXIMAL PRINCIPAL STRESS AND B) MAXIMAL OCCURRING DEFORMATION.

Adhesive thickness and Young's modulus Recent experimental research on local adhesive point-fixings has shown that the Young's modulus of the adhesive has a significant influence (Dispersyn et al. 2014). Relatively stiff adhesive will mostly be applied with a small thickness and relatively flexible adhesive with a larger thickness. The influences of these two parameters are illustrated in Figure 6.15a and b for the maximal value of the maximal principal stress and deflection. With increasing young's modulus of the adhesive, the maximum principal stress in the glass panel will rise (Figure 6.15a), and the maximum deflection will decrease (Figure 6.15b). This phenomenon was also visible with decreasing adhesive thickness. In contrast, thick and flexible adhesive layers will increase the deformation capacity of the glass panel but the stresses in the glass panel will reduce due to the higher mobility of the connection. In contrast to thinner and stiffer adhesive layers which locally strengthen the connection and thus restrict the movement of the connection and introduce higher stresses and smaller deflections.

FIGURE 6.15: INFLUENCE OF THE ADHESIVE YOUNG'S MODULUS AND THICKNESS FOR A) MAXIMAL OCCURRING MAXIMAL PRINCIPAL STRESS AND B) MAXIMAL OCCURRING DEFORMATION.

Width of the glass panel For the influence of the width of the glass panel, the length was kept constant at a value of 2 m. The maximal stress and deflection is depicted in Figure 6.16 for four different corner and edge distances. As expected, the stresses and deformation increased with an increase of the glass width. The location of the largest stresses moved also from the connection to the field for a width of 3000 mm since the span is significantly enlarged.
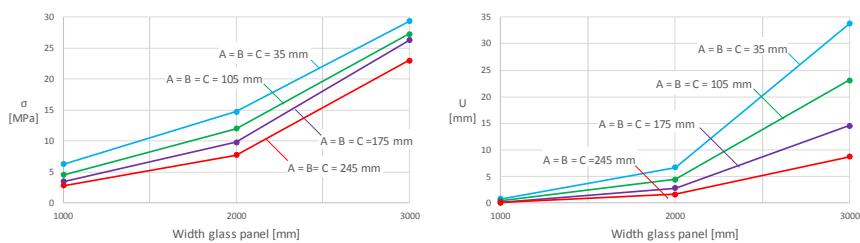
FIGURE 6.16: INFLUENCE OF THE WIDTH FOR A) MAXIMAL OCCURRING MAXIMAL PRINCIPAL STRESS AND B) MAXIMAL OCCURRING DEFORMATION.

Laminated glass Due to increasing safety demands, laminated glass is often required in construction. Because of this, the validated numerical model was modified to a laminated glass FEA model. Among the most used commercial polymeric films, polyvinyl butyral (PVB) and ionomers, e.g. Sentryglas® (SG), are the most commonly used. Ethylene vinyl acetate (EVA) is also commonly used, but its viscoelastic properties are similar to those of PVB (Galuppi & G. Royer-Carfagni 2012a) and therefore it was not considered here. The shear modulus of linear viscoelastic material can be modelled by a Prony's series, as given in Eq. (6.1). This series represents a relaxation model with multiple Maxwell elements, where G_0 represents the instantaneous shear modulus and the terms G_i and τ_i, are the relaxation shear moduli and the relaxation times of the i-th Maxwell element.

$$G(t) = G_0 - \sum_{i=1}^{N} G_i \left(1 - e^{-t/\tau_i}\right) \tag{6.1}$$

The considered material parameters for a temperature of 20°C are reported in Table 6.6 for PVB and SG (Belis 2006; Callewaert 2012; Galuppi & G. Royer-Carfagni 2012a; Bennison et al. 1999; D'Haene & Savineau 2007). These data are specific of a particular type of polymer, temperature and also for a specific range of strain rate, and may vary within the same category (PVB or SG). Therefore, these data should not be considered as universal values for design.

TABLE 6.6: ASSUMED TERMS OF THE PRONY'S SERIES FOR A PARTICULAR TYPE OF PVB (G_0 = 471 MPA) (BELIS 2006; BENNISON ET AL. 1999; GALUPPI & ROYER-CARFAGNI 2012A) AND FOR A PARTICULAR TYPE OF SG (G_0 = 150 MPA) (CALLEWAERT 2012).

Term index	G_i/G_0	τ_i [s]	Term index	G_i/G_0	τ_i [s]
1	0.1606000	3.256E-11	1	5.9320E-01	6.5173E-02
2	0.0787770	4.949E-09	2	1.1220E-01	9.6690E-01
3	0.2912000	7.243E-08	3	-5.1988E-03	8.2310E+01
4	0.0711550	9.864E-06	4	4.9333E-02	4.4630E+02
5	0.2688000	2.806E-03	5	2.0831E-02	5.6480E+03
6	0.0895860	1.644E-01	6	6.1392E-02	6.5132E+04
7	0.0301830	2.265E+00	7	4.3697E-02	5.0406E+05
8	0.0076056	3.536E+01	8	5.0251E-02	4.9084E+06
9	0.0009634	9.368E+03	9	2.9005E-02	3.3452E+07
10	0.0004059	6.414E+05	10	1.9283E-02	5.2363E+08
11	0.0006143	4.135E+07	11	7.3690E-03	7.7396E+09
			12	5.4495E-03	1.2613E+11

The mesh of the interlayer was chosen 5 times finer than the mesh of the glass, as the top and bottom surface were defined as a slave surface for the glass panels. The mesh of the adhesive, connector and both glass plates was the same as previously described. The thickness of the interlayer was set to 0.76 mm. The investigated configuration consisted of a glass panel with a symmetrical uniform load supported on four hinged point-fixings with a diameter of 50 mm and an

edge distance of 105 mm. Due to the viscoelastic behaviour of the interlayer, the load duration had an influence and was set to one hour and one day. The used mechanical behaviour was obtained for a temperature of 20°C. Figure 6.17 shows these two load durations for the two considered interlayers, i.e. SG-1h, SG-1d, PVB-1h and PVB-1d, for four glass thickness configurations, i.e. 4+4 mm, 6+6 mm, 8+8 mm and 10+10 mm. As expected, the highest stresses occurred in the glass panel with the thinnest glass thickness configuration, i.e. 4+4 mm. The influence of the interlayer type is also clearly distinguishable, with the more flexible interlayer PVB the stresses and deformation were higher than when using the more stiff interlayer SG. This is also visible in the load duration, the interlayers will behave more stiffly for shorter load durations. The stresses and deformations increased slightly for one day. As expected, the effect of interlayer type and load duration was smaller for thicker glass thickness configurations.
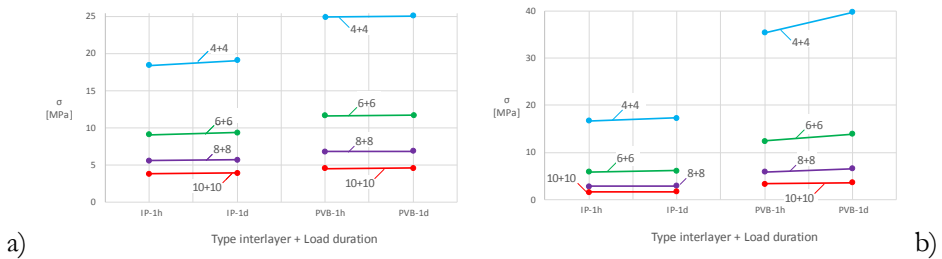

FIGURE 6.17: INFLUENCE OF INTERLAYER TYPE, LOAD DURATION AND GLASS THICKNESS CONFIGURATION ON A) THE MAXIMAL PRINCIPAL STRESS IN THE GLASS PANEL AND ON B) THE MAXIMAL DEFORMATION.

The influence of asymmetric glass thickness configurations is depicted in Figure 6.18, with each line representing a thickness of the upper panel. The investigated configuration is the same as above. For the interlayer only a load duration of 1 hour was taken into account. As excepted, stresses and deformations decreased with increasing top and bottom glass thicknesses. The larger the bottom panel thickness, the less the effect of increasing the top panel thickness and vice-versa. The highest stresses occurred in the bottom panel, giving more influence in increasing the bottom thickness than increasing the top thickness. For example, the configuration 4-6 mm (with 4 mm the thickness of the bottom panel and 6 mm the thickness of the upper panel) gave a maximal stress of 16.16 MPa and a maximal deformation of 19.19 mm, the configuration 6-4 mm gave 14.68 MPa and 18.4 mm. The stress and deformation can thus be limited by placing the thickest glass panel at the bottom, at the tension side of the panel.
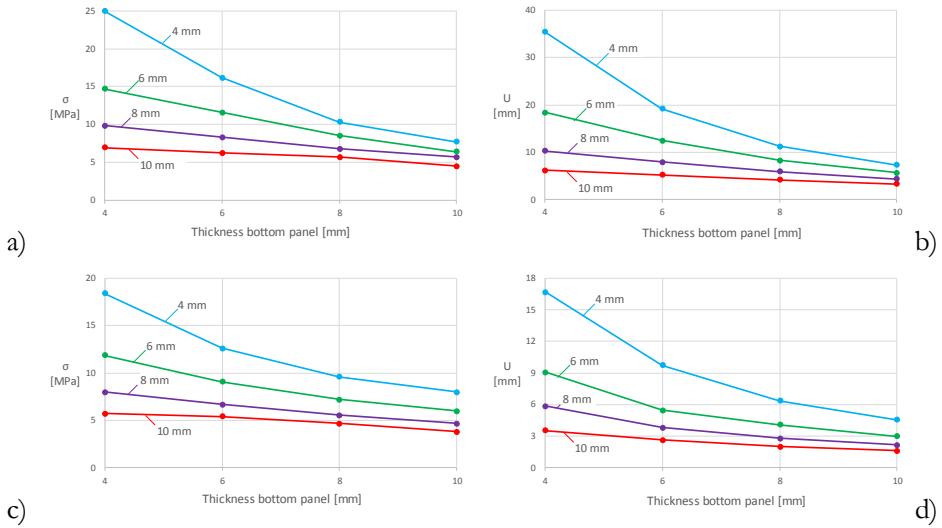
FIGURE 6.18: INFLUENCE OF ASYMMETRIC GLASS THICKNESS CONFIGURATIONS ON STRESSES AND DEFORMATIONS FOR A-B) A PVB INTERLAYER AND C-D) A SG INTERLAYER.

Note that it is possible to model the laminated panel as a monolithic panel with the same mechanical properties as the laminated panel by means of the effective thickness method. With this method the shear coupling between the panels through the polymer is taken into account. Several effective thickness methods exist (prEN 16612 2013; NEN 2608 2014; Callewaert 2012; Bennison et al. 2009; Galuppi & Royer-Carfagni 2012b; Galuppi & Royer-Carfagni 2012c). The effective thickness must be calculated separately for the determination of the occurring deformations and occurring stresses because their definitions are different. With the enhanced effective thickness (EET) method, developed by Galuppi & Royer-Carfagni (2012b), the effective thickness for the determination of the deformation, i.e. the deflection-effective thickness $\hat{h}_{eff,w}$, can be determined with Eq. (6.2). The effective thickness for the determination of the occurring stress in the i-th glass panel, i = 1,2, i.e. the stress-effective thickness $\hat{h}_{i,eff,\sigma}$, can be determined with Eq. (6.3) and (6.4).

$$\hat{h}_{eff,w} = \sqrt[3]{\dfrac{1}{\dfrac{\eta}{h_1^3 + h_2^3 + 12I_s} + \dfrac{1 - \eta}{h_1^3 + h_2^3}}} \tag{6.2}$$

$$\hat{h}_{1,eff,\sigma} = \sqrt{\frac{1}{\dfrac{2\eta h_{s,2}}{h_1^3 + h_2^3 + 12I_s} + \dfrac{h_1}{\hat{h}_{eff,w}^3}}} \tag{6.3}$$

$$\hat{h}_{2,eff,\sigma} = \sqrt{\frac{1}{\dfrac{2\eta h_{s,1}}{h_1^3 + h_2^3 + 12I_s} + \dfrac{h_2}{\hat{h}_{eff,w}^3}}} \tag{6.4}$$

With   - η the parameter as a non-dimensional quantity, tuning the behaviour from the

    layered limit ($\eta = 0$, i.e. shear modulus of the polymeric interlayer $G_{inter} \rightarrow$ 0) to   the monolithic limit ($\eta = 1$, i.e. $G_{inter} \rightarrow \infty$),

- h_i the thickness of the i-th glass panel,

- $I_s = \frac{h_1 \cdot h_2}{h_1 + h_2} \cdot H^2$,

- $H = \frac{h_1 + h_2}{2} + t_{inter}$ (with t_{inter} the thickness of the interlayer),

- $h_{s,i} = \frac{H \cdot h_i}{h_1 + h_2}$.

Bolted connection A comparison between a glass panel supported by adhesive point-fixings and bolted point-fixings was numerically investigated. There are several different geometries for bolted point-fixings. The geometry of the bolted point-fixing chosen in this numerical research is based on the work of Siebert (2007). Siebert mentions the advantages of using a raised head fixture instead of a countersink fixture. According to Siebert (2007) the raised head fixture has a better residual resistance than the countersink fixture. Therefore, the raised head fixture was used. The selected bolted point-fixing was a V2105 fixed bolt type of Sadev (2015), with the different components depicted in Figure 6.19a. The dimensions of the point fixing were obtained from the technical data-sheet provided by Sadev. The outer diameter is equal to 50 mm, and the diameter of the borehole in the glass is 28.8 mm, as depicted in Figure 6.19b. The material of the different components is given in Table 6.7, together with their Young's modulus E and Poisson's ratio ν. A fixed connection was considered by applying a fixed boundary condition on the threaded axle in Abaqus®. The length of the threaded axle was chosen so that that the fixed boundary condition for both bolted and adhesive point-fixing had the same coordinates.
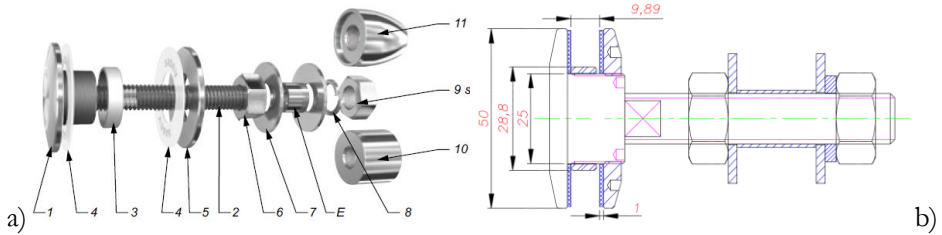
FIGURE 6.19: A) COMPONENTS OF A RAISED HEAD BOLTED POINT FIXING AND B) THE DIMENSIONS (SADEV 2015) (ALL DIMENSIONS ARE IN MM).

TABLE 6.7: DESIGNATION OF PARTS OF BOLTED POINT FIXING (SADEV 2015).

No.	Name	Material	E [MPa]	ν [-]
1	Body	Stainless steel (AISI 316L)	200 000	0.30
2	Threaded axle	Stainless steel (AISI 316L)	200 000	0.30
3	Bushing	Aluminium (AW-1050A)	70 000	0.33
4	Contact washer	Polyethylene	110	0.46
5	Glass nut	Stainless steel (AISI 316L)	200 000	0.30
6	Nut DIN 934	Stainless steel (AISI 316L)	200 000	0.30

A mesh study was performed on the model similarly to the mesh study in the case of the adhesive point-fixings. As high stress concentrations at the point-fixing were expected, a finer mesh was introduced near the point-fixing, as illustrated in Figure 6.20. Contact surfaces were defined between the glass and the bolted point-fixing. The convergence study showed that 80 elements along the circumference of the borehole gave the most adequate results in terms of correct stresses/deformations and calculation time. The investigated configuration consisted of a single glass panel of 10 mm thickness with a symmetrical uniform load supported on four bolted point-fixings for the five considered edge distances in Table 6.2.
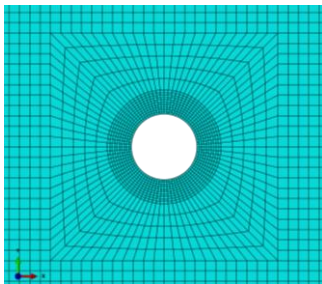

FIGURE 6.20: DENSER MESHPATERN AROUND BOLT HOLE.

The numerical results of the bolted point-fixing were compared with adhesive point-fixings for four paths: σ_x, $\sigma_{x'}$, U_z (1) and U_z (2). The diameter of the adhesive point-fixings is set equal to the outer diameter of the bolted point-fixings, i.e. 50 mm. The comparison is depicted in Figure 6.21 with the legend for the graphs given in Table 6.8. The peak stresses were much higher for bolted point-fixings than for adhesive point-fixings (a factor 20 for edge distance 35 mm). The stresses in the centre of the plate were lower for bolted than for adhesive point-fixings. Due to the more restricted boundary condition with bolted point-fixings, the displacements are lower for the latter (a factor 4 for edge distance 245 mm). The high stress concentrations in the glass panel with bolted point-fixings and the absence of these with adhesive point-fixings substantiates the advantages of adhesive point-fixings over bolted point-fixings.

TABLE 6.8: LEGEND FOR THE COMPARISON GRAPHS FOR THE FULL SCALE NUMERICAL MODEL.

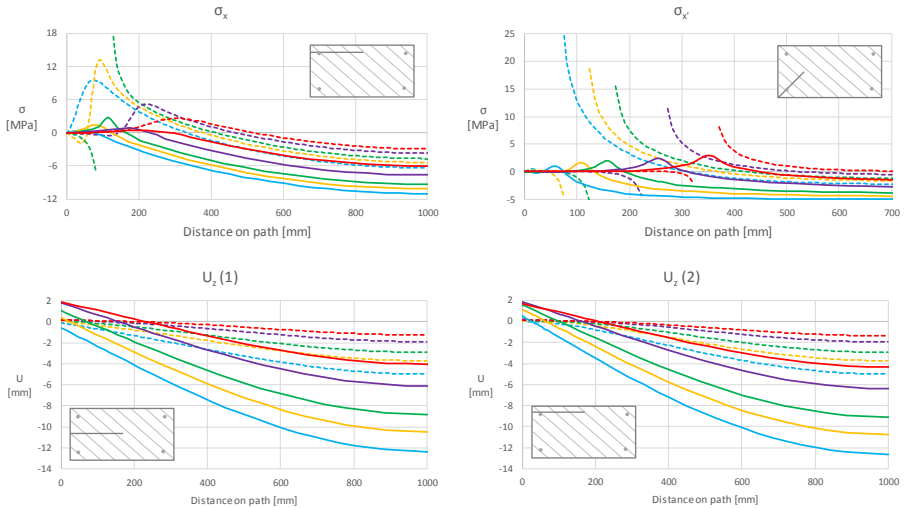| Edge distance [mm]	Adhesive point-fixings	Bolted point-fixings
35		
70		
105		
175		
245		

FIGURE 6.21: COMPARISON OF STRESSES AND DEFORMATIONS FOR PATHS σ_x, $\sigma_{x'}$, U_z (1) AND U_z (2) BETWEEN GLASS SUPPORTED BY ADHESIVE AND BOLTED POINT-FIXINGS.

6.6.　　　Summary and conclusions

In this chapter, the total model for the SLG-method was experimentally validated. A transversally loaded glass panel was experimentally investigated by means of a modular test frame for a glass panel of 1 m by 2 m supported by adhesive point-fixings. The experimental results demonstrated that the highest stresses were reached with the smallest edge distances. This was also shown in the research in the steel area (Rex et al. 2003; Duerr & Asce 2006) and the research on bolted point-fixings (Klinkenberg et al. 1998; Overend 2005; Maniatis 2006a; Maniatis 2006b; Nielsen et al. 2009; Amadio et al. 2008; Overend et al. 2013). With a small edge distance the stresses in the field were much higher compared to a larger edge distance, where the field stresses were more uniform. However, stress peaks occurred at the connection. As expected the deformations were significantly larger with small edge distances compared to higher edge distances. The highest deformation occurred in the centre of a half panel. The rigidity of the connection was also investigated. It was demonstrated that higher glass stresses were reached with a fixed connection compared to a hinged connection.

The experimental results of 68 combinations were used to validate a numerical model. The numerical results corresponded very well with the experimental values. However, the numerical analyses yielded stress peaks which were not visible in the experiments. This highlights the benefits and necessity of numerical investigation. With a smaller corner and edge distance stress peaks were more prominent. In contrast, the stresses were more uniform with larger distances. The difference between the fixed and hinged connection system was also clear: the fixed system introduced larger stresses in the glass panel. In contrast, the deformation was smaller with the fixed system. As also the experiments showed, varying the corner and edge distance had a greater influence on the stress distribution with fixed connections than with hinged connections.

The validated numerical model was used to investigate the geometrical and material aspects more thoroughly. The results from this parametric study pointed out that the maximal occurring stresses will increase with a decrease of the glass thickness, the diameter of the connection, adhesive thickness and with an increase of the adhesive stiffness and width of the glass panel. Furthermore, the maximal deformation of the glass panel could be reduced by increasing the glass thickness, the connection diameter, adhesive stiffness and by decreasing the adhesive thickness and width of the glass panel.

The behaviour of laminated glass panels depends on the stiffness of the interlayer, the load duration and the glass thickness. Increasing the load duration corresponds to a decrease in interlayer stiffness. Increasing the interlayer stiffness and glass thickness will decrease the maximal principal stress and the maximal deformation. Compared to adhesive point-fixings, bolted point-fixings give higher peak stresses at the connection, but lower stresses and deformation at the centre of the plate.

Chapter 7: SLG-method

> Look up at the stars and not down at your feet.
>
> Try to make sense of what you see,
>
> and wonder about what makes the universe exist.
>
> Be curious.
>
> *Stephen Hawking*

7.1.   Introduction

The suitability of the SLG-method for adhesive point-fixings will be discussed in detail in this chapter. The validation of the SLG-method for adhesive point-fixings will consist of a FEA comparison between the stress distributions conducted by the SLG-method on the one hand, i.e. the superposition of a global and local components, and on the other hand by the total component. The latter is already described and validated in Chapter 6, the local components in Chapter 4 and the global component in Chapter 5. The aim of this chapter is to validate the superposition, as indicated in Figure 7.1.
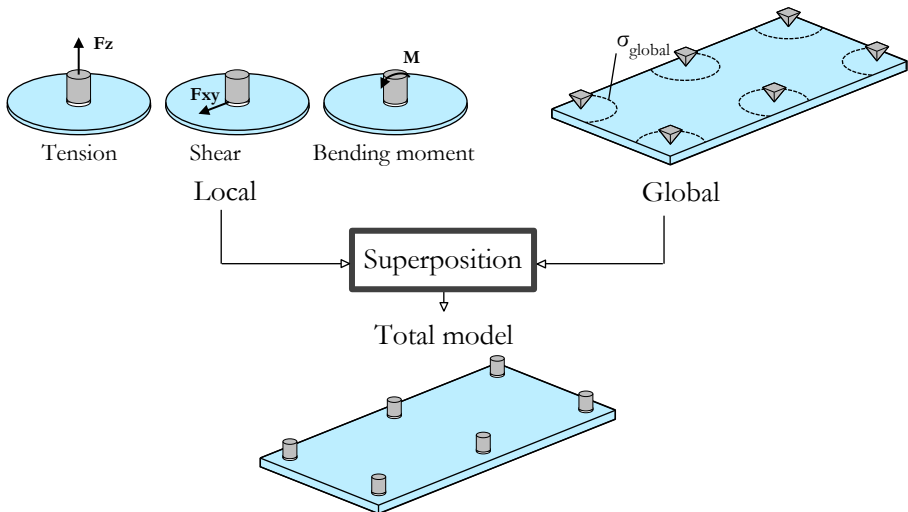

FIGURE 7.1: SLG-METHOD FOR ADHESIVE POINT-FIXINGS.

7.2.   Combined component

Based on the principle of Saint-Venant, Beyer (2007) assumed that changing geometrical characteristics of the point-fixing will only have an influence on the stress distribution in a local region around the joints, while the influences decrease further away from the connection. This principle allows the separation of the entirety from the connections (the global component), and the connections from the entirety (the local component). From the global model the stresses at the boundary between the global and local component are determined, which is referred to as the global stress σ_{global}. Furthermore, from the global model the support reactions of the point fittings (F_z, F_{xy}, M) are determined. The glass plate around the borehole and the connection are modelled in detail representing the local component. By applying the reaction forces and moments on the connection derived from the global component, the reaction stresses σ_{Fz}, σ_{Fxy} and σ_M are determined. The sum of these stresses and the global stresses multiplied with a stress concentration factor k must be less than the critical stress σ_R according to Eq. (7.1). The stress concentration factor is derived from FEA, in which a plate with the exact borehole geometry is modelled and subjected to bending.

$$\sigma_{F_z} + \sigma_{F_{xy}} + \sigma_M + k \cdot \sigma_{global} \leq \sigma_R \tag{7.1}$$

The purpose of this chapter is to reconstruct the total stress distribution based on the stress distributions of the global and the local component. Due to the absence of a borehole, the stress concentration factor k will be equal to unity. The validation of the SLG-method for adhesive point-fixings will be performed as given in Eq. (7.2).

$$\sigma_{total} = \sigma_{global} + \sigma_{F_z} + \sigma_{F_{xy}} + \sigma_M \tag{7.2}$$

7.3.1. Glass stress distribution at the rear side

The considered configuration consisted of a glass panel of 2 m by 1 m and a glass thickness of 10 mm. The panel is considered to be connected vertically as a facade element. The applied forces were the dead weight of the panel as a shear load and a wind load of 2 kPa as a surface load. The wind load was first applied as wind suction, causing the connection to be loaded in tension, the most severe condition.

The diameter of the adhesive connection was 50 mm and 3M as the adhesive type. Four edge distances were considered, i.e. 35 mm, 105 mm, 175 mm and 245 mm, with two different boundary conditions, i.e. hinged and fixed. Also two different number of point-fixings were tested, i.e. four and six point-fixings. The configuration is depicted in Figure 7.2. Also in Figure 7.2, the path on the rear side of the panel is depicted along which the stress S22 was derived for the validation. This path goes through the point-fixings, so the position of the path depends on the edge distance. The point-fixings along the path are numbered for an easy reference. The configuration with six pinned point-fixings and an edge distance of 245 mm will be explained as an example.
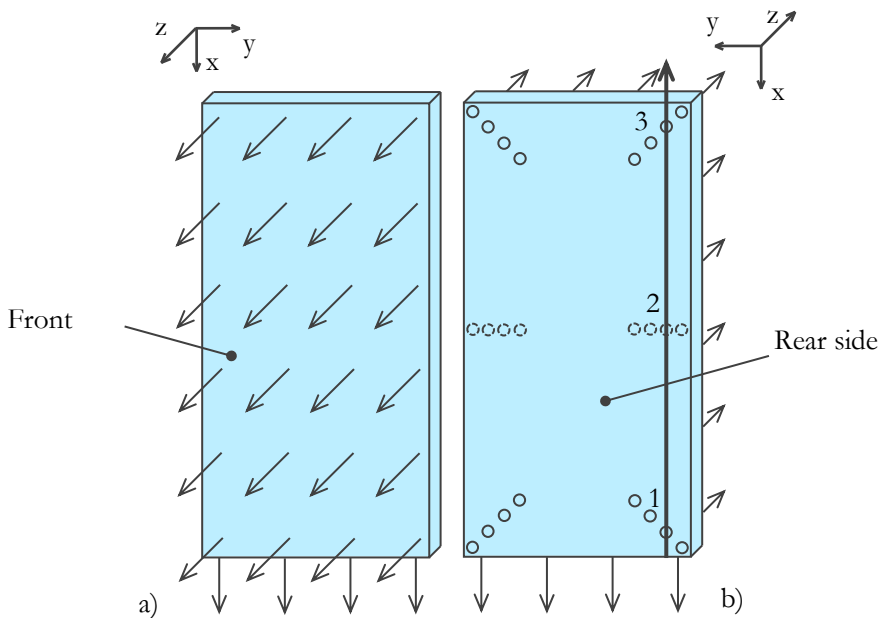
FIGURE 7.2: SLG VALIDATION CONFIGURATION FOR WIND SUCTION AT A) THE FRONT OF THE GLASS PANEL AND THE PATH AT B) THE REAR SIDE OF THE GLASS PANEL.

Note that the depicted configuration in Figure 7.2 does not correspond with real-life applications, as on all connections shear forces will be applied. This is not the case in real-life applications, where only the top connections will take up vertical shear forces. For bolted point-fixings, the connections at the bottom of the glass panel will be slotted or oversized to allow in-plane deformation of the glass panel. This is to avoid thermal stresses in the glass panel; as the panel will expand with increasing temperature, deformation is allowed by the oversized connections. This

principle is depicted in Figure 7.3 and in Figure 7.4 for a spider connection. For flexible adhesives this configuration is unnecessary as the deformation of the adhesive can take up the thermal deformation of the glass. For stiff adhesives, the principle of oversized connections will have to be implemented. The investigated configuration in this dissertation does not take this into account, however, the aim of the investigation is to compare two stress distributions to validate the SLG-method rather than to determine the stress distribution itself.
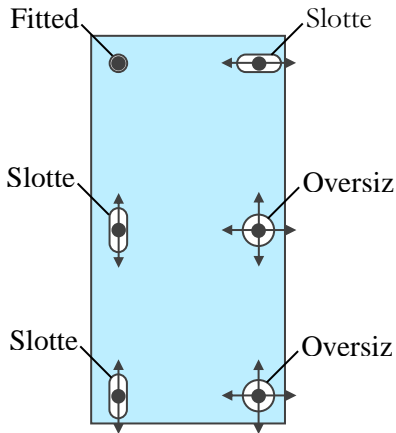
FIGURE 7.3: SLOTTED AND OVERSIZED CONNECTIONS TO AVOID THERMAL STRESSES. CONNECTIONS ARE OVERDIMENSIONED DEPICTED.
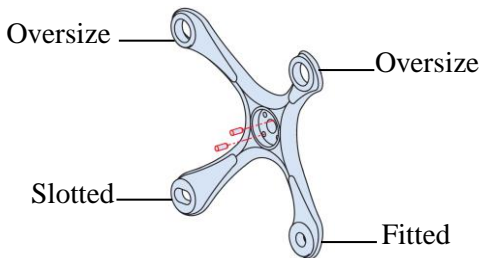
FIGURE 7.4: OVERSIZED CONNECTION HOLES IN A SPIDER (SADEV 2015)

In Figure 7.5 the S22 stress distribution is depicted for the **total** model from Chapter 6. As mentioned before, this total model is modelled with the glass panel and the connections in detail. The local zones where the global model is deemed not reliable, are defined as the circular area around the connector with a diameter equal to six times the diameter of the connection. With a connection diameter of 50 mm, the local area diameter was 300 mm. These local zones are depicted in Figure 7.5 in grey and marked by dotted lines.
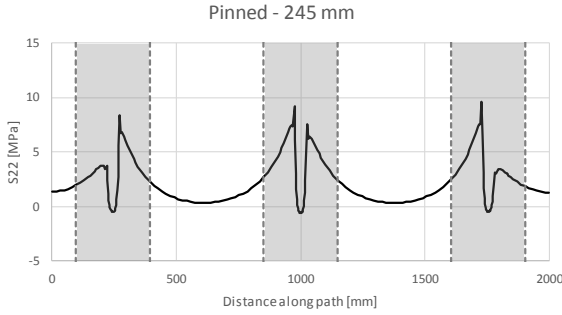
FIGURE 7.5: STRESS S22 DISTRIBUTION OF THE **TOTAL** MODEL.

The **global** stress S22 distribution from Chapter 5 along the path is depicted in Figure 7.6. Indeed, at the connections the global stress distribution is different from the total stress distribution. At the intersection of the global stresses and the local area, the global stresses σ_{global} are derived; they are equal to 2.53 MPa, 3.06 MPa and 2.14 MPa for point-fixing 1, 2 and 3, respectively.
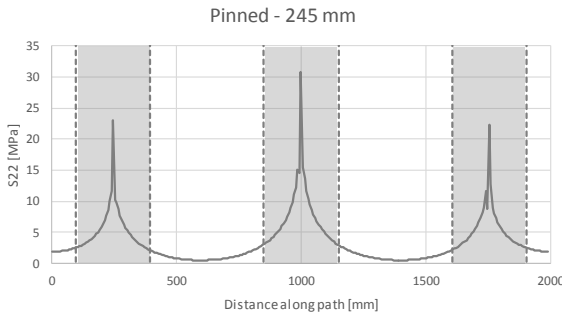

FIGURE 7.6: STRESS S22 DISTRIBUTION OF THE **GLOBAL** MODEL.

The reaction forces and reaction moments for each point-fixing are derived from this global model and are given in Table 7.1. Due to the hinged configuration, no reaction moments were registered at the support. The influence of the applied shear load can be seen by the difference in magnitude between point-fixing 1 and 3. Point-fixing 1 will take more shear load and as the shear force is opposite to the membrane force, the total load and stress will be lower for point-fixing 1. As in the total model, the connection has a height of 30 mm, these membrane forces will introduce a bending moment due to the leverage.

R_x (Shear)		R_y (Shear)		R_z (Tension)	
1	468.04 N	1	-357.92 N	1	-589.14 N
2	-83.96 N	2	-365.81 N	2	-819.79 N
3	-634.03 N	3	-352.83 N	3	-590.93 N

The reaction forces are applied on the local models from Chapter 4 and the local stresses S22 are derived. As depicted in Figure 7.7 for point-fixing 1, the acting shear loads, F_x and F_y, will introduce a bending moment due the eccentricity. The latter is equal to the height of the connector, i.e. 30 mm. Hence, the shear loads can be separated in pure shear components, F_x and F_y, and bending moment components, M_x and M_y. The **local** stresses from the five acting forces and bending moments on point-fixing 1 are depicted in Figure 7.8. The tensile force will introduce the largest stresses in the glass panel. The local stresses from the forces and bending moments perpendicular on the stress path, F_y and M_y, are small compared to the forces and bending moments parallel to the stress path, F_x and M_x. From the latter, the bending moment M_x will introduce higher stresses than the shear force F_x.
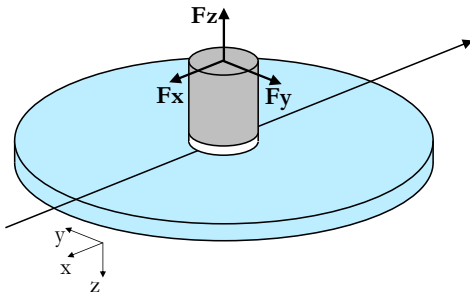

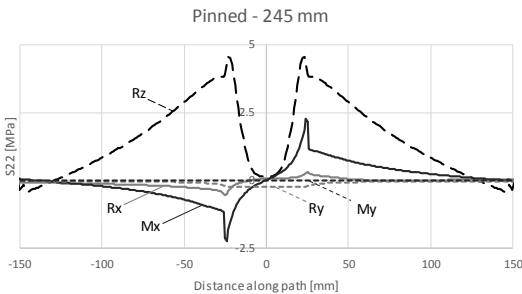FIGURE 7.7: ACTING FORCES ON POINT-FIXING 1 FOR WIND SUCTION.

FIGURE 7.8: STRESS DISTRIBUTION S22 OF THE **LOCAL** STRESSES FOR POINT-FIXING 1.

The sum of these local stresses and the global stress replace the global stress distribution in the local zones, as depicted in Figure 7.9. Figure 7.10 gives the comparison between the stress distribution obtained from the total model and the SLG-method. The SLG-method describes the stresses in the field well, also the discontinuous distribution at the connection is visible in the SLG-method.
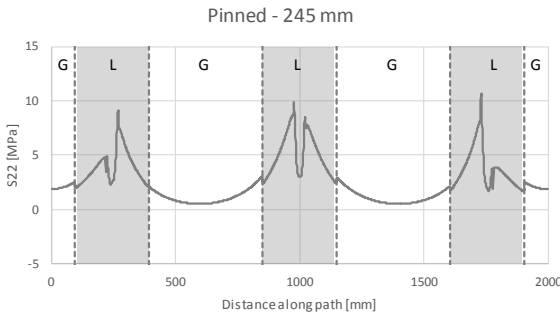

FIGURE 7.9: STRESS S22 DISTRIBUTION WITH THE SLG-METHOD, COMBINING GLOBAL (G) AND LOCAL (L) STRESSES.
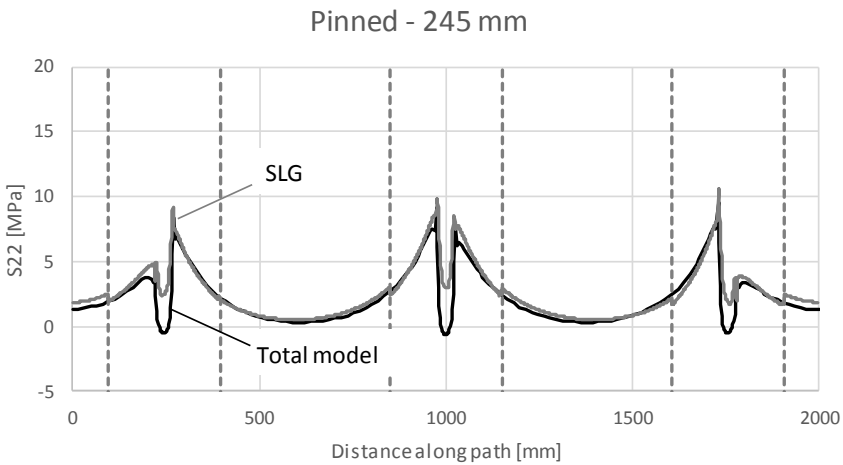

FIGURE 7.10: COMPARISON BETWEEN THE STRESS DISTRIBUTION OF THE TOTAL MODEL AND THE SLG-METHOD FOR SIX HINGED POINT-FIXINGS WITH A CONNECTOR DIAMETER OF 50 MM.

Comparison between the total stress distribution and the SLG-method for four point-fixings is given in Figure 7.11 and for six point-fixings in Figure 7.12. The peak stresses were always higher when calculated with the SLG-method than with the total model. Hence, the SLG-principle will give conservative stress distributions.
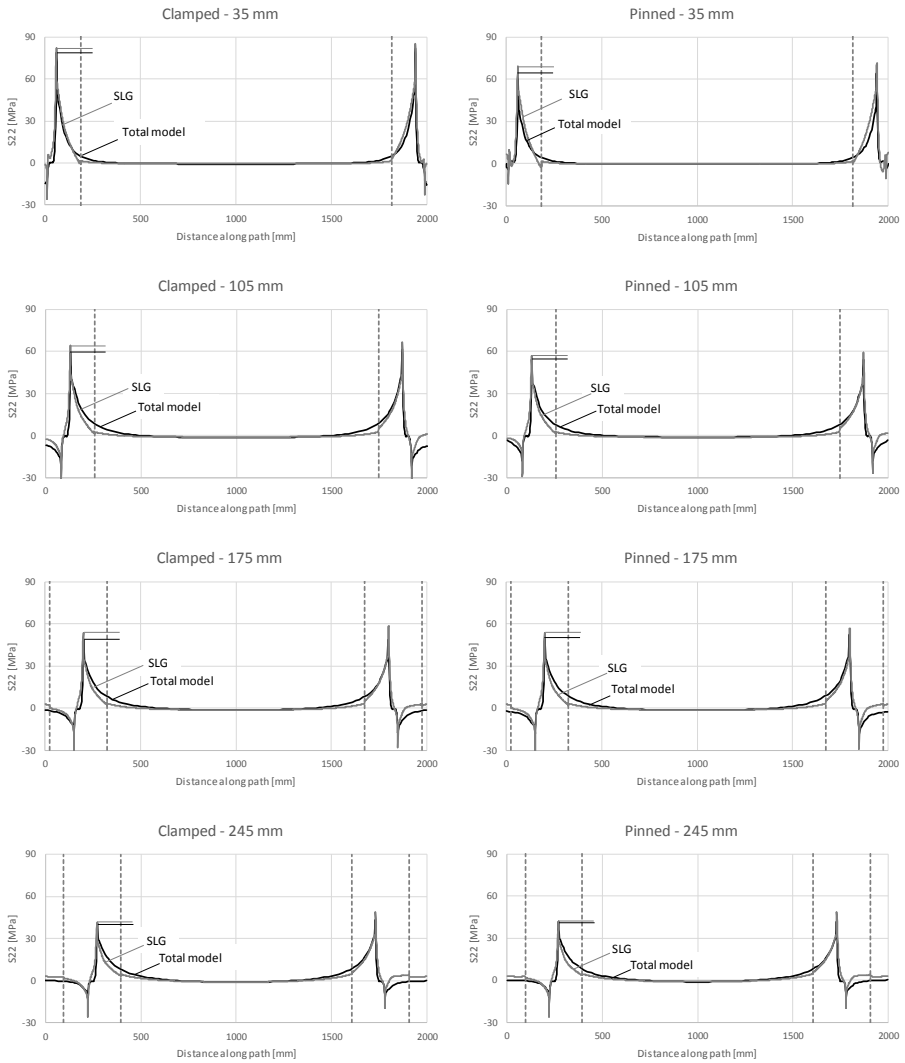
FIGURE 7.11: COMPARISON BETWEEN THE STRESS DISTRIBUTION OF THE TOTAL MODEL AND THE SLG-METHOD MEASURED AT THE REAR FOR FOUR POINT-FIXINGS FOR WIND SUCTION.
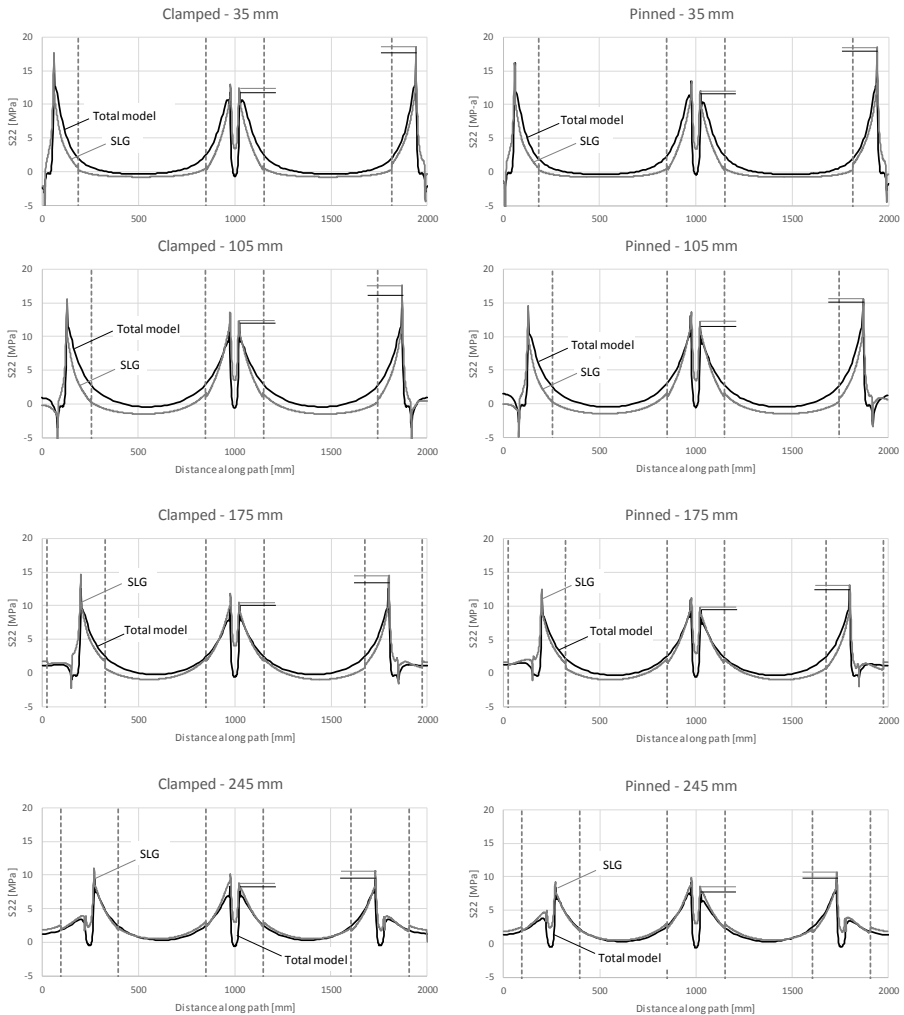
FIGURE 7.12: COMPARISON BETWEEN THE STRESS DISTRIBUTION OF THE TOTAL MODEL AND THE SLG-METHOD MEASURED AT THE REAR FOR SIX POINT-FIXINGS FOR WIND SUCTION.

Despite small deviations, the SLG-method predicts conservatively and accurately the occurring stresses. Due to the limited deflection of the glass panel with six point-fixings, i.e. a maximal deflection of 0.70 mm for the hinged configuration with an edge distance of 245 mm, the membrane forces are limited. In contrast, as the maximal deflection for the same configuration but with four point-fixings is equal to 8.35 mm, the membrane forces increased with a factor of over 20, explaining the higher peak stresses for the configurations with four point-fixings.

The influence of the edge distance is also clearly distinguishable. The stresses decrease when the edge distance is increased. Furthermore, the small influence of the boundary condition is also visible. As the rotation of the glass panel is prevented with the fixed boundary condition, the stresses become higher. This effect is only noticeable for small edge distances, as for larger edge distances the rotation of the glass panel will be small at the support.

7.3.2.   Glass stress distribution at the front.

The stress at the front of the glass panel is also verified. The path, along which the stress S22 was derived, is depicted in Figure 7.13. As with the previous path, the position depends on the edge distance. The reaction forces are the same as for the previous configuration. Contrary to the previous configuration, the local stresses were determined at the front side of the glass panels. The comparison for four point-fixing is given in Figure 7.14 and for six point-fixings in Figure 7.15.
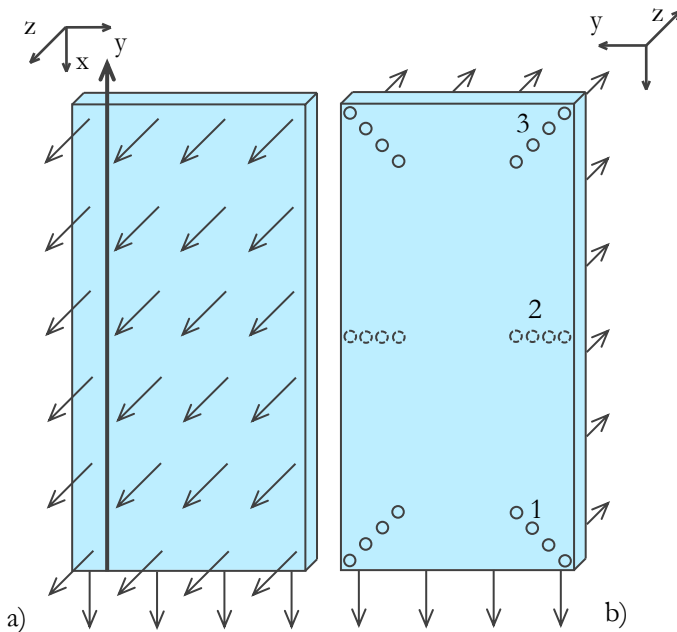

FIGURE 7.13: SLG VALIDATION CONFIGURATION FOR WIND SUCTION AND THE PATH AT A) THE FRONT OF THE GLASS PANE.
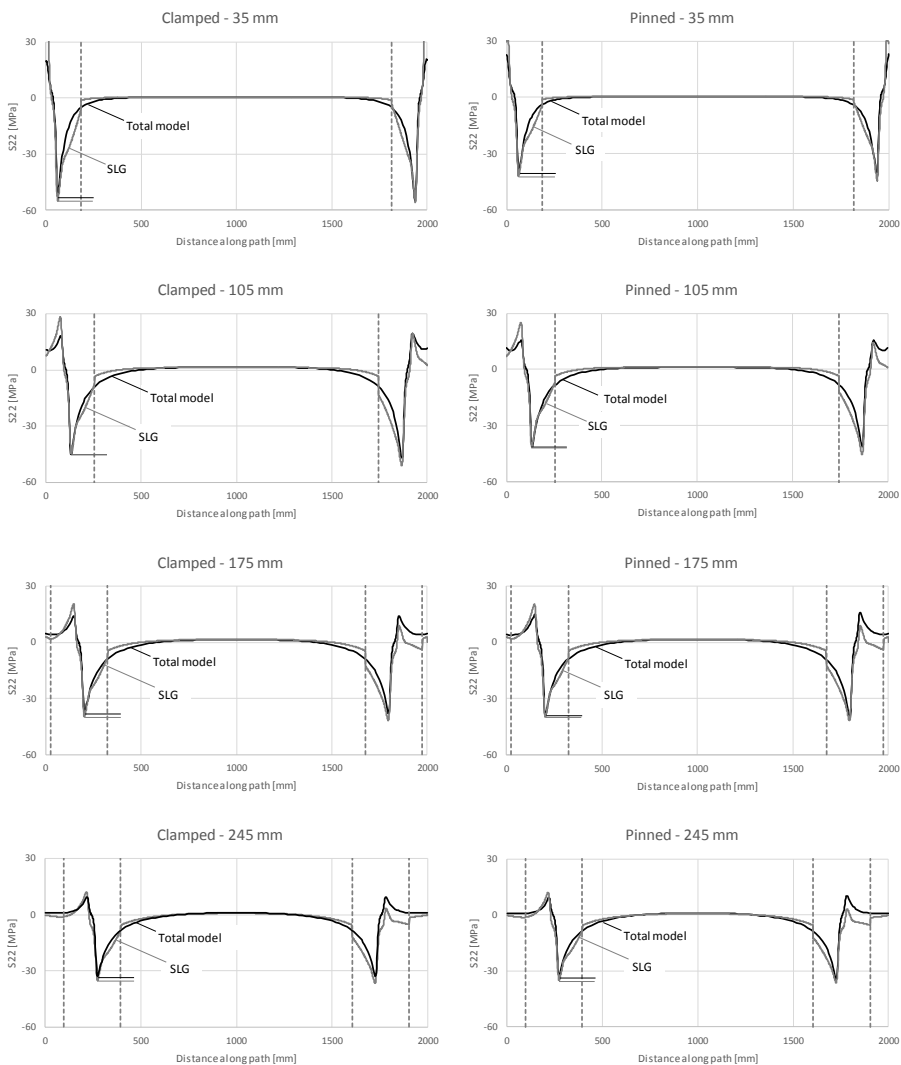
FIGURE 7.14: COMPARISON BETWEEN THE STRESS DISTRIBUTION OF THE TOTAL MODEL AND THE SLG-METHOD MEASURED AT THE FRONT FOR FOUR POINT-FIXINGS FOR WIND SUCTION.
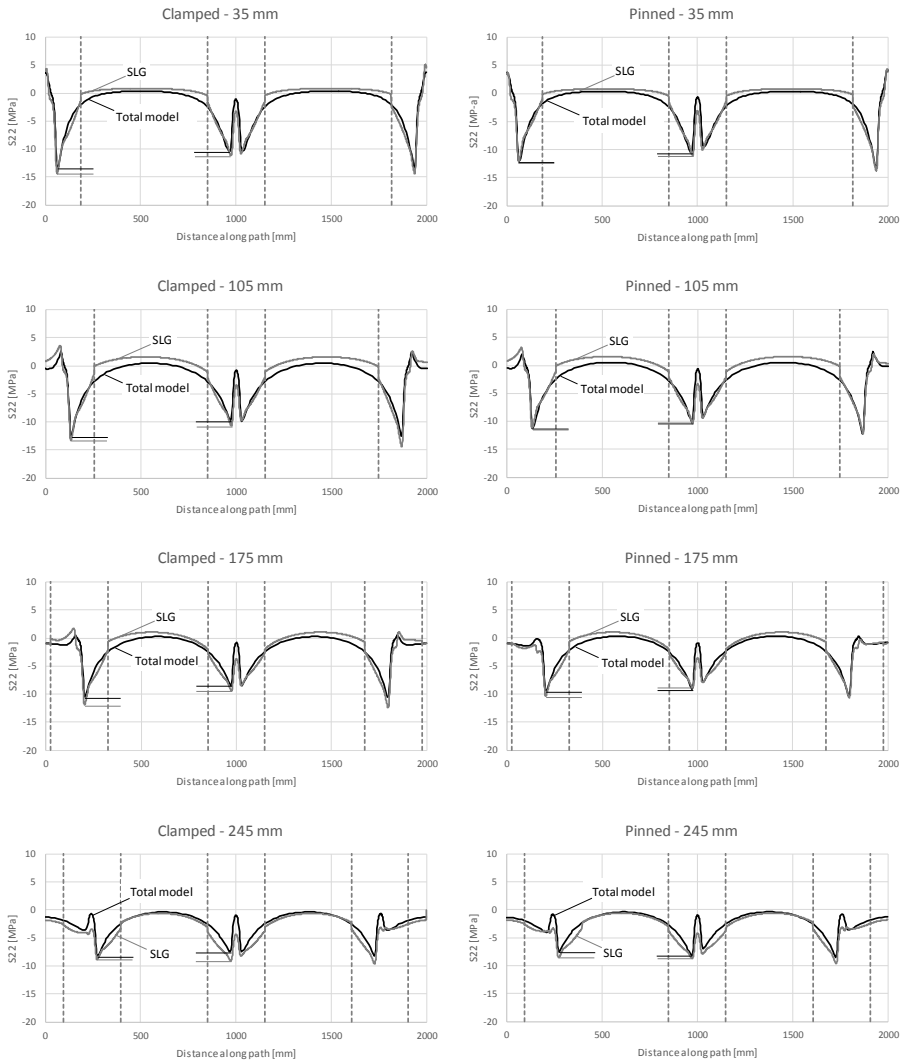
FIGURE 7.15: COMPARISON BETWEEN THE STRESS DISTRIBUTION OF THE TOTAL MODEL AND THE SLG-METHOD MEASURED AT THE FRONT FOR SIX POINT-FIXINGS FOR WIND SUCTION.

Also for the stress at the front panel side, the SLG-method gives good and conservative values compared with the stress from the total model. Here the influence of the number of point-fixings and of the edge distance is also clearly visible.

7.3.3. Adhesive stress distribution

The comparisons above demonstrate that the SLG-method is an adequate method to determine the stress distribution in a glass panel supported by adhesive point-fixings. However, glass failure is only one type of failure for glass panels supported by adhesive point-fixings, i.e. adhesive failure can also occur. To predict failure in the adhesive layer, the stress distribution in the adhesive layer must be known. The verification of obtaining the stress distribution in the adhesive layer with the SLG-method is described in this paragraph. The location of the stress distribution S22 path is located in the middle of the adhesive layer, as depicted in Figure 7.16.
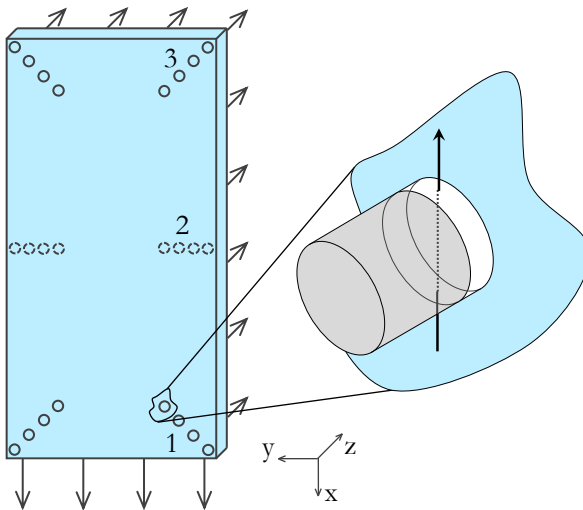

FIGURE 7.16: SLG VALIDATION CONFIGURATION FOR THE ADHESIVE LAYER WITH WIND SUCTION AND THE PATH IN THE ADHESIVE LAYER (NOT TO SCALE).

The stress distribution with the SLG-method in the adhesive layer consists only of the sum of the local stresses. The stress distribution obtained from the total model and obtained with the SLG-method for an edge distance of 35 mm and 105 mm is depicted in Figure 7.17 for four point-fixings and in Figure 7.18 for six point-fixings. In the title of each graph the edge distance is mentioned together with the number of the considered support. Also here, the stress perpendicular to the path is considered, i.e. S22. The local stresses are derived from the multi-axial model with the magnitude, angle and eccentricity of the resulting force derived with Eq. (4.3), (4.4) and (4.5) from Chapter 4. For an edge distance of 175 mm and 245 mm, the comparison is given in Appendix D.
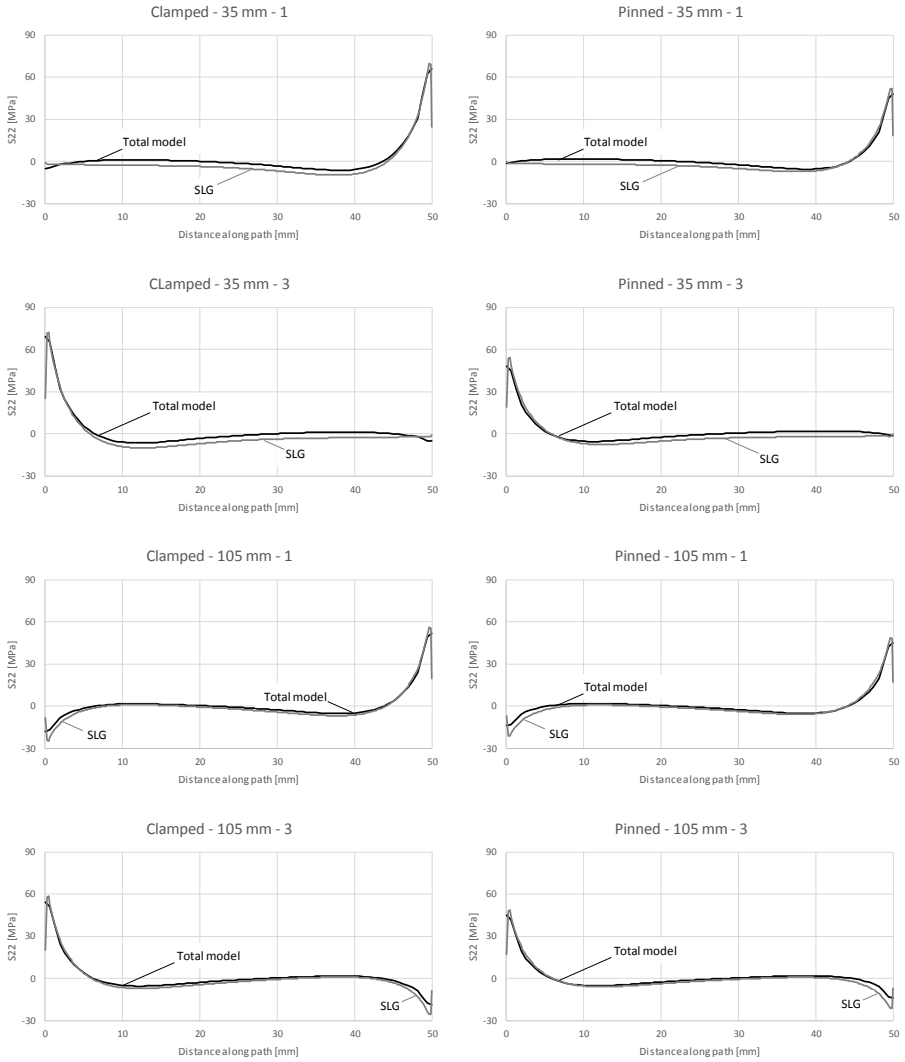
FIGURE 7.17: COMPARISON BETWEEN THE STRESS DISTRIBUTION OF THE TOTAL MODEL AND THE SLG-METHOD MEASURED IN THE ADHESIVE LAYER FOR FOUR POINT-FIXINGS FOR WIND SUCTION.

Clamped - 35 mm - 1

Pinned - 35 mm - 1

Clamped - 35 mm - 2

Pinned - 35 mm - 2

Clamped - 35 mm - 3

Pinned - 35 mm - 3

Clamped - 105 mm - 1

Pinned - 105 mm - 1

Clamped - 105 mm - 2

Pinned - 105 mm - 2
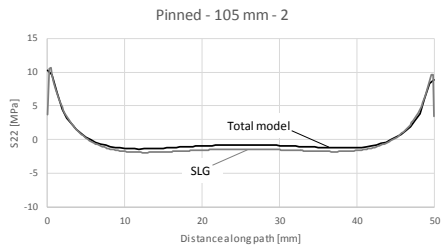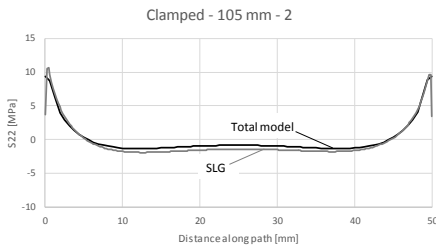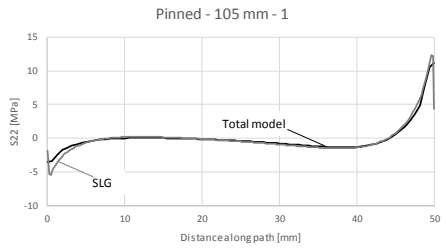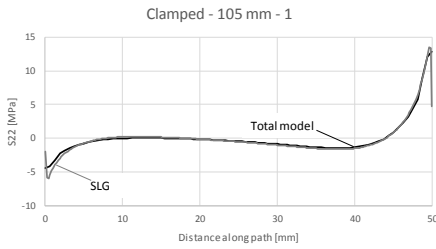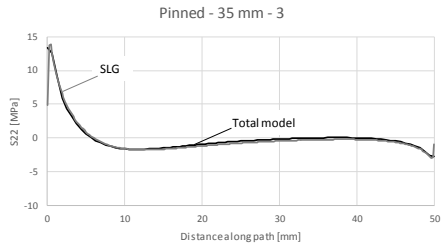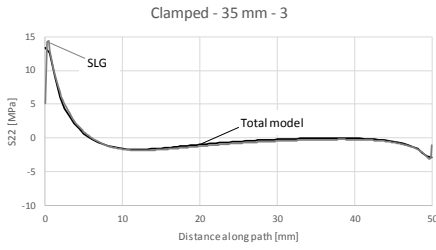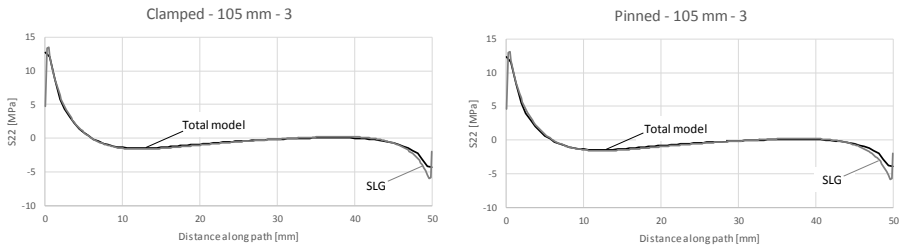
FIGURE 7.18: COMPARISON BETWEEN THE STRESS DISTRIBUTION OF THE TOTAL MODEL AND THE SLG-METHOD MEASURED IN THE ADHESIVE LAYER FOR SIX POINT-FIXINGS FOR WIND SUCTION.

The deviation between the stress distribution in the adhesive layer obtained with the SLG-method and from the total model is small. The shape and order of magnitude of the SLG-curve are close to the curve of the total model. Furthermore, the SLG-method gives generally larger stress peaks than the total model, resulting in slightly conservative stress distributions. As expected, the stress peaks are larger for small edge distances and are slightly higher for the clamped condition. The above comparisons were done for wind suction. The situation with wind pressure is summarized in Appendix E.

7.3. Deformation

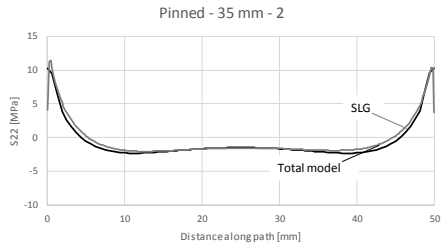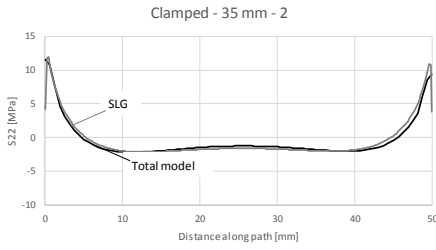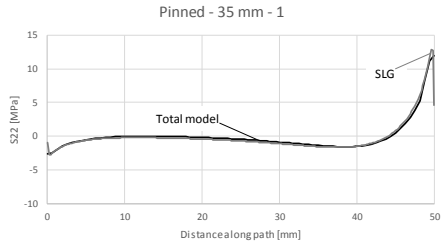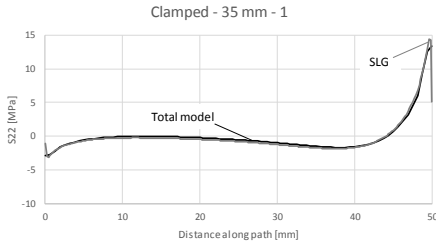In the design for bolted point-fixings, the maximum deformation in the field of the global model is determined and compared to the allowed deformation for glass panels. As the maximum occurring deformation is determined from the global model, this deformation will be larger than the actual occurring deformation, since the influence of the connector is not taken into account. The connection will locally prevent deformation of the glass panel. Hence, the deformation obtained from the global model will be conservative and safe. In this paragraph, the latter is investigated for adhesive point-fixings. The deformation along the path depicted in Figure 7.19 obtained from the global model is compared to the occurring deformation in the total model.
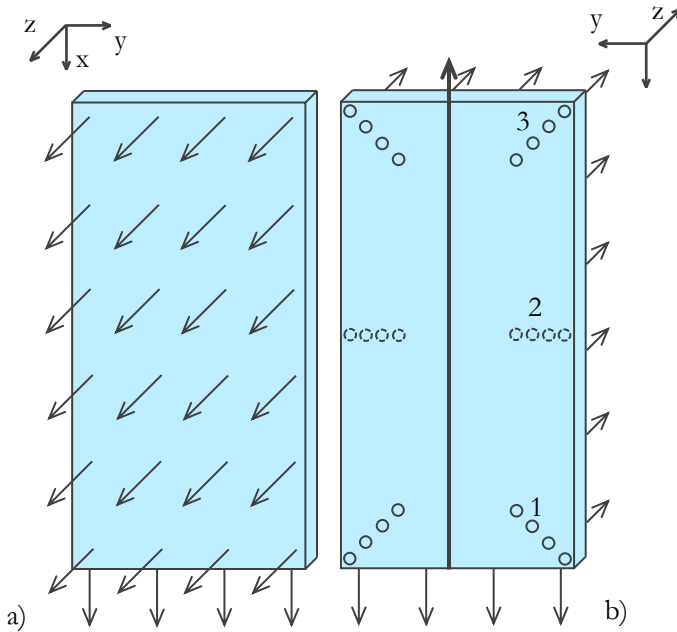
FIGURE 7.19: SLG VALIDATION CONFIGURATION FOR WIND SUCTION AND THE PATH AT A) THE FRONT OF THE GLASS PANE.

The deformation for the total model is obtained for three different diameters, i.e. 30 mm, 50 mm and 60 mm. The comparison between the deformation obtained with the total model and the global model is depicted in Figure 7.20 for four point-fixings and in Figure 7.21 for six point-fixings. As expected, the deformations from the global model are higher than from the total model. Hence, the deformation obtained from the global model will be conservative and safe. As also showed in Chapter 6, the smaller the diameter, the higher the deformation.
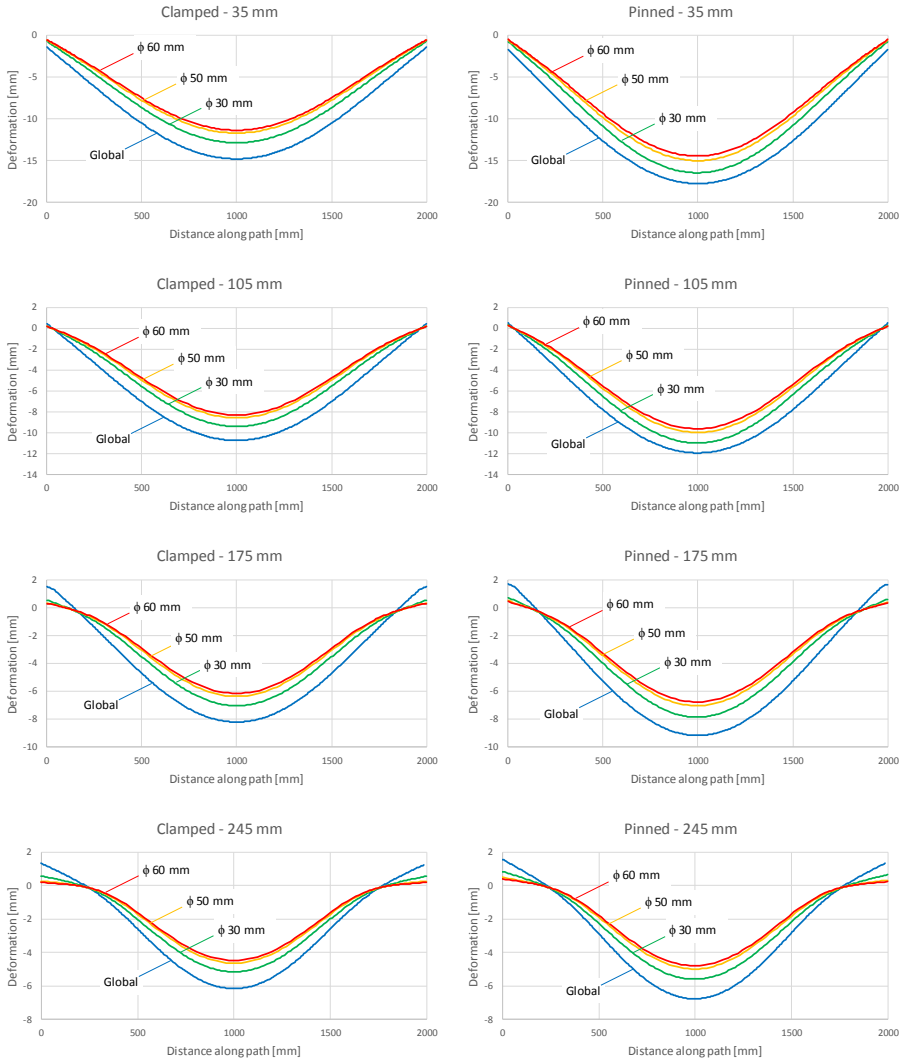
FIGURE 7.20: COMPARISON BETWEEN THE DEFORMATION OF THE TOTAL MODEL AND THE GLOBAL MODEL FOR FOUR POINT-FIXINGS FOR WIND SUCTION.
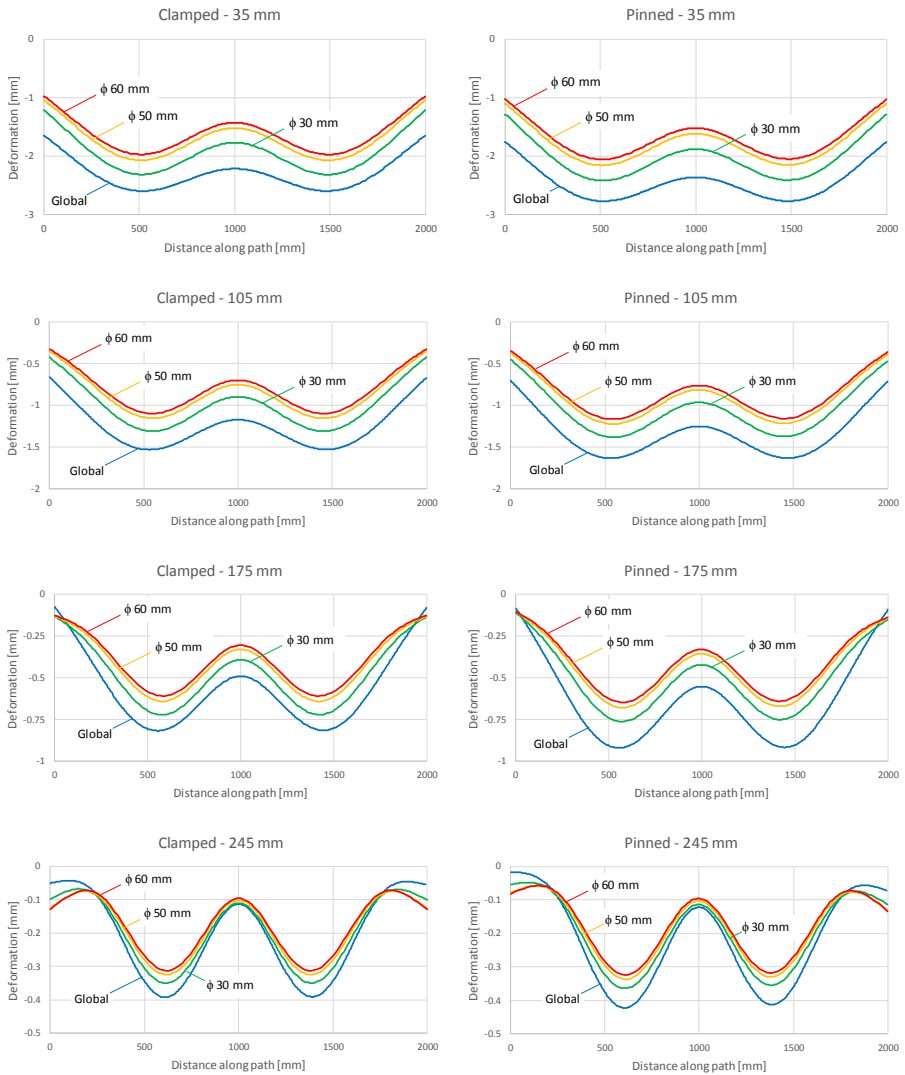
FIGURE 7.21: COMPARISON BETWEEN THE DEFORMATION OF THE TOTAL MODEL AND THE GLOBAL MODEL FOR SIX POINT-FIXINGS FOR WIND SUCTION.

7.4.　　　Summary and conclusions

The general conclusion of this chapter is that the SLG-point method applied on adhesive point-fixings gives accurate and conservative stress distributions. Different configurations were evaluated using the SLG-method. By applying this method the calculation of large glass plates connected with adhesive point-fixings can be done about 1000 times faster than when the glass plate is built up with a fine mesh pattern and about 100 times faster for smaller plates. Despite small deviations, the SLG-method predicts the occurring stresses in a glass panel supported by adhesive point-fixings conservatively and accurately. In addition, the SLG method gives much more accurate results compared to the global model. The stress distribution in the adhesive layer can also be determined with the SLG-method. For the latter, as the stress distribution consists of only the sum of the local stresses, these stresses were derived from the multi-axial model. The deviation between the SLG-method and the total model is small. Moreover, the SLG-method generally gives slightly larger stress peaks than the total model, giving conservative stress distributions. From the validation, a clamped boundary condition introduces slightly higher stresses than a pinned boundary condition. However, this effect is less pronounced for larger edge distances.

Chapter 8: Failure criterion

> The more that you read, the more things you will know.
> The more that you learn, the more places you'll go.
>
> *Dr. Seuss*

8.1.   Introduction

As with other civil structures, it is necessary for the design of an adhesive connection to calculate its strength and stiffness. By means of a failure criterion this strength can be assessed. For a given geometry, the occurring stresses and deformations are first calculated on the basis of a stress or deformation analysis. Secondly, the assessment of the adhesive strength needs a failure criterion, which subsequently allows to define the failure load. Next, any necessary adjustment of the geometry may further optimize the connection. As such, the design is an iterative process, which requires a stress analysis and a failure criterion to determine the optimal connection, as depicted in Figure 8.1. In this chapter, the aim is to determine an appropriate failure criterion for adhesive point-fixings between glass and metal.
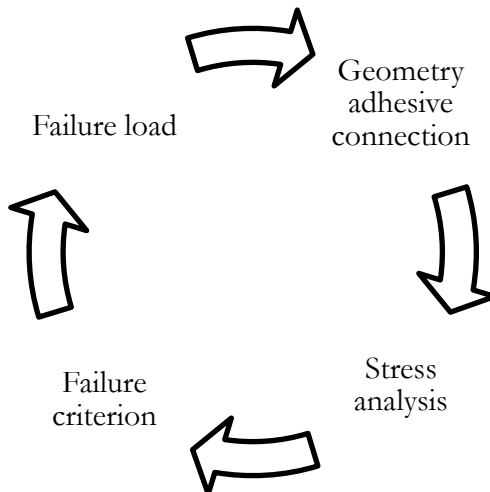

FIGURE 8.1: PROGRESS OF THE DESIGN OF AN ADHESIVE CONNECTION.

The determination of the occurring stresses and deformations can be performed with either an analytical method or a numerical method. Regarding the former, various methods are developed to determine the shear or normal stresses in a single lap joint (SLJ) under shear. The theory of Volkersen (1938) is the most basic analytical method for this configuration, and several other analytical methods have been proposed based on this theory (Goland & Reissner 1944; Hart-Smith 1974; Ojalvo & Eidinoff 1978; Bigwood & Crocombe 1989; Adams & Mallick 1992). As these analytical methods are out of the scope of this thesis, a reference is made to the work of da Silva et al. (2009; 2009) for a complete overview of the different analytical methods for a SLJ. As demonstrated in previous chapters, the determination of the occurring stresses and deformations in this thesis are performed with FEA.

For the design of an adhesive connection, a distinction has to be made between the different failure modes. The following five failure modes, or a combination of them, can occur in an adhesive point-fixing. They are illustrated in Figure 8.2.

- Substrate failure;
  - Metal failure;
  - Glass failure;
- Adhesive failure: failure at the interface between the adhesive layer and one of the substrates;
  - Adhesive failure interface adhesive-glass;
  - Adhesive failure interface adhesive-steel;
- Cohesive failure: failure within the adhesive layer.

Criteria for the following four main loading conditions exist and thus failure criteria differ between the load types of the adhesive joints. The experiments in this thesis were performed with a static load, hence the focus lies on the first kind of criterion.

- Criterion for static/impact loadings: predicts the load bearing capacity of the connection;
- Criterion for fatigue loading: predicts the lifetime of the connection under a cyclically varying load in terms of cycles to failure;
- Criterion for creep loading: predicts the lifetime of the connection under a constant load in terms of time to failure.
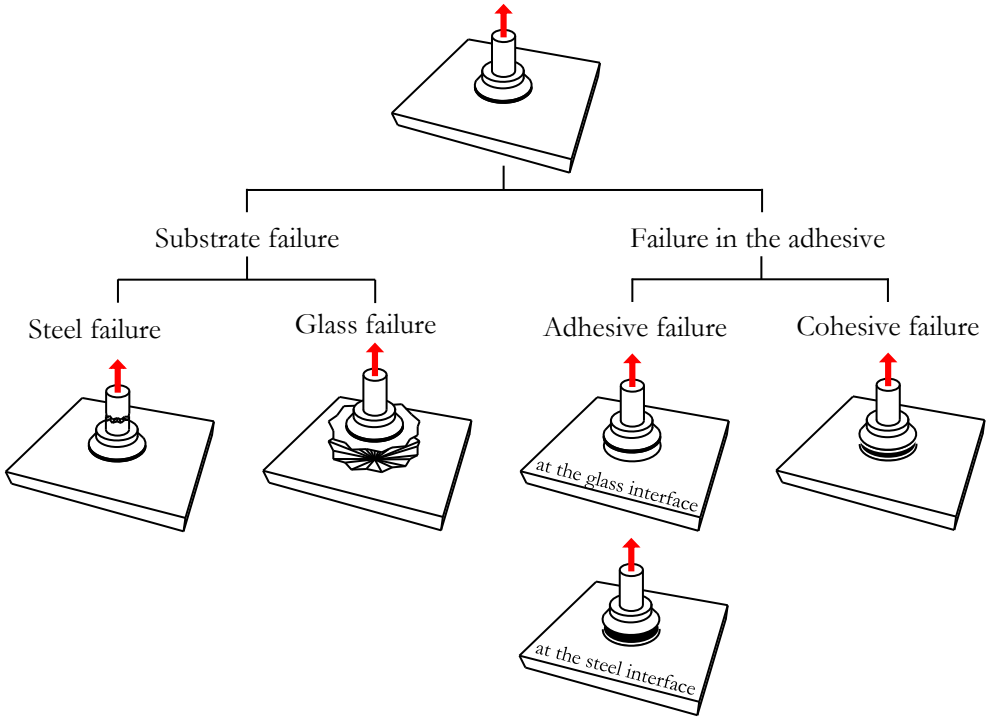
8.2.   Substrate failure

8.2.1. Metal failure

As illustrated in Figure 8.2, failure in a substrate can be divided in metal failure and glass failure. For metal failure, the von Mises yield criterion is a frequently used failure criterion (Kazimi 2001; Mises 1913; Singh 2007; Leckie & Bello 2009). The von Mises yield criterion stated that the metal will fail when the von Mises stress σ_v induced in the metal exceeds the yield strength σ_y of the metal. The expression for this criterion is given in Eq. (8.1) in function of the principal stresses.

$$\sigma_y \leq \sigma_v = \sqrt{\frac{(\sigma_1 - \sigma_2)^2 + (\sigma_2 - \sigma_3)^2 + (\sigma_3 - \sigma_1)^2}{2}} \tag{8.1}$$

8.2.2. Glass failure

The theoretical tensile glass strength based on molecular forces is very high and may reach 32 GPa (Haldimann et al. 2008). However, from the manufacturing and processing of the glass, defects are induced in the glass surface. These defects occur as mechanical flaws, almost invisible to the naked eye. Most of these flaws have dimensions between 30 µm and 300 µm (Haldimann et al. 2008). During the float process the glass surface is damaged by the rollers of the annealing process, and the strength is determined by the induced mechanical flaws. The research of Overend and Zammit (2012) shows the influence of the flaw size and load duration on the glass strength; the larger the flaw size, the smaller the failure stress (Figure 8.3). Also, it can be seen that the longer a stress is present, the lower is the glass strength.
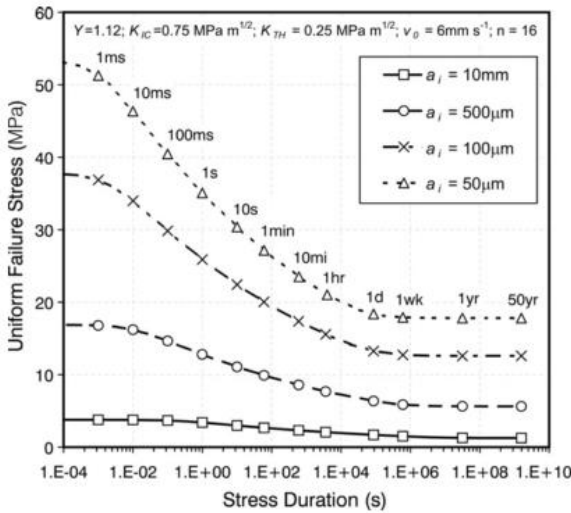
FIGURE 8.3: FAILURE STRESS VS. STRESS DURATION FOR A RANGE OF INITIAL FLAW SIZES FROM 50 TO 10000 µM (OVEREND & ZAMMIT 2012).

For glass failure, the existing failure criteria can be divided in two large groups, i.e. based on fracture mechanics and based on the classic material strength. In the former, the theory of linear elastic fracture mechanics (LEFM) describes the relation between the tensile strength and the flaw parameters, i.e. the flaw geometry and the flaw depth (Vandebroek 2014). For the use of fracture mechanics, the initial critical flaw depth has to be known.

To avoid the determination of the initial critical flaw depth, failure criteria according to the classical material strength can be used. More information about failure criteria for glass failure based on fracture mechanics can be found in Appendix F. For the classical material strength, the 5% characteristic surface tensile strength with a 95% confidence level is given in standards and literature (prEN 16612 2013; EN 12150-1 2015; ÖNORM B 3716-1 2009; NEN 2608 2014; DIN 18008 2010; EN 14179-1 2007; EN 1863-1 2012).

The design value of strength for annealed glass $f_{d,k}$ can be calculated with Eq. (8.2) and with Eq. (8.3) for prestressed glass $f_{d,k}$, where 45 MPa, 70 MPa and 120 MPa are the characteristic values of the bending strength of annealed glass $f_{g,k}$, heat strengthened glass and fully tempered glass $f_{b,k}$, respectively. These equation are still under discussion in the new technical specification (TS) for the future Eurocode about glass design. Therefore, these equations should not be considered as universal equations for glass design.

$$f_{g,d} = \frac{k_{mod} \cdot k_{sp} \cdot f_{g,k}}{\gamma_{M,a}} \tag{8.2}$$

$$f_{g,d} = \frac{k_{mod} \cdot k_{sp} \cdot f_{g,k}}{\gamma_{M,a}} + \frac{k_v \cdot (f_{b,k} - f_{g,k})}{\gamma_{M,v}} \tag{8.3}$$

With:
- $f_{g,k}$ the characteristic value of the bending strength of glass;
- $f_{b,k}$ the characteristic value of the bending strength of prestressed glass;
- $\gamma_{M,a}$ the material partial factor for glass, which is 1.8;
- $\gamma_{M,v}$ the material partial factor for prestressed glass, which is 1.2;
- k_{sp} the factor for glass surface profile, which is 0.6 for sandblasted glass and 1.0 for 'as produced' glass;
- k_v the factor for strengthening of prestressed glass, which is 1.0 for horizontal toughening and 0.6 for vertical toughening;
- k_{mod} the factor for load duration. In standard buildings, k_{mod} has a maximal value of 1.0 and a minimum of 0.25.

8.3. Failure in the adhesive

As illustrated in Figure 8.2, failure in the adhesive can be divided into two main groups, i.e. adhesive failure and cohesive failure. The former occurs when the location of failure is located at the interface between the adhesive layer and the substrate and can occur at the interface adhesive-glass or at the interface adhesive-steel. To explain adhesion, the interaction in the contact surface must be known. A distinction can be made between physical and chemical connections (Kinloch 1983; Van Straalen 2001; Habenicht 2009). The weaker physical connections are created by Van der Waals forces, dipole forces, and hydrogen bonds. These types of connections are established by an electrostatic attraction between the molecules. The stronger chemical connections are ionic, covalent and metallic bonds between different reactive chemical groups in the substrate and the adhesive layer. Some theories give a more advanced definition of adhesion (Bach et al. 2000; Ghani 2007; FME-CWM 2008). These theories suggest that adhesion is based on a combination of mechanical interlocking and diffusion. Mechanical interlocking occurs when the adhesive can enter in the seams and pores of the substrate. When the adhesive cures, this creates an anchoring of the adhesive into the substrate. With diffusion, the polymer chains of the adhesive molecular bonds with the molecules of polymer substrates. Hence, the latter will not occur with glass or metal substrates.

As most studies are about techniques of how to prevent adhesive failure and not the working of adhesion, little is known about the physical and mechanical behaviour of the adhesive at the location of the contact surface. Most designers also argue that the adhesive failure should not occur in a well-executed connection and that substrate and cohesive failure will primarily occur (Puller & Sobek 2008).

With cohesive failure, the location of the failure initiation is situated in the adhesive layer. This failure initiation occurs by a local crack which further branches until the connection fails (Crocombe et al. 1995). Because adhesives consist primarily of synthetic and organic material, the cohesive behaviour can be explained by means of polymer technology. Polymers are macromolecules formed from the reaction of smaller molecules, i.e. monomers. The polymers can be divided into four groups according to their molecular structure, namely linear structure, branched structure, cross-linked structure and network structure, as depicted in Figure 8.4.

A linear structure is composed of long chains of molecules that are only bounded by means of physical forces, i.e. Van der Waals forces. The branched polymers have side-branches, but the chains are still bounded only by weak physical forces. When these branches are also connected to other chains by means of strong chemical forces, a cross-linked structure is obtained. These interconnections occur only in one plane. This in contrast to a network structure, where the connections are three-dimensionally positioned. The latter structure is by means of the many chemical bonds the strongest structure. Most adhesives are cross-linked or network polymers.
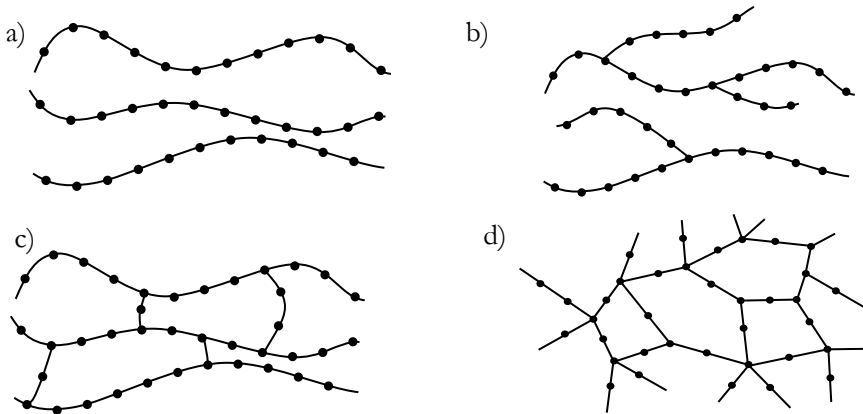
FIGURE 8.4: THE FOUR STRUCTURE GROUPS OF POLYMERS: A) LINEAR, B) BRANCHED, C) CROSS-LINKED AND D) NETWORK STRUCTURE

As for glass, failure criteria for adhesive connections can be divided in two main groups: one according to fracture mechanics and one according to continuum mechanics. As mentioned in previous paragraph, the former assumes that the structural joint fails by progressive crack growth. Within the domain of fracture mechanics, two subdivisions exist: linear elastic fracture mechanics (LEFM) and elastic plastic fracture mechanics (EPFM). The former assumes that when the crack propagates, the energy reduction in the material is only a consequence of the increased fracture. The latter assumes that plastic deformations will occur at the crack tip. A summary of failure in the adhesive based on fracture mechanics is given in Appendix F.

However, in practice a continuum mechanics approach is often preferable. Continuum mechanics assumes that the material is continuously distributed and filling the entire volume that it occupies. The material is fully homogeneous and

no cracks or discontinuities are present. According to this approach, the joint connection will fail cohesively when a critical stress or strain is reached in the adhesive. Several failure criterion based on this hypothesis have been suggested and applied to adhesive connections (Crocombe et al. 1995; McCarthy 1996; Crocombe & Kinloch 1994):

- Maximum shear stress;
- Maximum shear strain;
- Peak maximum principal strain;
- Maximum plastic energy density;
- Maximum von Mises equivalent stress;
- Peak maximum principal stress;

Most of these proposed failure criteria have been tested on single-lap joints (SLJ) (Figure 8.5). The ability to predict the strength of single-lap joints can provide the necessary insights in the behaviour of adhesive connections under a variety of loading conditions and allows to make conclusions for adhesive point-fixings.
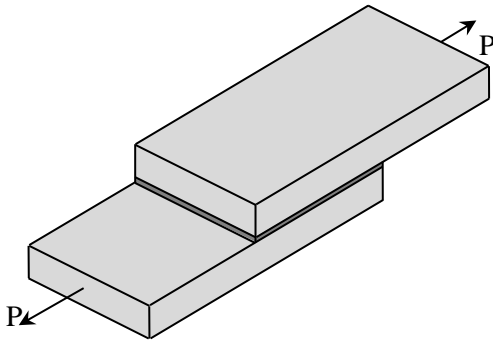
FIGURE 8.5: PRINCIPLE OF A SINGLE-LAP JOINT (SLJ).

8.3.1.   Failure criteria models in literature

Greenwood, Boag, and McLaren (1969) tried to predict the shear strength of single-lap joints (Figure 8.5) under a large range of loading conditions. A closed form analysis was used and the **maximum shear stress** was found to occur at an angle of 45° through the adhesive layer. Upon comparing the test results of the joint with the shear stresses obtained from a tensile test of the bulk adhesive, the predicted strength was found to be about 14% too low.

The **maximum peel stress criterion** was firstly introduced by Hart-Smith (1973) for a single-lap joint. More recently, Crocombe and Tatarek (1985) have adapted this criterion by performing a simple linear closed form analysis that modelled the peel stresses in the adhesive. Strength predictions were done for variously loaded T-joints by bonding steel plates with a thickness of 3 mm using an AY103/956 (epoxy resin) adhesive. From bulk tensile test data, the maximum adhesive tensile strength was found to be equal to 69 MPa which served as a critical value of the peel stress. This resulted in strength predictions within 6% for two different configurations but errors of 90% were observed in the configuration where substrate yielding was noted.

The **maximum shear or peel strain criterion** for shear or peel failure in the adhesive in lap joints was also firstly proposed by Hart-Smith (1973). Equations for the maximum peel stress have been derived for both single- and double-lap joints. For small adhesive thicknesses, peel stresses appeared not to be a problem. However, for standard adhesive thicknesses, the peel stresses were the determining factor for failure.

A failure criterion for tubular lap joints in torsion has been proposed by Lee and Lee (2006). In this research cohesive failure occurred for thin adhesive layers and interfacial failure for thicker adhesive layers (which included shear and peel strain). The former was governed by a **maximum strain criterion** while the latter was associated with a **maximum reduced stress criterion**. The torque capacity of the connection could be predicted accurately. Chai (1993) has noticed that the critical shear strain indeed decreases with increasing adhesive thickness.

In the research of Harris and Adams (1984), reasonable strength predictions have been obtained for single-lap joints using the **principal strain criterion** in conjunction with a non-linear FEA. The existing analytical approaches focus on the shear deformation of the adhesive, which can lead to significant errors since the behaviour in shear of an adhesive will be much more ductile than its behaviour in a connection. A criterion based on the uniaxial tensile properties of an adhesive is therefore more applicable than one based on the response of the material in pure shear. For two untoughened adhesives, brittle failure occurred in the joint and a maximum stress criterion was appropriate. For two toughened adhesives, a maximum strain criterion was found to be appropriate (Harris & Adams 1984).

The **maximum effective uniaxial plastic strain criterion** has been used for failure prediction in peel joints by using a large displacement elastoplastic FEA. Crocombe and Adams (1982) state that this strain is highly dependent on the mesh size. For different substrates bonded by the same adhesive, different critical strains had to be used in order to obtain reasonable failure predictions. This could be explained by differences in plastic zone sizes.

For the failure prediction of SLJ with varying geometry, the **maximum plastic energy density criterion** was used by Adams and Harris (1987). They combined a plastic energy density criterion with an elastoplastic FEA. The location of failure initiation in adhesive lap joints depends strongly on the geometry of the spew fillet of the overlap. The configurations considered are depicted in Figure 8.6. Note that it is specific to numerical approaches that the prediction of the joint strength is extremely dependent on local mesh refinement because of the existence of singularities in the stress or strain fields at critical points. In adhesive joints, these singularities arise at the corners between the adhesive and the substrate material as a result of the squareness of the model (Adams & Harris 1987).
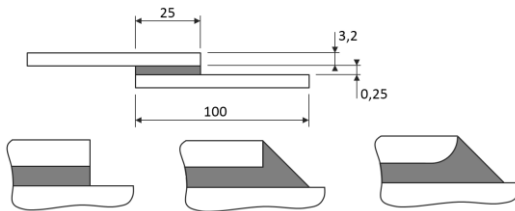
FIGURE 8.6: TEST CONFIGURATION OF THE ADHESIVE LAP JOINT (ADAMS & HARRIS 1987)

A continuation of the work of Adams and Harris (1987) was performed by Zhao and Adams (1989), who stated that the plastic energy density criterion is not able to predict the joint strength in case of sharp corners and that an arbitrary rounding of twice the adhesive thickness (double of the proposed rounding suggested by (Adams & Harris 1987)) should always be used to analyse normal joints. The degree of rounding has a high influence on the maximum energy density and thus, extensive parametric testing was required.

Ikegami et al. (1990) used the **von Mises equivalent stress criterion** to predict the strength of the adhesive connection between glass reinforced plastic (GRP) and metal scarf joints by means of an FEA. The von Mises stress provides an equivalent adhesive stress that can be related to the uniaxial yield stress. A disadvantage of this approach is that the criterion neglects the hydrostatic

component of stress which significantly affects the yield and deformation behaviour of polymers. The strength laws of the steel adherents and the adhesive layer are given by the von Mises conditions (Eq. (8.1)), and the strength law of the GRP is given by Hoffmann's criterion (Hoffman 1967). Note that for isotropic materials (which is assumed for the metal adherents as well as for the adhesive layer), the Hoffmann yield criterion reduces to the von Mises condition (Schellekens & Borst 1990). The applied stress value which causes failure in the material element was evaluated. The stress concentration in the adhesive layer and the adherent was the most pronounced at the adhesive edge and the effect of the adhesive length on failure strength is more pronounced in joints with short adhesive lengths than in joints with long adhesive lengths.

Castagnetti, Dragoni, and Spaggiari (2010) also used the **von Mises equivalent stress criterion** to determine numerically the failure load of a T-connection, as it was easier to implement in Abaqus. The tests were performed for two types of substrate, i.e. aluminium and steel, different substrate thicknesses and different overlap lengths. The numerical failure loads were compared to the experimental failure loads. The difference between the numerical and experimental failure loads differ from 0.6% to 16.4%. Castagnetti, Dragoni, and Spaggiari (2010) conclude that the used criterion is applicable to determine the failure load of a bonded connection. Note that in case of symmetry, where one dominant normal stress component exists, the von Mises criterion is almost equivalent to the maximum principal stress criterion that would be more appropriate to describe brittle failure (Castagnetti et al. 2010).

Amijima and Fujii (1989) used the **von Mises yield criterion** in order to determine which zones of the adhesive layer will yield, while the failure of the adhesive layer is given by the Mohr-Coulomb failure criterion. This failure criterion is expressed in Eq. (8.4), where k_0, k_1 and k_2 are experimentally determined constants. With a four-point bending load, progressive failure was introduced in the specimen. Small differences occur between the calculated values and the experimentally determined values during the failure processes. According to Amijima and Fujii (1989), these differences are caused by the simplified stress-strain curve of the adhesive.

$$F(\sigma_{y,a}, \tau_{xy,a}) = k_0 + k_1 \tau_{xy,a} + k_2 \tau_{xy,a}^2 - \sigma_{y,a} = 0 \qquad (8.4)$$

Also in the research of Hua et al. (2008) the **von Mises equivalent stress criterion** is used to determine the failure load of adhesive connections exposed to a humid and warm climate, with a relative humidity of 95.8% and a temperature of 50°C. The numerical failure loads corresponded well with the experimental failure loads.

To determine the strength of a single lap joint and a T-connection in function of the cure depth, Ashcroft, Comyn, and Tellwright (2009) used a FEA to determine the stresses in the adhesive. The stress peaks decreased in the connection as the cure time increased. Stress singularities at the location of the edges of the adhesive layer were avoided by using the "stress at a distance" approach. This approach uses the stresses that occurs at a certain distance from the stress singularity at the edge. Two distances were selected, i.e. half of the adhesive thickness (0,5t) and a quarter of the adhesive thickness (0,25t). The **von Mises stress** and **maximum principal stress** were determined at these locations. The critical von Mises $\sigma_{v,cr}$ and maximum principal stress $\sigma_{I,cr}$ were determined by an uniaxial tensile test. The failure load was determined as the load when the von Mises or the maximum principal stress reaches their critical value. The numerical and experimental failure loads for the single lap joint at 25°C and 2°C are depicted in Figure 8.7. The numerical failure loads are close together and it can be concluded that the failure loads are almost independent of the applied failure criterion and distance. Also, the scattering of the experimental values makes it difficult to determine a correct failure criterion.
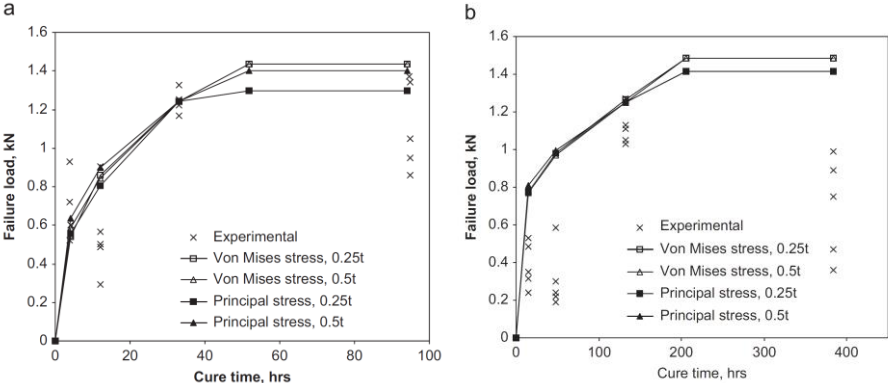

FIGURE 8.7: NUMERICAL AND EXPERIMENTAL FAILURE LOADS AT (A) 25°C AND (B) 2°C.

As mentioned above, two solutions for the problem of stress or strain singularities are the use of the stress or strain at a given distance from the point of singularity and a critical value averaged over a given region (Adams & Harris 1987; Zhao & Adams 1989; Ashcroft et al. 2009; Crocombe & Kinloch 1994). The former was first used in the composites field by Whitney and Nuismer (1974) to deal with the effect of stress concentrations in composites. The approach has been developed since then and works well over a limited data range (Crocombe & Kinloch 1994).

John, Kinloch, and Matthews (1991) stated that the **shear stress** reaches a critical value at a given normalized distance from the overlap end for bonded double lap joints with varying overlap lengths. However, in practice, this means that the critical distance varies with the overlap length and thus is not a unique parameter.

Zhao (1991) used an average value over a distance to predict failure in single lap-joints with fillets and various degrees of rounding on the embedded corner for two types of adhesive, i.e. a brittle epoxy and a rubber toughened epoxy. An **averaged stress failure criterion** had to be applied for the sharp corner and small radius configuration whilst a **maximum stress criterion** had to be used with the larger radii. The ultimate tensile stress obtained from bulk tests was used to predict the failure load.

Crocombe, Richardson, and Smith (1995) have considered numerous components of stress and strain from both elastic and elastoplastic finite element analyses of cracked and non-cracked untoughened epoxy joints subjected to various modes of loading. Good results were found by using a **critical peel stress** of about 20 MPa at around 0.3 mm from the singularity. However, this stress appears to have little physical significance and the distance is rather large, i.e. larger than the adhesive layer thickness, to characterize the singularity.

Clark and McGregor (1993) have used a slightly modified approach in that they postulate that the connection will fail if the **maximum principal stress** exceeds the ultimate tensile stress of the adhesive over a finite zone. The size of this zone is measured perpendicular to the maximum principal stress. This size was determined using a combination of experiment and FEA. For two different toughened epoxy adhesives and three joint types (single lap, double strap and flange joint), the criterion was able to predict the failure load within 5% with zones sizes of 1 and 0.68 mm and corresponding critical values of 67 and 70 MPa.

However, there is no physical justification for these zone sizes. They also showed that a criterion based on the ultimate tensile stress at a point produces a significant under-prediction of the strength due to stress singularities. The maximum principal stress in a material is defined as the maximum of Eq. (8.5), (8.6) or (8.7) with ϕ defined in Eq. (8.8).

$$\sigma_1 = \frac{I_1}{3} + \frac{2}{3}\left(\sqrt{I_1^2 - 3I_2}\right) \cdot cos\phi \tag{8.5}$$

$$\sigma_2 = \frac{I_1}{3} + \frac{2}{3}\left(\sqrt{I_1^2 - 3I_2}\right) \cdot cos\left(\phi + \frac{2\pi}{3}\right) \tag{8.6}$$

$$\sigma_3 = \frac{I_1}{3} + \frac{2}{3}\left(\sqrt{I_1^2 - 3I_2}\right) \cdot cos\left(\phi + \frac{4\pi}{3}\right) \tag{8.7}$$

$$\phi = \frac{1}{3}cos^{-1}\left(\frac{2I_1^3 - 9I_1I_2 + 27I_3}{2(I_1^2 - 3I_2)^{3/2}}\right) \tag{8.8}$$

This criterion has been used extensively by Adams and Harris (1987) in their study of the influence of the local geometry on the strength of adhesive joints but they first mentioned this criterion in 1984 (Harris & Adams 1984). Using a non-linear FEA, the application of the **maximum principal stress criterion** predicted the strength of single-lap joints with an accuracy of about 10%. In this work, four epoxy adhesives and three types of aluminium adherents were used. For each adherent/adhesive combination, a batch of 6 single-lap joints was manufactured. Parallel with the experimental test, a FEA was performed.

Dean et al. (2004) used rubber toughened adhesives to determine a failure criterion. These ductile adhesives have a large non-linear distortion before failure and were modelled as elastoplastic models in a FEA model. The study was performed for three adhesive connection configurations, i.e. a single lap joint, a T-connection and a scarf connection. Five different failure criteria were considered, i.e. **maximum principal stress**, **hydrostatic stress**, **effective von Mises stress**, **maximum principal strain** and **volumetric strain**. Depending on the applied failure criterion, the location of stress/strain peaks alters. By comparing the location of these peaks to the location of crack initiation, a conclusion was made about which failure criterion best indicates the location of crack initiation. Figure 8.8 indicates the location of crack initiation for the three different connection configurations. The maximum principal stress was the only criterion that predicted the location of

crack initiation for all three connection configurations correctly. Dean et al. (2004) also compared the numerical values of the peak stresses/strains for the different criteria at failure with their critical value. These critical values have been determined by a tensile test on bulk samples of the adhesive. This comparison showed that the maximum principal stress at failure in the connections only differs by 4% with the maximum principal stress at failure in the bulk sample.
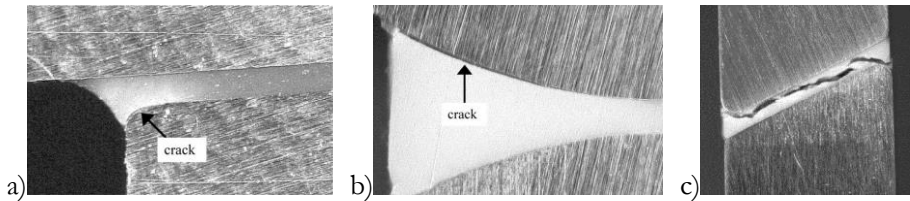

FIGURE 8.8: FAILURE LOCATION FOR A) SINGLE LAP JOINT, B) T-CONNECTION AND C) SCARF CONNECTION (DEAN ET AL. 2004)

Also in the research of Crocombe, Bigwood, and Richardson (1990), the **maximum principal stress** predicted the failure load the best. In this research two test configurations were set up, i.e. peel test and shear test, with three adhesive types, ESP (a two component epoxy), E27 (a one-component epoxy adhesive), and VOX (an acrylic-epoxy adhesive), and two substrate thicknesses, i.e. 3 mm and 4.75 mm. For each 12 connection configuration 15 samples were tested. Each experimental failure load was then applied to a FEA model and the stress and strain distributions were studied. They concluded that with a suitable failure criterion, which is based on a peak value of the stress or strain, this peak value must be the same for the thick and the thin adherents. In other words, the smaller the standard deviation of the peak values, the higher the accuracy of the failure criterion. According to this, the maximum principal stress gave a good indication of the strength of the connection. Also the peak values of the numerical maximum principal stress at failure was in a good agreement with the experimental measured maximum principal stresses in the bulk samples.

Christensen (2013) has **altered the von Mises criterion** to obtain a criterion which is valid over a large range of brittle and ductile materials. Failure is considered in an inclusive sense as both yielding and complete rupture. The theory is proposed in a three dimensional way which applies to full density materials of which the tensile strength is less than or equal to the compressive strength. This means that Eq. (8.9) can be designated as a generalized failure criterion, with T and C the respective tensile and compressive loadbearing capacity of the material.

Note that when *T=C*, Eq. (8.9) simplifies to the von Mises expression. For brittle failure, it has been postulated that the maximum principal stress will indeed be critical, as expressed by Eq. (8.10), with σ_I the maximum principal stress (Christensen 2013). The second criterion is only necessary when the tensile strength of the material is less than half the compressive strength. Both criteria should be checked simultaneously and whichever is more limiting will determine the failure load. These expressions have the advantage to be applicable over a larger range of material types.

$$\left(\frac{1}{T} - \frac{1}{C}\right)(\sigma_{11} + \sigma_{22} + \sigma_{33}) + \frac{1}{2TC}[(\sigma_{11} - \sigma_{22})^2 + (\sigma_{22} - \sigma_{33})^2 + (\sigma_{33} - \sigma_{11})^2]$$
$$+ \frac{3}{TC}(\sigma_{12}^2 + \sigma_{23}^2 + \sigma_{31}^2) \leq 1 \tag{8.9}$$

$$\sigma_I \leq T \text{ when } T \leq \frac{C}{2} \tag{8.10}$$

More complex failure criteria have also been developed in the past few years. Like the four-dimensional **generalized triaxial model** (GTM) developed by Santarsiero (2015) for the adhesives SentryGlas® and TSSA in laminated adhesive connections (Santarsiero 2015; Santarsiero & Louter 2016). The model accounts for a generic stress state by a governing equation expressed as a function of the stress tensor element, the strain rate and the temperature. It was noted that the experimental observations were in line with the model predictions, for varying temperature and hydrostatic angle.

From the above literature, the von Mises stress and the maximum principal stress are the most frequently used failure criteria in the continuum mechanics approach to predict cohesive failure in an adhesive connection. Furthermore, two solutions exist to solve the problem of stress singularities, i.e. the stress at a certain distance from the point of singularity or an averaged stress value over a given region. In the next paragraph several of the mentioned failure criteria are examined in the prediction of the failure load for cohesive failure in adhesive point-fixings.

8.4. Determination of failure criterion for cohesive failure in adhesive point-fixings

To determine the failure criteria for cohesive failure in adhesive point-fixings, a FEA model was created and validated with experiments to determine the occurring stresses and strains. Five failure criteria will be studied, in order to verify if they can predict the failure load for cohesive failure in adhesive point-fixings for the two selected adhesives.

8.4.1. Test configuration

Ten test specimens were fabricated for each adhesive. These specimens were tested in a pure tensile test with a displacement rate of 1 mm/min until failure. One could assume that only tensile forces would be present in the adhesive layer with this test configuration. However, where the two materials join, the lateral strain is limited by the stiffer adherent. This constraint will cause large radial shear stresses in the adhesive at the interface due to the Poisson effect. These radial shear stresses together with the tension will introduce complex stresses in the adhesive (Adams et al. 1997). This was also shown in the research of Jeandrau (1991); FEA demonstrated that the adhesive layer in a tensile butt joint was in a complex state of stress.

The tests were performed with the two selected adhesives (SO and 3M) and a connector diameter of 30 mm with a connector height of 30 mm. For the determination of a failure criterion for cohesive failure in adhesive point-fixings, the main focus is on the adhesive layer as such; not on the entire connection. This means that the support of the adhesive point-fixings described in this chapter was not at 6 times the connector diameter as it was in Chapter 4. The glass plate had a length of 250 mm, a width of 100 mm and a thickness of 12 mm. For SO, annealed glass and for 3M, fully tempered glass was used since high stresses were expected with the latter. SO was applied with a thickness of 2 mm while 3M was applied with a thickness of 0.2 mm. Before testing, the 20 specimens were stored for four weeks in a climate chamber at a constant temperature of 20°C and a relative humidity of 60% without any UV-radiation.

The glass plate was placed on top of a base plate. The top side of the glass panel was clamped on two sides at a distance of 75 mm from the edges. As such, a 'free' square of 100 x 100 mm emerged. All metal parts which were in direct contact with the glass panel were provided with a Teflon® layer in order to ensure good and safe contact between the glass and metal parts. The test setup is illustrated in Figure 8.9. The base plate was bolted onto a universal testing machine (UTM) with a load cell of 10 kN for the MS-polymer and a load cell of 50 kN for the epoxy. A threaded rod which introduces the tensile force, is screwed in the connector at one end and clamped in the UTM at the other end. Special effort was made to align the connector with the rod to eliminate parasitic forces and bending moments.
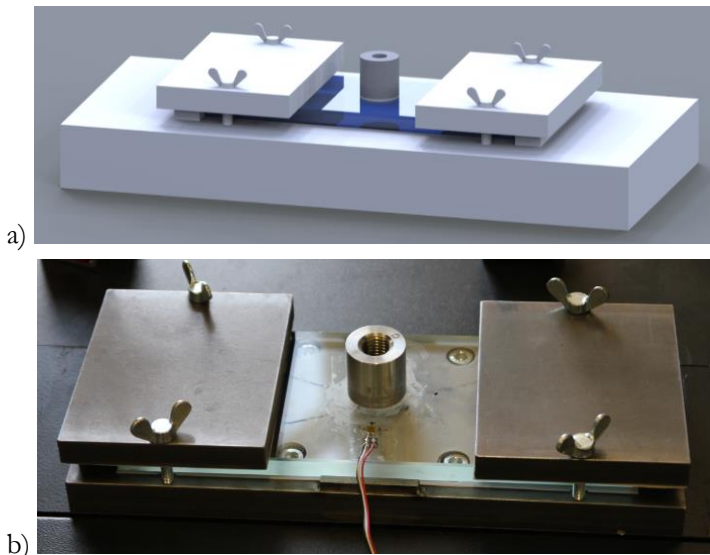

a)

b)

FIGURE 8.9: TENSILE TEST CONFIGURATION: A) VIZUALISATION AND B) ACTUAL CONFIGURATION.

To determine the occurring stresses and strains in the adhesive layer, a finite element model was constructed. Although the used FEA model is based on the numerical tensile local model of Chapter 4, the strains on the glass panel and the deformation of the glass panel were measured using strain gauges and a LVDT, respectively. Three strain gauges were placed on each test specimen to measure the radial strains. The gauges were located at 30 mm from the centre of the plate, as depicted in Figure 8.10 together with the position of the LVDT.
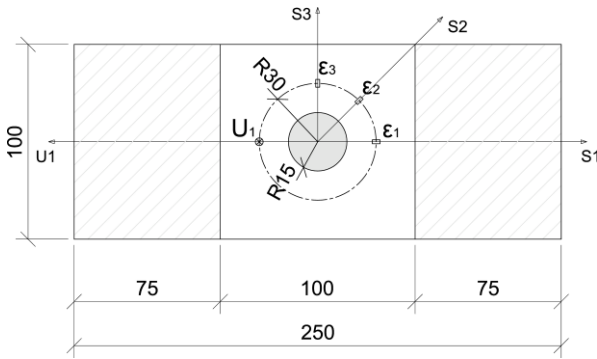
FIGURE 8.10: LOCATION OF STRAIN GAUGES AND LVDT.

The mean failure load for cohesive failure of SO was 1062 (± 183) N and 12766 (± 530) N for 3M. A typical cohesive failure of SO and 3M is depicted in Figure 8.11. For SO rupture started at the interface with the connector and then continued in the adhesive. The starting point is visible in the top left at the connector in Figure 8.11a. A thin film of epoxy remained when cohesive failure occurred with 3M (Figure 8.11b); this phenomenon is also known as the thin-layer cohesive (TLC) failure pattern (Lee et al. 2009).

FIGURE 8.11: FRACTURE SURFACES OF COHESIVE FAILURE WITH A) SOUDASEAL 270 HS AND B) 3M™ SCOTCH-WELD™ 9323 B/A.

8.4.2. Numerical model

As mentioned above, the numerical model is based on the numerical tensile model described in Chapter 4. Due to symmetry only a quarter of the glass plate was modelled. Local refinement of the mesh pattern around the connection was introduced. The adhesive layer was connected to the glass and the metal connector by means of a tie-constraint, with the adhesive layer each time as the slave surface. The build-up of the model is depicted in Figure 8.12. The force was applied on a reference point, tied by means of a multiple-points-constraint to the borehole surface in the connector.
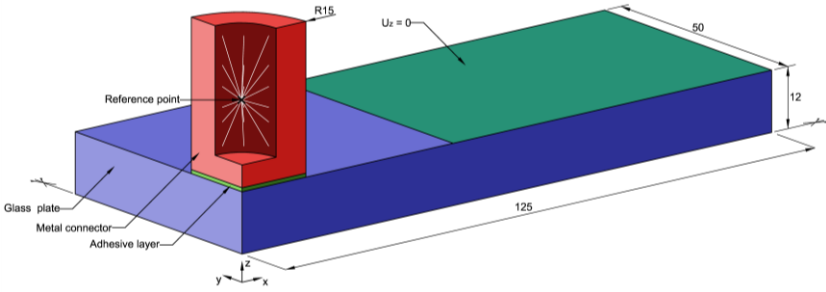
FIGURE 8.12: BUILD-UP OF THE NUMERICAL MODEL (ALL DIMENSIONS IN MM.).

The element type and mesh size for each component are summarized in Table 8.1. The given mesh size is the length of an element in the square at the centre of the considered component. The number of elements along the adhesive thickness is set on 16 for the FEA model with SO and 5 with 3M. The ratio of the height to the width of an element in the centre of the adhesive layer is 1/1 and 1/1.6 for SO and 3M, respectively. A maximum of a ratio 1/2 is advised (ABAQUS 2014). A visualisation of these ratios is given in Figure 8.13.

TABLE 8.1: ELEMENT SIZE AND TYPE FOR THE THREE MATERIALS.

Material	Element type	Element size [mm]	
		SO	3M
Glass	C3D20R	0.5	0.1
Steel	C3D20R	0.5	0.1
MS-polymer	C3D20H	0.125	/
2c-epoxy	C3D20	/	0.025

a)   b)
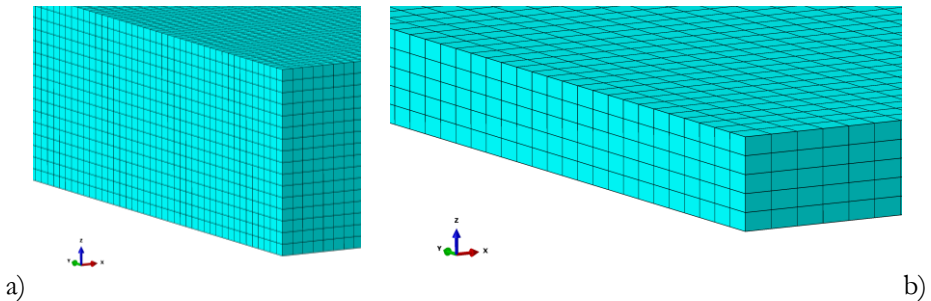
FIGURE 8.13: RATIO OF AN ELEMENT IN THE ADHESIVE LAYER FOR A) SO AND B) 3M.

The material properties of the two selected adhesives were determined in Chapter 3 and also used in Chapter 4. For SO, the stretch based phenomenological material model developed by Ogden (1973) gave the best results. The mathematical expression of the Ogden material model is given by Eq. (8.11). The obtained material constants μ_1 and α_1 are equal to 0.781 and 3.889, respectively. For 3M, the material characteristics were determined and were equal to 2267.37 MPa and 0.39 for the Young's modulus and the Poisson's ratio, respectively. The adherents were modelled using linear elastic behaviour, using the material properties given in Table 8.2.

$$W = \sum_{i=1}^{N} \frac{2\mu_i}{\alpha_i} \left(\lambda_1^{\alpha_i} + \lambda_2^{\alpha_i} + \lambda_3^{\alpha_i} - 3 \right) \tag{8.11}$$

TABLE 8.2: MATERIAL PROPERTIES OF THE ADHERENTS.

	Young's modulus E [MPa]	Poisson's ratio v [-]
Stainless steel EN10088-1 1.4404	195000	0.30
Annealed float glass	70000	0.23

8.4.3. Validation

As mentioned above, the numerical model was validated by means of the strain at three locations and the deformation at one location. The comparison between the experimental and numerical values is given for three strain paths (S1, S2 and S3) and one deformation path (U1), as depicted in Figure 8.10. The validation is obtained for a tensile force of 0.5 kN for SO and 3 kN for 3M. The comparison for SO is depicted in Figure 8.14, where the full line represents the numerical values and the bullets the experimental values. The deformation of the glass panel was too small to measure accurately with the LVDT. The comparison for 3M is depicted in Figure 8.15. Although a certain scatter occurs on the experimental values, in general the numerical and experimental values correspond well. From the latter combined with that the FEA model is based on the validated numerical tensile model of Chapter 5, it can be concluded that the model is validated.
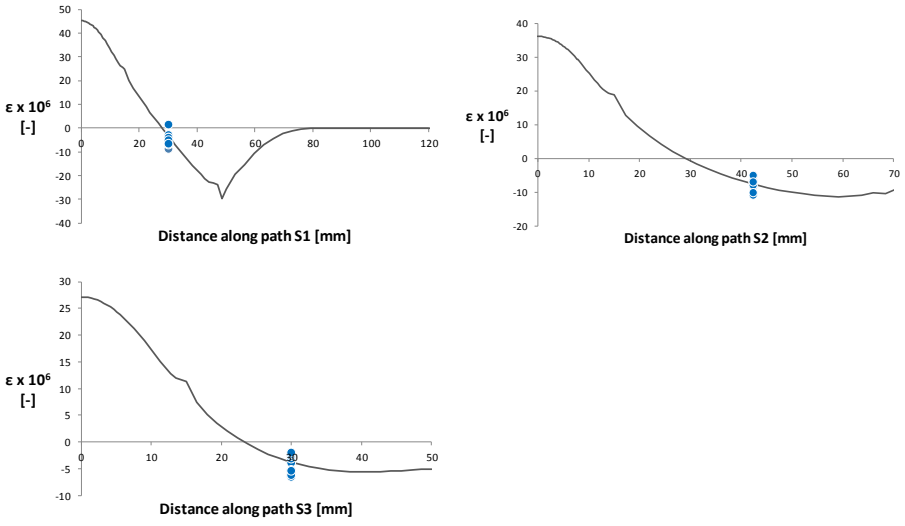
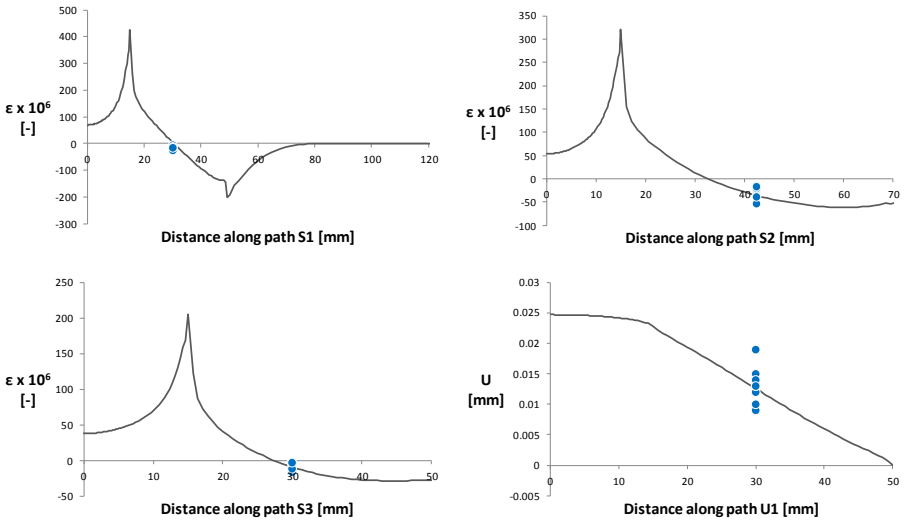**FIGURE 8.14**: COMPARISON BETWEEN EXPERIMENTAL AND NUMERICAL VALUES FOR SO.

FIGURE 8.15: COMPARISON BETWEEN EXPERIMENTAL AND NUMERICAL VALUES FOR 3M.

8.4.4. Determination failure criterion

The considered failure criteria were maximal principal stress, von Mises stress, shear stress, strain and shear strain. The numerical failure load was set as the load at which the stress or strain reaches a critical value. These critical values were obtained from the small-scale tests on bulk material in Chapter 3 and are given in Table 8.3. The experimental and numerical failure loads according to the failure criteria are given in Table 8.4.

TABLE 8.3: CRITICAL VALUES FROM BULK MATERIAL

	SO	3M
σ [MPa]	4.6 ($\pm$ 0.57)	34.6 ($\pm$ 1.3)
ε [-]	0.97 ($\pm$ 0.028)	0.021 ($\pm$ 3.2 E-3)
τ [MPa]	2.5 ($\pm$ 0.061)	22.4 ($\pm$ 0.36)
γ [-]	0.90 ($\pm$ 0.034)	0.060 ($\pm$ 5.3 E-3)

TABLE 8.4: EXPERIMENTAL AND NUMERICAL FAILURE LOADS FOR THE MAXIMAL STRESS/STRAIN

	SO	3M
Experimental	**1062 ($\pm$ 183) N**	**12766 ($\pm$ 530) N**
Maximal principal stress	1628 ($\pm$ 202) N	1276 ($\pm$ 46) N
von Mises stress	3769 ($\pm$ 468) N	2115 ($\pm$ 76) N
Shear stress	3718 ($\pm$ 92) N	6697 ($\pm$ 186) N
Strain	1812 ($\pm$ 54) N	2624 ($\pm$ 392) N
Shear strain	1081 ($\pm$ 41) N	15664 ($\pm$ 2400) N

The numerical failure loads for SO all overestimate the experimental failure load, except for the failure load obtained with the failure criterion **shear strain**. The latter even predicts the experimental failure load with a difference of 2%. With a load of 1081 N, the maximum occurring shear strain in the numerical model is equal to 0.90. This is the maximum shear strain from the TAST. Also the location of the maximum shear strain in the numerical model corresponds with the failure location in the experiments, i.e. the top of the adhesive, as depicted in Figure 8.16. For the 2c-epoxy almost all failure criteria underestimate the experimental failure load. As expected, this is due to the stress/strain singularities in the numerical model between the adhesive and the substrate material as a result of the squareness of the model. These concentrations are clearly visible in Figure 8.16 for the failure criterion of maximum principal stress.
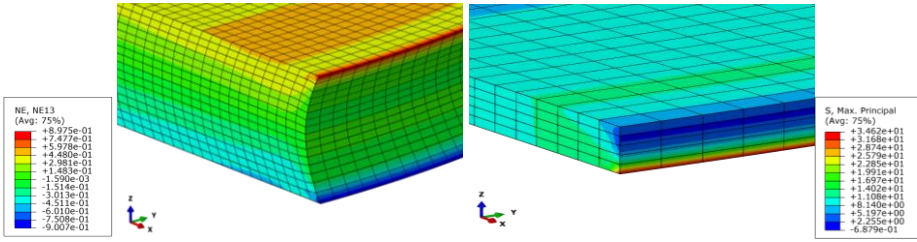
FIGURE 8.16: NUMERICAL RESULTS FOR THE SHEAR STRAIN IN SO AND THE MAXIMAL PRINCIPAL STRESS FOR 3M.

As discussed above, one of the two ways to deal with stress or strain singularities is to consider the stress or strain values at a certain distance of the maximal occurring stress or strain (Adams & Harris 1987; Zhao & Adams 1989; Ashcroft et al. 2009; Crocombe & Kinloch 1994; Whitney & Nuismer 1974; Clark & McGregor 1993; AD Crocombe et al. 1995; Zhao 1991; John et al. 1991). In this study, the distance was set to half the thickness of the adhesive and to the full thickness of the adhesive. The failure loads obtained when the numerical stress or strain at a distance of half the adhesive thickness from the stress or strain singularity is equal to the critical value are given in Table 8.5 and in Table 8.6 for a distance equal to the full adhesive thickness. As the stress or strain decreases away from the stress or strain singularity, the failure loads will increase. For the 2c-epoxy 3M only the shear stress failure criterion with the stress considered at a distance equal to the adhesive thickness predicts the experimental failure load. Taking into account the uncertainties of the experimental failure load and the critical values from bulk material, it can be concluded that this failure criterion predicts the failure load for stiff adhesives conservatively.

TABLE 8.5: EXPERIMENTAL AND NUMERICAL FAILURE LOADS AT A DISTANCE OF HALF OF THE ADHESIVE THICKNESS FROM THE MAXIMAL OCCURRING STRESS/STRAIN

	SO	3M
Experimental	**1062 (± 183) N**	**12766 (± 530) N**
Maximal principal stress	1621 (± 201) N	3450 (± 125) N
von Mises stress	7548 (± 937) N	5005 (± 181) N
Shear stress	7195 (± 178) N	9303 (± 276) N
Strain	4325 (± 128) N	6590 (± 985) N
Shear strain	2103 (± 80) N	21987 (± 8040) N

	SO	3M
Experimental	**1062 (± 183) N**	**12766 (± 530) N**
Maximal principal stress	1628 (± 202) N	3546 (± 128) N
von Mises stress	7927 (± 984) N	5520 (± 199) N
Shear stress	7547 (± 187) N	11894 (± 329) N
Strain	4502 (± 133) N	7079 (± 1058) N
Shear strain	2198 (± 84) N	26012 (± 2432) N

A general conclusion is formulated in Figure 8.17. For stiff adhesives, the failure load can be determined when the shear stress at a distance equal to the adhesive thickness from the maximum shear stress equals the maximum shear stress from bulk material. For more flexible adhesives, the failure load can be determined when the maximum numerical shear strain is equal to the maximum shear strain from bulk material. Between these types of adhesives, both failure criteria must be applied; the lowest failure load will be the actual failure load.
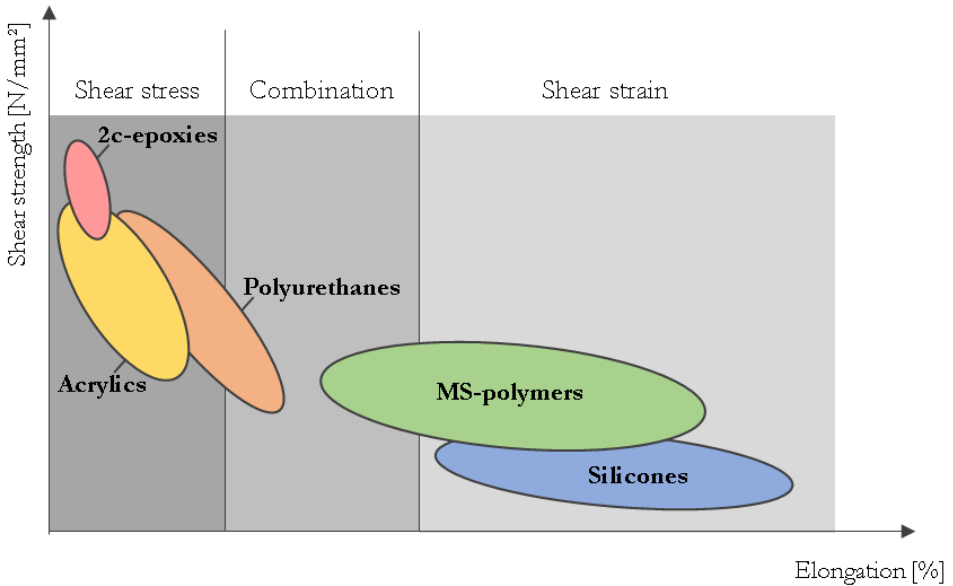

FIGURE 8.17: PROPOSED FAILURE CRITERIA FOR ADHESIVES FOR ADHESIVE POINT-FIXINGS.

8.5. Parametric study and experimental comparison

Together with the validated numerical tensile, shear and multi-axial local models, the obtained failure criteria enables a thorough investigation of the load eccentricity and multi-axial angle. The study was performed for the two selected adhesives, multi-axial angles of 0°, 22.5°, 45°, 67.5° and 90° and load eccentricities of 0 mm, 15 mm, 30 mm and 45 mm. The normal and transverse components of the force were determined for a maximum principal stress equal to 45 MPa in the glass. Also the components of the force were determined for a shear strain equal to 0.897 in the adhesive layer for the MS-polymer and for a shear stress of 22.42 MPa at a distance equal to the adhesive thickness from the maximum occurring shear stress for the 2c-epoxy. Furthermore the components of the force were determined for a maximum deformation of 4.5 mm of the glass, i.e. the span divided by 65 with the span equal to 300 mm (prEN 16612 2013). The outcome of this parametrical study is depicted in Figure 8.18. A comparison between the obtained numerical failure loads and the experimental failure loads from Chapter 5 is given in Table 8.7. Taking into account the sometimes large spread of the experimental results, the numerical model can predict the experimental failure loads mostly conservatively and accurately. From Figure 8.18, the stiff adhesive will locally strengthen the glass, causing a higher failure load for glass failure in tension. However, in shear the stiff adhesive will introduce higher stress concentrations in the glass than the flexible adhesive, causing lower failure loads for glass failure in shear. For failure in the adhesive, the flexible adhesive performs much better under tension than under shear. The opposite is true for the stiff adhesive as long as the eccentricity is not larger than 30 mm. With eccentricities larger than 30 mm, the peel stresses will be more dominate due to the increased bending moment. These peel stresses cause faster failure than in tension. For a similar deformation, larger forces are needed for the stiff adhesive compared to the flexible adhesive. This effect is due to the restrained glass deformations under the connector with the stiff adhesive. The glass will remain plane under the connector, while with the flexible adhesive the glass can deform freely which results in a larger deformation of the glass for the same load or in other words a lower load for the same deformation. This was also notable in the experiments (cfr. Figure 4.16 and Figure 4.17).
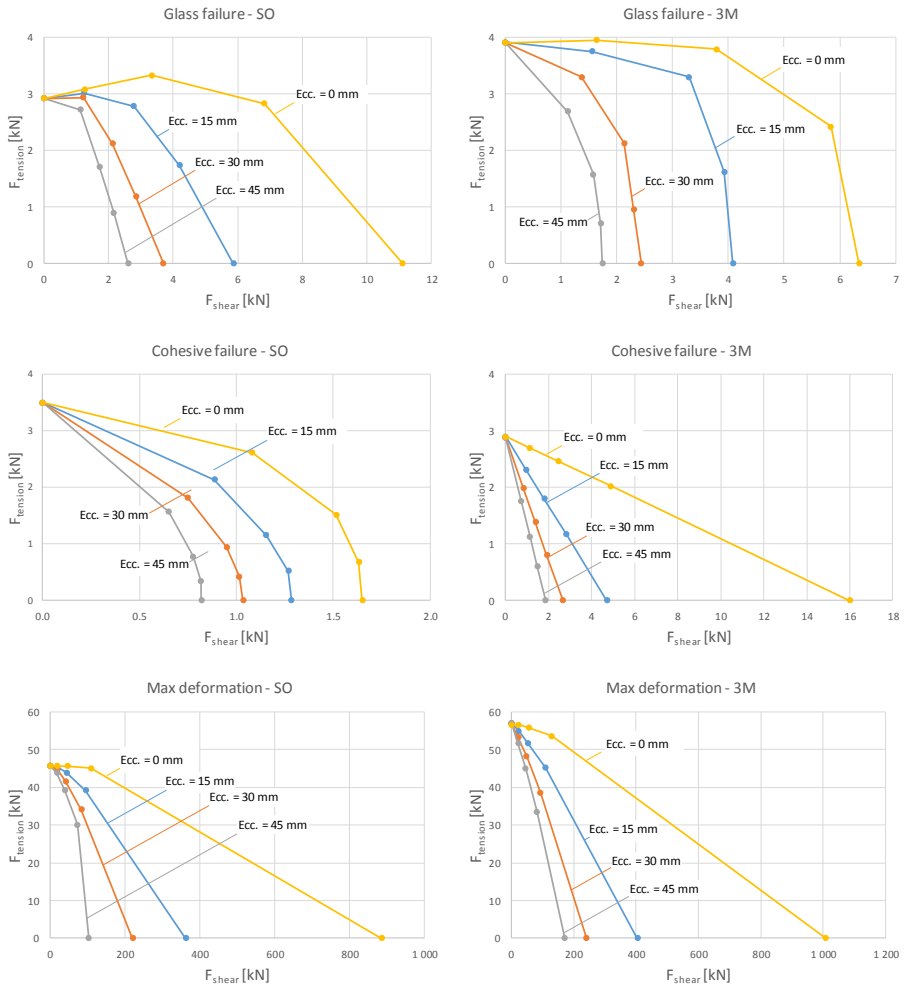
FIGURE 8.18: FAILURE LOADS COMPONENTS FOR GLASS FAILURE, COHESIVE FAILURE AND MAXIMAL DEFORMATION.

TABLE 8.7: COMPARISON BETWEEN EXPERIMENTAL FAILURE LOADS AND NUMERICAL FAILURE LOADS.

Type	Configuration	Exp. failure load [N]	Num. failure load [N]
SO	Tension Glass failure	$F_{tension} = 3161$ ($\pm$547.9)	$F_{tension} = 2924$
SO	Tension Cohesive failure	$F_{tension} = 3354$ ($\pm$520.1)	$F_{tension} = 3494$
SO	Shear Cohesive failure	$F_{shear} = 1531$ ($\pm$169.0)	$F_{shear} = 1650$
SO	Ecc. = 15 mm; $\theta = 45°$ Cohesive failure	$F_{tension} = F_{shear} = 1048$ ($\pm$102.5)	$F_{tension} = F_{shear} = 886$
3M	Tension Glass failure	$F_{tension} = 4697$ ($\pm$1345.0)	$F_{tension} = 3908$
3M	Tension Cohesive failure	$F_{tension} = 3510$ ($\pm$489.5)	$F_{tension} = 2900$
3M	Ecc. = 15 mm; $\theta = 45°$ Glass failure	$F_{tension} = F_{shear} = 4035$ ($\pm$546.6)	$F_{tension} = F_{shear} = 3297$

8.6. Summary and conclusions

In this chapter, the failure criteria for glass panels supported by adhesive point-fixings were determined.

For glass and adhesive failure, existing failure criteria were divided in two large groups, i.e. based on fracture mechanics or based on the classic material strength. In the former, the initial critical flaw depth has to be known. Non-destructive and destructive methods for the determination of the size of a flaw in a material are rather time consuming and expensive. To avoid the determination of the initial critical flaw depth, failure criteria according to the classical material strength can be used. For glass failure, in several standards, the 5% characteristic surface tensile strength with a 95% confidence level is given, where 45 MPa, 70 MPa and 120 MPa are the characteristic values of the bending strength of annealed glass, heat strengthened glass and fully tempered glass, respectively.

Also for failure in the adhesive in practice, a continuum mechanics approach is therefore often preferable. The existence of singularities in the stress or strain fields at critical points followed from literature. In a stiff adhesive connection, these singularities arise at the corners between the adhesive and the substrate material as a result of the squareness of the model. This was also noted in the FEA modelled with 3M. Two solutions exist to solve the problem of stress singularities, i.e. considering the stress at a certain distance from the point of singularity or an averaged stress value over a given region. To determine the failure criteria for adhesive point-fixings, an FEA model was modelled and validated with experiments to determine the occurring stresses and strains. The considered failure criteria were the maximum principal stress, the von Mises stress, the shear stress, the strain and the shear strain. The numerical failure load was set as the numerical stress or strain reaching a critical value. These critical values were obtained from the small-scale tests on bulk material in Chapter 3.

The failure load obtained from the failure criterion shear strain predicted the experimental failure load with a mere difference of 2% for SO. Due to the stress singularities in the adhesive layer with 3M the "stress at a distance" approach was applied for this adhesive. Only the shear stress failure criterion with the stress considered at a distance equal to the adhesive thickness from the stress singularity predicted the experimental failure load. It can be concluded that this failure criterion predicts the failure load for stiff adhesives conservatively. These criteria were also applied on the local FEA models from Chapter 4 to determine the numerical failure loads. The obtained failure criteria predicted the experimental failure loads conservatively and accurately. A general conclusion was formulated. For stiff adhesives, the failure load can be determined when the shear stress at a distance equal to the adhesive thickness from the maximum shear stress equals the maximum shear stress from bulk material. For more flexible adhesives, the failure load can be determined when the maximum numerical shear strain is equal to the maximum shear strain from bulk material. Between these types of adhesives, both failure criteria must be applied; the lowest failure load will be the actual failure load.

Part III

Design method
and future research

Chapter 9: Design method

> Look at situations from all angles,
> and you will become more open.
> *Dalai lama*

9.1.   **Introduction**

Before glass panels supported by adhesive point-fixings can be constructed, the glass panel and the adhesive connection have to be designed. In this design, for a given load, the different geometry and material parameters are assessed, such as the glass thickness, the connector diameter, adhesive type, etc. The design is an iterative process, as depicted in Figure 8.1.

9.2.   **Design method**

9.2.1.   Flowchart

For the design of glass panels supported by adhesive point-fixings, a flowchart is proposed, as depicted in Figure 9.1. The flowchart consists of several different steps, which are explained in the following paragraph.
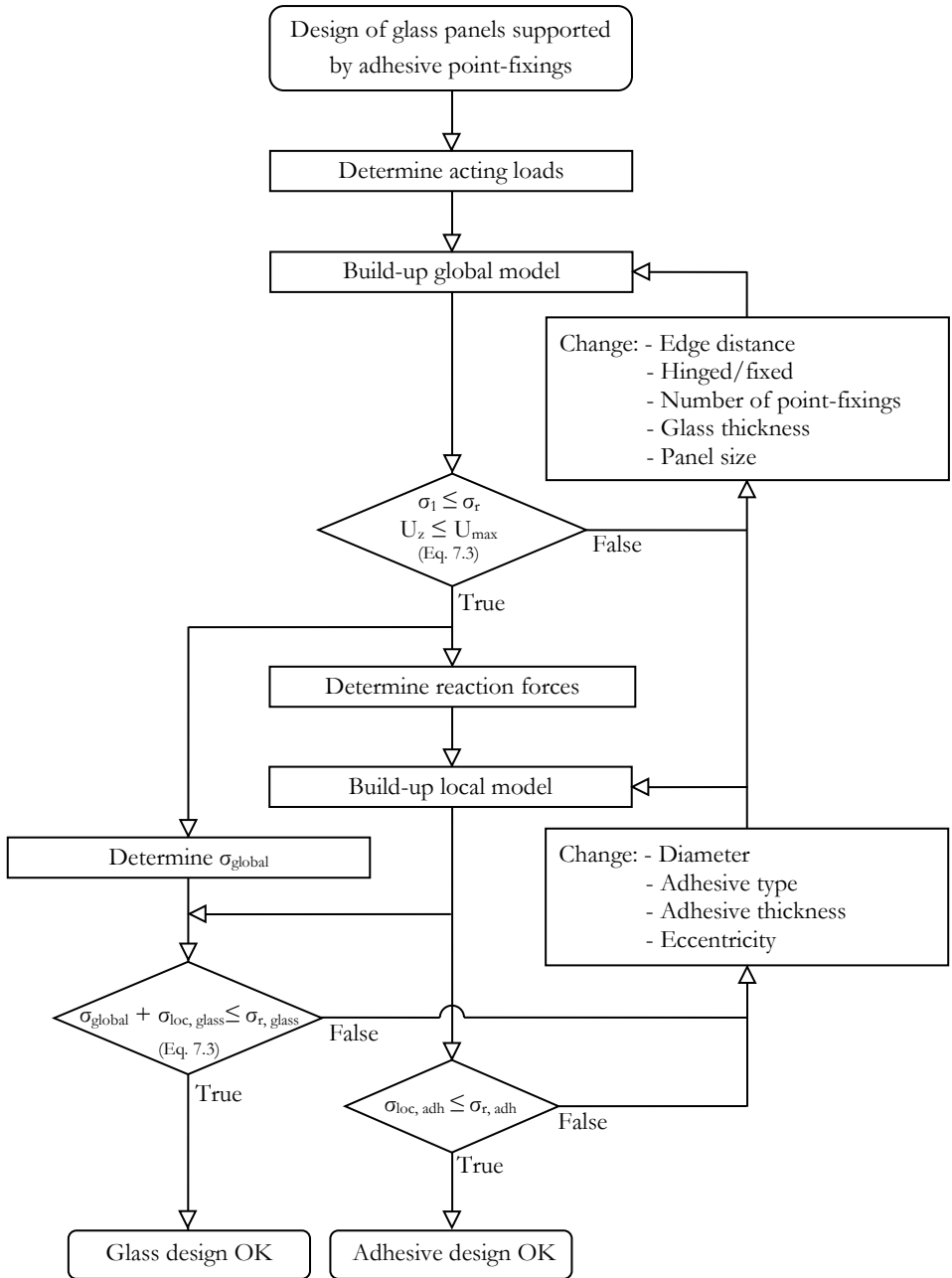
FIGURE 9.1: FLOWCHART FOR THE DESIGN OF GLASS PANELS SUPPORTED BY ADHESIVE POINT-FIXINGS.

9.2.2. Steps

The design flowchart in Figure 9.1 contains several steps that have to be carried out to achieve a valid design. These steps are clarified below.

> Design of glass panels supported by adhesive point-fixings

With this flowchart the design of glass panels supported by adhesive point-fixings can be completed. The flowchart is divided in two parts, i.e. the design of the glass panel and the design of the adhesive layer.

> Determine acting loads

The first step in the design is the determination of the acting loads on the glass panel. Depending on the configuration, the most frequent occurring loads will be the dead load of the glass panel, wind load and/or snow load. The order of magnitude of these loads can be determined with EN 1991-1-1, EN 1991-1-4 and EN 1991-1-3, respectively. Depending on the configuration and required specifications, other loads must be also taken into account, e.g. thermal loads, impact loads, etc.

> Build-up global model

The global model is a very general model, with the connections modelled as discrete points. As the connection can be pinned or clamped to the underlying structure, the point-fixing can be modelled in several ways, depending on the specific degrees of freedom, i.e. hinged or moment-resisting. These two boundary conditions are depicted in Figure 6.2. The geometrical parameters used in this model are the glass thickness, the number of point-fixings, the edge distance, the panel size and the boundary condition, i.e. hinged or fixed. For laminated glass panels, the EET method, described in Chapter 3, can be used to determine the effective glass thickness, i.e. Eq. (3.2) for the deflection-effective thickness and Eq. (3.3) for the stress-effective thickness.

For this type of model, shell elements are an obvious option. However, previous research has shown that shell elements in comparison with volumetric elements do not reduce the calculation time significantly and in some cases even increase the calculation time (De Jaegher 2014; Devos

2014; Tournoy 2014). Also shell elements did not give a good correspondence with the experimental values in Chapter 5. Following from this, the element type C3D20R is suggested with three elements over the glass thickness. A mesh refinement must be applied around the discrete supports, as depicted in Figure 5.7, with three elements between the panel edge and the point-fixing. This is equal to the number of elements that was proposed in Beyer's (2007) design-method.

$$\sigma_1 \leq \sigma_r$$
$$U_z \leq U_{max}$$

From the global model, the maximum principal stress and maximum deflection in the field are determined and are compared to the maximum classical material strength of glass and the maximum allowed deformation for glass panels. For the classical material strength, the 5% characteristic surface bending strength with a 95% confidence level is given in standards and literature (prEN 16612 2013; EN 12150-1 2015; ÖNORM B 3716-1 2009; NEN 2608 2014; DIN 18008 2010; EN 14179-1 2007; EN 1863-1 2012). The design value of strength for annealed glass can be calculated using Eq. (7.2) and (7.3) for prestressed glass, where 45 MPa, 70 MPa and 120 MPa are the characteristic values of the bending strength of annealed glass, heat strengthened glass and fully tempered glass, respectively. As the maximum occurring deformation is determined from the global model, this deformation will be larger than the actual occurring deformation, since the influence of the connector is not taken into account. The connection will locally prevent deformation of the glass panel. Hence, the deformation obtained from the global model will be conservative and safe.

Change: - Edge distance
       - Hinged/fixed
       - Number of point-fixings
       - Glass thickness
       - Panel size

When the occurring maximum principal stress and/or maximum deformation is larger than the maximum glass strength of glass or the maximum allowed deformation, the glass strength can be improved, by using e.g. heat strengthened glass or fully tempered glass, or the geometry can be altered to reduce the occurring stresses and/or deformation. As

depicted in Figure 8.1, this will be an iterative process. To reduce the stress or deformation of the glass panel following actions can be taken, in decreasing order of influence:

- Increase the number of connections;
- Decrease the panel size;
- Increase the edge distance;
- Increase the glass thickness;
- Change the boundary condition to pinned (for reducing the stress);
- Change the boundary condition to clamped (for reducing the deformation).

| Determine reaction forces |

When the occurring maximum principal stress and/or maximum deformation is smaller than or equal to the glass strength or the maximum allowed deformation, the reaction forces and reaction moments (F_z, F_x, F_y, M_x and M_y) on the connection can be obtained from the global model. These reaction forces and moments will be used in the next step.

| Build-up local model |

With the reaction forces and moments from the previous step the local model can be modelled. The numerical model is constructed with a more complex and dense mesh pattern than the global model. The local component is the glass panel with a diameter six times the diameter of the connector, as depicted in Figure 9.2 for a tensile force with simple supports along the circular support line. The material behaviour for more stiff adhesives can be modelled in a linear elastic manner, while for more flexible adhesives this linear behaviour will not be adequate. Elastic-plastic material modelling or even hyperelastic material behaviour imposes itself. The steel connector and the glass panel can be modelled assuming linear elastic behaviour.
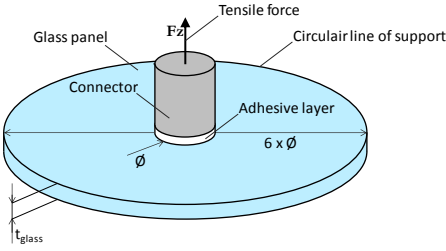
FIGURE 9.2: VISUAL REPRESENTATION OF THE LOCAL COMPONENT.

The forces acting on the local model are depicted in Figure 9.3. Due to the eccentricity in the hinged type, the shear forces F_x and F_y will introduce bending moments M_x and M_y, as depicted in Figure 9.4. The magnitude of these moments is equal to the respective shear forces multiplied by the eccentricity. The resulting shear forces and bending moments can be derived from Eq. (9.1) and (9.2), respectively.
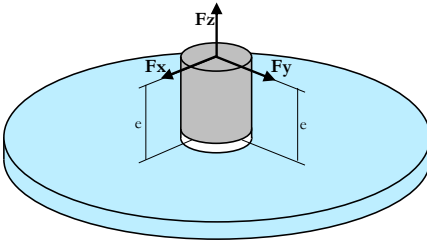

FIGURE 9.3: APPLIED FORCES ON THE LOCAL MODEL
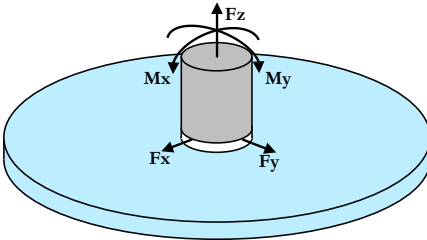
FIGURE 9.4: APPLIED FORCES AND BENDING MOMENT ON THE LOCAL MODEL

$$F_{xy} = \sqrt{F_x^2 + F_y^2} \qquad (9.1)$$

$$M_{xy} = \sqrt{M_x^2 + M_y^2} \qquad (9.2)$$

The normal reaction forces F_z can be applied on the numerical tensile model from Chapter 4, the resulting shear force F_{xy} on the numerical shear model and the resulting bending moment M_{xy} on the numerical moment model. These forces and the bending moment can also be applied on one model, i.e. the multi-axial model. As shown in Chapter 4, the applied force F, multi-axial angle θ and eccentricity e can easily be determined from Eq. (4.3), (4.4) and (4.5), respectively. This superposition is shown in Figure 4.40.

> Determine σ_{global}

From the global model the global stress σ_{global} is also obtained. This stress is the maximum occurring stress along the circumference around the point-fixing with a diameter equal to six times the connection diameter.

$\sigma_{global} + \sigma_{loc, glass} \leq \sigma_{r, glass}$

As the design is based on the SLG-method, the design consists of the superposition of the global and local component. From the local models, the occurring maximum principal stress in the glass panel in each model is determined. The sum of these local maximum principal stresses and the global stress must be lower than or equal to the maximum glass strength, as given in Eq. (9.3).

$$\sigma_{1,F_z} + \sigma_{1,F_{xy}} + \sigma_{1,M} + \sigma_{global} \leq \sigma_{r,glass} \qquad (9.3)$$

As stated above and in Chapter 5, the tensile model, shear model and moment model can be replaced by the multi-axial model. The sum of the occurring stresses in the tensile, shear and moment models is equal to the occurring stress in the multi-axial stress, as given in Eq. (9.4). Hence, Eq. (9.3) can be replaced by Eq. (9.5). The latter states that the sum of the occurring maximum principal stress in the multi-axial model and the global stress must be lower than or equal to the glass strength. This approach requires only two models, i.e. the global model and the multi-axial model.

$$\sigma_{F_z} + \sigma_{F_{xy}} + \sigma_M = \sigma_{multi} \tag{9.4}$$

$$\sigma_{1,multi} + \sigma_{global} \leq \sigma_{r,glass} \tag{9.5}$$

Change: - Diameter
       - Adhesive type
       - Adhesive thickness
       - Eccentricity

When the occurring stress in the glass panel at the connection exceeds the glass strength, the glass strength can be improved, by using e.g. heat strengthened glass or fully tempered glass or geometrical and material parameters can be changed. The same parameters as in the previous step where the global stress is examined, can be altered, i.e. the number of connections, the panel size, the edge distance, the glass thickness and the boundary condition. However, changing one of these parameters implies a new global model and new reaction forces.

The parameters affecting the local models can also be altered. For reducing the stress in the glass panel following actions can be taken, in decreasing order of influence:

- Decrease the eccentricity;
- Increase the connector diameter;
- Decrease the Young's modulus of the adhesive;
- Increase the adhesive thickness;
- Decrease the Poisson ratio of the adhesive.

Glass design OK

When the occurring stress in the glass panel at the connection does not exceed the glass strength, the glass panel will withstand the applied forces and the design for the glass panel is completed.

$\sigma_{loc, adh} \leq \sigma_{r, adh}$

To determine if the occurring stresses in the adhesive layer are lower than or equal to a critical value, the stress distribution in the adhesive layer must be known. As demonstrated in Chapter 6, the stress distribution with the

SLG-method in the adhesive layer can be obtained by only the local models. Furthermore, the local stresses can be derived from the multi-axial model with the magnitude, angle and eccentricity of the resulting force derived from Eq. (5.3), (5.4) and (5.5). The critical stress values are obtained from small-scale tests on bulk material of the adhesive. Which failure criterion has to be considered is formulated in Figure 7.18. For stiff adhesives, the adhesive will fail when the shear stress at a distance equal to the full adhesive thickness from the maximum shear stress exceeds the maximum shear stress from bulk material. For more flexible adhesives, failure will occur when the maximum numerical shear strain is equal to the maximum shear strain from bulk material. Between these types of adhesives, both failure criteria must be applied, both stresses have to be smaller than the corresponding critical value.

Safety coefficients should be applied to the characteristic values of the adhesive material properties, i.e. the critical values. An overall safety coefficient can be determined with available standards and guides, e.g. "The Structural Use of Adhesives" drawn up by the Institution of Structural Engineers (ISE) (1999). This standard gives an overall material safety coefficient, given by Eq. (9.6), in function of the type of loading, environment conditions, etc. The values of the various factors in Eq. (9.6) are given in Table 9.1. For adhesive connections subjected to long-term loading, the overall γ_m should not be less than 4.

$$\gamma_m = \gamma_{m1}\gamma_{m2}\gamma_{m3}\gamma_{m4}\gamma_{m5} \qquad (9.6)$$

The reduction with a factor of 2 for environmental conditions was also obtained for adhesive point-fixings exposed to moisture. The effect of moisture, temperature and UV-radiation on adhesive point-fixings is summarized in Appendix G

TABLE 9.1: RECOMMENDED VALUES FOR PARTIAL SAFETY COEFFICIENTS FOR ADHESIVE PROPERTIES (INSTITUTION OF STRUCTURAL ENGINEERS (ISE) 1999).

Source of the adhesive properties	γ_{m1}
Typical or textbook values	1.5
Values obtained by testing	1.25
Method of adhesive application	γ_{m2}
Manuel application, no adhesive thickness control	1.5
Manuel application, adhesive thickness control	1.25
Established application procedure with repeatable and controlled process parameters	1.0
Type of loading	γ_{m3}
Long-term loading	1.5
Short-term loading	1.0
Environmental conditions	γ_{m4}
Service conditions outside test conditions	2.0
Adhesive properties determined for the service conditions	1.0
Fatigue loading	γ_{m5}
Loading basically static	1.0
Adhesive subjected to significant fatigue loading	See Table 9.2

TABLE 9.2: PARTIAL COEFFICIENT γ_{m5} FOR FATIGUE STRENGTH.

Degree of inspection applications	γ_{m5}
Periodic inspection, good access	1.5
Periodic inspection, poor access	2.0
No inspection/maintenance	2.5

Change: - Diameter
- Adhesive type
- Adhesive thickness
- Eccentricity

When the considered stress in the adhesive layer exceeds the critical value, the adhesive strength can be improved, by using e.g. acrylics or 2c-epoxies or geometrical and material parameters must be changed. The same parameters as in the previous step where the global glass strength is examined, can be altered, i.e. the number of connections, the panel size, the edge distance, the glass thickness and the boundary condition.

However, changing one of these parameters implies a new global model and new reaction forces.

The parameters affecting the local models can also be altered. For reducing the stress in the adhesive layer following actions can be taken, in reducing order of influence:

- Decrease the eccentricity;
- Increase the connector diameter;
- Decrease the Young's modulus of the adhesive;
- Increase the adhesive thickness;
- Decrease the Poisson ratio of the adhesive.

Adhesive design OK

When the considered stress in the adhesive layer does not exceed the critical value, the adhesive connection can withstands the considered loads. Together with the glass design, a complete and safe design is obtained.

9.3.   Design example

To demonstrate the design of adhesive point-fixings between glass and metal, an example will be given below. Next configuration is considered:

- A vertical facade panel on the north-side of the building attached at an altitude of 100 m;
- Two tempered glass panels with a length of 2 m, width of 1 m and thickness of 8 mm laminated with PVB-interlayer of 0.76 mm;
- Four pinned adhesive point-fixings with a diameter of 50 mm, height of 15 mm and a corner distance of 50 mm;
- A stiff adhesive with a Young's modulus of 2000 MPa and Poisson ratio of 0.4;
- The adhesive thickness is 0.5 mm and has a critical shear stress of 20 MPa;
- The point-fixings are placed on the inside of the building and are sealed from moisture.

A visualisation of the considered configuration is depicted in Figure 9.5.
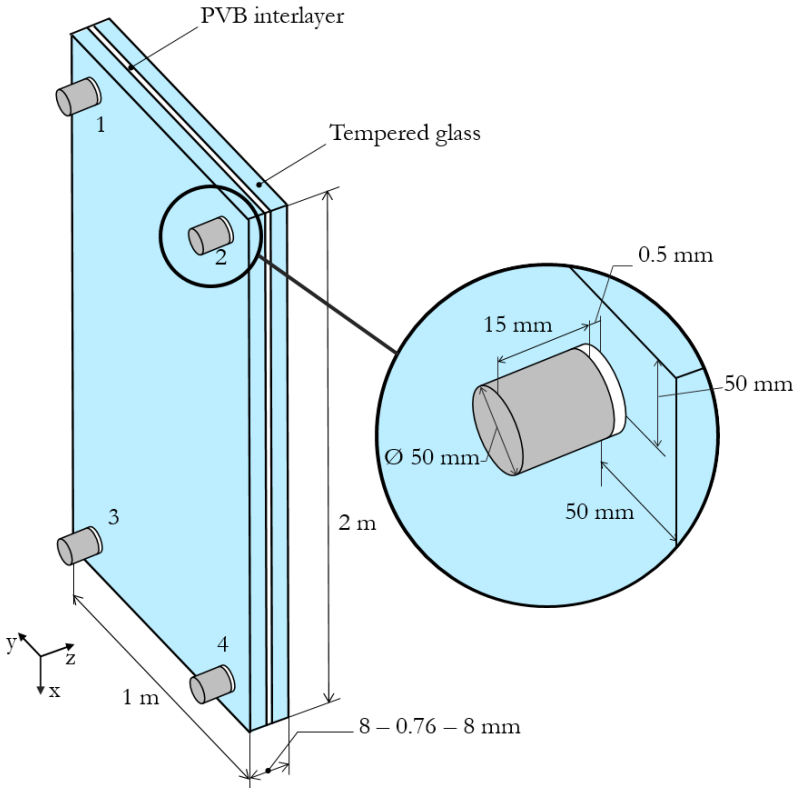
FIGURE 9.5: CONSIDERED CONFIGURATION FOR THE DESIGN EXAMPLE (NOT ON SCALE).

Note that with the above configuration, the outer glass panel is only attached with the interlayer to the inner glass panel. This is not common practice, as mechanical self-weight support will mostly be applied for this configuration. However, for the ease of the example and to demonstrate that mechanical self-weight supports can be omitted, mechanical self-weight supports were not considered. Furthermore, IGUs will mostly being used for façade elements. However, for the ease of the example the IGU functioning is being neglected, i.e. the loads applied on the outer panel of the IGU are considered to be on the laminated panel. The first step in the design of adhesive point-fixings in structural glass is the determination of the acting loads. The self-weight of the panel can be determined with the density of soda lime silica glass equal to 2500 kg/m³ (Haldimann et al. 2008). As tension is more severely for adhesive point-fixings, wind suction is considered. The magnitude of the wind pressure acting on the internal surfaces of a structure w_i can be determined with Eq. (9.7) (EN 1991-1-4).

$$w_i = c_{pi} \cdot q_p(z_i) \qquad (9.7)$$

c_{pi} is the pressure coefficient for the internal pressure. Worst case scenario is assumed, i.e. the area of the openings at the dominant face is at least 3 times the area of the openings in the remaining faces. The pressure coefficient for the latter scenario can be calculated with Eq. (9.8).

$$c_{pi} = 0.9 \cdot c_{pe} \tag{9.8}$$

c_{pe} is the pressure coefficient for the external pressure and is equal to 1 for the given configuration. In Eq. (9.7), $q_p(z_i)$ is the peak velocity pressure and can be determined with Eq. (9.9) with z_i the reference height for the internal pressure. The latter is equal to the reference height for the external pressure z_e and is equal to 100 m.

$$q_p(z_i) = c_e(z) \cdot q_b \tag{9.9}$$

$c_e(z)$ is the exposure factor and is equal to 2.92 according to Figure 4.2 in (EN 1991-1-4) for $h = 100$ m, $c_0 = 1$ (as no slope is considered, the orography factor will be 1), $k_l = 1$ (recommended value for the turbulence factor) and for terrain category IV, i.e. an area in which at least 15 % of the surface is covered with buildings and their average height exceeds 15 m. Furthermore, q_b is the basic velocity pressure and can be determined with Eq. (9.10).

$$q_b = \frac{1}{2} \cdot \rho \cdot v_b^2 \tag{9.10}$$

ρ is the air density and the recommended value is 1,25 kg/m³. v_b is the basic wind velocity and is considered to be equal to 25 m/s. With the above mentioned equations and values, the the wind pressure acting on the internal surfaces of the glass panel is equal to 1027 Pa. The characteristic values are multiplied with a partial safety coefficient of 1.35 for permanent load and a partial safety coefficient of 1.5 for variable load, this results in a design value of 3375 kg/m³ for the density and 1540 Pa for the wind load in ULS.

The next step in the design is the construction of the numerical global model. The effective thickness is determined with Eq. (6.2) for the deflection-effective thickness and Eq. (6.3) for the stress-effective thickness. The non-dimensional parameter η is considered to be equal to 0.85. The values for the deflection-effective thickness and the stress-effective thickness are given in Eq. (9.11) and (9.12), respectively.

$$\hat{h}_{eff,w} = \sqrt[3]{\cfrac{1}{\cfrac{0.85}{2 \cdot 8^3 + 12 \cdot 137.09} + \cfrac{1 - 0.85}{2 \cdot 12^3}}} = 10.98\ mm \qquad (9.11)$$

$$\hat{h}_{1,eff,\sigma} = \hat{h}_{2,eff,\sigma} = \sqrt{\cfrac{1}{\cfrac{2 \cdot 0.85 \cdot 3.38}{2 \cdot 8^3 + 12 \cdot 976.91} + \cfrac{8}{10.98^3}}} = 22.90\ mm \qquad (9.12)$$

As stated in Chapter 6, to avoid thermal stresses in the glass panel, only one point-fixing is fixed, as the other point-fixings are slotted or oversized. As no borehole are present, the allowed deformation is accomplished by the connectors. The used configuration is depicted in Figure 9.6.
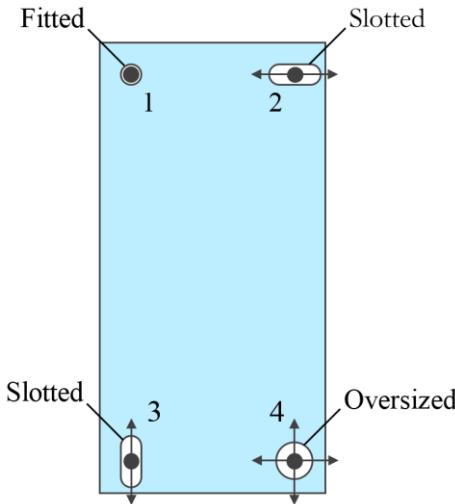
FIGURE 9.6: CONSIDERED BOUNDARY CONDITIONS FOR THE DESIGN EXAMPLE.

The maximum allowed deformation can be set as the span divided by 65 (prEN 16612 2013), i.e. a maximum deformation of 13.85 mm. As the standard prEN 16612 is under consideration for the new Eurocode for glass design, this maximum allowed deformation should applied cautiously. The maximal occurring deformation in the global numerical model is equal to 14.70 mm, as depicted in Figure 9.7. The occurring deformation is larger than the maximum allowed deformation. Geometrical and/or material parameters have to be changed to decrease the occurring deformation.
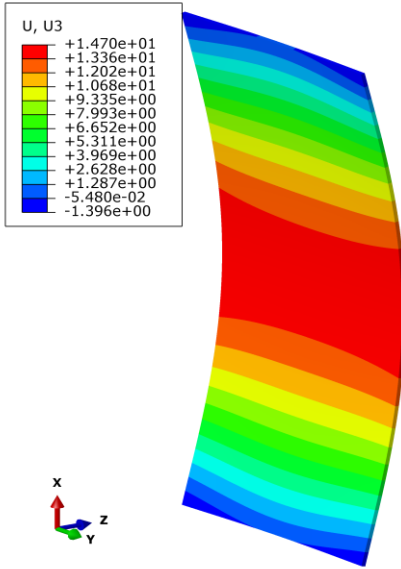
FIGURE 9.7: DEFORMATION OF THE GLASS PANEL (SCALE FACTOR OF 10).

The designer decides to increase the glass thickness to 12 mm and the corner distance from 50 mm to 100 mm. The effective glass thicknesses are given in Eq. (9.13) and (9.14). The maximal occurring deformation is now only 3.54 mm, as depicted in Figure 9.8, a reduction of more than a factor of four, compared to the first configuration.

$$\hat{h}_{eff,w} = \sqrt[3]{\frac{1}{\frac{0.85}{2 \cdot 12^3 + 12 \cdot 976.91} + \frac{1 - 0.85}{2 \cdot 12^3}}} = 21.59 \ mm \tag{9.13}$$

$$\hat{h}_{1,eff,\sigma} = \hat{h}_{2,eff,\sigma} = \sqrt{\frac{1}{\frac{2 \cdot 0.85 \cdot 6.38}{2 \cdot 12^3 + 12 \cdot 976.91} + \frac{12}{21.59^3}}} = 22.90 \ mm \tag{9.14}$$

To examine the maximal occurring stresses in the field, a thickness of 22.90 mm is applied for the global model. The glass strength is calculated with Eq. (7.3) and is equal to 81 MPa as given in Eq. (9.15), assuming short multiple wind gusts (k_{mod} = 0.74). The maximum occurring maximum principal stress in the field of the glass panel is equal to 6.82 MPa smaller than the glass strength.
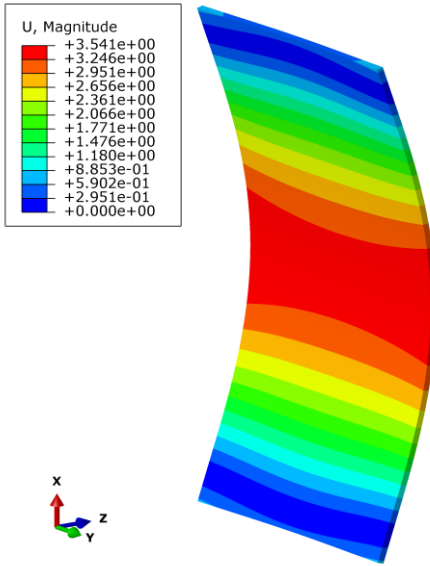
FIGURE 9.8: DEFORMATION OF THE GLASS PANEL WITH SIX POINT-FIXINGS (SCALE FACTOR OF 50).

$$f_{g,d} = \frac{0.74 \cdot 1 \cdot 45}{1.8} + \frac{1 \cdot (120 - 45)}{1.2} = 81 \; MPa \tag{9.15}$$

The next step in the design is the determination of the reaction forces of the point-fixings and the determination of the global stress around the point-fixings from the global model. The reaction forces for the point-fixings numbered as in Figure 9.5 and Figure 9.6 are summarized in Table 9.3, together with the maximum occurring stress along a perimeter with a diameter of 300 mm around the point-fixings.

TABLE 9.3: REACTION FORCES AND GLOBAL STRESSES.

	R_x (Shear) [N]	R_y (Shear) [N]	R_z (Tension) [N]	σ_{global} [MPa]
1	-768.30	2.03	-774.92	4.20
2	-777.43	0.0	-775.04	4.21
3	0.0	-2.03	-761.34	4.11
4	0.0	0.0	-761.22	4.11

These reaction forces are subsequently applied on the local models. The resulting shear force F_{xy} can be determined from the values in Table 9.3 and with Eq. (9.1). As mentioned above and in Chapter 5, only one local model can be considered, i.e. the multi-axial model. The applied force F, multi-axial angle θ and eccentricity

e can easily be determined with Eq. (5.3), (5.4) and (5.5), respectively. The considered resulting shear force Fxy, applied force F, multi-axial angle θ and eccentricity e are given in Table 9.4. As the considered configuration is pinned, no reaction moments are at the connections. Hence, the eccentricity is the height of the connector. Otherwise, the eccentricity was the sum of the height of the connector and the eccentricity by Eq. (5.5).

TABLE 9.4: RESULTING FORCE, MULTI-AXIAL ANGLE AND ECCENTRICITY FOR THE MULTI-AXIAL MODEL.

	F_{xy} [N]	F [N]	θ [°]	e [mm]
1	768.3	1091.2	44.8	15
2	777.4	1097.8	45.1	15
3	2.0	761.3	0.15	15
4	0	761.2	0	15

For the glass design, the sum of the maximum value for the maximum principal stress in the multi-axial model and the global stress must be less than the glass strength. The glass strength is already determined and is equal to 81 MPa as given in Eq. (9.15). Table 9.5 summarise the sum for the four point-fixings. Since the sum for any point-fixing exceeds the glass strength, the glass design is verified.

TABLE 9.5: SUM OF THE GLOBAL STRESS AND THE MAXIMUM VALUE FOR THE MAXIMUM PRINCIPAL STRESS.

	σ_{global} [MPa]	σ_1 [MPa]	$\sigma_{global} + \sigma_1$ [MPa]
1	4.20	7.24	11.44
2	4.21	7.24	11.45
3	4.11	6.55	10.66
4	4.11	6.52	10.63

The considered adhesive is a stiff adhesive. Hence, the failure criterion to be used is the shear stress at a distance equal to the adhesive thickness from the maximum shear stress. The latter must be lower than the critical design value. The critical characteristic value for the shear stress is 20 MPa. With the overall safety coefficient described by the Institution of Structural Engineers (ISE) (1999), the design value can be obtained. The overall safety coefficient γ_m is equal to 3.52 as given with Eq. (9.16). However, for adhesive connections subjected to long-term loading, the overall γ_m should not be less than four. Hence, the critical design value is equal to 5 MPa. In Table 9.6 the occurring shear stress in the adhesive layer at a

distance equal to the full adhesive thickness from the stress singularity for the four considered point-fixings is summarised. As the considered shear stress in the numerical model does not exceed the adhesive strength, the adhesive design is verified. Hence, the considered configuration can withstand the considered loads without glass or adhesive failure.

$$\gamma_m = 1.25 \cdot 1.25 \cdot 1.5 \cdot 1 \cdot 1.5 = 3.52 \qquad (9.16)$$

TABLE 9.6: OCCURRING SHEAR STRESS IN THE ADHESIVE LAYER AT A DISTANCE EQUAL TO THE FULL ADHESIVE THICKNESS FROM THE STRESS SINGULARITY.

	τ [MPa]
1	1.23
2	1.24
3	0.50
4	0.50

9.4.   Summary and conclusions

For the design of glass panels supported by adhesive point-fixings, a method was proposed in this chapter by means of a flowchart. The design is based on the SLG-method, a method developed by Beyer (2007) for glass panels supported by bolted point-fixings. In the flowchart, the design is divided in two parts, i.e. the glass design and the adhesive design. In the former, the glass panel is separated in a global component and a local component. The stress and deformation in the field are examined by means of the global model. The stresses in the vicinity of the connection are examined by the sum of the global stress and the maximum principal stress in the local models. For the adhesive design, only one local model can be considered, i.e. the multi-axial model. By applying the failure criteria from Chapter 7 the adhesive layer can be examined for the considered loads. The occurring stress in the glass panel and in the adhesive layer can be altered by chancing geometrical parameters and material parameters. When both design parts results in satisfactory values of the stresses and deformations, the design of glass panels supported by adhesive point-fixings for the considered configuration is completed.

Chapter 10: Conclusions and future research

> "The Answer to the Great Question...
> Of Life, the Universe and Everything...
> Is...
> Forty-two"
> said Deep Thought, with infinite majesty and calm.
> *Douglas Adams, The Hitchhiker's Guide to the Galaxy*

10.1. Introduction

Previous chapters have led to a design method for glass panels supported by adhesive point-fixings. The experimental studies in this dissertation focused on the validation of the numerical models (the total model, the local model and the global model) and the validation of the material models (linear elastic and hyper-elastic behaviour). Experiments were also conducted for the determination of a failure criterion and the determination of the influence of environmental conditions (humidity, temperature and UV-radiation). The experimental and numerical work performed in this work resulted in several conclusions, which are described in detail in the following paragraphs. Furthermore, suggestions for future research are given.

10.2.   Conclusions

The literature review in **Chapter 2** showed several advantages of adhesive point-fixings compared to bolted point-fixings;

- Stress redistributing ability with flexible adhesives;
- No weakening or residual stresses in the glass due to glass perforation;
- Use of regular annealed glass possible;
- Prevention of thermal bridges.

Furthermore, almost all design methods that have been developed over the years for bolted point-fixings in structural glass, make use of FEA. It is obvious that these methods require a significant computation time and consequently have a great cost, especially for complex geometries. Therefore Beyer developed the time-efficient SLG-method for the design of bolted point-fixings. Due to the separation into one global component that can be built up with a less dense mesh pattern and one local component that is built up with a more complex and dense mesh pattern, the stress distribution can be determined in a very time-efficient manner. This method appeared to offer a very appealing basis for the design of glass plates with adhesive point-fixings.

In **Chapter 3** the mechanical behaviour of a rubber-like adhesive (MS-polymer Soudaseal 270 HS) and a though adhesive (two-component epoxy 3M™ Scotch-Weld™ 9323) was obtained. Two-component epoxies and acrylates are thermosetting adhesives. The behaviour of these materials is typically elastic until failure and will fail at relatively small strains by the initiation and propagation of a crack. However, many adhesives are rubber-like materials, such as silicones and MS-polymers. Local deformations of the small-scale test specimens were measured through 3D-DIC. The comparison between the data from the test machine and the DIC-output revealed major differences between the measured deformations. This confirms that the use of DIC is needed to accurately measure the occurring strains during the small-scale tests. For Soudaseal 270 HS, the Poisson's ratio was determined to be 0.49. Consequently, the material is near to incompressible. After comparison of the numerical displacements with the experimental, it appeared that from the 98 calibrated hyper-elastic material models, the models calibrated by shear tests or by a combination of shear tests yielded the best results for Soudaseal 270 HS. In contrast to what is argued in literature, it is

not always advantageous to use and combine test data from as many experimental set-ups as possible. No optimal model was achieved, however, the material model developed by Ogden, calibrated by results from only shear tests or from a combination of tensile and compressive tests, predicted the experimental results the best based on the initial stiffness and deformation. For 3M™ Scotch-Weld™ 9323, the Young's modulus is equal to 2267.4 MPa, the Poisson's ratio to 0.39 and the shear modulus to 767.0 MPa and 723.9 MPa for the V-notched specimens and U-notched specimens, respectively.

These material models were used to validate the numerical local model in **Chapter 4** for different geometrical properties (three glass thicknesses and three diameter connectors), different material properties (two adhesive types) and three different load conditions (tension, shear and multi-axial load). By supporting the glass panel along a circumference with a diameter equal to six times the connector diameter, the deformation of the glass panel was also taken into account. This deformation causes important stress concentrations in the adhesive layer. For pure tension, it can be concluded from the experiments that the connector diameter is more determinative for more flexible adhesives and the glass thickness for rather stiff adhesives. The location of maximal strain was at the centre of the glass panel for the configuration with the flexible adhesive and at the outside of the connector with the stiff adhesive. This was also observed by the location of the glass crack initiation. For shear, the experiments demonstrated that the occurring strains are higher in case of a stiff adhesive and for a larger eccentricity. The multi-axial model showed that larger multi-axial angles will increase the bending moment acting on the glass panel. However, with increasing multi-axial angle the strains decrease more as the connection is loaded in shear instead of in tension. Shear forces will introduce lower strains in the glass panel than tensile forces will. Furthermore, the multi-axial local model can be used to directly determine the sum of the local stresses σ_{Fz}, σ_{Fxy} and σ_M.

In **Chapter 5**, the global model for the SLG-method is experimentally validated. A transversally loaded glass panel was experimentally investigated by means of a modular test frame for a glass panel of 1 m by 2 m supported by discrete point-fixings. The experimental results of four different edge distances were used to validate the numerical model. The numerical results corresponded very well with the experimental values

The total model for the SLG-method is experimentally validated in **Chapter 6**. The experimental results demonstrated that the highest stresses were reached for the smallest edge distances. This was also shown in the research in the steel area and the research on bolted point-fixings. As expected the deformations are significantly larger for small edge distances. The highest deformation occurs in the centre of the panel. The numerical analyses yield stress peaks which were not measured in the experiments. This highlights the benefits and necessity of numerical investigation. With a smaller corner and edge distance stress peaks are more prominent. The results from the parametric study point out that the maximum occurring stresses will increase with a decrease of the glass thickness, diameter of the connection, adhesive thickness and with an increase of the adhesive stiffness and width of the glass panel. Furthermore, the maximum deformation of the glass panel can be reduced by increasing the glass thickness, connection diameter, adhesive stiffness and by decreasing the adhesive thickness and width of the glass panel. The behaviour of laminated glass panels depends on the stiffness of the interlayer, the load duration and the glass thickness. Increasing the load duration corresponds to a decrease in interlayer stiffness. Increasing the interlayer stiffness and glass thickness will decrease the maximum principal stress and the maximum deformation. Compared to adhesive point-fixings, bolted point-fixings give higher peak stresses at the connection.

The suitability of the SLG-method for adhesive point-fixings was examined in **Chapter 7**. This validation of the SLG-method consisted of a FEA comparison between the stress distributions conducted on the one hand by the SLG-method and on the other hand by a FEA model in which the total glass plate with the adhesive connections is built up in detail with volumetric elements. Despite small deviations, the SLG-method predicted the occurring stresses in a glass panel supported by adhesive point-fixings conservatively and accurately. The stress distribution in the adhesive layer could also be determined with the SLG-method. For the latter, as the stress distribution consists of only the sum of the local stresses, these stresses were derived from the multi-axial model. The general conclusion was that the SLG-point method applied on adhesive point-fixings gives accurate and safe stress distributions. By applying this method the calculation of large glass plates connected with adhesive point-fixings can be done about 1000 times faster than when the glass plate is built up with a fine mesh pattern and about 100 times faster for smaller plates.

As with other civil structures, it is necessary for the design of an adhesive connection to calculate the strength of the connection. By means of a failure criterion this strength can be determined. In **Chapter 8** the failure criteria for the two selected adhesives were determined. The failure load obtained from the failure criterion *shear strain* predicted the experimental failure load with a mere difference of 2% for the MS-polymer Soudaseal 270 HS. Due to the stress singularities in the adhesive layer with the 2c-epoxy 3M™ Scotch-Weld™ 9323 B/A the "stress at a distance" approach was applied for this adhesive. Only the failure criterion *shear stress* with the stress considered at a distance from the stress singularity equal to the adhesive thickness predicted the experimental failure load. It could be concluded that this failure criterion predicts the failure load for stiff adhesives conservatively. The obtained failure criteria predicted the experimental failure loads in Chapter 5 conservatively and accurately. For adhesives between flexible adhesives and stiff adhesives, both failure criteria must be applied and the lowest failure load will be the actual failure load.

For the design of glass panels supported by adhesive point-fixings, a design method was proposed in **Chapter 9** by means of a flowchart. In the flowchart, the design is divided in two parts, i.e. the glass design and the adhesive design. In the former, the glass panel is separated in a global component and a local component. The stress and deformation in the field are examined by means of the global model. The stress in the vicinity of the connection is examined as the sum of the global stress and the maximum principal stress in the local models. For the adhesive design, only one local model can be considered, i.e. the multi-axial model. By applying the failure criteria from Chapter 7 the adhesive layer can be examined for the considered loads. The occurring stress in the glass panel and in the adhesive layer can be altered by chancing geometrical parameters and material parameters, i.e. the number of connections, panel size, edge distance, glass thickness, boundary condition, eccentricity, connector diameter, Young's modulus of the adhesive, adhesive thickness and Poisson ratio of the adhesive. When both designs are completed, the design of glass panels supported by adhesive point-fixings for the considered configuration is fulfilled.

10.3.   Future research

Throughout this dissertation several issues were addressed. However, some questions remain. Future research can help to give an answer to these questions.

The failure criteria obtained in Chapter 8 were determined for one loading configuration on one geometry. Although the failure criteria were also examined for the failure loads for the experiments in Chapter 4, a thorough investigation for other loading configurations on small-scale tests is recommended. The proposed tests consist of different geometrical parameters, such as different diameter connectors. Furthermore, the obtained failure criteria for adhesive point-fixings are based on the experimental results of only two adhesive types, so tests with more adhesive types may yield a more generally applicable criterion for a larger spectrum of adhesives.

The material models determined in Chapter 3 were obtained for ambient conditions. However, the results in Appendix G demonstrated that environmental conditions have a large influence on the mechanical behaviour of the adhesives. Material models developed by means of aged small-scale specimens will give a better understanding of the mechanical behaviour of aged adhesive connections. Also, these aged small-scale specimens will provide aged critical values and with these values it is possible to determine the failure load of aged adhesive connections.

As the experiments conducted in this dissertation were performed quasi-static with a certain displacement rate, long-term effects were not investigated. It would be interesting to investigate the long-term behaviour of adhesive point-fixings by means of creep tests, especially for ductile adhesives, with the applied loads in these creep tests in function of the failure load. Creep tests at ambient conditions will already give a better understanding. However, creep tests combined with artificial ageing will represent real-life applications even better, as environmental conditions and creep will occur simultaneously. Furthermore, in real-life applications the load will fluctuate, causing fatigue in the connection. Specimens where the load is applied in cycles and failure expressed in the number of cycles will provide information about the resistance of adhesive point-fixings against fatigue.

The conducted experiments in Appendix G revealed that moisture degraded the adhesive layer the most severely. The test specimens were exposed to 100% RH for two weeks, submerged for three weeks or six weeks. To be sure that the adhesives are completely saturated in these exposure periods, longer exposure periods for moisture are suggested. Furthermore, failure tests at elevated temperatures and lowered temperatures are also recommended, as the mechanical behaviour of adhesives changes significantly for temperatures below or above their glass transition temperature.

The safety coefficients for the characteristic values of the adhesive material properties, i.e. the critical values, given in Chapter 9 are derived from literature, i.e. "The Structural Use of Adhesives" drawn up by ISE (1999). This standard gives an overall material safety coefficient, given by Eq. (9.6), in function of the type of loading, environment conditions, etc. With the performed experiments and the experiments described above, a calibration of these safety coefficients will be possible and interesting, as not many standards are available to determine the safety coefficients for adhesive material properties.

As will be stated in the future Eurocode about glass, a glass consequence class (GCC) will have to be applied for glass design in the future. For non-structural glass components that cannot harm people when they fail, only service limit state (SLS) and ultimate limit state (ULS) have to verified. However, for structural glass components or glass components that can harm people, the situation during and after failure also have to be considered. For the post-fracture situation, two situations have to be verified, i.e. one panel has failed and all the panels have failed. The research of Belis et al. (2012) demonstrated that the tested adhesive point-fixings could take the impact of a 4 kg ball drop from 3 m, however, for the post-fracture situation the tempered glass configuration failed due to thin layer failure of the glass, and not to failure of the adhesive bond. These promising results demonstrate that more investigation is needed into the behaviour of adhesive point-fixings during impact or fracture and for post-fracture situations.

Part IV
Appendices

Stiff adhesive point-fixings in the Ciudad Financiera del Banco Santander
in Boadilla del Monte (Madrid) constructed by Bellapart
© Bellapart

Appendix A: Material models

In this appendix, the 14 considered material models of Chapter 3 are presented. Rivlin (1948) proposed a phenomenological theory, with the assumption that elastomers with elastic behaviour are isotropic and quasi incompressible. The elastic properties are expressed by the strain energy function W. The polynomial formulations of the strain energy function in terms of strain invariants or principal extension ratios is given in Eq. (A.1). His theory was based on the previous phenomenological theory of Mooney (1940). This elastic theory is also the starting point of several other developed material models (Chang et al., 1991; Yeoh & Fleming, 1997; Boyce, 2000; Arruda, 2000; Pucci & Saccomandi, 2002; Duarte & Achenbach, 2003). The models relying on the strain energy function assumed initially that there is no compressibility possible. With the latter assumption, I_3 is equal to 1. With the infinite sum replaced by a finite sum of N terms, the polynomial model of the strain energy function for incompressible materials is obtained, given by Eq. (A.2). The number of coefficients to be determined depends on the degree N of the polynomial. This value rarely exceeds three, because otherwise too many parameters have to be determined (Dias, 2012).

$$W = \sum_{i+j+k=1}^{\infty} C_{ijk} (I_1 - 3)^i \cdot (I_2 - 3)^j (I_3 - 1)^k \qquad \text{(A.1)}$$

$$W = \sum_{i+j=1}^{N} C_{ij} (I_1 - 3)^i \cdot (I_2 - 3)^j \qquad \text{(A.2)}$$

A.1.   Mooney-Rivlin

The Mooney-Rivlin model is a specific form of the basic (polynomial) model, in which the degree of the polynomial N is set equal to 1 (Mooney, 1940; Rivlin, 1948). The strain energy function for the Mooney-Rivlin material model is given in Eq (A.3). C_{10} and C_{01} are the material parameters (Marckmann & Verron, 2006).

$$W = C_{10}(I_1 - 3) + C_{01}(I_2 - 3) \qquad \text{(A.3)}$$

A.2. Neo-Hooke

The phenomenological model of Neo-Hooke is a simplified form of the Mooney-Rivlin model, where C_{01} is equal to zero, as can be seen in Eq (A.4) (Treloar, 1943). The strain energy function is only in function of the first invariant I_1. The Neo-Hooke model is the simplest hyper-elastic model, and is suitable when there is little test data available, for example, from only one load configuration. The characteristic S-shape of the stress-deformation diagram cannot be obtained with this model, as the model is too simple to be able to model a difference in curvature at large deformations. However for small deformations ($\lambda < 1.5$), the model provides sufficient accuracy (Steinmann, Hossain & Possart, 2012).

$$W = C_{10}(I_1 - 3) \tag{A.4}$$

A.3. Gent-Thomas

The phenomenological model proposed by Gent and Thomas is similar to the Mooney-Rivlin model, with the only difference that the natural logarithm is taken from the second term (Gent & Thomas, 1958). The formulation of the strain energy function of the Gent-Thomas model is given in Eq. (A.5). The remarks on this model are the same as for the model of Neo-Hooke. The model is not able to correctly predict large deformations because no higher terms of I_1 are present, but on the other hand it gives a good approximation for the behaviour at small strains (Steinmann, Hossain & Possart, 2012; Beda, 2007).

$$W = C_{10}(I_1 - 3) + C_{01}\ln\left(\frac{I_2}{3}\right) \tag{A.5}$$

A.4. Hart-Smith

Hart-Smith (1966) and Crisp (1967) also proposed a strain energy function and tried to achieve an even better accuracy. The Hart-Smith model is expressed with Eq. (A.6), (A.7) or with (A.8), with C_{10}, C_1 and C_{01} material parameters. Research by Hossain and Steinmann (2012) showed that the model of Hart-Smith gives better approaches and predictions than the Mooney-Rivlin model. This is due to the fact that the latter has only two material parameters, while the Hart-Smith model uses three. In addition, the logarithmic term provides a more accurate approximation of the stiffness at small strains.

$$\frac{\partial W}{\partial I_1} = C_{10}\exp(C_1[I_1 - 3]^2) \tag{A.6}$$

$$\frac{\partial W}{\partial I_2} = \frac{C_{10}\,C_2}{I_2} \tag{A.7}$$

or

$$W = C_{10}\left[\int \exp(C_1[I_1 - 3]^2)\,dI_1 + C_2\ln\left(\frac{I_2}{3}\right)\right] \tag{A.8}$$

A.5. Ogden

Although this phenomenological model is also expressed by the strain energy function, this function is directly expressed in function of the principal extension ratios λ_1, λ_2 and λ_3 for the Ogden model (Ogden, 1972). The strain energy function according to Ogden is given by Eq. (A.9), with λ_i the principal extension ratios according to the main axes. μ_i and α_i are the material parameters and have to be determined by means of test results. In order to meet the stability condition, the product of μ_i and α_i must be positive (Hosseini & Steinmann, 2012). It is stated that this strain energy function with the number of terms equal to three ($N = 3$), gives a sufficiently accurate approximation of the S-shaped behaviour of the material (Shariff, 2000; Marckmann & Verron, 2006). The model is able to simulate the behaviour at large deformations and will become even more accurate with more data from a variety of experimental tests.

$$W = \sum_{i=1}^{N} \frac{\mu_i}{\alpha_i}\left(\overline{\lambda_1}^{\alpha_i} + \overline{\lambda_2}^{\alpha_i} + \overline{\lambda_3}^{\alpha_i} - 3\right) \tag{A.9}$$

With $N = 1$ and $\alpha_1 = 2$ in the Ogden model, the Neo-Hooke model is obtained, directly expressed in function of the principal extension ratios (Bol & Reese, 2006). The latter is expressed by Eq. (A.10) where the material parameter C_{10} is equal to $\mu_1/2$. The models of Ogden and Neo-Hooke give for a given set of material parameters, theoretically the same expression, although they have a different structure. Besides Ogden others also develop their own model based on existing models, where the strain energy function is written as a function of the principal extension ratios (Shariff, 2000; Attard & Hunt, 2003, 2004).

$$W = \frac{\mu_1}{2}\left(\lambda_1{}^2 + \lambda_2{}^2 + \lambda_3{}^2 - 3\right) = C_{10}(I_1 - 3) \tag{A.10}$$

A.6.   Reduced polynomial model - Yeoh

The phenomenological model according to Yeoh is based on the polynomial model, in which the influence of the second invariant is assumed irrelevant (Yeoh, 1990). The strain energy function without I_2 is given in Eq. (A.11). The model is a reduction of the polynomial model and is thereby also called the reduced polynomial model (Peeters & Kussner, 1999). The Yeoh model is obtained by aborting the infinite sum after three terms. The mathematical expressing is given in Eq. (A.12). This model is used quite a lot, as it provides the opportunity to describe large deformations. In addition, the model is able to predict the behaviour of different load configurations with test data from only one test configuration.

$$W = \sum_{i=1}^{\infty} C_{i0} \, (I_1 - 3)^i \tag{A.11}$$

$$W = C_{10}(I_1 - 3) + C_{20}(I_1 - 3)^2 + C_{30}(I_1 - 3)^3 \tag{A.12}$$

In order to achieve an even better prediction of the mechanical behaviour, Yeoh (1993) modified the model, adding a correction term to the expression for the strain energy function, as given by Eq. (A.13). The parameters A and B are two additional material parameters. The modified model Yeoh consists of two mechanisms where one mechanism (first term) mainly dominates small strain, while the second mostly models large deformations (Yeoh & Fleming, 1997).

$$W = \frac{A}{B}\left[1 - e^{-B(I_1-3)}\right] + \sum_{i=1}^{\infty} C_{ij} \, (I_1 - 3)^i \tag{A.13}$$

A.7.   Gent

Gent proposes a material model, which also uses only the first invariant (Gent, 1996), as expressed by Eq. (A.14). In this expression J_m is a value for the finite extension of the polymer chains and μ represent the shear modulus. The model has a very good validity for large deformations, but is inadequate for small deformations (Pucci & Saccomandi, 2002).

$$W = -J_m . \frac{\mu}{2} \ln\left(1 - \frac{I_1 - 3}{J_m}\right) \tag{A.14}$$

A.8. Yeoh-Fleming

The Gent model can be combined with the correction term by Yeoh, allowing better approximations at small strains. The extended Yeoh model is called the Yeoh-Fleming model (Yeoh & Fleming, 1997). The formulation of the latter is given by Eq. (A.15). Note that the material parameters increases from two to four.

$$W = \frac{A}{B}\left[1 - e^{-B(I_1 - 3)}\right] - C(I_m - 3)\ln\left(1 - \frac{I_1 - 3}{I_m - 3}\right) \tag{A.15}$$

With:

- $C = \frac{\mu}{2}$;
- $J_m = I_m - 3$.

A.9. Pucci-Saccomandi

Pucci and Saccomandi add an extra term to the strain energy formulation of the model of Gent, so that it also depends on the second invariant, as given by Eq. (A.16) (Pucci & Saccomandi, 2002). Due to the addition of the second invariant in a logarithmic form, the initial high stiffness for small strains can be modelled much better than when using the model of Gent (Steinmann et al., 2012).

$$W = -J_m \frac{\mu}{2}\ln\left(1 - \frac{I_1 - 3}{J_m}\right) + C_2\ln\left(\frac{I_2}{3}\right) \tag{A.16}$$

A.10. Lopez-Pamies

Lopez-Pamies proposes a phenomenological model that also only depends on the first invariant, as the Neo-Hooke, Yeoh and Gent model. The number of material parameters is kept as small as possible in the model (Lopez-Pamies, 2010). The strain energy function for the Lopez-Pamies material model is given in Eq. (A.17). Validation of the model shows that a good approximation of the material behaviour is obtained, i.e. the characteristic S-shape of the stress-strain diagram is well approximated at large deformations. Even more important is the good simulation of the high initial stiffness at small strains (Steinmann et al., 2012).

$$W = \sum_{i=1}^{N} \frac{3^{1-\alpha_i}}{2\alpha_i}\mu_i\left(I_1^{\alpha_i} - 3^{\alpha_i}\right) \tag{A.17}$$

A.11. Van der Waals

The phenomenological model of Van der Waals is also known as the Kilian model, where the polymer is considered to be an ideal gas and the polymer chains are simulated as particles. The strain energy function is a function of the generalized invariant $\tilde{I}$ and is expressed by Eq. (A.18) (Kilian, 1980), with η, a, λ_m and β the material parameters. The model has micromechanical foundations, but with the introduction of the phenomenological parameter β, the model is still considered as phenomenological (Kaliske & Rothert, 1997; Marckmann & Verron, 2006). Recent research shows that the model with four parameters is not more accurate than the Lopez-Pamies model (Hossain & Steinmann, 2012). In addition, the model is only applicable for deformations that are smaller than the locking stretch (Peeters & Kussner, 1999).

$$W = -\mu[\lambda^2{}_m - 3][\ln(1 - \eta) + \eta] - \frac{2}{3}a\mu\left(\frac{\tilde{I} - 3}{2}\right)^{\frac{3}{2}} \qquad \text{(A.18)}$$

With:
- $\tilde{I} = \beta\bar{I}_1 + [1 - \beta]\bar{I}_2$,
- $\eta = \sqrt{\frac{\tilde{I}-3}{\lambda^2{}_m-3}}$,
- $\lambda_m =$ locking stretch.

The 11 models discussed above are some of the phenomenological models. This list is not finite, but provides a summary of the most used models. These 11 models were calibrated and validated by the finite element model in Chapter 4. Furthermore, the three most common micro-mechanical models were also considered, given a total of 14 material models. The three considered micro-mechanical models are cited below.

The basis of the statistical (micromechanical) theory is described by Treloar (1975). According to Treloar, elastic rubber-like materials are defined as follows:

- The material contains flexible molecules consisting of long chains,
- The chains are connected together by weak intermolecular forces,
- The network is formed by cross-linking of the individual molecular chains at various locations along the length of the chains.

The theory assumes that the molecular chains are Gaussian distributed. The strain energy function of the material is given by Eq. (A.19), with N the number of network chains per unit volume, k the Boltzmann constant and T the absolute temperature. Note that this strain energy function is similar to the phenomenological Hooke-Neo model, given by Eq. (A.20) (Achenbach & Duarte, 2003). Although the statistical models generally predict the mechanical behaviour well, they appear to be valid only for small strains up to 30%. Discrepancies arise especially between prediction and reality, when different loading conditions are combined (Yeoh & Fleming, 1997).

$$W = \frac{1}{2} NkT (\lambda_1^2 + \lambda_2^2 + \lambda_3^2 - 3) \tag{A.19}$$

$$W = C_{10}(I_1 - 3) = C_{10}(\lambda_1^2 + \lambda_2^2 + \lambda_3^2 - 3) \tag{A.20}$$

A.12. Arruda & Boyce

The micromechanical model according to Arruda and Boyce is a physical model based on the behaviour of a network of molecular chains (Arruda & Boyce, 1993). A general strain energy function is still considered, as given in Eq. (A.21). In this equation the following constants are applied: $C_2 = \frac{1}{20}$; $C_3 = \frac{11}{1050}$; $C_4 = \frac{19}{7000}$; $C_5 = \frac{519}{673750}$; and where G is equal to the shear modulus and λ_m represents the locking stretch. The strain energy function is equal to the sum of the strain energies of the individual molecular chains. These chains are randomly orientated in space (Raoult et al., 2005). Although the second invariant is excluded, the model allows accurate approximations for smaller deformations (Seibert & Schoche, 2000). Since the strain energy function is considered to be independent of the second invariant, only one single test configuration is required in order to predict the behaviour of the material. Therefore, the model cannot accurately predict the behaviour for different load configurations, in contrast to models with multiple invariants. Despite this, an acceptable approach is obtained and the model is easy in use (Marlow, 2003).

$$W = G \sum_{i=1}^{5} \frac{C_i}{\lambda_m^{2i-2}} (I_1^i - 3) \tag{A.21}$$

A.13. 3-chain model

The micromechanical 3-chain model is based on a polymer network consisting of three chains, according to the three main directions (James & Guth, 1943; Wang & Guth, 1952). The model assumes that the chain at micro level is divided into a certain number of segments. The strain energy function is obtained by Eq. (A.22). Recent research shows that the model can only properly predict the behaviour of the load situation for which it is calibrated (Hossain & Steinmann, 2012).

$$W = \frac{\mu N}{3} \sum_{i=1}^{3} \left[\bar{\gamma}_i \, \lambda_{r,i} + ln \left(\frac{\bar{\gamma}_i}{\sinh \bar{\gamma}_i} \right) \right] \qquad (A.22)$$

with:

- μ = shear modulus,
- N = number of segments per chain,
- $\lambda_{r,i} = \frac{1}{\sqrt{N}} \lambda_i$, the relative elongation of the chain,
- $\bar{\gamma}_i = \mathcal{L}^{-1}(\lambda_{r,i}) \approx \lambda_{r,i} \frac{3 - \lambda_{r,i}^2}{1 - \lambda_{r,i}^2}$, the inverse of the Langevin function.

A.14. 8-chain model

The 8-chain model is based on the micromechanical Arruda & Boyce model, where the latter is reformulated. It provides a better approach for the ultimate elongation of the polymer network, i.e. larger deformations. In this model, 8 chains are considered at micro level. As given in Eq. (A.23), again only two material parameters are needed, the shear modulus μ and the number of segments per chain N. The relative elongation of the chain λ_r is a function of the first invariant I_1 and γ is the inverse of the Langevin function. The model is less sensitive to the locking stretches of the chains than the 3-chain model, making the model usable for both small and large deformations (Hossain & Steinmann, 2012).

$$W = \mu N \left[\lambda_r + ln \left(\frac{\gamma}{\sinh \gamma} \right) \right] \qquad (A.23)$$

Appendix B: Validation multi-axial model

In this appendix, the results are presented for the validation of the multi-axial model for the three strain paths of Figure 4.28c. The graphs are always constructed in the same way, with the dots representing the experimentally measured strains and the full line the numerical strain. Four test configurations are given in Chapter 4, the other 14 configurations are depicted from Figure B.1 to Figure B.7. As expected, a certain scatter in the experimental results occurred. Despite this, a good agreement between the numerical and experimental results is achieved.
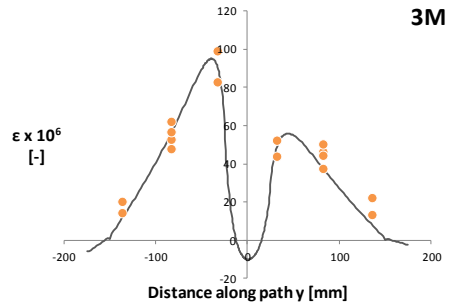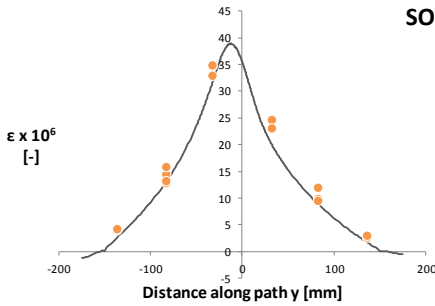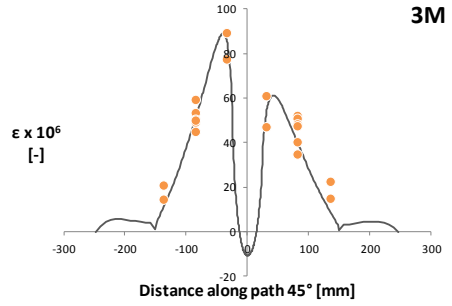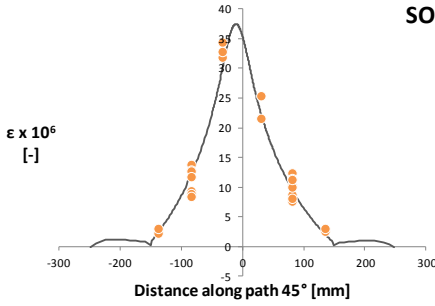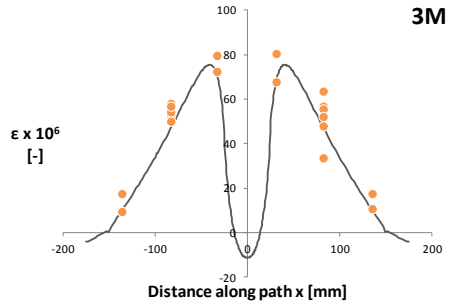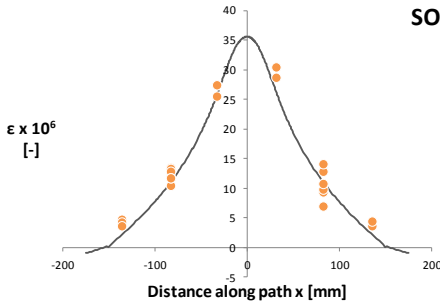
FIGURE B.1: ECCENTRICITY OF 30 MM AND MULTI-AXIAL ANGLE OF 22.5°.
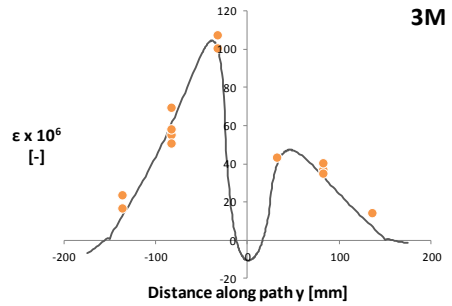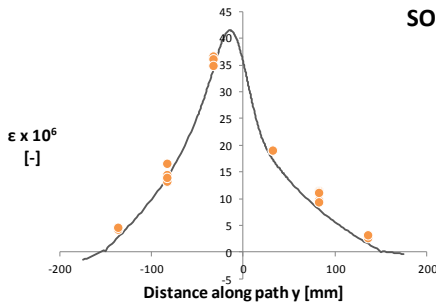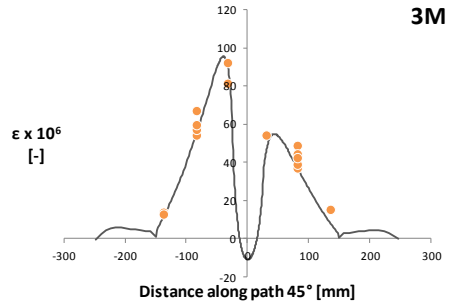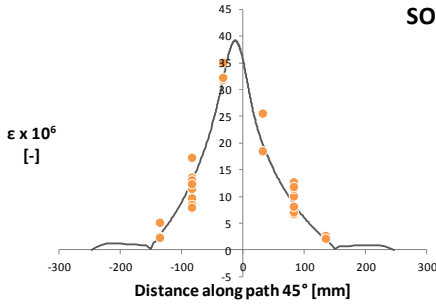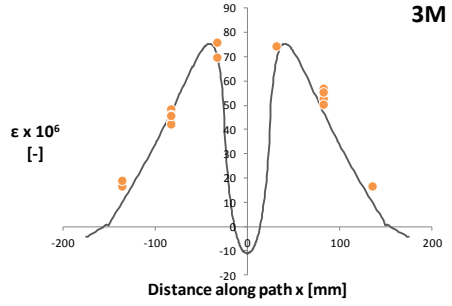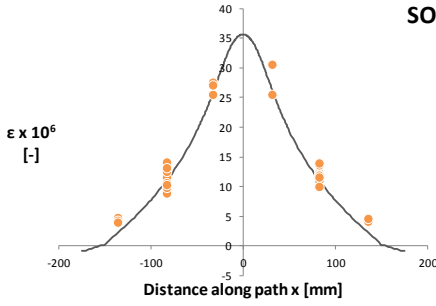
FIGURE B.2: ECCENTRICITY OF 45 MM AND MULTI-AXIAL ANGLE OF 22.5°.
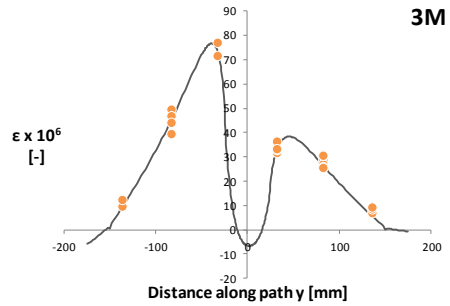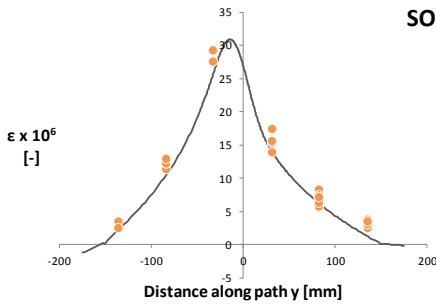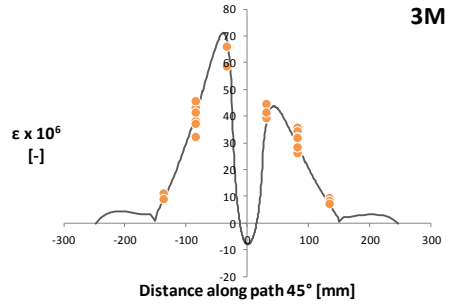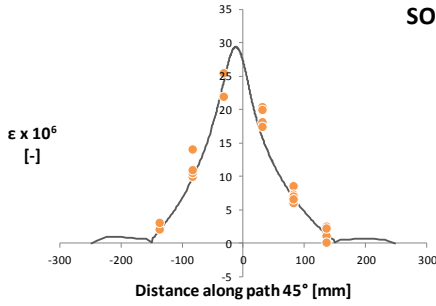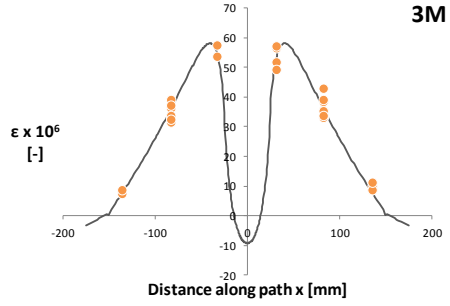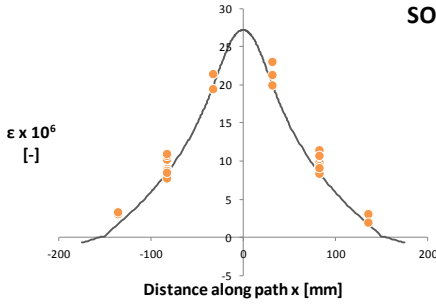
FIGURE B.3: ECCENTRICITY OF 15 MM AND MULTI-AXIAL ANGLE OF 45.0°.
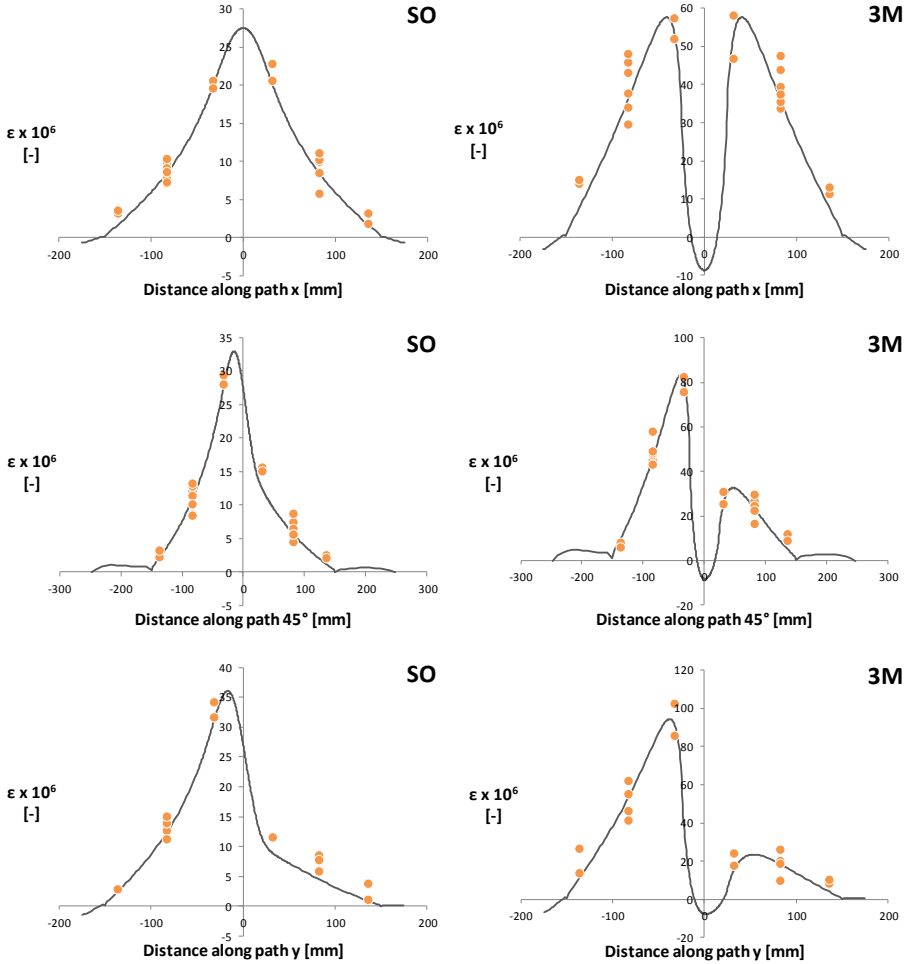
FIGURE B.4: ECCENTRICITY OF 30 MM AND MULTI-AXIAL ANGLE OF 45.0°.
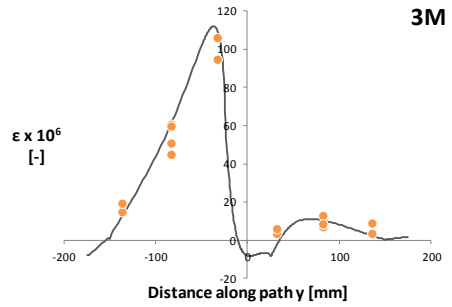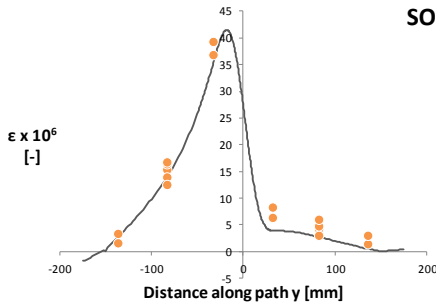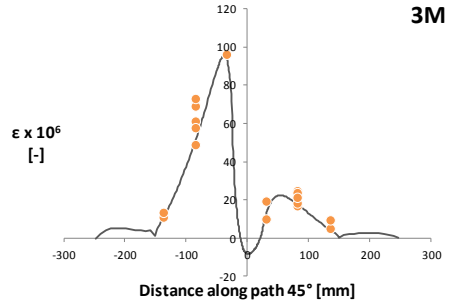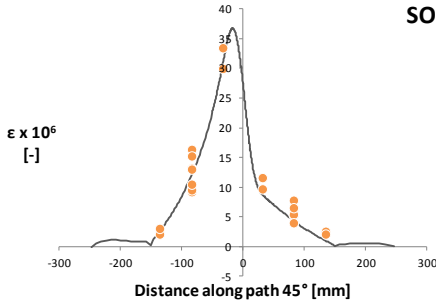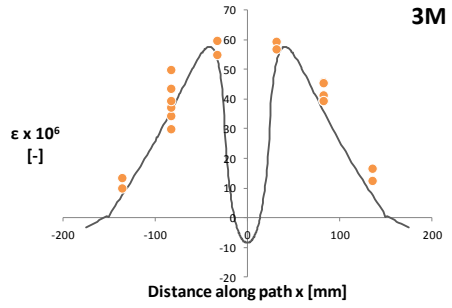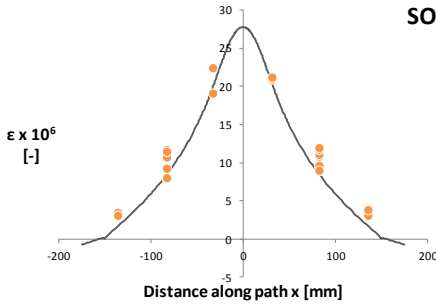
FIGURE B.5: ECCENTRICITY OF 45 MM AND MULTI-AXIAL ANGLE OF 45.0°.
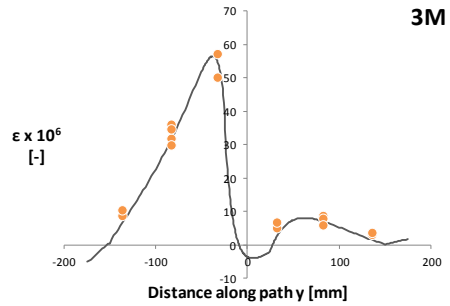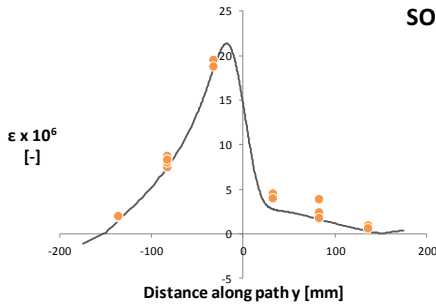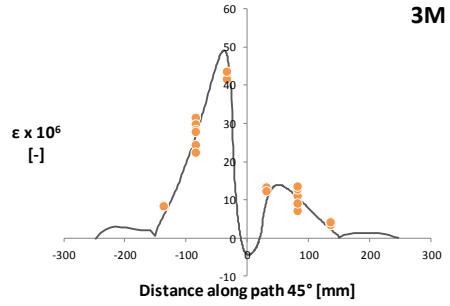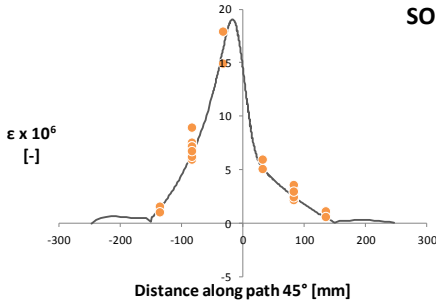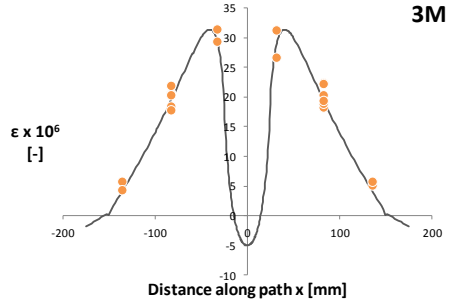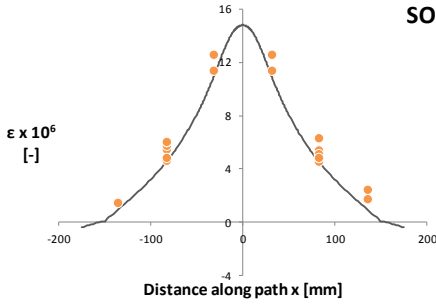
FIGURE B.6: ECCENTRICITY OF 15 MM AND MULTI-AXIAL ANGLE OF 67.5°.
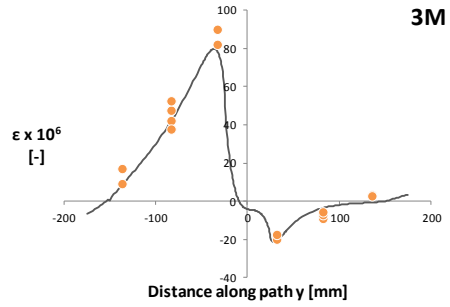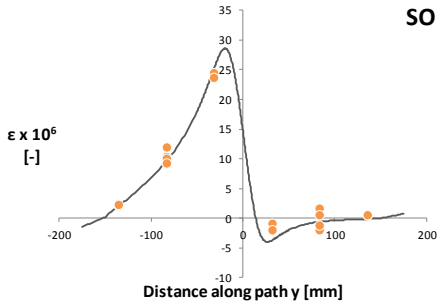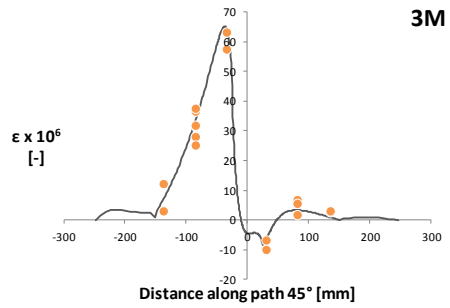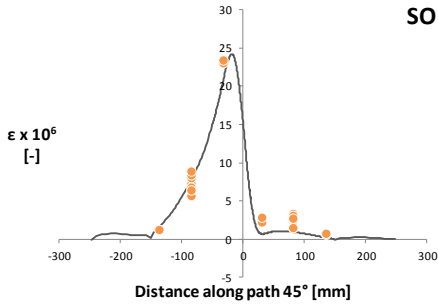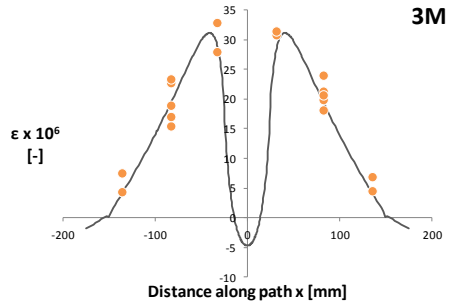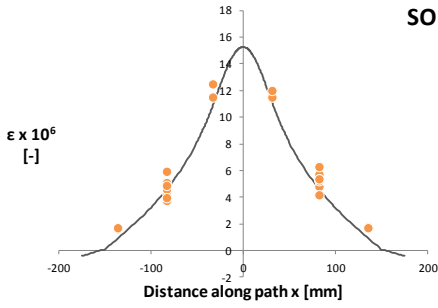
FIGURE B.7: ECCENTRICITY OF 30 MM AND MULTI-AXIAL ANGLE OF 67.5°.

Appendix C: Validation total model

In this appendix, the comparison between the numerical and experimental values are given for 54 from the 68 configurations for the total model. In Table C.1 the configurations that were tested are depicted. The 14 configurations that are already compared in Chapter 3 are put in bold. The comparisons are depicted in Figure C.1 to Figure C.11. Despite a certain small difference between the experimental and numerical results, a good agreement between the numerical and experimental results is achieved.

TABLE C.1: TESTED CONFIGURATIONS FOR THE TOTAL MODEL IN FUNCTION OF THE DIAMETER (D), THE EDGE DISTANCES (E), THE UNIFORM LOAD (U), THE POINT LOAD (P), THE SYMMETRICAL LOAD (S), THE ASYMMETRICAL LOAD (A), FOUR POINT-FIXINGS (4), SIX POINT-FIXINGS (6), HINGED BOUNDARY CONDITION (H) AND FIXED BOUNDARY CONDITION (F).

				D [mm] 30 — E [mm] 35	70	105	175	245	D [mm] 50 — E [mm] 35	70	105	175	245	D [mm] 70 — E [mm] 35	70	105	175	245
U	S	4	H	X	X	X	X	X	X	X	X	X	X	X	X	X	X	X
U	S	4	F	**X**	**X**	**X**	**X**	**X**	X	X	X	X	X	X	X	X	X	X
U	S	6	H						**X**		**X**	**X**	**X**					
U	S	6	F						X		X	X	X					
U	A	4	H						X	X	X	X	X					
U	A	4	F						X	X	X	X	X					
U	A	6	H															
U	A	6	F						X	X	X	X	X					
P	S	4	H	X	X	X	X	X						X	X	X	X	X
P	A	6	F						**X**	**X**	**X**	**X**	**X**					

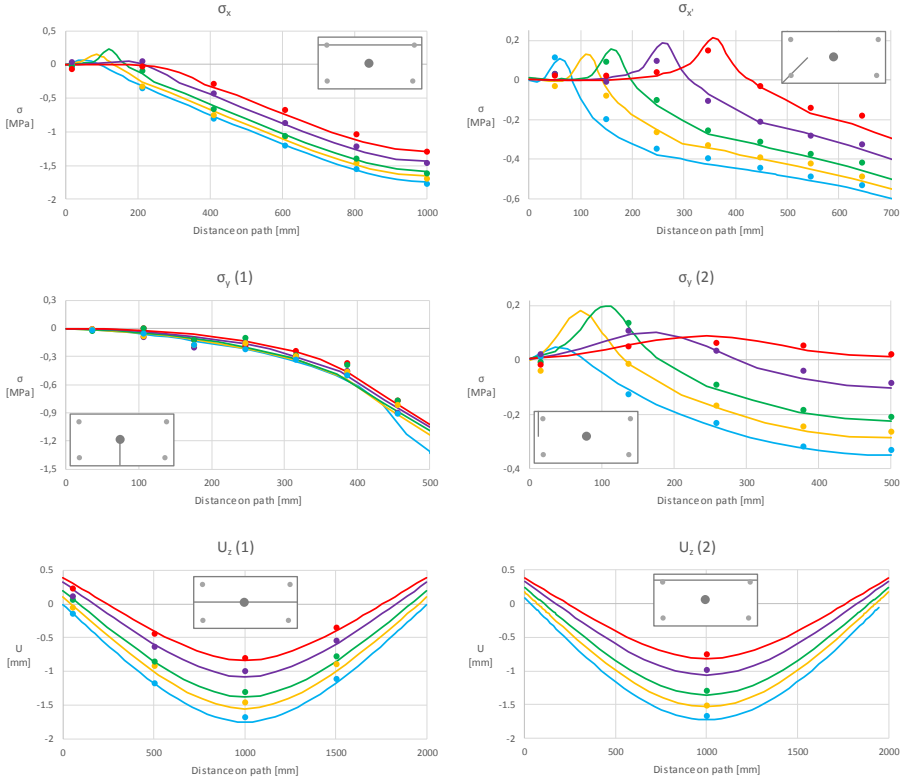**FIGURE C.1**: SYMMETRICAL POINT LOAD AND FOUR 30 MM HINGED POINT-FIXINGS.

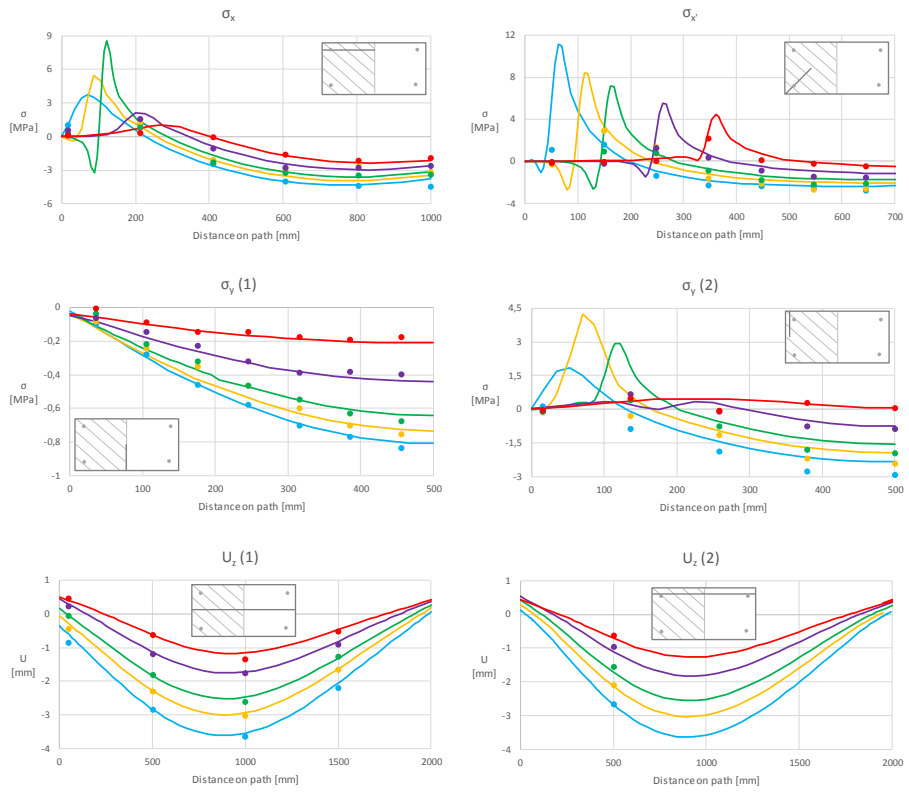FIGURE C.2: SYMMETRICAL POINT LOAD AND FOUR 70 MM HINGED POINT-FIXINGS.

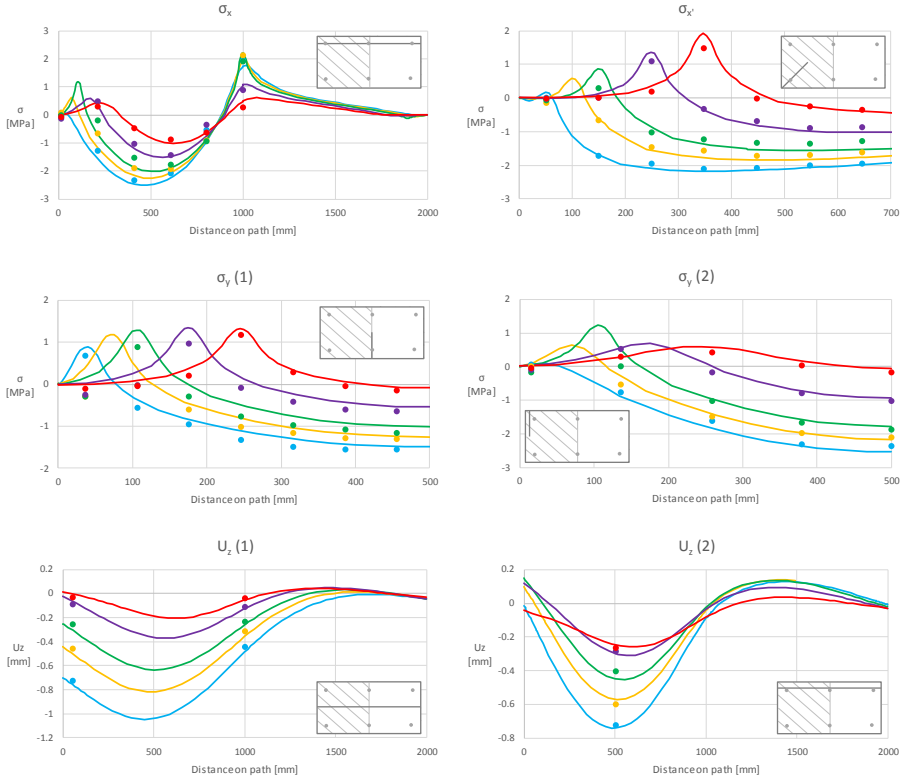**FIGURE C.3**: ASYMMETRICAL UNIFORM LOAD AND FOUR 50 MM FIXED POINT-FIXINGS.

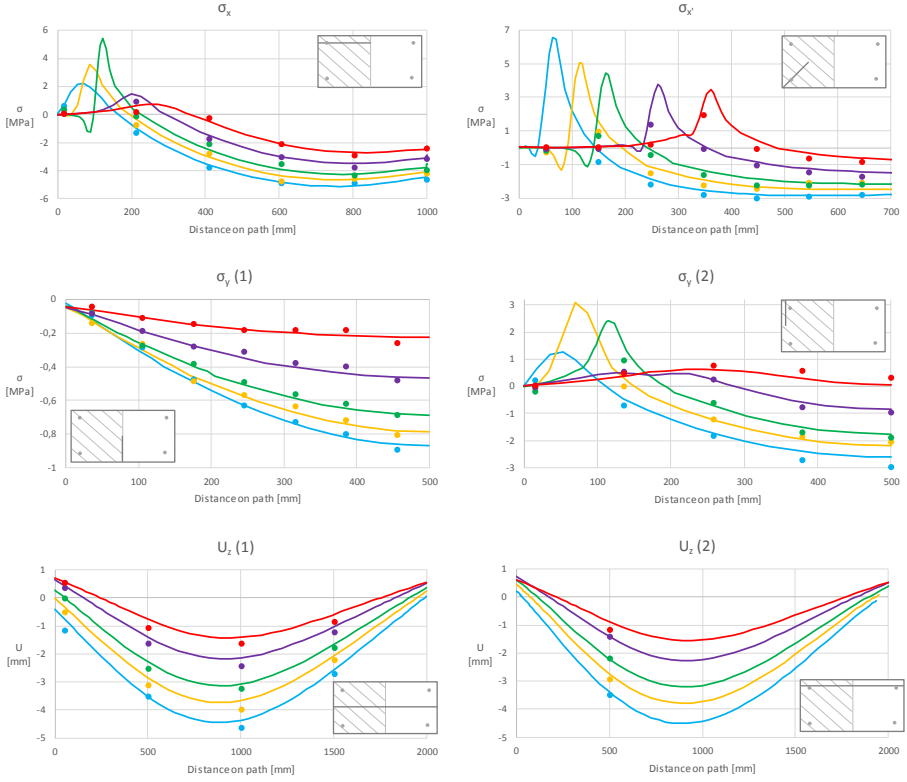**FIGURE C.4** ASYMMETRICAL UNIFORM LOAD AND SIX 50 MM FIXED POINT-FIXINGS.

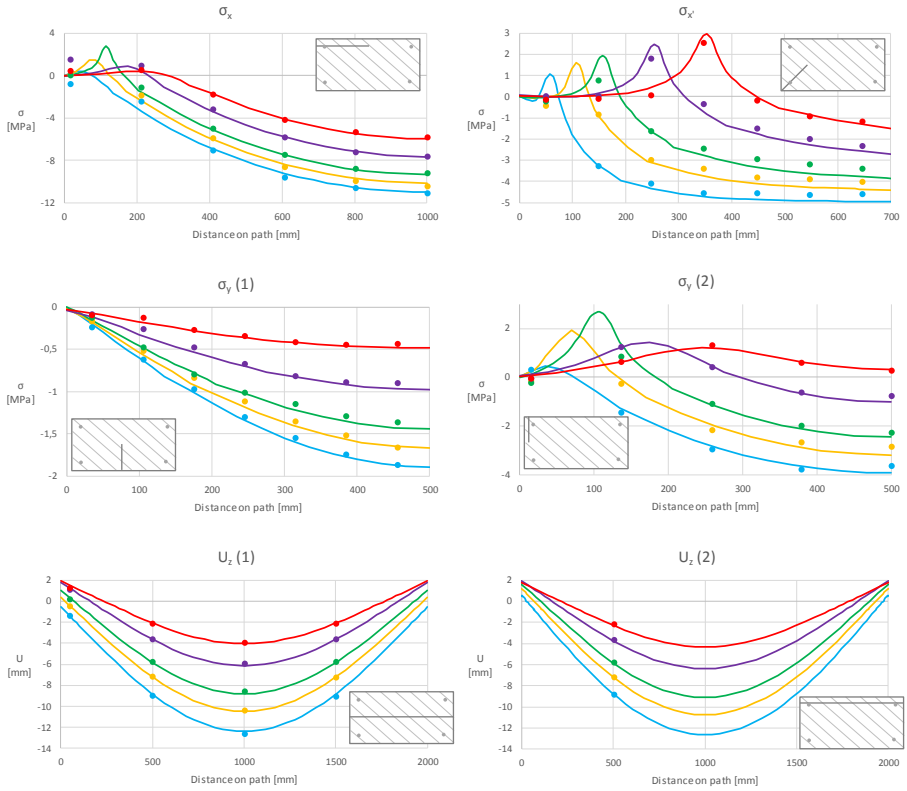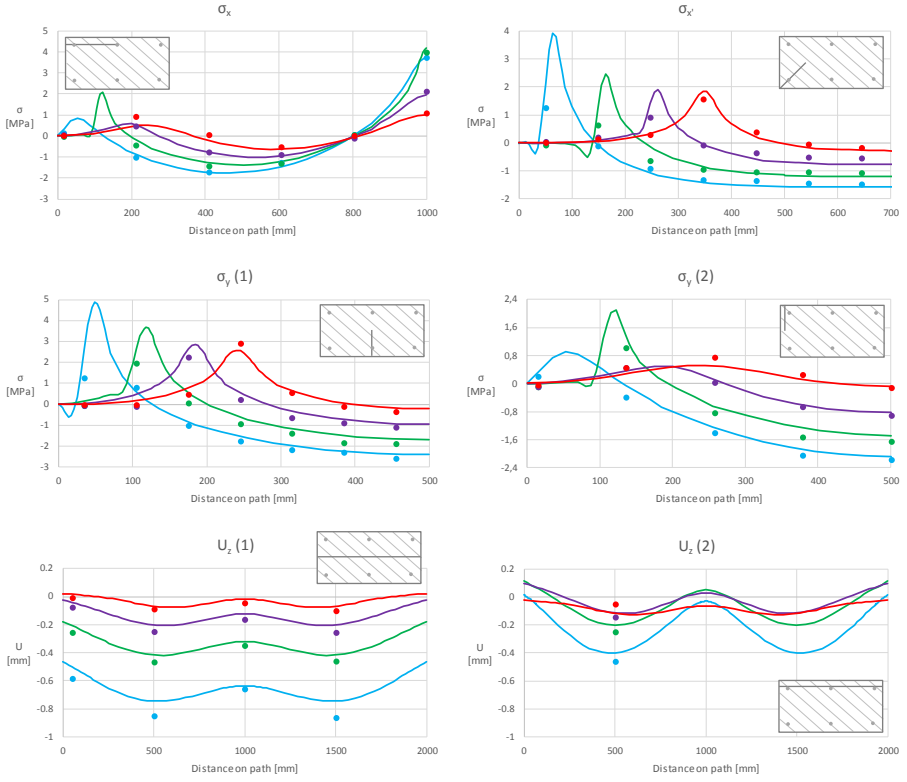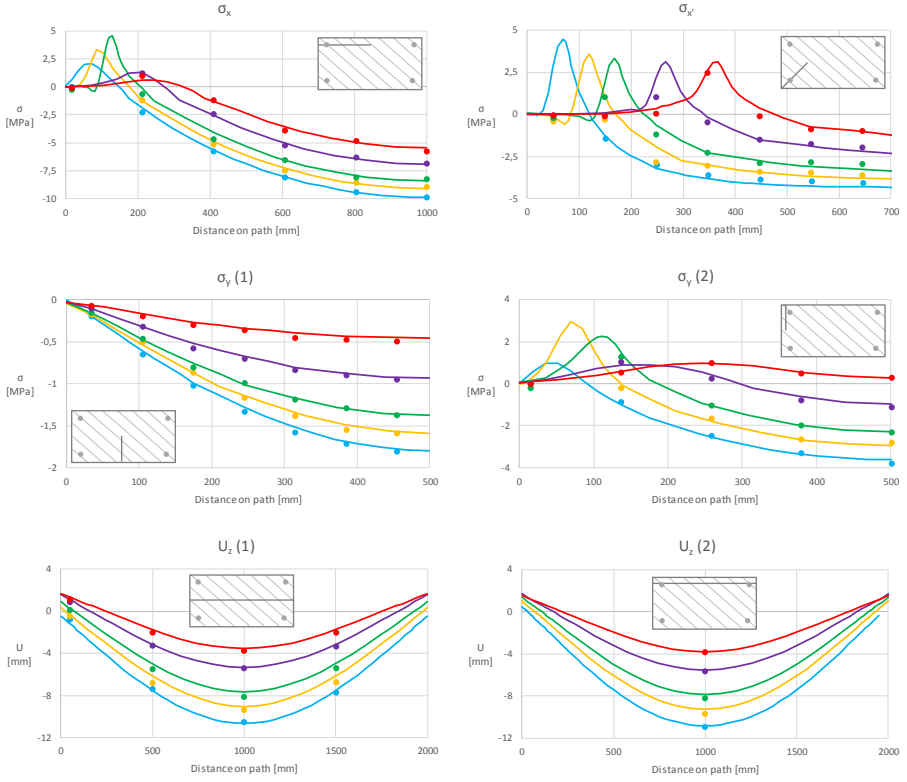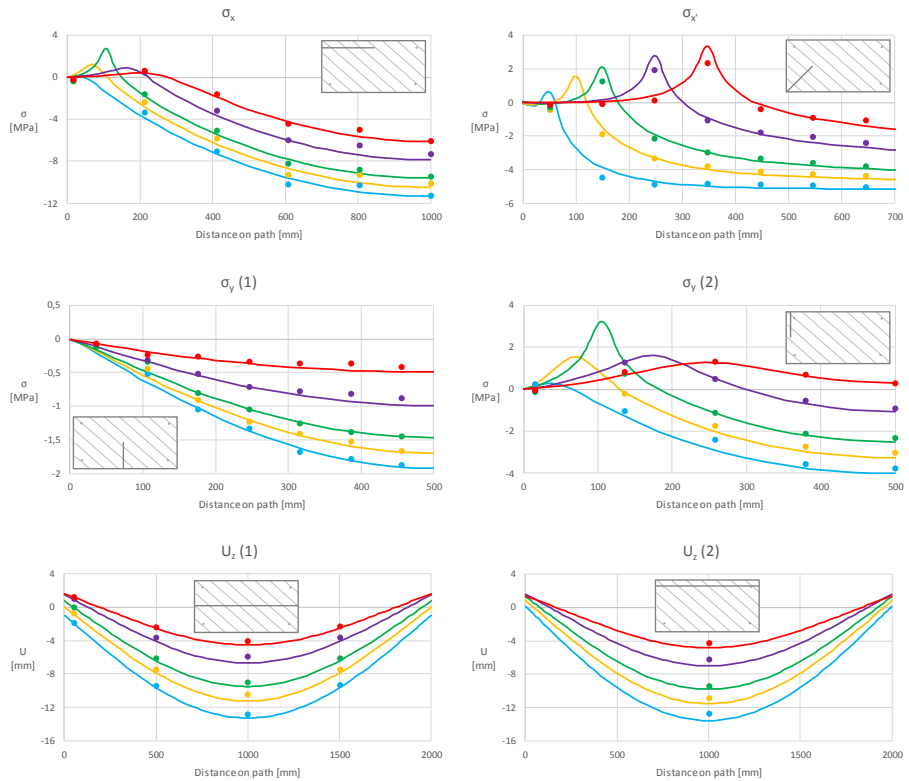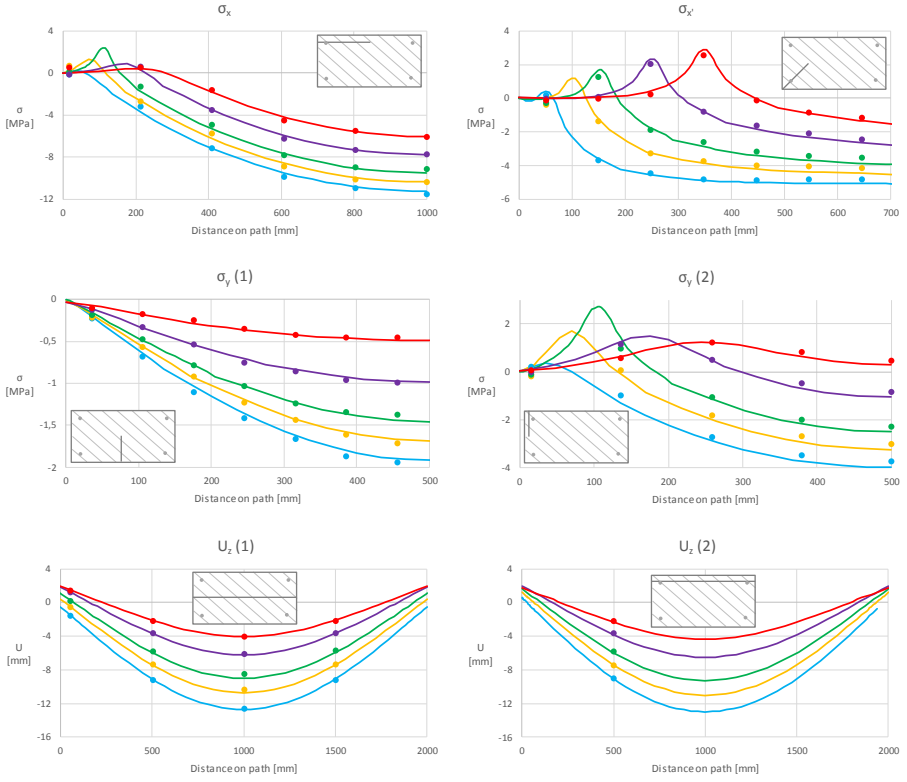**FIGURE C.5**: ASYMMETRICAL UNIFORM LOAD AND FOUR 50 MM HINGED POINT-FIXINGS

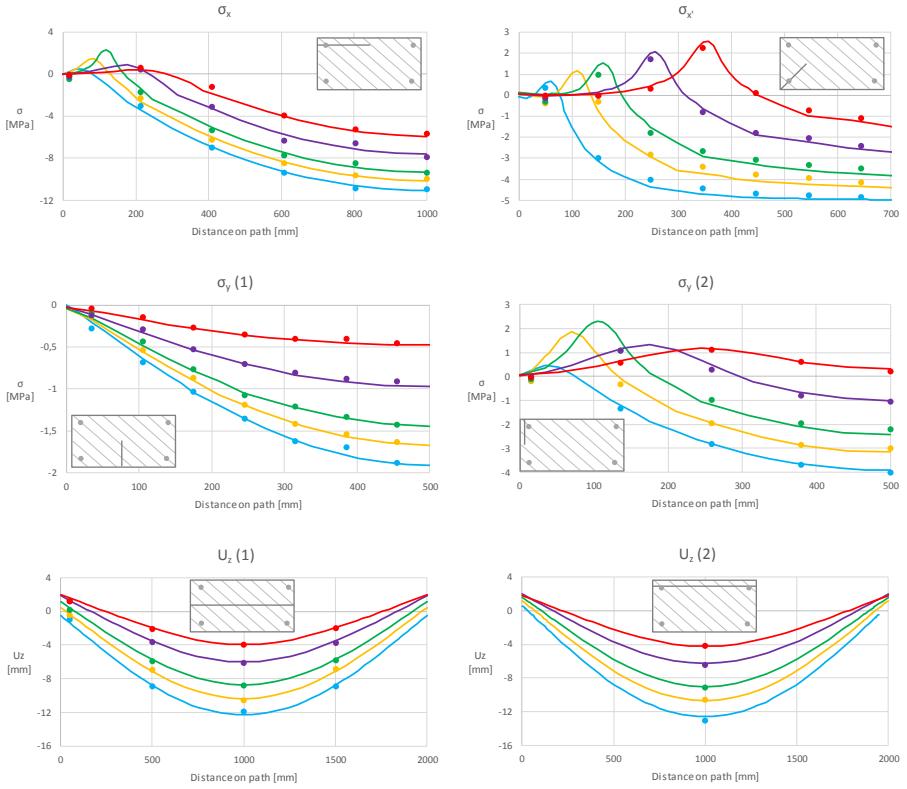**FIGURE C.6** SYMMETRICAL UNIFORM LOAD AND FOUR 50 MM FIXED POINT-FIXINGS

FIGURE C.7: SYMMETRICAL UNIFORM LOAD AND SIX 50 MM FIXED POINT-FIXINGS

FIGURE C.8: SYMMETRICAL UNIFORM LOAD AND FOUR 70 MM FIXED POINT-FIXINGS

FIGURE C.9: SYMMETRICAL UNIFORM LOAD AND FOUR 30 MM HINGED POINT-FIXINGS

FIGURE C.10: SYMMETRICAL UNIFORM LOAD AND FOUR 50 MM HINGED POINT-FIXINGS

FIGURE C.11: SYMMETRICAL UNIFORM LOAD AND FOUR 70 MM HINGED POINT-FIXINGS

Appendix D: SLG-verification in the adhesive layer

The comparisons between the stress distribution in the adhesive layer obtained from the total model and from the SLG-method in Chapter 7 are only given for an edge distance of 35 mm and 105 mm. In this appendix the comparison is given for an edge distance of 175 mm and 245 mm in Figure D.1 for four point-fixings and in Figure D.2 for six point-fixings.
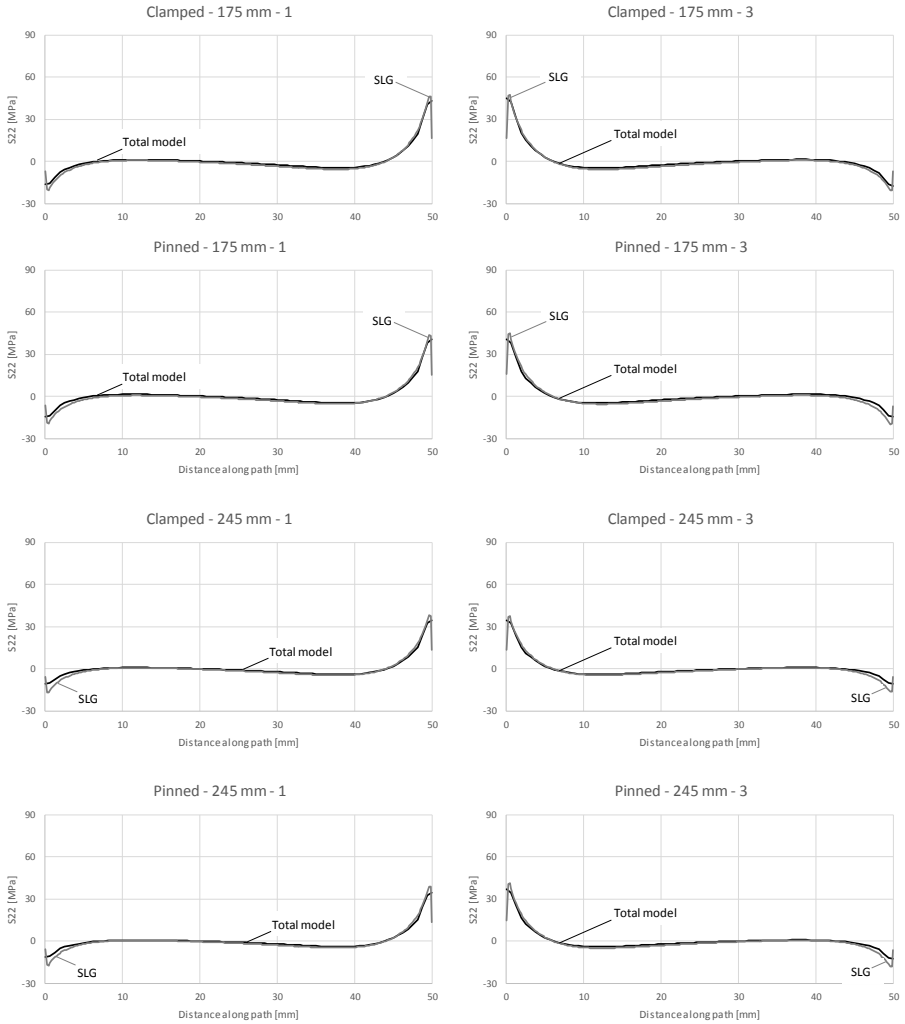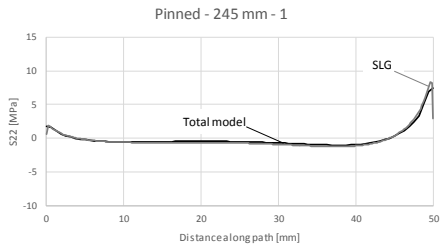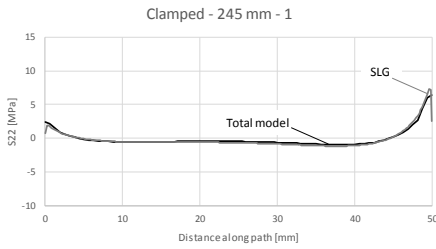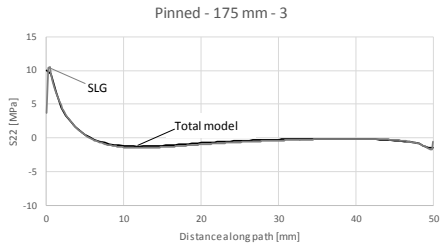
FIGURE D.1: COMPARISON BETWEEN THE STRESS DISTRIBUTION OF THE TOTAL MODEL AND THE SLG-METHOD MEASURED IN THE ADHESIVE LAYER FOR FOUR POINT-FIXINGS FOR WIND SUCTION.

Clamped - 175 mm - 1

Pinned - 175 mm - 1

Clamped - 175 mm - 2

Pinned - 175 mm - 2

Clamped - 175 mm - 3

Pinned - 175 mm - 3

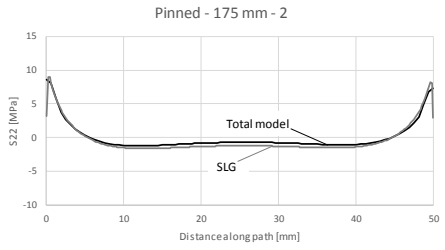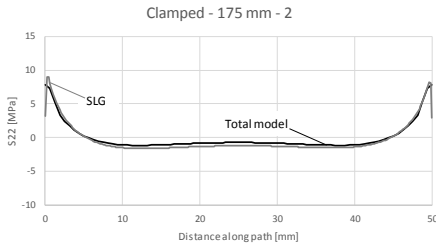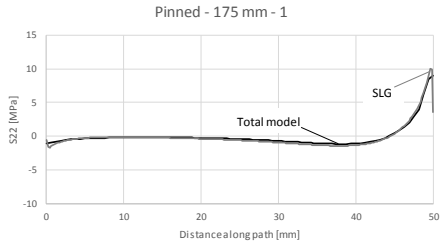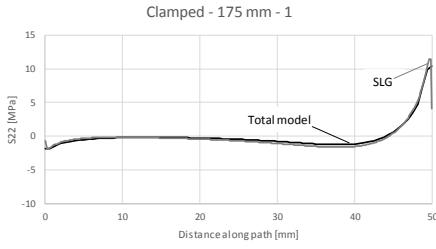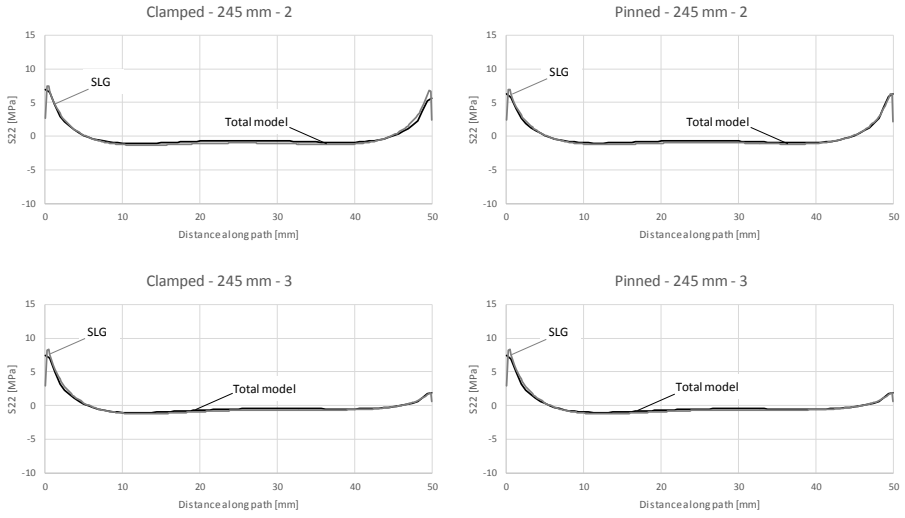Clamped - 245 mm - 1

Pinned - 245 mm - 1
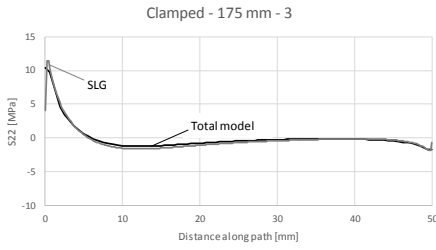
FIGURE D.2: COMPARISON BETWEEN THE STRESS DISTRIBUTION OF THE TOTAL MODEL AND THE SLG-METHOD MEASURED IN THE ADHESIVE LAYER FOR SIX POINT-FIXINGS FOR WIND SUCTION.

Appendix E: SLG-verification for wind pressure

The comparisons between the stress distribution obtained from the total model and from the SLG-method in Chapter 7 were assumed wind suction. Obviously, wind pressure will also occur. Hence the verification of the SLG-method was also performed for the situation with wind pressure for the stress distribution on the glass and in the adhesive layer, and is summarized in this appendix.

E.1.　Glass stress distribution at the rear side

The configuration is illustrated in Figure E.1, with the used path at the backside of the glass panel. The comparisons for four point-fixings are depicted in Figure E.2 and in Figure E.3 for six point-fixings.

FIGURE E.1: SLG VALIDATION CONFIGURATION FOR WIND PRESSURE AND THE PATH AT THE BACKSIDE OF THE GLASS PANEL.

FIGURE E.2: COMPARISON BETWEEN THE STRESS DISTRIBUTION OF THE TOTAL MODEL AND THE SLG-METHOD MEASURED AT THE BACK FOR FOUR POINT-FIXINGS FOR WIND PRESSURE.

FIGURE E.3: COMPARISON BETWEEN THE STRESS DISTRIBUTION OF THE TOTAL MODEL AND THE SLG-METHOD MEASURED AT THE BACK FOR SIX POINT-FIXINGS FOR WIND PRESSURE.

For the configuration with six point-fixings and small edge distances, the global stress deviates more from the stress from the total model, compared to larger edge distances. However, the stresses are overestimated by the global model, giving a conservative and safe stress distribution.

E.2.   Glass stress distribution at the front

As for wind suction, the stresses were also derived from the front of the glass panel for wind pressure. As with the previous path, the position of this path depends on the edge distance and is depicted in Figure E.4. The comparisons between the stress distributions obtained with the SLG-method and from the total model are given in Figure E.5 for four point-fixings and in Figure E.6 for six point-fixings.
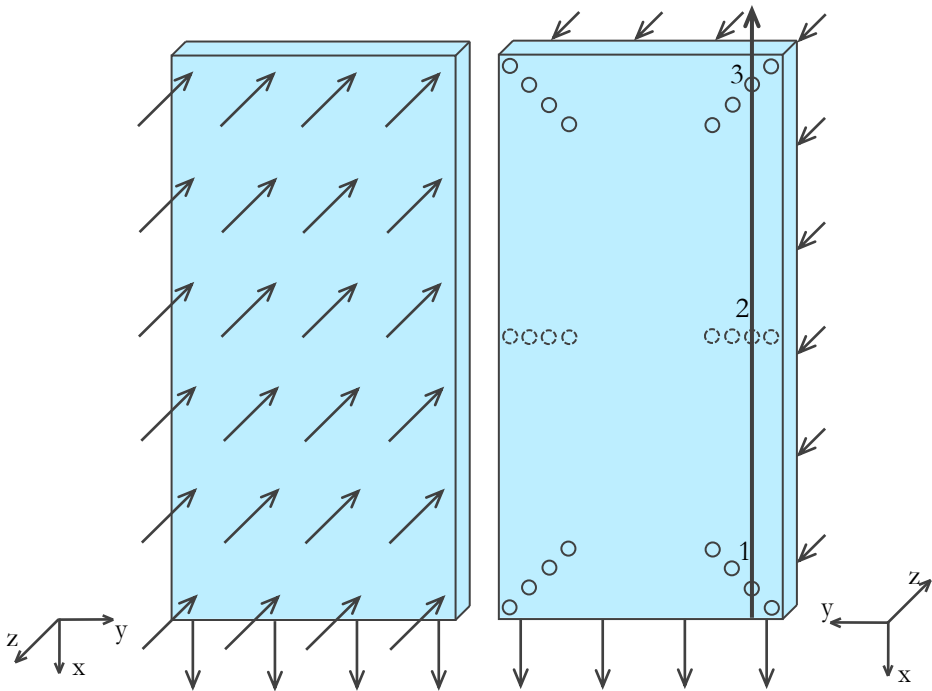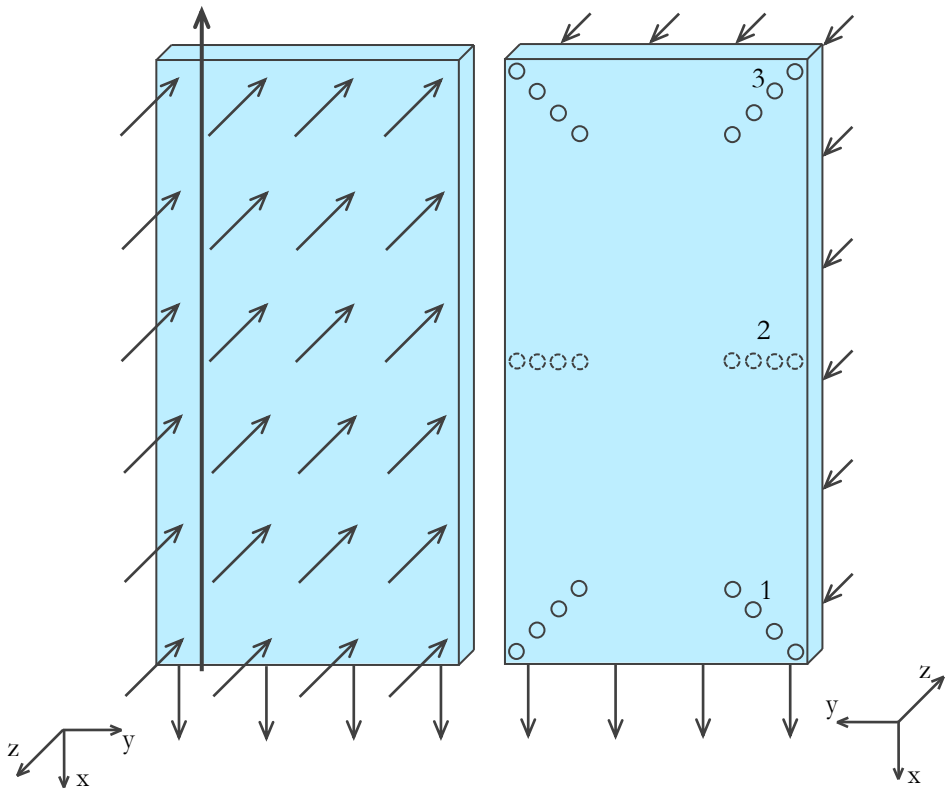

FIGURE E.4: SLG VALIDATION CONFIGURATION FOR WIND PRESSURE AND THE PATH AT THE BACKSIDE OF THE GLASS PANEL.
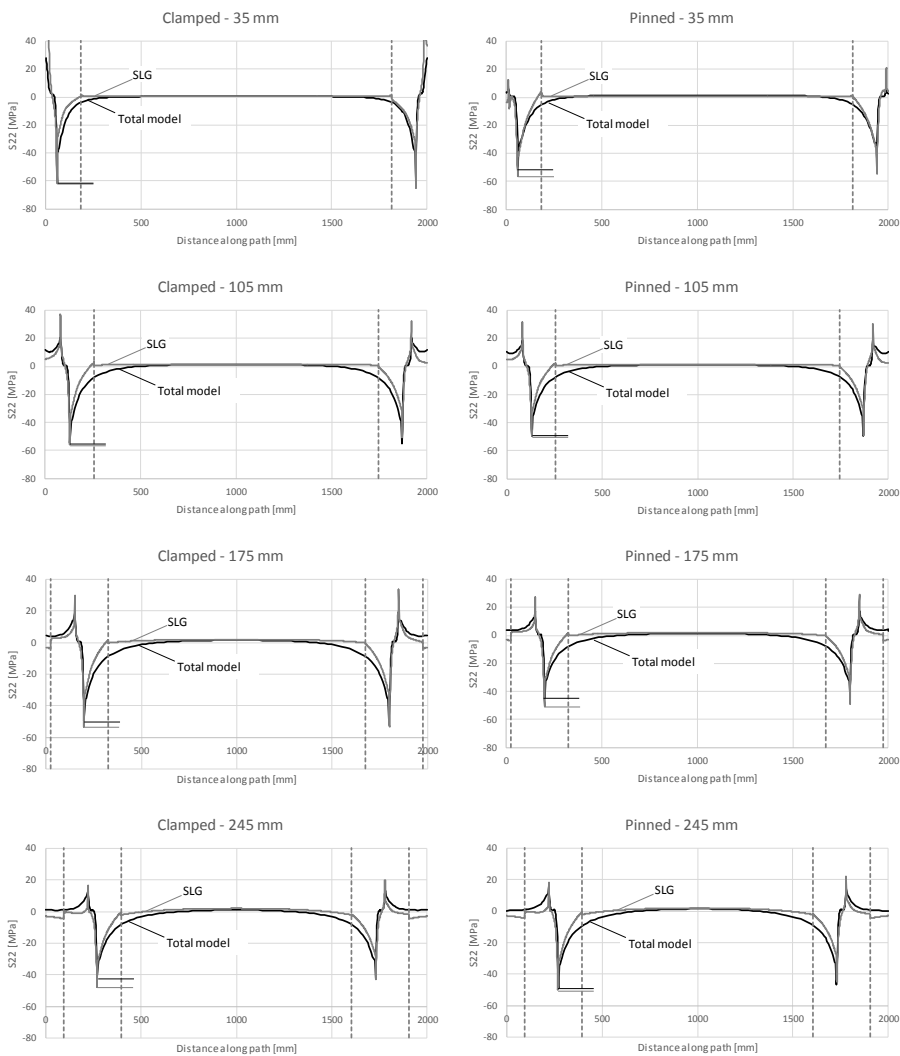
FIGURE E.5: COMPARISON BETWEEN THE STRESS DISTRIBUTION OF THE TOTAL MODEL AND THE SLG-METHOD MEASURED AT THE FRONT FOR FOUR POINT-FIXINGS FOR WIND PRESSURE.
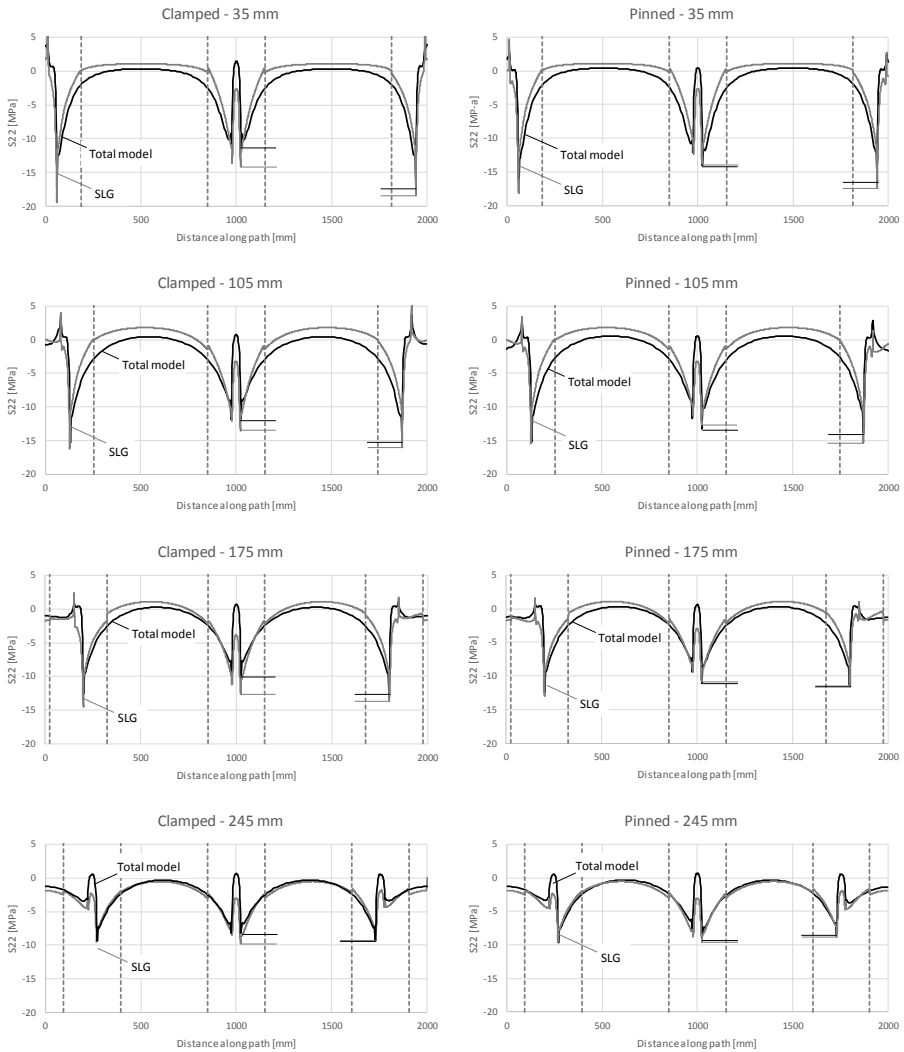
FIGURE E.6: COMPARISON BETWEEN THE STRESS DISTRIBUTION OF THE TOTAL MODEL AND THE SLG-METHOD MEASURED AT THE FRONT FOR SIX POINT-FIXINGS FOR WIND PRESSURE.

Again it is noticeable that for small edge distances, the global stress deviates more from the stress obtained from the total model. However, the stresses are still overestimated by the global model, giving a conservative and safe stress distribution.

E.3. Adhesive stress distribution with wind pressure

The SLG-method for the stress distribution in the adhesive layer is also verified for wind pressure. The investigated configuration is depicted in Figure E.7. The comparison between the stress distribution of the total model and obtained with the SLG-method for four point-fixings is given in Figure E.8 for the two point-fixings and in Figure E.9 for the three point-fixings of glass panels with six point-fixings. The local stresses are obtained from the multi-axial model.
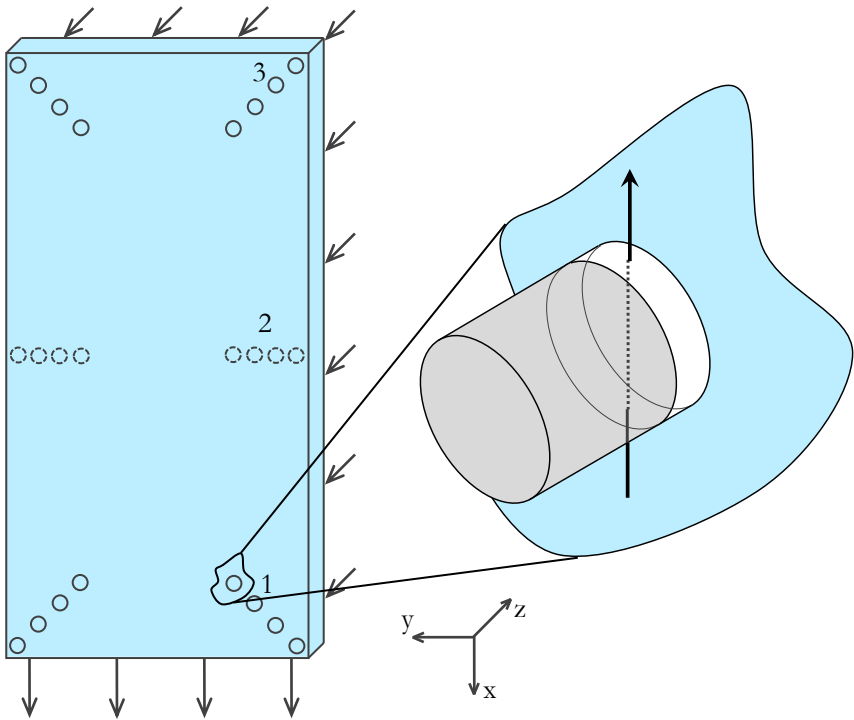
FIGURE E.7: SLG VALIDATION CONFIGURATION FOR THE ADHESIVE LAYER WITH WIND PRESSURE AND THE PATH IN THE ADHESIVE LAYER (NOT TO SCALE).
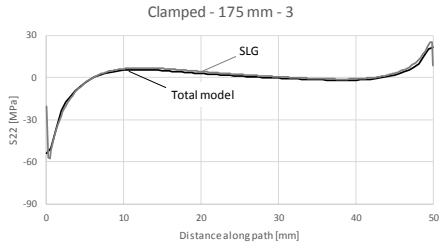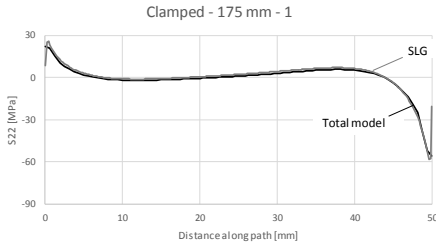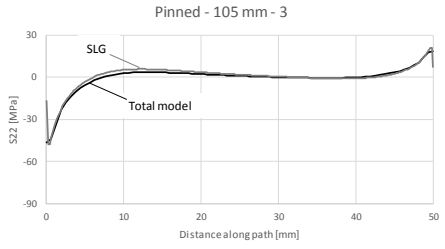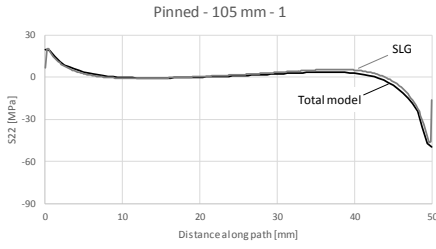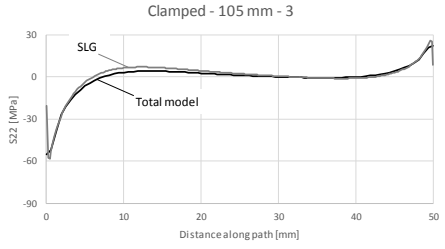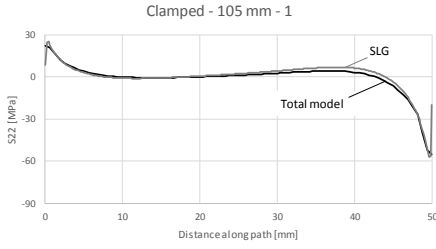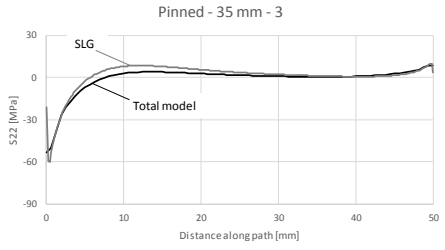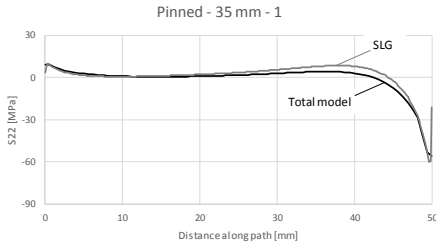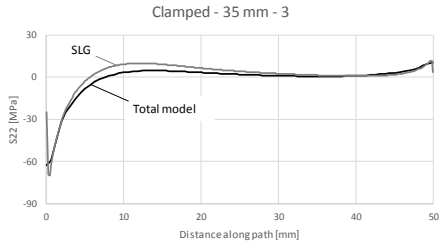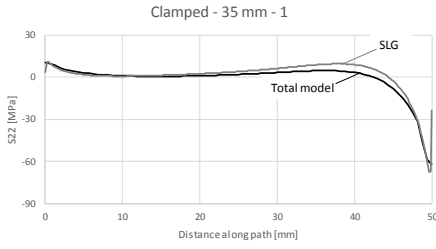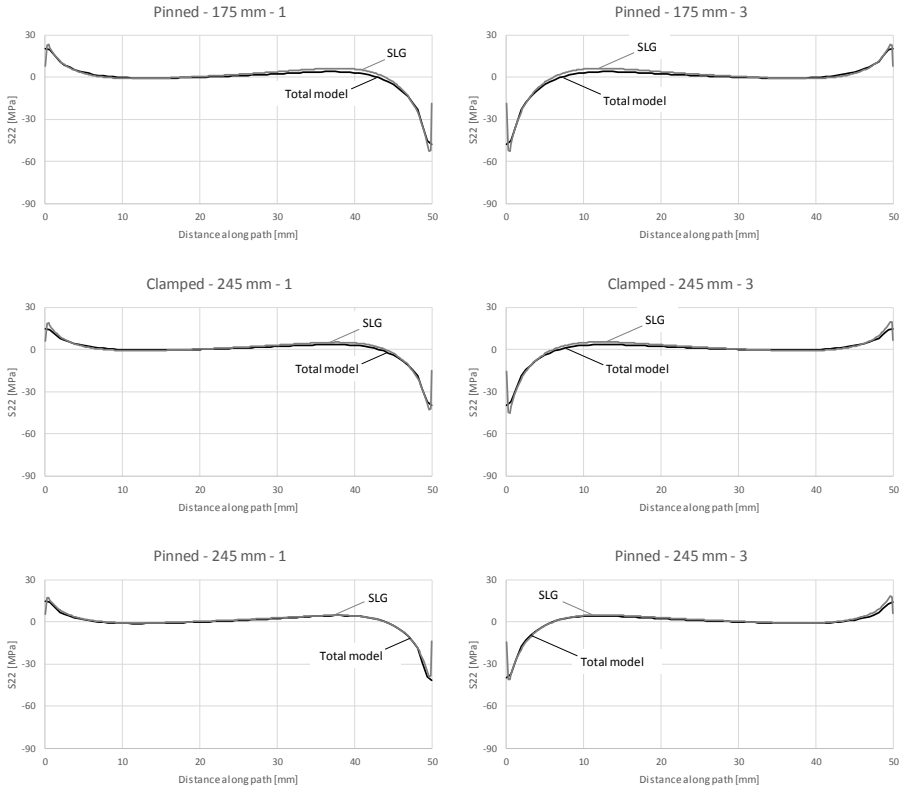
FIGURE E.8: COMPARISON BETWEEN THE STRESS DISTRIBUTION OF THE TOTAL MODEL AND THE SLG-METHOD MEASURED IN THE ADHESIVE LAYER FOR FOUR POINT-FIXINGS FOR WIND PRESSURE.

Clamped - 105 mm - 3

Pinned - 105 mm - 3

Clamped - 175 mm - 1

Pinned - 175 mm - 1

Clamped - 175 mm - 2

Pinned - 175 mm - 2

Clamped - 175 mm - 3

Pinned - 175 mm - 3
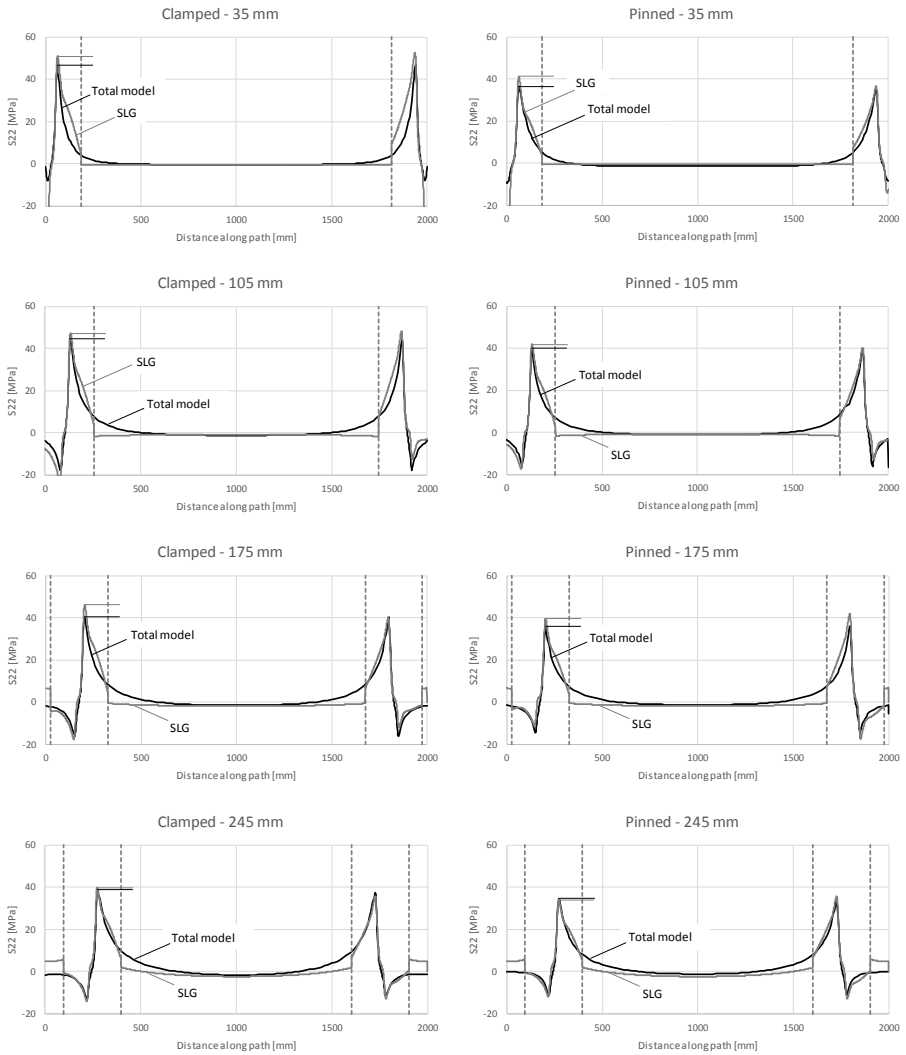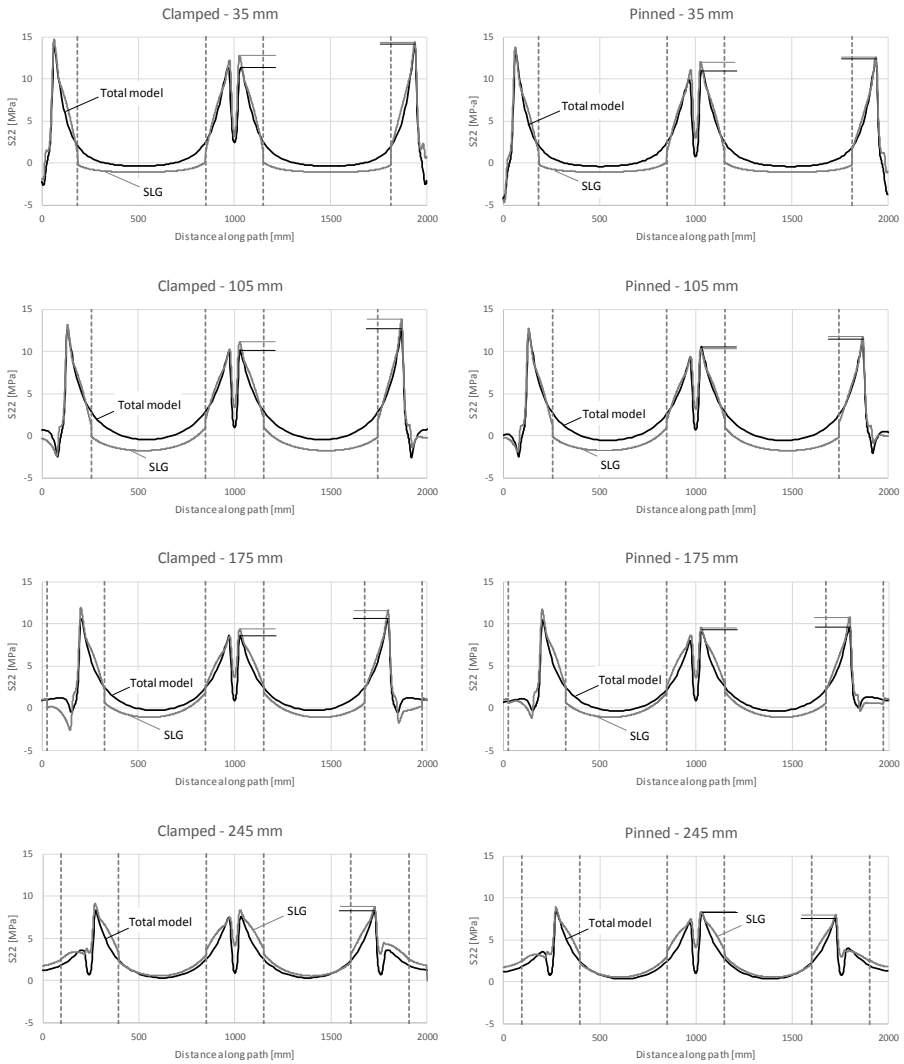
Clamped - 245 mm - 1

Pinned - 245 mm - 1
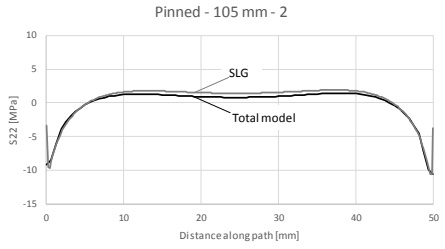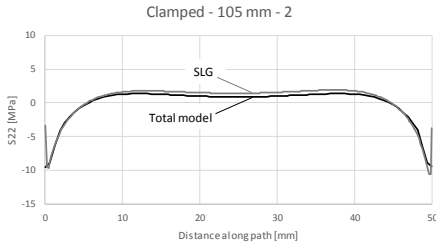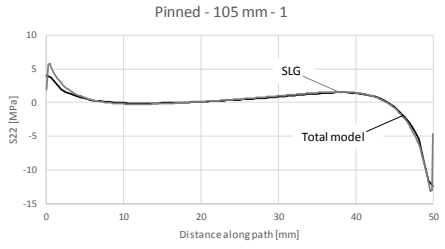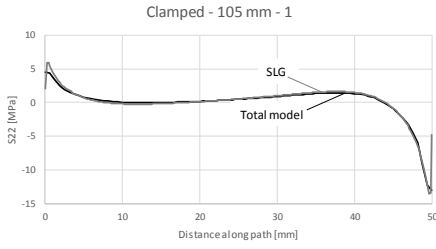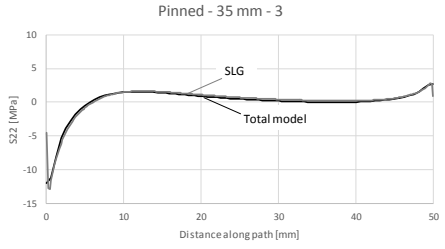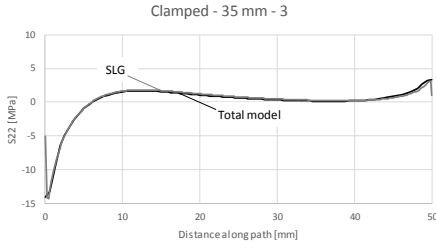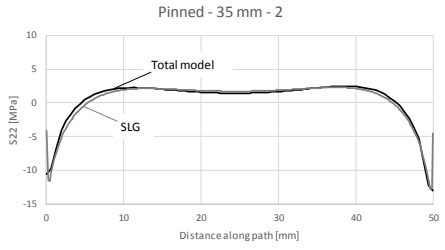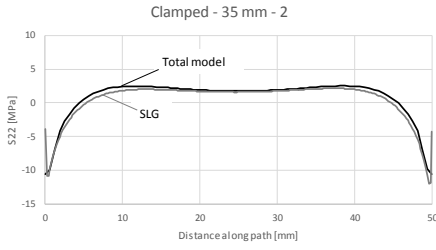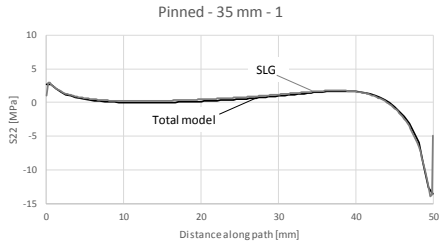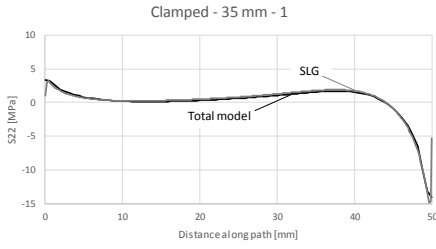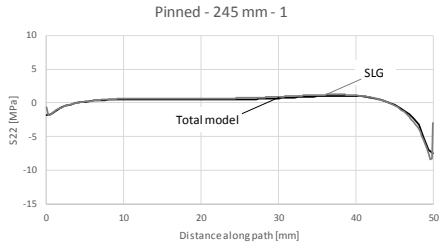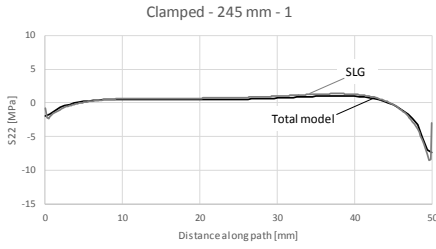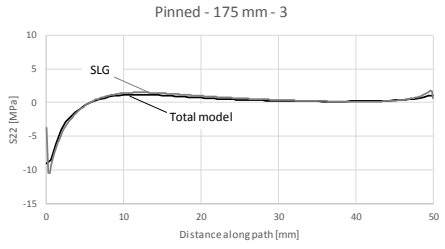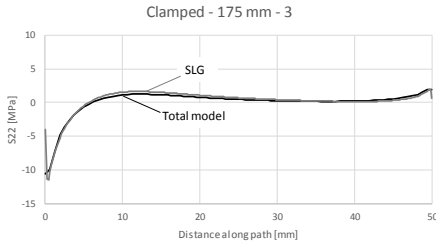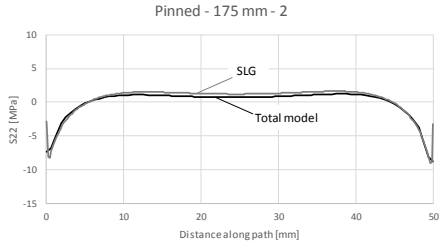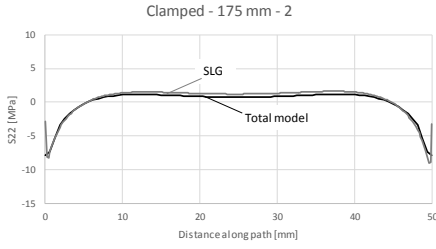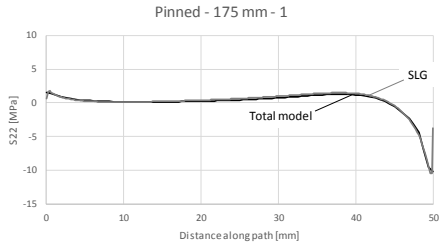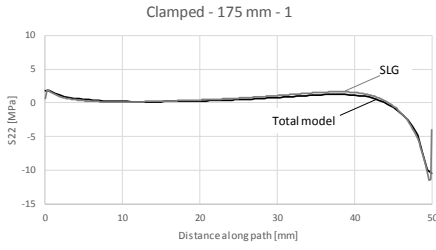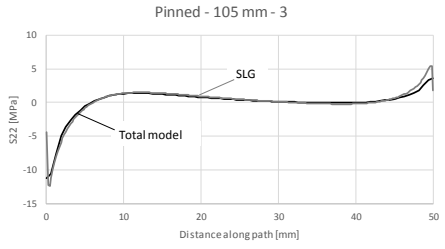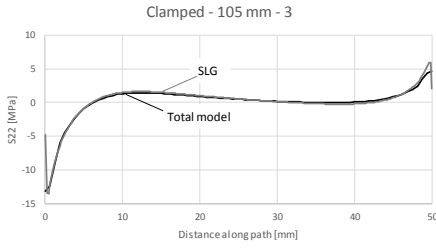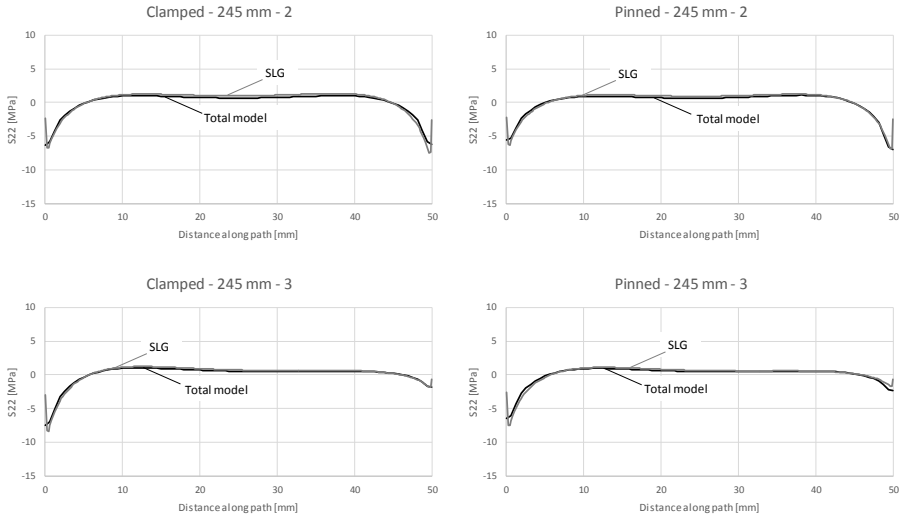
FIGURE E.9: COMPARISON BETWEEN THE STRESS DISTRIBUTION OF THE TOTAL MODEL AND THE SLG-METHOD MEASURED IN THE ADHESIVE LAYER FOR SIX POINT-FIXINGS FOR WIND PRESSURE.

Again it can be seen that the deviation between the stress distribution in the adhesive layer obtained with the SLG-method and from the total model is relatively small. The shape and order of magnitude of the SLG-curve are close to the curve of the total model. Also here, the SLG-method generally gives larger stress peaks than the total model, giving conservative stress distributions. As expected, the stress peaks are larger for small edge distances and are slightly higher for the clamped condition.

Appendix F: Fracture mechanics

In this appendix, a small summary is given about failure criteria based on fracture mechanics for glass and adhesive failure.

F.1.   Fracture mechanics for glass failure

Since Griffith (1921) demonstrated that flaws determine the strength of glass, and as glass shows a perfectly elastic behaviour up till failure, linear elastic fracture mechanic (LEFM) theory is generally accepted in glass design. According to the theory of LEFM, at inert conditions, i.e. when no water vapour affects the flaws, the stress intensity factor K characterizes the amount of the elastic stresses and strains around a crack (Irwin 1957). This factor is dependent on

-   Crack length and width;
-   Crack configuration (continuous, at the surface or hidden);
-   Geometry of the structural element;
-   The three different fracture modes (depicted in Figure F.1);
    •   Mode I: opening or tensile mode (fracture surfaces normal to the load);
    •   Mode II: sliding or in-plane shear mode (crack surfaces slide over one another in the direction perpendicular to the leading edge of the crack);
    •   Mode III: tearing or out-of-plane shear mode (fracture surfaces move relatively parallel to each other and away from each other).

Mode I   Mode II   Mode III
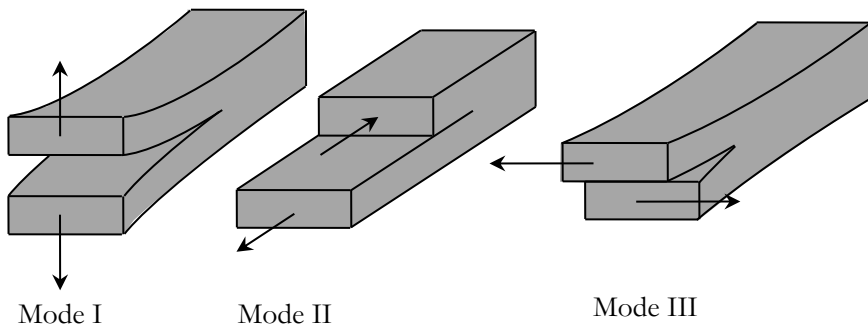
In the study of brittle materials, mode I and II are the most important and mode I is even more prominent for glass. For mode I the stress intensity factor K_I for an infinite plate with a crack length $2a$ in the centre, can be determined with Eq. (F.1), where σ is the normal stress in the plate as illustrated in Figure F.2.

$$K_I = \sigma\sqrt{\pi a} \tag{F.1}$$
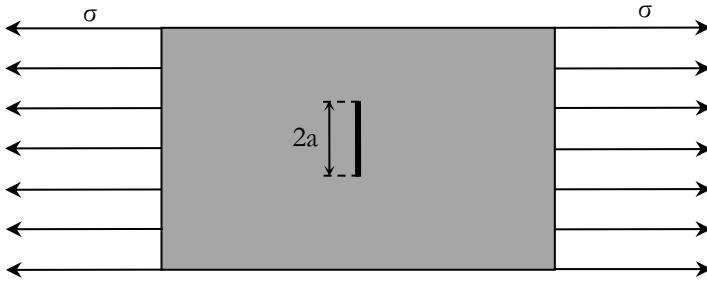
FIGURE F.2: INFINITE PLATE WITH A CENTRAL CRACK LENGTH 2A.

The definition of the stress intensity factor K_I according to Eq. (F.1) is only valid for an infinite plate with a central flaw. For other configurations, this factor will be different. For a plate with a finite thickness t, a geometry factor $f(\bar{a})$ will be introduced, which takes into account the crack geometry, location of the crack and width of the plate. The stress intensity factor with the geometry factor is given in Eq. (F.2).

$$K_I = f(\bar{a}) \cdot \sigma\sqrt{\pi a} \tag{F.2}$$

The parameter $\bar{a}$ is defined as

$$\bar{a} = \frac{2a}{t} \tag{F.3}$$

For a central crack, the geometry factor $f(\bar{a})$ can be estimated with following formulas

$$f(\bar{a}) = 1 + 0,256\bar{a} + 1,152\bar{a}^2 + 12,2\bar{a}^3 \tag{F.4}$$

$$f(\bar{a}) = \sqrt{\sec(\pi\bar{a})} \tag{F.5}$$

$$f(\bar{a}) = \frac{1}{\sqrt{1 - (2\bar{a})^2}} \tag{F.6}$$

For a crack through the edge, as depicted in Figure F.3, the geometry factor is equal to Eq. (F.7). When the crack length is negligibly small with respect to the width of the plate, the shape factor is equal to 1.12, and the stress intensity factor can be expressed by Eq. (F.8).

$$f(\bar{a}) = 1{,}12 - 0{,}231 \cdot \bar{a} + 10{,}55 \cdot \bar{a}^2 - 21{,}72 \cdot \bar{a}^3 + 30{,}39 \cdot \bar{a}^4 \tag{F.7}$$

$$K_I = 1{,}12 \cdot \sigma\sqrt{\pi a} \tag{F.8}$$
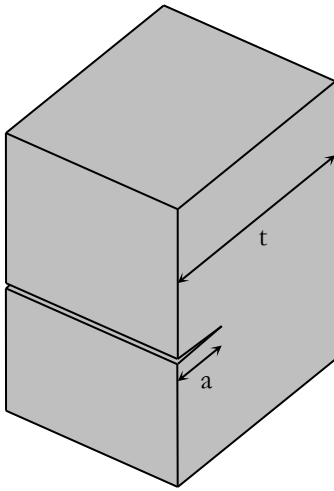
FIGURE F.3: CRACK THROUGH THE EDGE

The stress intensity factor can be used as a failure criterion, i.e. instantaneous failure will occur when the stress intensity factor reaches a critical stress intensity factor or fracture toughness $K_{I,cr}$ (Griffith 1921; Irwin 1957; Haldimann et al. 2008; Vandebroek 2014).

$$K_{I,cr} = f(\bar{a}) \cdot f_{ct,inert}\sqrt{\pi a_{ci}} \tag{F.9}$$

where $K_{Ic} = 0.75$ MPa.m$^{1/2}$ is a good practical value for the fracture toughness of modern soda-lime silica glass (Haldimann et al. 2008; Overend & Zammit 2012); $f_{ct,inert}$ is the inert strength corresponding to a constant loading and a_{ci} is the initial critical flaw depth, i.e. the depth of the crack which caused failure but measured before loading the specimen (Vandebroek 2014).

Under the combined influence of water vapour and an applied load, small surface flaws grow continuously until failure. This phenomenon is called stress corrosion. The relation between the crack propagation speed v and the stress intensity factor K_I in region I (Figure F.4) is given by Eq. (F.10), with v_0 the crack propagation speed when $K_I = K_{Ic}$ (Wiederhorn 1967; Lawn 1993; Haldimann et al. 2008; Vandebroek 2014).

$$v = v_0 \cdot \left(\frac{K_I}{K_{Ic}}\right)^n \tag{F.10}$$

Since structural elements are generally expected to be in service for several years, only region I (Figure F.4) is taken into account. Haldimann (2006) assumes that in laboratory conditions, a value of $v_0 = 0.01$ mm/s is an appropriate value for a surface strength model.
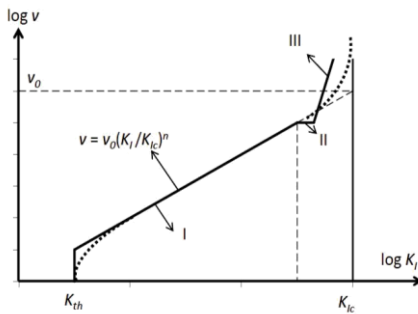
FIGURE F.4: RELATIONSHIP BETWEEN CRACK PROPAGATION SPEED AND STRESS INTENSITY (WIEDERHORN 1967; LAWN 1993; HALDIMANN ET AL. 2008; VANDEBROEK 2014)

For the use of fracture mechanics, the initial critical flaw depth has to be known. The determination of the size of a flaw in a material can be done in a non-destructive way, e.g. ultrasonic measurements, digital shearography and X-ray radiography (Toh et al. 1991; Steinchen et al. 1997; Hung 1982; Arias & Achenbach 2004; Steiner et al. 1995; Maslov 2000; Cloetens et al. 1997; Buffiere et al. 2010). The initial critical flaw depth can also be determined in a destructive manner, by looking at the mirror zone after failure. The critical flaw is located at the centre of the mirror zone. The mirror zone depth can be measured according to ASTM C1678 - 10 (2015) and is about 10 times larger than the critical flaw depth (Rodichev et al. 2007). However, these non-destructive and destructive methods are rather time consuming and expensive.

F.2. Fracture mechanics for failure in the adhesive

As for glass, the stress intensity factor can also be used as a failure criterion for an adhesive connection. Failure will occur when the stress intensity factor reaches a critical stress intensity factor or fracture toughness. The critical stress intensity factor $K_{I,cr}$ is given in Eq. (F.9). This critical stress intensity factor is a material parameter, and the determination for adhesives can be accomplished by prescribed tests, common used test configurations are depicted in Figure F.5 (ASTM D3433 2012; ISO 25217 2009).
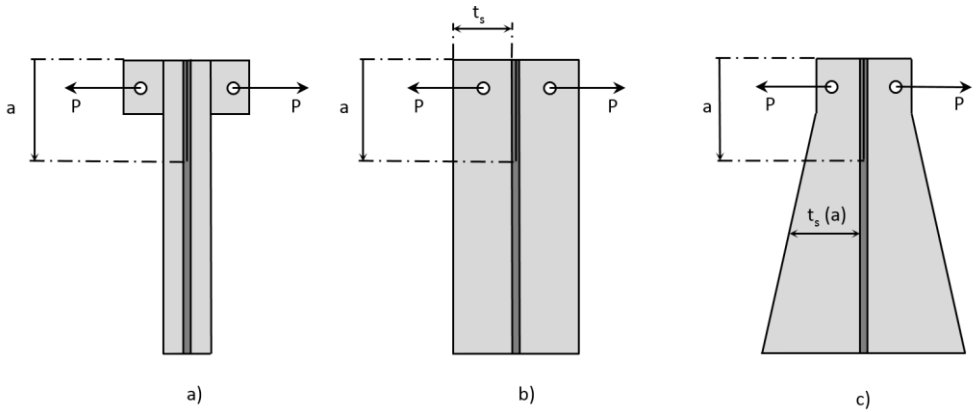
FIGURE F.5: COMMON USED TEST SETUPS FOR THE DETERMINATION OF $K_{I,CR}$: A) THE DOUBLE CANTILEVER BEAM (DCB) WITH LOAD-BLOCKS, B) THE DOUBLE CANTILEVER BEAM (DCB) WITH DRILLED HOLES AND C) THE TAPERED DOUBLE CANTILEVER BEAM (TDCB).

For the double cantilever beams, the stress intensity factor $K_{I,cr}$ can be determined by Eq. (F.11), where b is the width of the specimen and P the applied load. When $K_{I,cr}$ is determined, the critical stress and flaw size can be derived from Eq. (F.12) and (F.13), respectively. The higher the value for $K_{I,cr}$; the higher the occurring stresses and flaw sizes have to be in order to result in failure of the material.

$$K_{I,cr} = \frac{2P_{cr}}{b} \sqrt{\frac{3a^2}{t_s^3} + \frac{1}{t_s}} \tag{F.11}$$

$$\sigma_{I,cr} = \frac{K_{I,cr}}{\sqrt{\pi a}} \tag{F.12}$$

$$a_{cr} = \left(\frac{K_{I,cr}}{\sigma}\right)^2 \cdot \frac{1}{\pi} \tag{F.13}$$

Another commonly used parameter in LEFM is the energy release factor G. The energy release factor is a measure for the energy dissipated during fracture per unit of created fracture surface area. This quantity is central to fracture mechanics because the energy that must be supplied to a crack tip for it to grow must be balanced by the amount of energy dissipated due to the formation of new surfaces and other dissipative processes such as plasticity. As such, the energy release factor is defined as in Eq. (F.14), with U the potential energy available for crack growth, V the work associated with any external forces acting, and A the interfacial crack area (crack length for two-dimensional problems). The relationship between the energy release factor G and the stress intensity factors K for the three modes for general loading in plane strain is given in Eq. (F.15), μ being the shear modulus and ν the Poisson coefficient. Eq. (F.15) can be rewritten to Eq. (F.16). An advantage of the energy release rate is the fact that the mechanical energy released during incremental crack extension is independent of the loading configuration. Both cases of constant force (dead-weight loading) or constant displacement (fixed-grips loading) result in the same U and hence in the same energy release factor G (Lawn 1993). As such, the constant displacement configuration can always be considered without the loss of generality which defines the strain energy release rate per unit width of the crack front.

$$G = \frac{\vartheta(U - V)}{\vartheta A} \tag{F.14}$$

$$G = K_I^2 \left(\frac{1 - \nu^2}{E}\right) + K_{II}^2 \left(\frac{1 - \nu^2}{E}\right) + K_{III}^2 \left(\frac{1}{2\mu}\right) \tag{F.15}$$

$$G = \frac{K_I^2}{E} + \frac{K_{II}^2}{E} + \frac{K_{III}^2(1 + \nu)}{E} \tag{F.16}$$

Since an adhesive point-fixing is mainly subjected to a tensile load, the main stress components in the adhesive layer will be mostly tensile. This will result in a dominant effect of the energy release factor of mode I failure. The critical energy release factor $G_{I,cr}$ for mode I can be determined with the same test configurations for the determination of $K_{I,cr}$ (Figure F.5) (Blackman et al. 2003). During the tests, for each value of crack length, the corresponding values of load and displacement are measured. In order to obtain the energy release factor from this data, three different analysis methods can been used, namely the simple beam theory (SBT),

the corrected beam theory (CBT) and an experimental compliance method (ECM) (Mostovoy et al. 1967; Blackman et al. 2003; Cotterell et al. 2006; Williams 1989; Berry 1960). All these approaches essentially stem from the Irwin-Kies equation (Kanninen & Popelar 1985) in which the adhesive fracture energy $G_{I,cr}$ is deduced directly from Eq. (F.17), with P the applied load, B the width of the joint, C the compliance and a the crack length. The compliance is defined as the ratio of vertical displacement δ to the applied load P, as given in Eq. (F.18).

$$G_{I,cr} = \frac{P^2}{2B}\frac{dC}{da} \qquad\qquad \text{(F.17)}$$

$$C = \frac{\delta}{P} \qquad\qquad \text{(F.18)}$$

The dominance of mode I failure has been explained by Anderson (2005) as follows. A propagating crack seeks the path of least resistance (or the path of maximum driving force) which is not necessarily confined to its initial plane. If the material is isotropic and homogeneous, the crack will propagate in such a way as to maximize the energy release rate. What follows is an evaluation of the energy release rate as a function of propagation direction in mixed-mode problems. Consider for example Figure F.6, which illustrates a more typical scenario for an angled crack introduced by a combination of mode I and mode II. When fracture occurs, the crack tends to propagate orthogonally to the applied normal stress, i.e., the mixed-mode crack becomes a mode I crack. Moreover, if mode II or mixed-mode cracks occur, expressions for the critical energy release factor have also been derived for mode II (Baziard et al. 1995; Kim & Lee 2009) and for a combination of mode I and II (Marannano et al. 2008; Azari et al. 2009; Zhang et al. 2013; Zhou et al. 2014).
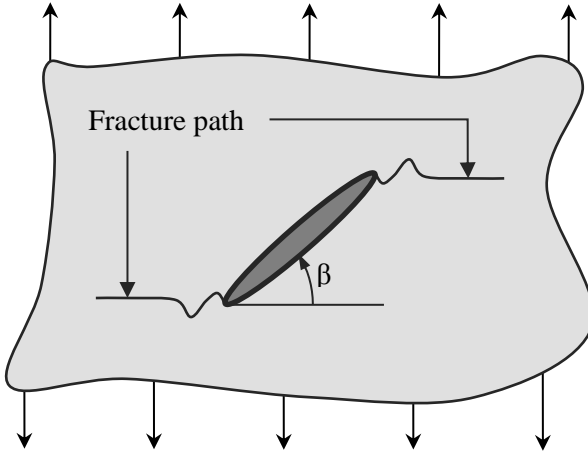
FIGURE F.6: TYPICAL PROPAGATION FROM AN INITIAL CRACK THAT IS NOT ORTHOGONAL TO THE APPLIED NORMAL STRESS (BASED ON (ANDERSON 2005)).

As mentioned above, the stresses are increased in the vicinity of the crack tip. Elastic plastic fracture mechanics assumes that these stresses will locally exceed the material's yield stress σ_y which results in the formation of a plastic zone. This induces a redistribution of the stresses within this zone. The magnitude of the yielding zone r_y and plastic zone r_p are depicted in Figure F.7 and can be determined using Irwins method (Irwin 1957) and are given for mode I failure in case of plane stress in Eq. (F.19) and (F.20), respectively.
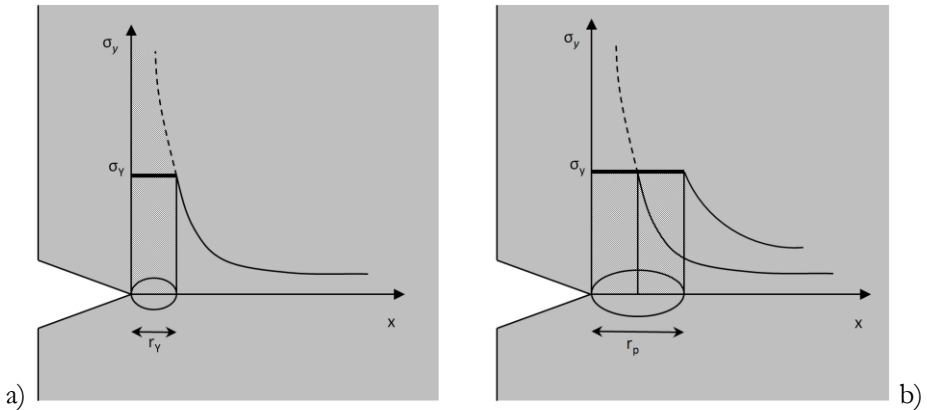
FIGURE F.7: A) SCHEMATIC REPRESENTATION OF THE DISTANCE TO YIELDING r_y AND B) REPRESENTATION OF THE PLASTIC ZONE r_p

$$r_y = \frac{1}{2\pi}\left(\frac{K_I}{\sigma_Y}\right)^2 \tag{F.19}$$

$$r_p = \frac{1}{\pi}\left(\frac{K_I}{\sigma_Y}\right)^2 = 2 \cdot r_y \tag{F.20}$$

The crack tip opening displacement (CTOD) can be used in order to postulate a first failure criterion according to the elastic plastic fracture mechanics (EPFM). The CTOD can be calculated with Eq. (F.21). Irwin (1957) argued that the occurrence of plasticity makes the crack behave as if it were longer than its physical size (the displacements are longer and the stiffness is lower than in the elastic case). When using Irwins method, the distance of the yielding zone r_y should be added to the crack length a in order to work with the effective crack length, as given in Eq. (F.22) (Irwin 1957). This length is visualized in Figure F.8. From Eq. (F.22), the crack opening at the following specific locations can be calculated; for x = a with Eq. (F.23) and for x = 0 with Eq. (F.24) (Denys 2010). Other expressions for CTOD have also developed by other researchers (Burdekin & Stone 1966; Dugdale 1960; Barenblatt 1962).

$$CTOD = \delta = 2 \cdot v_{tip} = 2\frac{2\sigma\sqrt{a^2 - x^2}}{E} \tag{F.21}$$

$$CTOD_{Irwin} = \delta_{Irwin} = \frac{4\sigma}{E}\sqrt{(a + r_Y)^2 - x^2} \tag{F.22}$$

$$\delta_{tip,Irwin} = \frac{4\sigma}{E}\sqrt{r_Y^2 + 2a \cdot r_Y} \tag{F.23}$$

$$\delta_{central,Irwin} = \frac{4\sigma}{E}(a + r_Y) \tag{F.24}$$
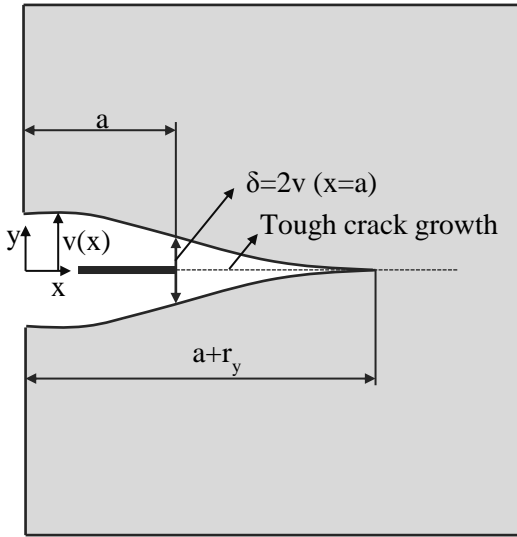
FIGURE F.8: VISUALISATION OF THE CRACK TIP OPENING DISPLCAMENT (CTOD) (BASED ON(DENYS 2010))

The J-integral can be used in order to postulate a second failure criterion according to EPFM. This integral is almost identical to the energy release factor proposed in LEFM which expresses the amount of energy needed to induce crack propagation. Contrary to the energy release factor, the J-integral takes the size of the plastic zone into account. The J-integral can be calculated along a path Γ which encloses the crack tip and with the start and end point on the two crack surfaces. The acting forces and moments at the crack tip with a path Γ is depicted in Figure F.9. Mathematically, the J-integral is expressed in Eq. (F.25), where Γ is the path, W the strain energy density, T the tensile vector, u the displacement vector and ds an infinitely small distance along the aforementioned path. The strain energy density W and the tensile vector T are given by Eq. (F.26) and (F.27), with n the normal unity vector perpendicular to the perimeter.

$$J = \int_{\Gamma} \left[W dy - T \frac{du}{dx} ds \right] \tag{F.25}$$

$$W = \int \sigma d\varepsilon \tag{F.26}$$

$$T = \sigma n \tag{F.27}$$

A simplified J-integral in function of the acting forces and moments at the crack tip of an adhesive bond is developed by Fernlund (Fernlund et al. 1994; Fernlund & Spelt 1991). Comparison between the failure load predicted by the energy release factor and the J-integral, showed almost no difference between those two (Abdel Wahab et al. 2001).
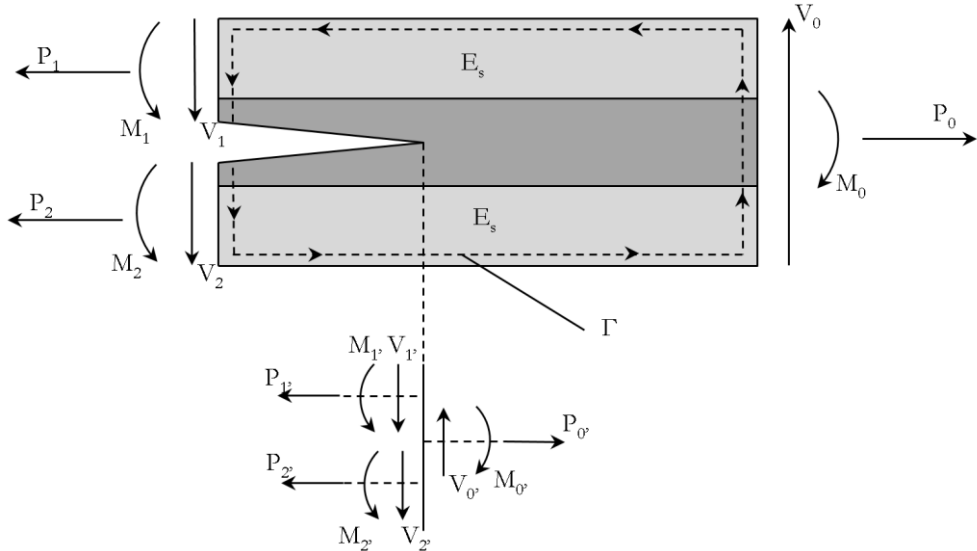
As a general conclusion it can be stated that the critical energy release factor is the most widely used failure criterion in fracture mechanics for adhesive connections. Failure loads determined from this criterion give good agreement with experiments. This criterion is also largely standardized which simplifies the use. Furthermore, Yuan and Xu (2008) have shown that the effective stress occurring at the location of the crack tip by adhesive connection is not higher than the yield strength of the material. Causing the plastic zone around the crack tip to be small and the energy input for plastic deformation negligible, which means that the use of linear elastic fracture mechanics is substantiated.

In the use of the fracture mechanics, it is also necessary to know the size of defects in the adhesive layer for the determination of the ultimate load. Common defects in an adhesive layer are shown in Figure F.10.
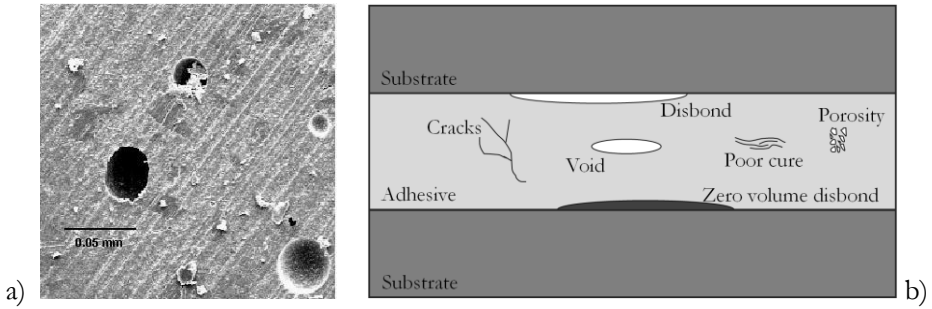
FIGURE F.10: A) ACTUAL DEFECTS IN AN ADHESIVE LAYER (HADJ-AHMED ET AL. 2001) AND B) VISUALISATION OF TYPICAL ADHSIVE DEFECTS (BASED ON (ADAMS & WAKE 1984) AND (TAVROU ET AL. 2010))

It is possible to determine the flaw size in a non-destructive way by means of ultrasonic testing (e.g. ultrasonic measurements, digital shearography and X-ray radiography) on specimens with a thickness of several millimetres. The inherent complexity and cost of these tests, combined with the uncertainty about material properties makes fracture mechanics unfavourable. In practice, a continuum mechanics approach is often preferable.

Appendix G: Ageing

G.1.   Introduction

The material safety coefficient of 2 for environment conditions in Chapter 9 for the reduction of the adhesive strength, indicates that environment conditions such as humidity, UV-radiation and thermal cycling, can cause degradation of the mechanical adhesive properties. The aim of this chapter is to determine this degradation for the two selected adhesives. Determination of reduction factors in function of environment conditions is out of the scope of this chapter, as long-term ageing testing on more than two adhesives is required for this. However, the results of the artificial ageing will indicate how adhesive point-fixings will behave in environment conditions.

In this chapter first an artificial ageing schedule is proposed for adhesive point-fixings based on available standards and guidelines. In this scheme, the most important environmental factors are included, i.e. moisture, temperature and UV-radiation. Next, the two selected adhesives are examined for their durability by imposing the proposed artificial ageing procedures. For these, the effects of individual and combined influential factors on the mechanical properties were assessed by performing experimental tests. The results described in this appendix have already been published in Van Lancker et al. (2016b). Hence, this chapter is generally based on this publication.

G.2.   Artificial ageing

During their service life, adhesive connections are subjected to various environmental and operational conditions (Wolf 1999; Dillard 2010; Silva et al. 2011; Pethrick 2015). The external environment of a facade exposes structural adhesives to humidity, water absorption, temperature, thermal cycles, daily thermal movements, UV-radiation, cleaning products, etc. Knowledge regarding the long-term behaviour and durability of structural adhesive connections used in building construction is important, to ensure the minimum service lifetime of 20 to 25 years. Therefore, artificial ageing is often used to determine the effects of environmental conditions on the mechanical properties of adhesive connections in a relatively short time period. Under laboratory conditions, specimens are subjected to ageing procedures that accelerate the deterioration of their mechanical properties and afterwards tested to quantify these. To be able to estimate the service life of an adhesive or adhesive connection, it is necessary to correlate the artificial ageing time to real in-service time. Nevertheless, this extrapolation of the mechanical properties to longer periods than tested, is not obvious as other authors already pointed out (Wolf 1999; Adams et al. 1997; Ebnesajjad & Landrock 2014).

An excess of durability standards and technical guidelines has become manifest throughout the years. The performance-based specifications for adhesives and adhesive connections developed by standard organisations, such as CEN, ISO, ASTM, DIN, etc. need to have a wide applicability and need to represent actual service conditions (Broughton & Mera 1997). Hence, to perform research on the durability of adhesive connections for certain applications, it is important to first select relevant and useful standards and technical guidelines for the considered application. Next, an artificial ageing schedule can be designed based on these documents with, if necessary, adaptations to confirm the long-term performance of the adhesive or adhesive connection. The proposed artificial ageing schedule to study the individual effects and the sum of degrading effects of the environmental factors moisture, temperature and radiation on the long-term behaviour of adhesive point-fixings is depicted in Figure G.1. The crosses in this figure represent a test phase during which particular mechanical properties of a series of test specimens were determined. Reference tests on unaged specimens (Series A) enabled the comparison with aged specimens and therefore the evaluation of the long-term behaviour of structural adhesive glass-metal connections.
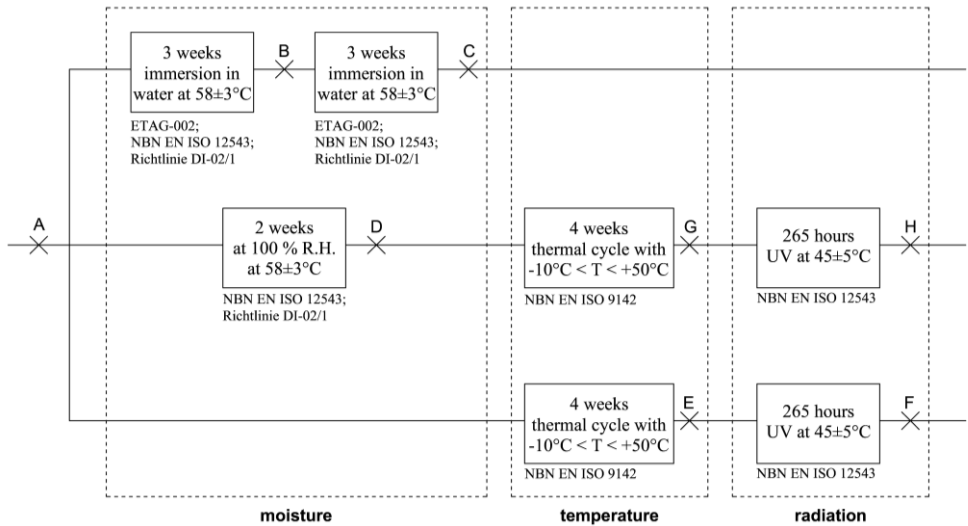
FIGURE G.1: PROPOSED ARTIFICIAL AGEING SCHEDULE (THE CROSSES AND CORRESPONDING LETTERS REPRESENT A TEST PHASE).

G.3.   Experimental programme

Using the proposed artificial ageing schedule, an extensive experimental program was conducted to investigate the effect of a number of environmental parameters on the long-term behaviour of adhesive point-fixings. A stainless steel connector with a diameter and a height of 30 mm was adhesively bonded to a 250 mm by 100 mm monolithic glass panel with a thickness of 12 mm. In case of the MS-polymer, annealed float glass was used whereas for the stiff epoxy, fully tempered float glass was used, the same test configuration as in Chapter 8. For each series (Series A to Series H) of both the MS-polymer and the epoxy, five samples were produced. After production at ambient RH and temperature, the specimens were stored in a climatic chamber with a temperature of 20°C and a RH of 60% for four weeks. Subsequently, the reference series (Series A) was tested, while all other series (Series B to Series H) underwent the artificial ageing procedures as depicted in Figure G.1.

As in Chapter 7, tension was considered. Therefore, displacement-controlled axial tensile tests on the adhesive point-fixings were performed with a displacement rate of 1 mm/min. The test ended when either the adhesive layer fails or the glass panel broke. The test setup is illustrated in Figure G.2.
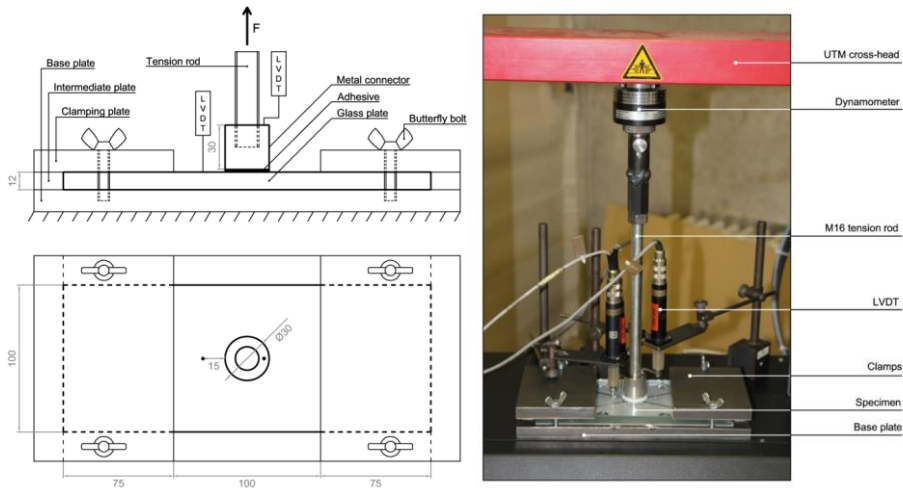
FIGURE G.2: SCHEMATIC TEST SETUP (DIMENSIONS IN MM) AND ACTUAL TEST SETUP FOR THE TENSILE TESTS (VAN LANCKER ET AL. 2016A).

G.4. Results

G.4.1. Soudaseal 270 HS (SO)

After the artificial ageing procedures investigating moisture or thermal cycling, no visual degradation of the adhesive layer was observed. However, after exposure to UV-radiation (Series F-SO and Series H-SO), yellowing of the MS-polymer had occurred. This yellowing is depicted in Figure G.3. Failure, for the reference series (Series A-SO) as well as for all aged series (Series B-SO to Series H-SO), presented itself in cohesive failure or in a combination of adhesive and cohesive failure. At the peak load, cracks appeared at the top of the adhesive layer, after which they propagated throughout the adhesive with an increasing vertical displacement. At some points, the adhesive simply detached gradually further from the steel, causing partial adhesive failure of the connection.
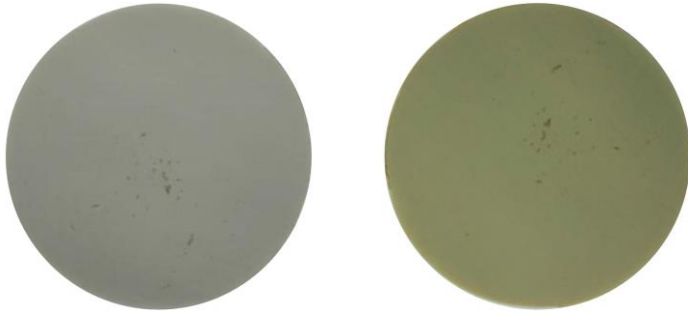
FIGURE G.3: YELLOWING OF SO, PICTURES FROM BEFORE AND AFTER UV-RADIATION.

Ductile behaviour was observed for SO, due to its hyperelastic material nature. The relationship between the applied force and the displacement of the adhesive layer was used to derive a stress-strain curve for the adhesive. Based on Dispersyn et al. (2014), the ratio of the difference in stress $\Delta\sigma$ for the corresponding difference in strain $\Delta\varepsilon$ equal to 0.2, as written in Eq. (G.1), was defined as the stiffness K.

$$K = \frac{\Delta\sigma}{\Delta\varepsilon} \qquad (G.1)$$

A summary of the calculated values for the initial stiffness and the measured failure loads is presented in Table G.1. A graphical representation of the results, normalised with respect to the reference series (Series A-SO), is provided in Figure G.4. Immersion in water for three weeks (Series B-SO) decreased the stiffness and strength substantially. After six weeks of immersion (Series C-SO) the stiffness no longer decreased significantly. Strength, however, did increase compared with three weeks immersion, but remained below the reference values of the unaged series. Exposure to a RH of 100% (Series D-SO) also deteriorated the stiffness and strength, but less than in case of immersion in water. Thermal cycling (Series E-SO) resulted in a stiffer and stronger connection. Additionally, exposure to UV-radiation (Series F-SO) further increased strength and stiffness. Combining thermal cycling with humidity (Series G-SO) gave rise to a similar stiffness as for thermal cycling alone (Series E-SO), although the strength was lower. The effect of humidity, thermal cycling and exposure to UV-radiation (Series H-SO) increased strength, and stiffness. The additional exposure to UV-radiation increased the average stiffness, however, dispersion on the results were largest for these series.

Series	Ageing procedure	Stiffness K [N/mm²]	Failure load P_f [kN]
A-SO	REF	4.285 ± 0.597	0.93 ± 0.13
B-SO	3W H_2O	2.256 ± 0.347	0.40 ± 0.07
C-SO	6W H_2O	2.209 ± 0.095	0.49 ± 0.03
D-SO	2W 100% R.H.	3.520 ± 0.386	0.79 ± 0.02
E-SO	ΔT	5.807 ± 0.647	1.43 ± 0.15
F-SO	ΔT+UV	8.311 ± 1.521	1.75 ± 0.05
G-SO	2W 100% R.H. +ΔT	5.676 ± 0.638	1.27 ± 0.10
H-SO	2W 100% R.H. +ΔT+UV	6.007 ± 1.176	1.32 ± 0.05
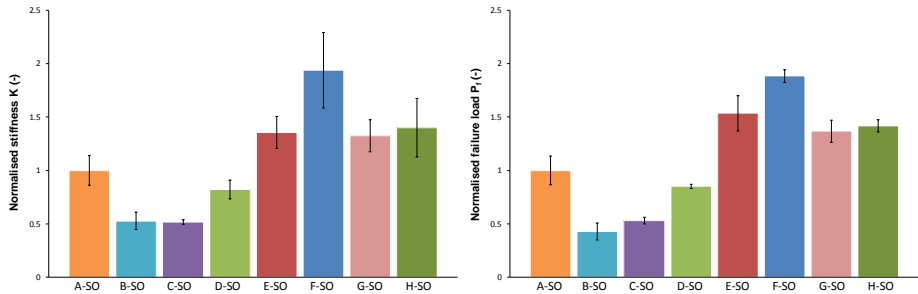
FIGURE G.4: NORMALISED STIFFNESS AND NORMALISED FAILURE LOAD OF UNAGED AND AGED SPECIMENS WITH SOUDASEAL 270 HS.

The applicability of SO for adhesive point-fixings can be reasoned from a durability point of view. Although the resistance against moisture is limited, for the practical application in facades this is less important. Under the considered thermal cycling conditions, whether or not combined with exposure to humidity and/or UV-radiation, mechanical properties even improve. As such, it can be important to take into account an increased stiffness and strength from a mechanical point of view during the design as the overall structural behaviour of the adhesive point connection could change.

G.4.2. 3M™ Scotch-Weld™ 9323 B/A (3M)

After all ageing procedures, except for four weeks of thermal cycling (Series E-3M), visual degradation in terms of a discolouration of the adhesive layer was clearly visible. The state of the adhesive layer is depicted in Figure G.5.

| Series A-3M | Series B-3M | Series C-3M | Series D-3M |
| Series E-3M | Series F-3M | Series G-3M | Series H-3M |
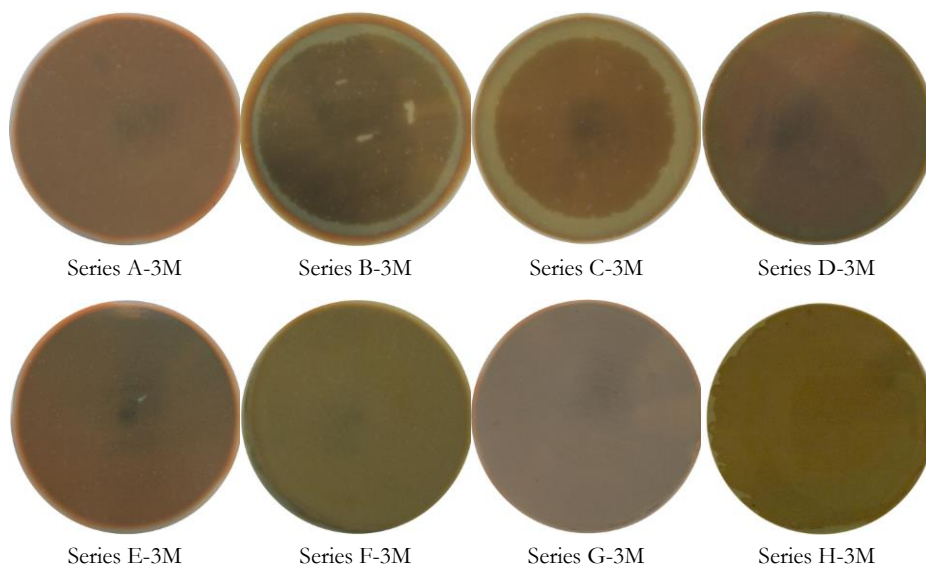
FIGURE G.5: DEGRADATION OF 3M.

The exposure to moisture (Series B-3M to Series D-3M) resulted in a darkening of the bulk adhesive material. After two weeks of exposure to a RH of 100% (Series D-3M), the outer perimeter had a lighter colour than the remainder of the adhesive layer. Three weeks of immersion in water (Series B-3M) led to the origination of a thin circumferential band at the outer perimeter, which expanded significantly to the centre after another three weeks of immersion (Series C-3M). Although no visual degradation was discoverable after four weeks of thermal cycling (Series E-3M), the fracture pattern after testing had a foamy texture as illustrated in Figure G.6, which was also the case for the other ageing procedures including thermal cycling (Series G-3M and Series H-3M). Combining thermal cycling with exposure to UV-radiation (Series F-3M) changed the colour of the adhesive from pink-orange to yellowish. Humidity combined with thermal cycling (Series G-3M) caused similar deterioration as for the exposure to a RH of 100% solely.

FIGURE G.6: FOAMY FRACTURE PATTERN FOR SERIES E-3M.

Failure of the adhesive happens in a very brittle manner. Either failure in the adhesive occurred or the glass substrate failed and brittle cohesive substrate failure was detected. The strength of the connections which resulted in glass failure represent a lower boundary of the inherent strength of the adhesive interlayer. The durability of the adhesive layer was the main interest; therefore specimens that experienced substrate failure were not considered for strength analysis. From the stress-strain curve, the stiffness K was calculated. Table G.2 contains the values for the average stiffness and average strength of the adhesive layer for the unaged and aged test series (Series A-3M to Series H-3M). Figure G.7 contains a graphical representation of the obtained results of the mechanical properties of the aged series relative to the reference series.

The exposure to moisture of the 2c-epoxy led to significant damage of the adhesive layer resulting in a decrease in stiffness and strength. The effect of immersion in water for three weeks (Series B-3M) resulted in a significant decrease in stiffness and strength compared to the reference series. The failure mode of most specimens of this series was almost pure adhesive failure at the glass substrate, resulting in very low failure loads. Two weeks of exposure to a RH of 100% (Series D-3M) resulted in a loss of stiffness comparable to the loss in stiffness after six weeks of immersion in water. Exposure to thermal cycling (Series E-3M) decreased stiffness and strength, although the dispersion on the results was rather high. For subsequent exposure to UV-radiation (Series F-3M), the failure load remained approximately equal, but again the scatter on the results was relatively high. The stiffness, nevertheless, increased again. Exposure to four weeks of thermal cycling after two weeks of exposure to humidity (Series G-3M) overall decreased stiffness and strength. Compared to Series D, the additional thermal cycles increased stiffness and strength again.

TABLE G.2: STIFFNESS AND FAILURE LOAD OF UNAGED AND AGED STRUCTURAL ADHESIVE POINT-FIXINGS WITH 3M.

Series	Ageing Procedure	Stiffness K [N/mm²]		Failure load P_f [kN]	
A-3M	REF	2.084 $\pm$ 0.172		18.48 $\pm$ 3.15	
B-3M	3W H_2O	1.895 $\pm$ 0.140		4.11 $\pm$ 1.04	
C-3M	6W H_2O	1.599 $\pm$ 0.055		9.03 $\pm$ 0.31	
D-3M	2W 100% R.H.	1.581 $\pm$ 0.153		11.26 $\pm$ 0.73	
E-3M	ΔT	1.769 $\pm$ 0.160		14.93 $\pm$ 3.29	
F-3M	ΔT+UV	2.034 $\pm$ 0.172		14.46 $\pm$ 2.03	
G-3M	2W+ΔT	1.654 $\pm$ 0.040		14.03 $\pm$ 0.13	
H-3M	2W+ΔT+UV	1.294 $\pm$ 0.069		10.65 $\pm$ 1.75	
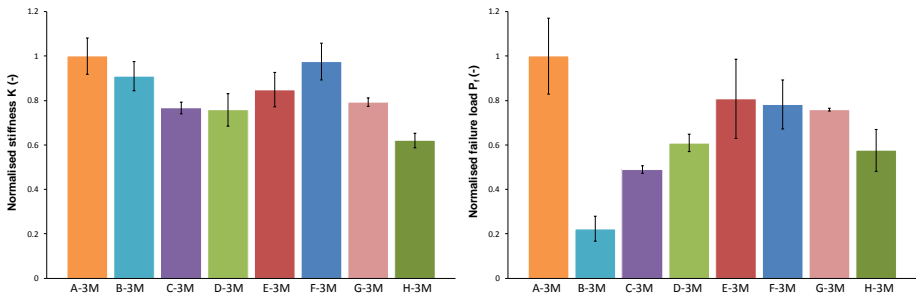
FIGURE G.7: NORMALISED STIFFNESS AND NORMALISED FAILURE LOAD OF UNAGED AND AGED SPECIMENS WITH 3M.

The two-component epoxy 3M™ Scotch-Weld™ 9323 B/A demonstrates good resistance against thermal cycling, whether or not combined with exposure to UV-radiation. However, moisture can lead to significant damage of the adhesive layer, which can be aggravated by exposure to UV-radiation. Nevertheless, for the application of point-fixings in facades, moisture is of less importance as the connection is exposed to an interior environment which can be controlled easily. Hence, from a durability point of view, this adhesive is a good alternative for the considered application.

G.5.   Summary and conclusions

From the abundance of available standards, technical specifications and guidelines regarding the durability of structural adhesives and structural adhesive connections, an appropriate artificial ageing schedule for adhesive point-fixings was derived. The most important environmental factors, i.e. moisture, temperature and UV-radiation were emphasized in this scheme. Next, adhesive point-fixings were tested after being subjected to the procedures from the schedule. Axial tensile tests were performed on the point-fixings to assess the effect of the different artificial ageing procedures on the stiffness and strength.

The resistance of the MS-polymer SO against immersion in water and exposure to humidity was limited as both stiffness and strength decreased significantly. Thermal cycling meliorated the mechanical properties of the connection. Exposure to UV-radiation had no significant influence on the mechanical properties. Although an increase in the mean strength and stiffness after thermal cycling was observed, there was no effect of UV-radiation after subsequent exposure to humidity and thermal cycling.

The exposure to moisture, either as vapour (humidity) or as liquid (immersion), led to significant damage of the adhesive layer of 2c-epoxy 3M resulting in a decrease in stiffness and strength. This epoxy showed good resistance against thermal ageing, although there was a small decrease in stiffness. The strength of the connection was not significantly affected by this artificial ageing procedure. UV-radiation aggravated previous damage caused by moisture, which was not so in case of previous exposure to thermal cycling.

From the investigated environmental parameters, exposure to moisture is proven to be the most severely. As stated in Table 8.1. in Chapter 8, when it is not possible to eliminate moisture, by applying a sealant or placing the point-fixing on the inside of the structure, a reducing factor of 2 has to be applied. From the experiments in this chapter, moisture indeed reduced the failure load by a factor of 2. It will be important to take exposure to moisture in the design of adhesive point-fixings, regardless of the adhesive type. Furthermore, temperature and UV-radiation will reduce the adhesive strength for stiff adhesives.

Bibliography

ABAQUS, 2014. *Getting started with Abaqus/Standard, Version 6.14.*, USA: Dassault Systèmes Simulia Corp.

Abdel Wahab M.M., Ashcroft I.A., Crocombe A.D., Hughes D.J. & Shaw S.J., 2001. "The effect of environment on the fatigue of bonded composite joints. Part 2: fatigue threshold prediction". *Composites Part A: Applied Science and Manufacturing*, 32(1), pp. 59–69.

Achenbach M. & Duarte J., 2003. "A finite element methodology to predict age-related mechanical properties and performance changes in rubber components". In *Constitutive Models for Rubber III: Proceedings of the Third European conference on constitutive models for rubber*. London, UK, pp. 59–67.

Adams M.R. & Garton A., 1993. "Surface modification of bisphenol-A-polycarbonate by far-UV radiation. Part II: In air". *Polymer Degradation and Stability*, 42(2), pp. 145–151.

Adams R.D. & Harris J.A., 1987. "The influence of local geometry on the strength of adhesive joints". *International Journal of Adhesion and Adhesives*, 7(2), pp. 69–80.

Adams R.D. & Mallick V., 1992. "A Method for the Stress Analysis of Lap Joints". *The Journal of Adhesion*, 38(3), pp. 199–217.

Adams R.D., Comyn J. & Wake W.C., 1997. "*Structural adhesive joints in engineering*", Houten, The Netherlands: Springer Netherlands.

Ali A., Hosseini M. & Sahari B.B., 2010. "A Review of Constitutive Models for Rubber-Like Materials". *American Journal of Engineering and Applied Sciences*, 3(1), pp. 232–239.

Almeida J.R.M. & Monteiro S.N., 2000. "The Iosipescu test method as a method to evaluate the tensile strength of brittle materials". *Polymer Testing*, 18(1999), pp. 407–414.

Amadio C., Asce M., De Luca O., Fedrigo C., Fragiacomo M. & Sandri C., 2008. "Experimental and Numerical Analysis of a Glass-to-Steel Joint". *Journal of Structural Engineering*, 134(8), pp. 1389–1398.

Amadio C., Brasseur M., Carbary L. & Wolf A., 2008. "Experimental and Numerical Analysis of a Glass-to-Steel Joint". *Journal of Structural Engineering*, 134(8), pp. 1389–1398.

Amijima S. & Fujii T., 1989. "Extension of a one-dimensional finite element model program for analysing elastic-plastic stresses and progressive failure of adhesive bonded joints". *International Journal of Adhesion and Adhesives*, 9(4), pp. 243–249.

Anderson T.L., 2005. "*Fracture Mechanics: Fundamentals and Applications, Third Edition*", Boca Raton, USA: CRC Press Taylor & Francis Group.

Appelfeld D., Hayez V. & Kragh M., 2015. "High performance curtain wall solutions - optimization by simulations". In *Glass Performance Days 2015*. Tampere, Finland, pp. 18–22.

Arias I. & Achenbach J.D., 2004. "A model for the ultrasonic detection of surface-breaking cracks by the scanning laser source technique". *Wave Motion*, 39(1), pp. 61–75.

Arruda E.M. & Boyce M.C., 1993. "Evolution of plastic anisotropy in amorphous polymers during finite straining". *International Journal of Plasticity*, 9(6), pp. 697–720.

Ashcroft I., Comyn J. & Tellwright S., 2009. "Adhesives for automotive windscreen replacement: Kinetics of cure and bond strength". *International Journal of Adhesion and Adhesives*, 29(2), pp. 155–166.

ASTM C1678-10, 2015. *Standard Practice for Fractographic Analysis of Fracture Mirror Sizes in Ceramics and Glasses,*

ASTM D1002, 2010. *Standard Test Method for Apparent Shear Strength of Single-Lap-Joint Adhesively Bonded Metal Specimens by Tension Loading (Metal-to-Metal),*

ASTM D3163, 2008. *Standard Test Method for Determining Strength of Adhesively Bonded Rigid Plastic Lap-Shear Joints in Shear by Tension Loading,*

ASTM D3433, 2012. *Standard Test Method for Fracture Strength in Cleavage of Adhesives in Bonded Metal Joints,*

ASTM D3983, 2011. *Standard Test Method for Measuring Strength and Shear Modulus of Nonrigid Adhesives by the Thick-Adherend Tensile-Lap Specimen,*

ASTM D5379, 2012. *Standard Test Method for Shear Properties of Composite Materials by the V-Notched Beam Method,*

ASTM D5656, 2010. *Standard Test Method for Thick-Adherend Metal Lap-Shear Joints for Determination of the Stress-Strain Behavior of Adhesives in Shear by Tension Loading*.

ASTM D695, 2010. *Standard Test Method for Compressive Properties of Rigid Plastics*.

Attard M.M., 2003. "Finite strain—isotropic hyperelasticity". *International Journal of Solids and Structures*, 40(17), pp. 4353–4378.

Attard M.M. & Hunt G.W., 2004. "Hyperelastic constitutive modeling under finite strain". *International Journal of Solids and Structures*, 41(18), pp. 5327–5350.

Azari S., Eskandarian M., Papini M., Schroeder J.A. & Spelt J.K., 2009. "Fracture load predictions and measurements for highly toughened epoxy adhesive joints". *Engineering Fracture Mechanics*, 76(13), pp. 2039–2055.

Bach A., Dreifert M. & Greuling H., 2000. "*Die Kunst des Klebens*", Frankfurt am Main, Germany: Fonds der Chemischen Industrie im & Verband der Chemischen Industrie e.V.

Baitinger M. & Feldmann M., 2010a. "Design concept for bolted Glass". In *Challenging Glass 2*. Delft, The Netherlands, pp. 239–248.

Baitinger M. & Feldmann M., 2010b. "Ein Bemessungskonzept für SL-belastete Anschlüsse im konstruktiven Glasbau". *Stahlbau*, 79(S1), pp. 60–69.

Baker M. & Ericksen J., 1954. "Inequalities restricting the form of the stress-deformation relations for isotropic elastic solids and Reiner-Rivlin fluids". *Journal of the Washington Academy of Sciences*, pp. unknown.

Barenblatt G.I., 1962. "The Mathematical Theory of Equilibrium Cracks in Brittle Fracture". *Advances in Applied Mechanics*, 7, pp. 55–129.

Baziard Y., El Abdi R., Amara D., Petit J.A. & Levallois F., 1995. "Study of critical failure parameters for an adhesive-bonded single lap joint with ceramic adherends". *International Journal of Adhesion and Adhesives*, 15(3), pp. 155–160.

Belis J., 2006. "*Kipsterkte van monolitische en gelamineerde liggers*", PhD Disseratation, Ghent, Belgium, Universiteit Gent.

Belis J., Callewaert D. & Van Hulle A., 2011. "*Bouwen met Glas en Adhesieven*", Ghent, Belgium: Laboratory for Research on Structural Models.

Belis J., Van Hulle A., Callewaert D. & Dispersyn J., 2012. "Experimental investigation of unconventional canopy prototypes, suspended bij adhesive bonds". In *Challenging Glass 3*. Delft, The Netherlands, pp. 177–186.

Belis J., Van Hulle A., Out B., Bos F., Callewaert D. & Poulis H., 2011. "Broad screening of adhesives for glass-metal bonds". In *Glass Performance Days 2011*. Tampere, Finland, pp. 286–289.

Bennison S.J., Jagota A. & Smith C.A., 1999. "Fracture of Glass/Poly(vinyl butyral) (Butacite®) Laminates in Biaxial Flexure". *Journal of the American Ceramic Society*, 82(7), pp. 1761–1770.

Bennison S.J., Stelzer I., Davies P.S., Sloan J.G., Huang X. & Gang L.,2009. "Calculation Methods for the Structural Behavior of Laminated Glass". In *Glass Performance Days 2009*. Tampere, Finland, pp. 433–434.

Bernard F. & Daudeville L., 2009. "Point fixings in annealed and tempered glass structures: Modeling and optimization of bolted connections". *Engineering Structures*, 31(4), pp. 946–955.

Bernard F., 2008. "Optimization of Bolted Connections in Loadbearing Glass Elements". In *Challenging Glass*. Delft, The Netherlands, pp. 165–174.

Berry J., 1960. "Some kinetic considerations of the Griffith criterion for fracture— I Equations of motion at constant force". *Journal of the Mechanics and Physics of Solids*, 8(3), pp. 194–206.

Beyer J. & Unterweger R., 2007. "*Brought to the point*". Report Fisher Connect It, issue 8.

Beyer J., 2007. "*Ein Beitrag zum Bemessungskonzept für punktgestützte Glastafeln"*. PhD Disseratation, Darmstadt, Germany, Technischen Universität Darmstadt.

Beyer J., 2008. "A new Concept for the Design of Structural Glass supported by Point Fittings". In *Challenging Glass*. Delft, The Netherlands, pp. 175–184.

Bigwood D.A. & Crocombe A.D., 1989. "Elastic analysis and engineering design formulae for bonded joints". *International Journal of Adhesion and Adhesives*, 9(4), pp. 229–242.

Blackman B.R.K., Kinloch A.J., Paraschi M. & Teo, W.S., 2003. "Measuring the mode I adhesive fracture energy, GIC, of structural adhesive joints: The results of an international round-robin". *International Journal of Adhesion and Adhesives*, 23(4), pp. 293–305.

Blandini L., 2007. "Structural use of adhesives for the construction of frameless glass shells". *International Journal of Adhesion and Adhesives*, 27(6), pp. 499–504.

Blyberg L., Serrano E., Enquist B. & Sterley M., 2012. "Adhesive joints for structural timber/glass applications: Experimental testing and evaluation methods". *International Journal of Adhesion and Adhesives*, 35, pp. 76–87.

Böl M. & Reese S., 2006. "Finite element modelling of rubber-like polymers based on chain statistics". *International Journal of Solids and Structures*, 43(1), pp. 2–26.

Bos F. & Veer F., 2007. "Transparent polymer joints in glass structures". In *Glass Performance Days 2007*. Tampere, Finland, pp. 62–67.

Boubakri A., Elleuch K., Guermazi N. & Ayedi H.F., 2009. "Investigations on hygrothermal aging of thermoplastic polyurethane material". *Materials & Design*, 30(10), pp. 3958–3965.

Boubakri A., Guermazi N., Elleuch K. & Ayedi H.F., 2010. "Study of UV-aging of thermoplastic polyurethane material". *Materials Science and Engineering: A*, 527(7-8), pp. 1649–1654.

Boubakri A., Haddar N., Elleuch K. & Bienvenu Y., 2010. "Impact of aging conditions on mechanical properties of thermoplastic polyurethane". *Materials & Design*, 31(9), pp. 4194–4201.

Boyce M.C. & Arruda E.M., 2000. "Constitutive Models of Rubber Elasticity: A Review". *Rubber Chemistry and Technology*, 73(3), pp. 504–523.

Brendler S. & Schneider S., 2004. "Bemessung von punktgelagerten Verglasungen mit verifizierten". *DIBt Mitteilungen*, 6, pp. 196–203.

Brewis D.M., Comyn J. & Tegg J.L., 1980. "The durability of some epoxide adhesive-bonded joints on exposure to moist warm air". *International Journal of Adhesion and Adhesives*, 1(1), pp. 35–39.

Broughton W. & Mera R., 1997. "*Review of durability test methods and standards for assessing long term performance of adhesive joints"*, Middlesex, UK: National Physical Laboratory.

Bues M., Bucak Ö. & Illguth M., 2009. "Bonded point fixities for constructive architectural glass applications". In *Glass Performance Days 2009*. Tampere, Finland, pp. 250–253.

Buffiere J.Y., Maire E., Adrien J., Masse J.P. & Boller E., 2010. "In Situ Experiments with X ray Tomography: an Attractive Tool for Experimental Mechanics". *Experimental Mechanics*, 50(3), pp. 289–305.

Burdekin F.M. & Stone D.E.W., 1966. "The crack opening displacement approach to fracture mechanics in yielding materials". *The Journal of Strain Analysis for Engineering Design*, 1(2), pp. 145–153.

Callewaert D., Belis J., Van Impe R., Lagae G. & De Beule M., 2007. "Glued and preloaded bolted connections for laminated float glass". In *Glass Performance Days 2007*. Tampere, Finland, pp. 654–657.

Callewaert, D., 2012. *"Stiffness of Glass/Ionomer Laminates in Structural Applications"*, PhD Disseratation, Ghent, Belgium, Universiteit Gent.

Castagnetti D., Dragoni E. & Spaggiari A., 2010. "Failure analysis of bonded T-peel joints: Efficient modelling by standard finite elements with experimental validation". *International Journal of Adhesion and Adhesives*, 30(5), pp. 306–312.

Chagnon G., Marckmann G. & Verron E., 2004. "A Comparison of the Hart-Smith Model with Arruda-Boyce and Gent Formulations for Rubber Elasticity". *Rubber Chemistry and Technology*, 77(4), pp. 724–735.

Chai H., 1993. "Observation of deformation and damage at the tip of cracks in adhesive bonds loaded in shear and assessment of a criterion for fracture". *International Journal of Fracture*, 60(4), pp. 311–326.

Christensen R.M., 2013. *"The Theory of Materials Failure"*, Oxford, UK: Oxford University Press.

Clark J.D. & McGregor I.J., 1993. "Ultimate Tensile Stress over a Zone: A New Failure Criterion for Adhesive Joints". *The Journal of Adhesion*, 42(4), pp. 227–245.

Claude B., Gonon L., Duchet J., Verney V. & Gardette J.L., 2004. "Surface cross-linking of polycarbonate under irradiation at long wavelengths". *Polymer Degradation and Stability*, 83(2), pp. 237–240.

Cloetens P., Pateyron-Salomé M., Buffière J.Y., Peix G., Baruchel J., Peyrin F. & Schlenker M., 1997. "Observation of microstructure and damage in materials by phase sensitive radiography and tomography". *Journal of Applied Physics*, 81(9), pp. 58-78.

Cotterell B., Hbaieb K., Williams J.G., Hadavinia H. & Tropsa V., 2006. "The root rotation in double cantilever beam and peel tests". *Mechanics of Materials*, 38(7), pp. 571–584.

Crocombe A.D. & Adams R.D., 1982. "An elasto-plastic investigation of the peel test". *The Journal of Adhesion*, 13(3-4), pp. 241–267.

Crocombe A.D. & Kinloch A.J., 1994. *"MTS Adhesive Project 2: Failure modes and criteria - Report no. 1: Review of adhesive bond failure criteria"*, Oxfordshire, UK.

Crocombe A.D. & Tatarek A., 1985. "A unified approach to adhesive joint analysis". In *Proceedings of adhesives, sealants and encapsulants 85*, London, UK, pp. unknown.

Crocombe A.D., Bigwood D.A. & Richardson G., 1990. "Analysing structural adhesive joints for failure". *International Journal of Adhesion and Adhesives*, 10(3), pp. 167–178.

Crocombe A.D., Richardso, G. & Smith P., 1995. "A unified approach for predicting the strength of cracked and non-cracked adhesive joints". *The Journal of Adhesion*, 49(3-4), pp. unknown.

Crocombe A.D., Hancox N. & Mccarthy J.C., 1995. "*MTS Adhesives Project 2 Failure Modes and Criteria - Task 1 : Detailed Study of Joint Failure - Summary Report*", Oxfordshire, UK.

CSTB (Centre Scientifique et Technique du Bâtiment) 3574-V2, 2012. *Vitrages extérieurs attachés (VEA) faisant l'objet d'un Avis Technique*,

Cui T., Chao Y.J. & Van Zee J.W., 2013. "Thermal stress development of liquid silicone rubber seal under temperature cycling". *Polymer Testing*, 32(7), pp. 1202–1208.

D'Haene P. & Savineau G., 2007. "Mechanical properties of laminated safety glass - FEM Study". In *Glass Performance Days 2007*, Tampere, Finland, pp. 594–598.

da Silva L., Öchsner A. & Adams R., 2011. "*Handbook of adhesion technology*", Berlin, Germany: Springer Heidelberg.

da Silva L.F.M., das Neves P.J.C., Adams R.D. & Spelt J.K., 2009. "Analytical models of adhesively bonded joints-Part I: Literature survey". *International Journal of Adhesion and Adhesives*, 29(3), pp. 319–330.

da Silva, L.F.M., das Neves, P.J.C., Adams, R.D., Wang, A. & Spelt J.K., 2009. "Analytical models of adhesively bonded joints-Part II: Comparative study". *International Journal of Adhesion and Adhesives*, 29(3), pp. 331–341.

Daiyan H., Andreassen E., Grytten F., Osnes H. & Gaarder R.H., 2012. "Shear Testing of Polypropylene Materials Analysed by Digital Image Correlation and Numerical Simulations". *Experimental Mechanics*, 52(9), pp. 1355–1369.

Das P.K., Deslauriers P.J., Fahey D.R., Wood F.K. & Comforth F.J., 1995. "Photodegradation and photostabilization of poly (p-phenylene sulfide). Part 2. UV induced physicochemical changes". *Polymer Degradation and Stability*, 48, pp.11–23.

De Jaegher J., 2014. *"Experimenteel en numeriek onderzoek naar glaspanelen ondersteund door verlijmde"*. Thesis Disseratation, Ghent, Belgium, Universiteit Gent.

De Neve B.N. & Shanahan M.E.R., 1992. "Effects of humidity on an epoxy adhesive". *International Journal of Adhesion and Adhesives*, 12(3), pp.191–196.

Dean G., Crocker L., Read B. & Wright L., 2004. "Prediction of deformation and failure of rubber-toughened adhesive joints". *International Journal of Adhesion and Adhesives*, 24(4), pp. 295–306.

Dean G.D., Duncan B.C., Adams R., Thomas R. & Vaughn L., 1996. "*MTS Adhesives Project 1 Report No 9 - Comparison of Bulk and Joint Specimen Tests for Determining the Shear Properties of Adhesives*", Teddington, Middlesex, UK.

Denys R., 2010. *"Breukmechanica"*, Ghent, Belgium: Ghent University.

Devos S., 2014. *"Onderzoek naar het afschuifgedrag van een adhesieve puntverbinding tussen glas en metaal"*. Thesis Disseratation, Ghent, Belgium, Universiteit Gent.

Dias V. , Hechler O., Odenbreit C. & Scholzen F., 2012. "Development of material law for silicone to simulate structural afhesive connections". In *Engineered transparency International Conference at Glasstec*. Düsselfdorf, Germany, pp. 323–333.

Dias V., Odenbreit C., Hechler O., Scholzen F. & Ben Zineb T., 2014. "Development of a constitutive hyperelastic material law for numerical simulations of adhesive steel–glass connections using structural silicone". *International Journal of Adhesion and Adhesives*, 48, pp. 194–209.

Dillard D., 2010. "*Advances in structural adhesive bonding"*, Cambridge, UK: CRC Press LLC & Woodhead Publishing Limited.

DIN 14869-2, 2004. *Structural adhesives - Determination of shear behaviour of structural bonds - Part 2: Thick adherends shear test*,

DIN 18008, 2010. *Glass in Building - Design and construction rules*,

DIN 54451, 1978. *Testing of adhesives for metals and of bonded metal joints; tensile shear test for the determination of the shear stress-strain diagram of an adhesive in a bonded joint*,

Ding S.H. & Liu D.Z., 2006. "Durability evaluation of building sealants by accelerated weathering and thermal analysis". *Construction and Building Materials*, 20(10), pp. 878–881.

Dispersyn J., Belis J. & Sonck D., 2015. "New glass design method for adhesive point-fixing applications". *Proceedings of the Institution of Civil Engineers - Structures and Buildings*, 168(7), pp. 479–489.

Dispersyn J., Santarsiero M., Belis J. & Louter C., 2014. "A preliminary study of the nonlinearity of adhesive point-fixings in structural glass facades". *Journal of Facade Design and Engineering*, 2, pp. 85–107.

Dodd G., 1997. "Essential elements of bolted structural glass systems". In *Proc., ICBEST'97*. Bath, UK, pp. 79–84.

Duarte I., Rotter A., Malvestiti A., Silva M. & Paulo S., 2009. "The role of glass as a barrier against the transmission of ultraviolet radiation: an experimental study". *Photodermatology, Photoimmunology & Photomedicine*, 25(9), pp. 181–184.

Duerr D. & Asce M., 2006. "Pinned Connection Strength and Behavior". *Journal of Structural Engineering*, 132(2), pp. 182–194.

Dugdale D.S., 1960. "Yielding of steel sheets containing slits". *Journal of the Mechanics and Physics of Solids*, 8(2), pp. 100–104.

Ebnesajjad S. & Landrock A., 2014. "*Adhesives technology handbook*", London, UK: Elsevier - William Andrew.

EN 12150-1, 2015. *Glass in building - Thermally toughened soda lime silicate safety glass - Part 1: Definition and description*, CEN, Europe.

EN 14179-1, 2007. *Glass in building - Heat soaked thermally toughened soda lime silicate safety glass - Part 1 : Definition and description*, CEN, Europe.

EN 1863-1, 2012. *Glass in building - Heat strengthened soda lime silicate glass - Part 1: Definition and description*, CEN, Europe.

EN 1991-1-1, *Eurocode 1: Actions on structures -Part 1-1: General actions -Densities, self-weight, imposed loads for buildings*,

EN 1991-1-3, *Eurocode 1: Actions on structures -Part 1-3: General actions - Snow loads*,

EN 1991-1-4, *Eurocode 1: Actions on structures -Part 1-4: General actions - Wind actions*,

ETAG 002, 2002. *Guideline for European Technical Approval for Structural Sealant Glazing Kits (SSGK) - Part2: Coated Aluminium Systems*,

Feng C.W., Keong C.W., Hsueh Y.P., Wang Y.Y., Sue H.J., 2005. "Modeling of long-term creep behavior of structural epoxy adhesives". *International Journal of Adhesion and Adhesives*, 25(5), pp. 427–436.

Fernlund G. & Spelt J.K., 1991. "Failure load prediction of structural adhesive joints". *International Journal of Adhesion and Adhesives*, 11(4), pp. 221–227.

Fernlund G., Papini M., McCammond D. & Spelt J.K., 1994. "Fracture load predictions for adhesive joints". *Composites Science and Technology*, 51(4), pp. 587–600.

Fischer H.R., Semprimoschnig C., Mooney C., Rohr T., van Eck E.R.H. & Verkuijlen M.H.W., 2013. "Degradation mechanism of silicone glues under UV irradiation and options for designing materials with increased stability". *Polymer Degradation and Stability*, 98(3), pp. 720–726.

FME-CWM, 2008. "*VM87 - Lijmen van metalen*", Zoetermeer, The Netherlands: Vereniging FME-CWM, vereniging van ondernemers in de technologisch-industriële sector

Galuppi L. & Royer-Carfagni G.F., 2012a. "Effective thickness of laminated glass beams: New expression via a variational approach". *Engineering Structures*, 38, pp.53–67.

Galuppi L. & Royer-Carfagni G.F., 2012b. "The effective thickness of laminated glass plates". *Journal of Mechanics of Materials and Structures*, 7(4), pp. 375–400.

Galuppi L. & Royer-Carfagni G.F., 2012c. "Laminated beams with viscoelastic interlayer". *International Journal of Solids and Structures*, 49(18), pp. 2637–2645.

Gao L., Chen X. & Gao H., 2012. "Shear strength of anisotropic conductive adhesive joints under hygrothermal aging and thermal cycling". *International Journal of Adhesion and Adhesives*, 33, pp. 75–79.

Gent A.N. & Thomas A.G., 1958. "Forms for the stored (strain) energy function for vulcanized rubber". *Journal of Polymer Science*, 28(118), pp. 625–628.

Gent A.N., 1996. "A New Constitutive Relation for Rubber". *Rubber Chemistry and Technology*, 69(1), pp. 59–61.

Ghani,Z.A., 2007. "Principles of adhesion", Adelaide, Australia: Royal Australasian College of Dental Surgeons..

Goland M. & Reissne, E., 1944. "The stresses in cemented joints". *Journal of Applied Mechanics*, 11, pp. 17–27.

Goss B., 2002. "Bonding glass and other substrates with UV curing adhesives". *International Journal of Adhesion and Adhesives*, 22(5), pp. 405–408.

Greenwood L., Boag T. & McLaren A., 1969. *"Stress distribution in lap joints"*. In Adhesion-Fundamentals and Practice, London, UK/ McLaren, London.

Griffith A.A., 1921. "The Phenomena of Rupture and Flow in Solids". *Philosophocal Transactions of the Royal Society of Londen*, 221, pp. 163–198.

Habenicht G., 2009. "*Kleben*", Berlin, Germany: Springer Berlin Heidelberg.

Hadj-Ahmed R., Foret G. & Ehrlacher A., 2001. "Probabilistic analysis of failure in adhesive bonded joints". *Mechanics of Materials*, 33(2), pp. 77–84.

Haese A., 2007. "Experimental analysis of point fixings." In *Glass Performance Days 2007*. Tampere, Finland, pp. 360–361.

Hagl A., 2010. "Bonded Point-Supports : Understanding Today – Optimizing for the Future". In *Challenging Glass 2*. Delft, The Netherlands, pp. 259–268.

Haldimann M., 2006. "*Fracture strength of structural glass elements – analytical and numerical modelling, testing and design*". PhD Disseratation, Lausanne, Switzerland, École Polytechnique Fédérale de Lausanne.

Haldimann M., Luible A. & Overend M., 2008. "*Structural use of Glass (Structural Engineering Documents 10)*", Zürich, Switzerland: IABSE-AIPC-IVBH.

Harman A., Risborg A. & Wang C.H., 2008. "Experimental testing of BMI laminates with stress concentrations and the evaluation of SIFT to predict failure". *Composite Structures*, 86(1-3), pp. 85–95.

Harris J. & Adams R., 1984. "Strength prediction of bonded single lap joints by non-linear finite element methods". *International Journal of Adhesion and Adhesives*, 4(2), pp. 65-78.

Hart-Smith L.J., 1966. "Elasticity parameters for finite deformations of rubber-like materials". *Zeitschrift für angewandte Mathematik und Physik ZAMP*, 17(5), pp. 608–626.

Hart-Smith L.J. & Crisp J.D.C., 1967. "Large elastic deformations of thin rubber membranes". *International Journal of Engineering Science*, 5(1), pp. 1–24.

Hart-Smith L.J., 1973. "*Adhesive-bonded single-lap joints*", Technical Report CR-112235, Florida, USA: National Aeronautics and Space Administration.

Hart-Smith L.J., 1974. "*Analysis and design of advanced composite bonded joints*", Florida, USA: National Aeronautics and Space Administration.

Herrmann T., 2005. "Design Rules for Glass Panes Fixed by Embedded Point Fittings". In *Glass Processing Days 2005*. Tampere, Finland, pp. 485–489.

Hertelé S., Verstraete M., Van Minnebruggen K., Denys R. & De Waele W., 2013. "Applications of digital image correlation in girth weld testing". In *6th International Pipeline Technology Conference*, Ostend, Belgium, pp. unknown.

Heshmati M., Haghani R. & Al-Emrani M., 2015. "Environmental durability of adhesively bonded FRP/steel joints in civil engineering applications: State of the art". *Composites Part B: Engineering*, 81, pp. 259–275.

Hoffman O., 1967. "The brittle strength of orthotropic materials". *Journal of Composite Materials*, 1(2), pp. 200-206.

Hoss L. & Marczak R.J., 2009. "A new constitutive model for rubber-like materials". *Mecánica Computacional* , 29, pp. 2759-2773.

Hossain M. & Steinmann P., 2013. "More hyperelastic models for rubber-like materials: consistent tangent operators and comparative study". *Journal of the Mechanical Behavior of Materials*, 22, pp. 1–24.

Hua Y., Crocombe A.D., Wahab M.A. & Ashcroft I.A., 2008. "Continuum damage modelling of environmental degradation in joints bonded with EA9321 epoxy adhesive". *International Journal of Adhesion and Adhesives*, 28(6), pp. 302–313.

Hung Y.Y., 1982. "Shearography: A New Optical Method For Strain Measurement And Nondestructive Testing". *Optical Engineering*, 21(3), pp. unknown.

Ift-Richtlinie DI-02/1, 2009. *DI-02/1: Verwendbarkeit von Dichtstoffen, Teil 2: Prüfung von Materialien in Kontakt mit der Kante von Verbund- und Verbundsicherheitsglas*,

Ikegami K., Takeshita T., Matsuo K. & Sugibayashi T., 1990. "Strength of adhesively bonded scarf joints between glass fibre-reinforced plastics and metals". *International Journal of Adhesion and Adhesives*, 10(3), pp. 199–206.

Institution of Structural Engineers (ISE), 1999. *"A Guide to the Structural Use of Adhesives"*, London, UK: Institution of Structural Engineers.

Irwin G.R., 1957. "Analysis of Stresses and Strains Near the End of a Crack Traversing a Plate". *Journal of Applied Mechanics*, 24, pp. 361–364.

ISO 11003-2, 2001. *Adhesives - Determination of shear behaviour of structural adhesives - Part 2: Tensile test method using thick adherends*,

ISO 25217, 2009. *Adhesives -- Determination of the mode 1 adhesive fracture energy of structural adhesive joints using double cantilever beam and tapered double cantilever beam specimens*,

ISO 4587, 2003. *Adhesives - Determination of tensile lap-shear strength of rigid-to-rigid bonded assemblies*,

ISO 527, 1996. *Determination of Tensile Properties of Plastics, International Organization for Standardization.*

ISO 604, 2002. *Plastics - Determination of compressive properties.*

ISO 6721, 2012. *Plastics - Determination of dynamic mechanical properties - Part 11: Glass transition temperature.*

James H.M. & Guth E., 1943. "Theory of the Elastic Properties of Rubber". *The Journal of Chemical Physics*, 11(10), p. 455.

Jeandrau J.P., 1991. "Analysis and design data for adhesively bonded joints". *International Journal of Adhesion and Adhesives*, 11(2), pp. 71–79.

John S., Kinloch A. & Matthews F., 1991. "Measuring and predicting the durability of bonded carbon fibre/epoxy composite joints". *Composites*, 22(2), pp. 121–127.

Kaliske M. & Rothert H., 1997. "On the finite element implementation of rubber-like materials at finite strains". *Engineering Computations*, 14(2), pp. 216–232.

Kanninen M.F. & Popelar C.H., 1985. "*Advanced Fracture Mechanics*", Oxford, UK: Oxford University Press.

Kasper R., 2006. "Berechnungskonzept für die Bemessung von punktförmig gelagerten Glasscheiben". *Stahlbau*, 75(6), pp.454–461.

Kazimi S.M.A., 2001. "*Solid Mechanics*", New Delhi, India: Tata McGraw-Hill Education.

Keshavaraj R., Tock R.W. & Vallabhan C.V.G., 1994. "Effects of moisture on structural silicone rubber sealants used in window glazing applications". *Construction and Building Materials*, 8(4), pp. 227–232.

Khalili S.M.R., Jafarkarimi M.H. & Abdollahi M.A., 2009. "Creep analysis of fibre reinforced adhesives in single lap joints—Experimental study". *International Journal of Adhesion and Adhesives*, 29(6), pp. 656–661.

Kilian H.G., 1980. "A molecular interpretation of the parameters of the van der Waals equation of state for real networks". *Polymer Bulletin*, 3(3), pp. 151–158.

Kim W.S. & Lee J.J., 2009. "Fracture characterization of interfacial cracks with frictional contact of the crack surfaces to predict failures in adhesive-bonded joints". *Engineering Fracture Mechanics*, 76(12), pp. 1785–1799.

Kinloch A., 1983. *"Durability of Structural Adhesives"*, New York, USA: Springer, New York.

Klinkenberg A., Jäger B. & Saal H., 1998. "Untersuchungen zur statisch optimalen Halterposition bei punktgestützten Glastafeln". *Stahlbau*, 67(4), pp. 275–280.

Klinkenberg A., Jäger B. & Saal H., 1998. "Untersuchungen zur statisch optimalen Halterposition bei punktgestützten Glastafeln". *Stahlbau*, 67(4), pp. 275–280.

Lawn B., 1993. *"Fracture of brittle solids - second edition"*, Cambridge, USA: Cambridge University Press.

Leckie F.A. & Bello D.J., 2009. *"Strength and Stiffness of Engineering Systems"*, New York, USA: Springer, New York.

Lee H.K., Pyo S.H. & Kim B.R., 2009. "On joint strengths, peel stresses and failure modes in adhesively bonded double-strap and supported single-lap GFRP joints". *Composite Structures*, 87(1), pp. 44–54.

Lee S.J. & Lee D.G., 2006. "Development of a Failure Model for the Adhesively Bonded Tubular Single Lap Joint". *The Journal of Adhesion*, 40(1), pp. 1–14.

Lettieri M. & Frigione M., 2012. "Effects of humid environment on thermal and mechanical properties of a cold-curing structural epoxy adhesive". *Construction and Building Materials*, 30, pp. 753–760.

Lopez-Pamies O., 2010. "A new I1-based hyperelastic model for rubber elastic materials". *Comptes Rendus Mécanique*, 338(1), pp. 3–11.

Machalická K. & Eliášová M., 2013. "Influence of various factors to mechanical properties of glued joint in glass". In *International Conference on Structures and Architecture*, Guimarães, Portugal, pp. 321–328.

Maniatis I., 2006a. *"Numerical and Experimental Investigations on the Stress Distribution of Bolted Glass Connections under In-Plane Loads"*. PhD Disseratation, München, Germany, Technische Universität München.

Maniatis I., 2006b. "Spannungsermittlung punktgelagerter Verglasungen unter Beanspruchung in Scheibenebene". *Stahlbau*, 75(8), pp. 658–662.

Marannano G.V., Mistretta L., Cirello A. & Pasta S., 2008. "Crack growth analysis at adhesive-adherent interface in bonded joints under mixed mode I/II". *Engineering Fracture Mechanics*, 75(18), pp. 5122–5133.

Marckmann G. & Verron E., 2006. "Comparison of Hyperelastic Models for Rubber-Like Materials". *Rubber Chemistry and Technology*, 79(5), pp. 835–858.

Marlow R.S., 2003. "A general first-invariant hyperelastic constitutive model". In *Constitutive Models for Rubber III: Proceedings of the Third European conference on constitutive models for rubber*. London, UK, pp. 157–160.

Maslov K., 2000. "A new technique for the ultrasonic detection of internal transverse cracks in carbon-fibre/bismaleimide composite laminates". *Composites Science and Technology*, 60(12-13), pp. 2185–2190.

McCarthy J.C., 1996. *MTS Adhesive Project 2: Failure modes and criteria - Report no. 6: failure criteria for adhesive joints - Summary report*, Oxfordshire, UK.

Meunier L., Chagnon G., Favier D., Orgéas L. & Vacher P., 2008. "Mechanical experimental characterisation and numerical modelling of an unfilled silicone rubber". *Polymer Testing*, 27(6), pp. 765–777.

Miehe C., 2004. "A micro-macro approach to rubber-like materials?Part I: the non-affine micro-sphere model of rubber elasticity". *Journal of the Mechanics and Physics of Solids*, 52(11), pp. 2617–2660.

Mises R.V., 1913. "Mechanik der festen Körper im plastisch- deformablen Zustand. Nachrichten von der Gesellschaft der Wissenschaften zu Göttingen", *Mathematisch-Physikalische Klasse*, pp. 582–592.

Mocibob D. & Belis J., 2010. "Coupled experimental and numerical investigation of structural glass panels with small slenderness subjected to locally introduced axial compression". *Engineering Structures*, 32(3), pp. 753–761.

Mocibob D. & Crisinel M., 2007. "Glass panel under in-plane shear loading: Experimental investigation on structural glass panel point support". In *Glass Performance Days 2007*. Tampere, Finland, pp. 380–383.

Mooney M., 1940. "A Theory of Large Elastic Deformation". *Journal of Applied Physics*, 11(9), p. 582-592.

Mostovoy S., Crosley P. & Ripling E., 1967. "Use of crack-line-loaded specimens for measuring plane-strain fracture toughness". *Journal of Materials*, 2, pp. 661–681.

Mubashar A., Ashcroft I.A., Critchlow G.W. & Crocombe A.D., 2009. "Moisture absorption-desorption effects in adhesive joints". *International Journal of Adhesion and Adhesives*, 29, pp. 751–760.

NBN EN 12150-1, 2015. *Glass in building - Thermally toughened soda lime silicate safety glass - Part 1: Definition and description.*

NBN EN ISO 9142: 2004, 2004. *Adhesives - Guide to the selection of standard laboratory ageing conditions for testing bonded joints (ISO 9142:2003).*

NBN EN ISO12543-4:2011, 2011. *Glass in building - Laminated glass and laminated safety glass - Part 4: Test methods for durability.*

NEN 2608, 2014. *Glass in building - Requirements and determination method.*

Nguyen T.C., Bai Y., Zhao X.L. & Al-Mahaidi R., 2012. "Effects of ultraviolet radiation and associated elevated temperature on mechanical performance of steel/CFRP double strap joints". *Composite Structures*, 94(12), pp. 3563–3573.

Nhamoinesu S. & Overend M., 2012. "The Mechanical Performance of Adhesives for a Steel-Glass Composite Façade System". In *Challenging Glass 2*. Delft, The Netherlands, pp. 293–306.

Nielsen J.H., Olesen J.F., Poulsen P.N. & Stang H., 2009. "Simulation of residual stresses at holes in tempered glass: a parametric study". *Materials and Structures*, 43(7), pp. 947–961.

Nogueira P., Ramírez C., Torres A., Abad M.J., Cano J., López J., López-Bueno I. & Barral L., 2001. "Effect of Water Sorption on the Structure and Mechanical Properties of an Epoxy Resin System". *Journal of Applied Polymer Science*, 80, pp. 71–80.

Ogden R.W., 1972. "Large Deformation Isotropic Elasticity - On the Correlation of Theory and Experiment for Incompressible Rubberlike Solids". *Proceedings of the Royal Society A: Mathematical, Physical and Engineering Sciences*, 326(1567), pp. 565–584.

Ogden R.W., Saccomandi G. & Sgura I., 2004. "Fitting hyperelastic models to experimental data". *Computational Mechanics*, 34(6), pp. 484–502.

Ojalvo I.U. & Eidinoff H.L., 1978. "Bond Thickness Effects upon Stresses in Single-Lap Adhesive Joints". *American Institute of Aeronautics and Astronautics (AIAA) Journal,* 16(3), pp.204–211.

ÖNORM B 3716-1, 2009. *Glass in building — Structural glass construction — Part 1: Basic principles*, ON, Austria.

Outeiro J.C., Umbrello D. & M'Saoubi R., 2006. "Experimental and numerical modelling of the residual stresses induced in orthogonal cutting of AISI 316L steel". *International Journal of Machine Tools and Manufacture*, 46(14), pp. 1786–1794.

Overend M. & Zammit K., 2012. "A computer algorithm for determining the tensile strength of float glass". *Engineering Structures*, 45, pp. 68–77.

Overend M., 2005. "Optimising connections in structural glass". In *2nd International Conference on Glass in Buildings*. Bath, UK, pp. 179–188.

Overend M., Jin Q. & Watson J., 2011. "The selection and performance of adhesives for a steel–glass connection". *International Journal of Adhesion and Adhesives*, 31(7), pp. 587–597.

Overend M., Nhamoinesu S. & Watson J., 2013. "Structural Performance of Bolted Connections and Adhesively Bonded Joints in Glass Structures". *Journal of Structural Engineering*, pp. 1–12.

Panait A., He Q., Morcant K. & Cossavella M., 2005. "Friction-grip Bolted Connections for Structural Glass Elements : Practical Solutions Using an Experimental and Numerical Coupled Approach". In *Glass Processing Days 2005*. Tampere, Finland, pp. 471–475.

Peeters F. & Kussner M., 1999. "Material law selection in the finite element simulation of rubber-like materials and its practical application in the industrial design process". In *Proceedings of the First European Conference on Constitutive Models for Rubber*. Vienna, Austria, pp. 29–36.

Pethrick R.A., 2015. "Design and ageing of adhesives for structural adhesive bonding - A review". *Journal of Materials: Design and Applications*, 229(5), pp. 349–379.

Petrie E.M., 2000. "Handbook of adhesives and sealants", New York, USA: McGraw-Hill Education.

Petrie E.M., 2011. "How Moisture Affects Adhesives, Sealants, and Coatings". *Metal Finishing*, 109(7), pp. 36–48.

prEN 16612, 2013. *Glass in building — Determination of the load resistance of glass panes by calculation and testing*,

Pucci E. & Saccomandi G., 2002. "A Note on the Gent Model for Rubber-Like Materials". *Rubber Chemistry and Technology*, 75(5), pp. 839–852.

Puller K. & Sobek W., 2008. "Glass-Steel Connections Using Acrylate Adhesives". In *Challenging Glass*. Delft, The Netherlands, pp. 273–278.

Pye A. & Ledbetter S., 1998. "The selection of an adhesive for the construction of a glass-adhesive T-beam". *International Journal of Adhesion and Adhesives*, 18(3), pp. 159–165.

Radim V., Eliasova M. & Netusil M., 2008. "Connections of glass structures by used shear bolts in a row". In *Eurosteel 2008*. Graz, Austria, pp. 923–928.

Raoult I., Stolz C. & Bourgeois M., 2005. "A constitutive model for the fatigue life prediction of rubber". In *Constitutive Models for Rubber IV: Proceedings of the fourth European conference for constitutive models for rubber*. Stockholm, Sweden, pp. 129–134.

Rex C.O., Asce M. & Easterling W.S., 2003. "Behavior and Modeling of a Bolt Bearing on a Single Plate". *Journal of Structural Engineering*, 129(6), pp. 792–800.

Rivlin R.S., 1948. "Large Elastic Deformations of Isotropic Materials. IV. Further Developments of the General Theory". *Philosophical Transactions of the Royal Society of London A: Mathematical, Physical and Engineering Sciences*, 241(835).

Rivlin R.S. & Saunders D.W., 1997. "*Large Elastic Deformations of Isotropic Materials*". In Collected Papers of R.S. Rivlin: Volume I and II. New York, USA: Springer New York, pp. 157–194.

Rodichev Y., Maslov V., Netychuk A., Bodunov V. & Yevplov Y., 2007. "Bending strength and fracture of glass materials under the different loading conditions". In *Glass Performance Days 2007*, Tampere, Finland, pp. 615–618.

Roesler F.C., 1956. "Brittle fractures near equilibrium". *Proceedings of the physical society*, 69, pp. 981–992.

Rosu L., Cascaval C.N., Ciobanu C., Rosu D., Ion E.D., Morosanu C. & Enachescu M., 2005. "Effect of UV radiation on the semi-interpenetrating polymer networks based on polyurethane and epoxy maleate of bisphenol A". *Journal of Photochemistry and Photobiology A: Chemistry*, 169(2), pp. 177–185.

Roylance D., 2001. *"Engineering viscoelasticity"*, Cambridge, USA: Massachusetts Institute of Technology.

Sadev, 2015. *V 2105 Glass drilling*, datasheet

Santarsiero M. & Louter C., 2013. "Embedded and point laminated adhesive connections for glass structures : parametric non-linear numerical investigations". In *Glass Performance Days 2013*. Tampere, Finland, pp. 265–273.

Santarsiero M. & Louter C., 2016. "Failure Criteria for SentryGlas® Ionomer and TSSA Silicon : A Theoretical Introduction to a Novel Generalized Triaxial Model (GTM)". In *Challenging Glass 5*, Ghent, Belgium, pp. unknown.

Santarsiero M., 2015. "*Laminated connections for structural glass applications*". PhD Disseratation, Lausanne, Switzerland, École Polytechnique Fédérale de Lausanne.

Santarsiero M., Louter C. & Lebet J., 2013. "Parametric numerical investigation of adhesive laminated point connections". In *COST Action TU0905 Mid-term Conference on Structural Glass*. Poreč, Croatia, pp. 507–516.

Santarsiero M., Louter C. & Lebet J., 2014. "The mechanical behavior of SentryGlas® and TSSA laminated polymers in cured and uncured state in uniaxial tensile test". In *Challenging Glass 4 & COST Action TU0905 Final Conference*. Lausanne, Switzerland, pp. 375–384.

Sasso M., Palmieri G., Chiappini G. & Amodio, D., 2008. "Characterization of hyperelastic rubber-like materials by biaxial and uniaxial stretching tests based on optical methods". *Polymer Testing*, 27(8), pp. 995–1004.

Schellekens J. & De Borst R., 1990. "The use of the Hoffman yield criterion in finite element analysis of anisotropic composites". *Computers & Structures*, 37(6), pp. 1087–1096.

Seel,M. & Siebert G., 2012. "Analytische Lösungen für Kreis- und Kreisringplatten unter symmetrischer und antimetrischer Einwirkung". *Stahlbau*, 81(9), pp. 711–718.

Seibert D.J. & Schöche N., 2000. "Direct Comparison of Some Recent Rubber Elasticity Models". *Rubber Chemistry and Technology*, 73(2), pp. 366–384.

Seneviratne W., Tomblin J. & Davies C., 2010. "Alternative method for adhesive characterization". In *International Conference on Composites/Nano Engineering 18*. Alaska, USA, p. 404-406.

Siebert B., 2003. "Calculation of Point Bearings for Glass as Load- Bearing Element in Structural Engineering". In *Glass Processing Days 2003*. Tampere, Finland, pp. 758–761.

Siebert B., 2006. "Anforderungen für ein Berechnungskonzept für die Bemessung punktgelagerter Verglasungen". *Stahlbau*, 75(8), pp. 652–657.

Siebert B., 2007. "Safety aspects of point-fixed glass constructions". In *Glass Performance Days 2007*. Tampere, Finland, pp. 432–436.

Siebert G. & Herrmann T., 2010. "Glazing with countersunk point fittings". In *Challenging Glass 3*. Delft, The Netherlands, pp. 335–348.

Siebert G., 2005. "New Generation of Point Fixings – Architecture and Safety Aspects". In *Glass Processing Days 2005*. Tampere, Finland, pp. 530–533.

Silvestru V.A. & Englhardt O., 2014. "Application study for hybrid adhesively bonded glass-steel façade elements". In *Challenging Glass 4 & COST Action TU0905 Final Conference*. Lausanne, Switzerland, pp. 277–284.

Singh A.K., 2007. *"Mechanics of Solids"*, New Jersey, USA: Prentice Hall of India.

Sitte S. & Wolf A., 2012. "TSSA-bonded point-supported structural glazing of insulating glass units at Dow Corning's European Distribution Center". In *Engineered transparency International Conference at Glasstec*. Düsseldorf, Germany, pp. unknown.

Sitte S., Brasseur M., Carbary L. & Wolf A., 2011. "Preliminary Evaluation of the Mechanical Properties and Durability of Transparent Structural Silicone Adhesive (TSSA) for Point Fixing in Glazing" *Journal of ASTM International*, 8(10), pp. 1–27.

Soudal, 2003. *Soudaseal 270HS*, datasheet.

Steinchen W., Yang L.X., Kupfer G. & Maeckel P., 1997. "Nondestructive testing of microcracks using digital speckle pattern shearing interferometry". In *Lasers and Optics in Manufacturing II*, Munich, Germany, pp. 528–535.

Steiner K.V., Eduljee R.F., Huang X. & Gillespie J.W., 1995. "Ultrasonic NDE techniques for the evaluation of matrix cracking in composite laminates". *Composites Science and Technology*, 53(2), pp. 193–198.

Steinmann P., Hossain M. & Possart G., 2012. "Hyperelastic models for rubber-like materials: consistent tangent operators and suitability for Treloar's data". *Archive of Applied Mechanics*, 82(9), pp. 1183–1217.

Stumpf F. & Marczak R., 2010. "Optimization of constitutive parameters for hyperelastic models satisfying the Baker-Ericksen inequalities". In *Mecánica Computacional Vol XXIX*, Buenos Aires, Argentina, pp. 2901-2916.

Sutton M., Orteu J. & Schreier H., 2009. *"Image correlation for shape, motion and deformation measurements"*. New York, USA: Springer, New York.

Tavrou S., Siores E. & Sbarski I., 2002. "Ultrasonic Inspection of Adhesive Bonds", In *Profiles in Industrial Research: Knowledge and Innovation 2002*, Melbourne, Australia, pp. 115-121.

The Adhesive and Sealant Council, 2009. "Surface treatment". *Metal Finishing*, 98, pp.73.

Tibolt M., Hechler O. & Odenbreit C., 2013. "Numerical investigation of insulation glass units with undercut point fittings". In *COST Action TU0905 Mid-term Conference on Structural Glass*. Poreč, Croatia, pp. 437–445.

Toh S.L., Shang H.M., Chau F.S., Tay C.J. & Tay T.E., 1991. *"Fracture of Engineering Materials and Structures"*. Dordrecht, The Netherlands: Springer Netherlands,

Tournoy K., 2014. *"Onderzoek naar het gedrag van adhesieve puntverbindingen tussen floatglas en metaal onder multi-axiale belasting"*. Thesis Disseratation, Ghent, Belgium, Universiteit Gent.

Treloar L.R.G., 1943. "The elasticity of a network of long-chain molecules-II". *Transactions of the Faraday Society*, 39(2), pp. 241–246.

Treloar L.R.G., 1975. "*The Physics of Rubber Elasticity*", Oxford, UK: Oxford University Press.

Truesdell C., Noll W. & Pipkin A.C., 2004. "*The Non-Linear Field Theories of Mechanics*", Berlin, Germany: Springer, Berlin.

Van Hulle A., Belis J., Callewaert D. Scheerlinck L. & Out Bas., 2011. "Development of structural adhesive point-fixings". In *Glass Performance Days 2011*. Tampere, Finland, pp. 661–64.

Van Lancker B., Dispersyn J., Belis J., Hertelé S., De Waele W. & De Corte, W., 2016a. "Application of digital image correlation in linear structural adhesive glass-metal connection testing". In *GlassCon Global 2016*, Boston, USA, pp. 305–313.

Van Lancker B., Dispersyn J., De Corte W. & Belis J., 2016b. "Durability of adhesive glass-metal connections for structural applications". *Engineering Structures*, 126, pp. 237–251.

Van Straalen I., 2001. "*Development of design rules for structural adhesive bonded joints: a systematic approach*". PhD Disseratation, Delft, The Netherlands, Technische Universiteit Delft.

Vandebroek M., 2014. "*Thermal Fracture of Glass*", PhD Disseratation, Ghent, Belgium, Universiteit Gent.

Vogt D., 2009. "*Durability of Adhesively Boned Stainless Steel Joints under Accelerated Ageing Conditions*", PhD Dissertation Kaiserslautern, Germany, Technische Universität Kaiserslautern.

Volkersen O., 1938. "Die Nietkraftverteilung in zugbeanspruchten Nietverbindungen mit konstanten Laschenguerschnitten". *Luftfahrtforschung*, 15(1), pp. 41–47.

Vyzantiadou M.A. & Avdelas A.V., 2004. "Point fixed glazing systems: technological and morphological aspects". *Journal of Constructional Steel Research*, 60(8), pp. 1227–1240.

Wang M.C. & Guth E., 1952. "Statistical Theory of Networks of Non-Gaussian Flexible Chains". *The Journal of Chemical Physics*, 20(7), pp. 1144.

Weller B. & Kothe C., 2011. "Investigation of surface modifi cation methods to improve adhesive joints in glass construction". In *Glass Performance Days 2011*. Tampere, Finland, pp. 677–680.

Weller B. & Schadow T., 2007. "Designing of bonded joints in glass structures". In *Glass Performance Days 2007*. Tampere, Finland, pp. 74–76.

Weller B. & Tasche S., 2005. "Adhesive Fixing in Glass Construction". In *Glass Processing Days 2005*. Tampere, Finland, pp. 265–268.

Weller B. & Vogt I., 2008. "Calculating Bonded Joints with Acrylates". In *Challenging Glass*. Delft, The Netherlands, pp. 295–300.

Weller B. & Vogt I., 2009. "Determination of Material Properties for Light- Curing Acrylates". In *Glass Performance Days 2009*. Tampere, Finland, pp. 363–365.

Weller B., Nicklisch F. & Wünsch J., 2009. "Dynamic Behaviour of Adhesives for Structural Glass Applications". In *Glass Performance Days 2009*. Tampere, Finland, pp. 366–370.

Wellershoff F., Sedlacek G. & Kasper R., 2004. "Design of joints, members and hybrid elements for glass structures". In *International Symposium on the application of architectural glass (ISAAG) 2004*. pp. unknown.

Whitney J. & Nuismer R., 1974. "Stress fracture criteria for laminated composites containing stress concentrations". *Journal of composite materials*, 8(3), pp. 253–265.

Wiederhorn S.M., 1967. "Influence of Water Vapor on Crack Propagation in Soda-Lime Glass". *Journal of American Ceramic Society*, 50, pp. 407–414.

Williams J.G., 1989. "End corrections for orthotropic DCB specimens". *Composites Science and Technology*, 35(4), pp. 367–376.

Wolf A., 1999. *"Durability of Building Sealants: State-of-the-art Report of RILEM Technical Committee 139-DBS, Durability of Building Sealants"*, Cachan, France: RILEM Publications S.A.R.L.

Woo R., Zhu H., Leung C. & Kim J., 2008. "Environmental degradation of epoxy-organoclay nanocomposites due to UV exposure: Part II residual mechanical properties". *Composites Science and Technology*, 68(9), pp. 2149–2155.

Xu L.R., Sengupta S. & Kuai H., 2004. "An experimental and numerical investigation of adhesive bonding strengths of polymer materials". *International Journal of Adhesion and Adhesives*, 24(6), pp.455–460.

Yeoh O. & Fleming P., 1997. "A new attempt to reconcile the statistical and phenomenological theories of rubber elasticity". *Journal of Polymer Science-B-Polymer*.

Yeoh O.H., 1990. "Characterization of Elastic Properties of Carbon-Black-Filled Rubber Vulcanizates". *Rubber Chemistry and Technology*, 63(5), pp. 792–805.

Yeoh O.H., 1993. "Some Forms of the Strain Energy Function for Rubber". *Rubber Chemistry and Technology*, 66(5), pp. 754–771.

Young W. & Budynas R., 2002. *"Roark's formulas for stress and strain"*, New York, USA: McGraw Hill Professional.

Yu X., Crocombe A. & Richardson G., 2001. "Material modelling for rate-dependent adhesives". *International Journal of Adhesion and Adhesives*, 21(3), pp. 197–210.

Yuan, H. & Xu, Y., 2008. "Computational fracture mechanics assessment of adhesive joints". *Computational Materials Science*, 43(1), pp. 146–156.

Zangenberg J., Poulsen S.H., Bagger A., Stang H. & Olesen J.F., 2012. "Embedded adhesive connection for laminated glass plates". *International Journal of Adhesion and Adhesives*, 34, pp. 68–79.

Zhang F., Wang H.P., Hicks C., Yang X. Carlson, B.E. & Zhou Q., 2013. "Experimental study of initial strengths and hygrothermal degradation of adhesive joints between thin aluminum and steel substrates". *International Journal of Adhesion and Adhesives*, 43, pp. 14–25.

Zhao X.L. & Adams R.D., 1989. "Adhesive joint strength predictions for real boundary conditions". In *Proceedings of Structural Adhesives in Engineering II*, London, UK, pp. unknown.

Zhao X.L., 1991. "*Stress and failure analysis of adhesively bonded joints*". PhD Disseratation, Bristol, UK, University of Bristol.

Zhou Y., Jiang K., Gou M., Li N., Zhu P., Wang D. & Qu Z., 2014. "Prediction of debonding strength of tensile hybrid bonded joints using fracture mechanics". *Materials & Design*, 61, pp. 87–100.